



HAL
open science

p-block elements as negative electrode materials for Magnesium-ion batteries : electrochemical mechanism and performance

Fabrizio Murgia

► **To cite this version:**

Fabrizio Murgia. p-block elements as negative electrode materials for Magnesium-ion batteries : electrochemical mechanism and performance. Other. Université Montpellier, 2016. English. NNT : 2016MONTT210 . tel-01759234

HAL Id: tel-01759234

<https://theses.hal.science/tel-01759234>

Submitted on 5 Apr 2018

HAL is a multi-disciplinary open access archive for the deposit and dissemination of scientific research documents, whether they are published or not. The documents may come from teaching and research institutions in France or abroad, or from public or private research centers.

L'archive ouverte pluridisciplinaire **HAL**, est destinée au dépôt et à la diffusion de documents scientifiques de niveau recherche, publiés ou non, émanant des établissements d'enseignement et de recherche français ou étrangers, des laboratoires publics ou privés.

THÈSE

Pour obtenir le grade de
Docteur

Délivré par l'**Université de Montpellier**

Préparée au sein de l'école doctorale
Sciences Chimiques Balard
Et de l'unité de recherche Institut Charles Gerhardt
Montpellier – UMR 5253

Spécialité : **Chimie et Physicochimie des Matériaux**

Présentée par **Fabrizio MURGIA**

***p*-block elements as negative electrode
materials for Magnesium-ion batteries:
electrochemical mechanism and
performance**

Soutenue le 3 Novembre 2016 devant le jury composé de

Pr. Jean-Louis BOBET	Université de Bordeaux - ICMCB	Referee
Pr. Robert DOMINKO	Nat. Institute of Chemistry - Slovenia	Referee
Pr. Pétr NOVAK	Paul Scherrer Institut - Switzerland	Examiner
Dr. Sébastien MARTINET	CEA Grenoble	Examiner
Pr. Lorenzo STIEVANO	Université de Montpellier - ICGM	Director
Dr. Romain BERTHELOT	Université de Montpellier - ICGM	Co-supervisor



Acknowledgements

The PhD thesis is not just a three-year job that at the end gives us a title. It's a veritable trip along an unstoppable turn of events that, as in a roller-coaster, you can't control all the time: as Lorenzo said during my defence we wanted to start from something but actually we arrived, even with a lot of satisfaction, to a completely different point. So you just have to enjoy the ride and know that at the end you can turn back, recognising how mad it was. And then you feel a better student, chemist, person.

So for everything that this experience gave to me I have to deeply acknowledge some people: take a seat, the list could be long.

First of all I want to deeply acknowledge the Jury that accepted to referee and examine this PhD thesis. All the members have brought interesting remarks and comment which undoubtedly increased the overall quality of the present work. Moreover their interesting questions led to a stimulating and fruitful discussion during the defence. Thank you also for your positive comments on the overall quality of this work.

If this work has been positively judged the merit is mainly due to my supervisors: the director of the thesis Professor Lorenzo Stievano and the Doctor Romain Berthelot. I have been really lucky to have such chiefs. Lorenzo has been always there, he's paid every time a lot of attention to my work and he's took every time the best decision during these three years. Thank also for introducing me to your fantastic family (many thanks to Isabella and Antonio, too!) and thank you very much for the concert in the cave, the theatre, the Montpeyroux wine festival and for last Easter!

Romain was the actual engine of my thesis: he's the chance to still have the time for working into the lab and this was crucial for me: we almost never had meetings, simply because we worked together all along these three years, we both start headlong into this new subject and we share all the knowledge that we achieve along the days. To be more precise, I've learn an enormous number of skills in all the fields: how to approach a new topic, the methodology of work, the interpretation of data not limited to the result that one can achieve at first sight, the will to keep on to obtain the maximum from the work. And the list could be longer. Thank you very much for all, for all the effort that you put in my thesis, in all the aspects. Thank you also for the friendship and the constant help outside the lab. I hope we will keep collaborating! Thank you also to Léa and all the best for you two and for the future little chemist!

Huge thanks to my former supervisors at the University of Sassari: Prof. Stefano Enzo, Prof. Gabriele Mulas and Dr. Sebastiano Garroni that gave me solid basis to afford the PhD adventure.

Thanks to all the AIME team and in particular to the people of BAT team. Starting from the chief Laure Monconduit that even if did not directly supervise my work, she has been always present and interested in all my projects and progress, always bringing its experience and knowledge. I must deeply acknowledge also the research engineers Bernard Fraisse, Julien Fullenwarth and Moulay Tahar Srougati, for their competence and helpfulness.

Thanks to the other BAT members: Nicolas Louvain, Nicolas Bibent, Laurent Aldon, Pierre-Emmanuel Lippens for the enriching exchanges and Olivier Fontaine and Marie-Liesse Doublet for the fruitful discussion that help me to understand the problems related on both practical and theoretical approach to the electrochemistry. Thank you also to Dr. Antonella Iadencola for its work at SOLEIL synchrotron, Danielle Lauencin for the NMR measurements, Monique Tillard for the FAAS analysis, Didier Cot (IEM) for the SEM images, Sara Cavaliere and Evelina Colacino.

A special thanks to the closest people with I shared this adventure: the “burodufond”, starting by the commander Doctor David Duveau, with I’ve had many excellent moments along the first two years of thesis (Requista I and II, LiBD in Arcachon, and so on) and that introduces me to a very special group of people here in Montpellier (See below). Many thanks to Philippe Antitomaso, doctor within few days, which I proudly share the work on the CP synthesis with. Thank you for the laughter, the ski (thanks to Laura too), the excellent sight from your flat, the FIFA matches and the helpfulness in every moment. Thanks also to almost doctor Alix Ladam, which even if was placed in the office at the lower floor, has share this years with us. Many thanks for the excellent weekend that allows me to discover the Ocean. I hope that new PhD students have the same cohesion that we had: Gael Coquil, that’s for you! And thank you very much too!

Many thanks to the other people that for different reason works on the AIME team: Fred, Sara, Fred again, Marie, Cathy, Anne-Marie, Fabrice, ... Thanks also to all the PhD student, post-docs, master’s students that were and are in our team and in the building 15: Ali, Khalil, Laura, Linda, Nacho, Youn, Aude, Vincent, Romain, Ephrem, Dimitri, Angelo, Rakhi, Anna, Susan, Delhia, Fatma, Hao, Aurelien, Nacho, Vincent, Paul, Paul (allez le verts), Surya, Emmeline, David,... A special thought for Julien and its family.

Thank you very much to the Italian crew: Nicola, Stefano, Filippo, Eliana, Giorgio, Francesco, Luca, thank you to bring the Italian way of life inside and outside the lab: keep speaking loud, eating pasta and sharing all that with the baguette-eaters.

An enormous thanks should be deserved to the potes de Montpellier, Dr Jo, Manon, Camille, Matou, Laura, Seb, Antoine, Agathe, Anja, Coralie: it’s thank to you if I’ve learn French, the French

culture and way of life and if my experience here was so extraordinary. Thank you for making discover your birthplaces, your families, your roots. A special thanks to the fights against Camille when the blood amount in the alcohol neared dangerously low limits and for the useful book of sentences to use in case that you are in such condition. I hope that we can still keep sharing all of this and you all know that next reunion should be done “on an island”.

Thank you also to the other people that I’ve met in Montpellier, starting to my flatmate Barbara and all the other fantastic people: Ewelina, Laurent, Safa, Simona, Nobuko, Kaito, Loic, ...

Thank you to the people that supported me beyond the Mediterranean Sea: Pierluigi, Alberto, Beatrice, Claudio, Michele and all my friends and colleagues in Sassari: Antonio, Valeria, Valentina, Elisa, Francesca, Nina, Stefano, Alessio, Elisabetta, ...

Thank you to all my family and especially to my mother. They support me all the time and are always there.

Finally, I want to say thank you to my girlfriend Sara: it has been difficult to stay so far but we know that we’ve managed to do it thank to our love. All the fears disappear when we are together. All is easier when there is the love.

Abstract

One of the most challenging hurdles that the World has to face in the next decades is the sustainable use of energy. In a scenario where western societies are largely dependent of the fossil fuels for maintaining their wellness, *i.e.*, for heating, automotive transportation and electricity production, and developing countries need to feed their growing economies, it is worth underlying both the major impact on the environment due to the indiscriminate use of such combustibles but also the geopolitical issues for the non-producing countries. Energy harvesting by renewable sources can help limiting the dependence on fossil fuels but cannot perfectly replace conventional power plants due to the intrinsic intermittency of renewable energy sources.

Batteries are the devices that can solve this situation, since they can stock the energy surplus when the plant is operating and then feed it to the power grid when there is a lack of production. Moreover, they are also targeted to fulfil the even growing demand of energy for portable applications (mobile phones and computers, and nowadays cars and trucks). The excellent performance and the well-established technology of Lithium-ion batteries (LIBs) put them in a crucial position for supporting this new energy revolution. However their ubiquitous role has been recently questioned for two main reasons: i) of the low availability of Li, which is a rare and not-uniformly spread element that may lead to the similar problems caused by fossil fuels. And ii) the effective capacity to satisfy the highly energy-demanding applications, since Li-ion technology seems reaching its upper limit in terms of overall performance. Therefore cheaper and more powerful alternative to Li-based systems are needed.

Post-Lithium-based batteries, based on other charge carriers than Li^+ , may represent a safer, more sustainable and performing alternative to LIBs. Mg is a promising candidate to replace Li in electrochemical systems due to its abundance, low cost and a theoretical volumetric capacity twice as high as that of Li. Although the efforts devoted to the realization of rechargeable Mg batteries were made in the last 15 years, the major hurdle represented by the low compatibility between metallic Mg and conventional electrolytes still obliges the use of hazardous salt/solvent mixtures in research prototypes. Searching negative electrodes alternative to the Mg metal, *i.e.*,

compounds able to reversibly react with Mg at low potential, may pave the way for a veritable Magnesium-ion battery (MIB), allowing the use of conventional electrolytes.

The present thesis is devoted to investigate the electrochemical behaviour of several *p*-block elements that can reversibly alloy with Mg at low potential (In, Sn, Sb, Bi). Possible synergies between these elements are also explored, realizing composite materials (Sn-Bi), solid solutions ($\text{Bi}_x\text{Sb}_{1-x}$) or intermetallic phases (InBi) that are employed as negative electrodes in MIBs. The chosen synthetic route for obtaining micrometric-sized particles is mechanical milling/alloying, since it is simple, cost-effective and easily upscalable. Particular attention is paid to the study of electrochemical mechanisms via *operando* X-ray diffraction. The evaluation of the electrochemical performance allows selecting the best candidate for an effective test as negative electrode in a MIB prototype.

Résumé

Parmi les défis que le Monde devra affronter dans les prochaines décennies, le plus difficile est l'utilisation de sources d'énergie durables. Dans un scénario où les sociétés occidentales sont fortement dépendantes des combustibles fossiles pour garder leur niveau de bien-être (chauffage domestique, transport et production d'électricité), complété par les pays en voie de développement qui ont besoin d'alimenter leurs économies croissantes, il est nécessaire de souligner l'impact négatif sur l'environnement causé par l'utilisation de ces ressources fossiles mais aussi les problèmes géopolitiques pour les pays « non producteurs ». La collecte d'énergie provenant des sources renouvelables peut limiter la dépendance des combustibles fossiles, pourtant cette dernière ne peut remplacer les centrales électriques classiques à cause de son caractère intermittent.

Les batteries sont des dispositifs qui peuvent résoudre définitivement cette limitation, puisqu'elles sont capables d'accumuler l'excès d'énergie produit afin de le délivrer au moment souhaité. De plus elles ont été envisagées comme les dispositifs principaux pour toutes les applications portables (téléphones et ordinateurs portables mais aussi véhicules). Grâce à leurs excellentes performances et leur technologie bien développée, les batteries lithium-ion ont un rôle déterminant dans le support de cette nouvelle révolution énergétique. Pourtant leur usage répandu a été récemment remis en question à cause de la faible disponibilité de lithium, qui est un élément rare et concentré seulement dans certaines zones du monde. L'emploi du lithium pourrait donc engendrer les mêmes problèmes que les combustibles fossiles. De plus, cette technologie semble avoir atteint son niveau de développement maximal et ne pourrait plus être suffisante pour satisfaire des applications de plus en plus énergivores. Il est donc nécessaire d'envisager des alternatives au lithium en axant les recherches sur des ressources plus abondantes que lithium et à moindre coût mais aussi sur des systèmes plus performantes.

Les batteries post-lithium, qui sont basées sur d'autres porteurs de charges que le Li^+ , pourrait représenter des alternatives plus sécurisées, respectueuses de l'environnement et aussi plus attractives en termes de capacité stockée. Le magnésium est un candidat prometteur pouvant remplacer le lithium dans les systèmes électrochimiques de stockage d'énergie, grâce à son abondance, son faible

coût et sa capacité volumique qui est doublé par rapport à celle du lithium. Cependant, l'obstacle le plus important au développement des batteries rechargeables au magnésium est la mauvaise compatibilité entre les électrolytes classiques et le magnésium métal. Dans cette optique il est encore nécessaire d'utiliser des mélanges de sels/solvants extrêmement dangereux dans les prototypes proposés. En revanche, la recherche de possible alternatives au magnésium métal, c.-à-d. des matériaux capable de réagir à bas potentiel avec le Mg, permettrait de réaliser une véritable batterie magnésium-ion (MIB), compatible avec des formulations d'électrolyte classiques.

Cette thèse est dédiée à l'investigation des propriétés électrochimiques de plusieurs éléments du bloc *p* (In, Sn, Sb, Bi) qui peuvent s'allier réversiblement avec le Mg à bas potentiel. Des possibles synergies entre ces éléments ont été aussi explorées, en étudiant des composés de nature différente (composite Sn-Bi, solution solide $\text{Bi}_x\text{Sb}_{1-x}$ et phase intermétallique InBi) qui pourraient être employés comme électrodes négatives pour MIBs. Des poudres micrométriques ont été obtenues par broyage/alliage mécanique, technique de synthèse simple à mettre en œuvre. Une attention particulière a été portée à l'étude des mécanismes électrochimiques d'alliage, qui a été réalisé par diffraction des rayons X en mode *operando*. L'évaluation des performances électrochimiques a permis de sélectionner le meilleur candidat qui a été ensuite teste comme électrode négative dans un prototype de batterie magnésium-ion.

Table of Contents

I Introduction..... 9

1.1.	General context	9
1.2.	Batteries' overview	14
1.3.	Li-ion technology	17
1.4.	Beyond Li-ion? Resources, consumption, forecasts	19
1.5.	Na-ion technology	22
1.5.1.	Alloy-type negative electrodes for NIBs	24
1.6.	Punching more electrons per cation: multivalent elements	25
1.6.1.	Calcium.....	27
1.6.2.	Zinc	29
1.6.3.	Aluminium	29
1.7.	Magnesium.....	30
1.7.1.	Stripping/plating on Mg metal.....	33
1.7.2.	Electrolytes.....	34
1.7.3.	Positive electrodes.....	43
1.7.3.1.	Chevrel phases	44
1.7.3.2.	Other positive electrodes.....	47
1.7.4.	Negative electrodes	53
1.7.4.1.	Sb and Bi.....	53
1.7.4.2.	Sn.....	57
1.7.4.3.	Pb.....	60
1.7.4.4.	Other elements	61
1.8.	Conclusion and aim of the work.....	62

II Experimental section: methods and characterizations.....65

2.1.	Mechanical milling and alloying	65
2.2.	Characterization techniques	70
2.2.1.	X-rays diffraction (XRD)	70
2.3.	Electrode formulation	74
2.3.1.	Self-supported electrode	74
2.3.2.	Electrodes casted on metallic current collectors	76
2.3.3.	Preparation of the electrolytes	78
2.3.3.1.	EtMgCl/2Et ₂ AlCl in THF	78
2.3.3.2.	Other formulations	79
2.4.	Electrochemical tests	80
2.4.1.	Cell preparation	81
2.4.1.1.	Cyclic voltammetry	82
2.4.1.2.	Galvanostatic Cycling with Potential Limitation	83
2.4.1.3.	Galvanostatic Intermittent Titration Technique	85
2.5.	Coupled analyses	86
2.5.1.	<i>Operando</i> XRD	86

III Screening on *p*-block elements.....89

3.1.	Sn.....	89
3.2.	Sb.....	96
3.3.	Bi	97
3.3.1.	Bi-Mg reversible alloying reaction.....	99
3.3.2.	<i>Operando</i> XRD study	103
3.3.3.	Performance evaluation.....	106
3.3.4.	Mg ₃ Bi ₂	110
3.4.	Indium.....	115
3.4.1.	<i>Operando</i> XRD analysis	118
3.4.2.	Performance evaluation	120
3.4.3.	MgIn	122
3.5.	Conclusions	124

IV Synergy between Bi and other elements..... 125

4.1.	Sn-Bi.....	126
4.1.1.	<i>Operando</i> XRD	130
4.1.2.	Performance evaluation of different Sn-Bi mixtures.....	132
4.2.	$\text{Bi}_x\text{Sb}_{1-x}$	138
4.3.	InBi.....	145
4.3.1.	Electrochemical mechanism	147
4.3.2.	Electrochemical performance	155
4.4.	Conclusions	159

V Perspectives – Toward a full Mg-ion battery..... 161

5.1.	Synthesis of a “conventional” electrolyte: $\text{Mg}(\text{TFSI})_2$ in DGM.....	161
5.2.	Synthesis of the positive electrode for Mg-ion battery: Mo_6S_8	162
5.3.	Electrochemistry of Mo_6S_8 vs. Mg.....	164
5.4.	Full Mg-ion cell: Mo_6S_8 vs. Mg_3Bi_2	165
5.5.	A more efficient synthesis for ternary CP: solid-state microwave assisted reaction .	168

VI General Conclusion..... 175

<i>Scientific production</i>	179
<i>Résumé étendu</i>	180
<i>Bibliography</i>	203

I Introduction

1.1. General context

People generally think that the most important invention for mankind's progress is wheel. But what about the discovery of how to make the wheel turn?

The evolution of the human being, from its apparition on Earth to the present day, has been always dependent on the ability of harvesting and managing energy for different purposes. Primarily, for survival and for the leadership on other species, and then for the technical and scientific progress, which account for the innate instincts of evolution and self-preservation.

Looking at the history of mankind, it is easy to understand that it was marked by tremendous energetic revolutions. From the control of fire, through slavery and until the exploitation of fossil fuels, the achievements in the field of energy management always opened new horizons of wealth, population expansion and overall growth. However, the preservation of these conditions was sometimes dependent on the urgent need of alternative resources and/or energy vectors. This scenario seems to come up nowadays, when the relative prosperity of western societies has a deep impact on the outstanding growing rates of the emerging countries (China, India, Brazil, etc.), which need to feed their increasing population and fuel their industrial expansion (Figure 1).

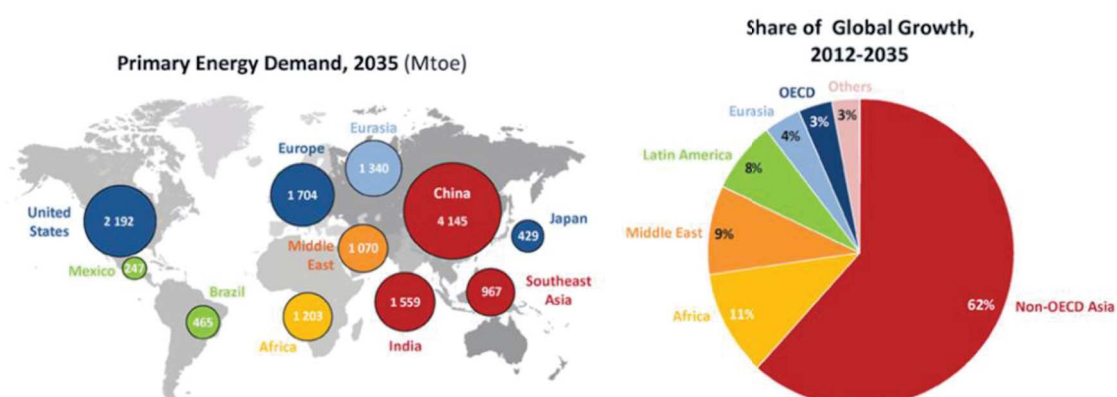


Figure 1 – World has to face the raise of energy need, which should support both the technological progress in western countries and the booming of growing economies (Reproduction from [1]).

However, important issues on the energetic sustainability of this scenario inevitably arise, taking into account the complex geopolitical situation in most of the oil producing countries. Although the extraction of crude oil was boosted during last years, with consequent price reductions and more positive forecasts of their reserves (Figure 2), an excessive dependence on fossil fuels put non-producing countries in an unfavourable position and therefore can negatively influence their developing strategies.

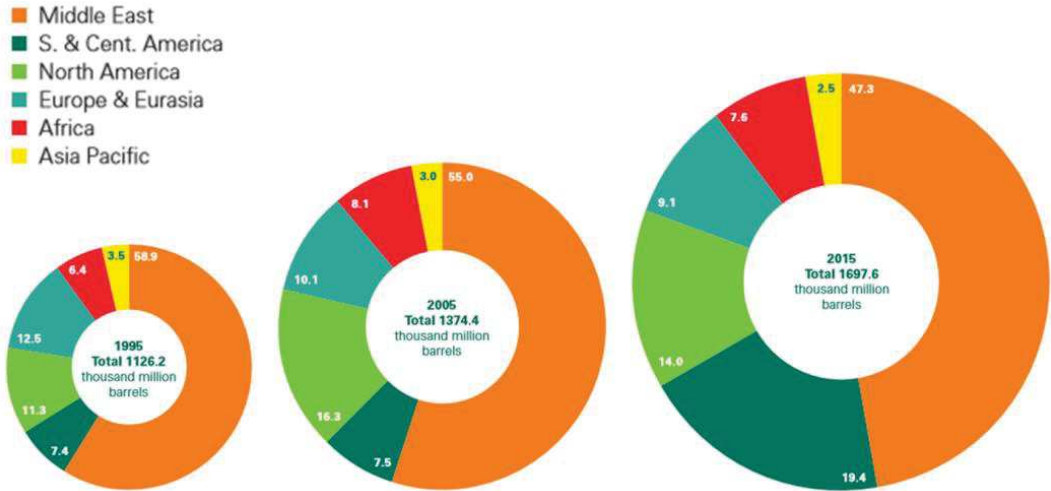


Figure 2 – Progress in extraction technology and new discoveries results in more crude oil availability respect to 10 or 20 years ago (Reproduction from [2]).

In a wider optic, even producing countries should be discouraged to use fossil fuels, because of their negative impact on global environment. Indeed, CO₂ originated from combustion reactions contributes to the increase of the natural greenhouse effect, leading to substantial global warming (Figure 3).[3]

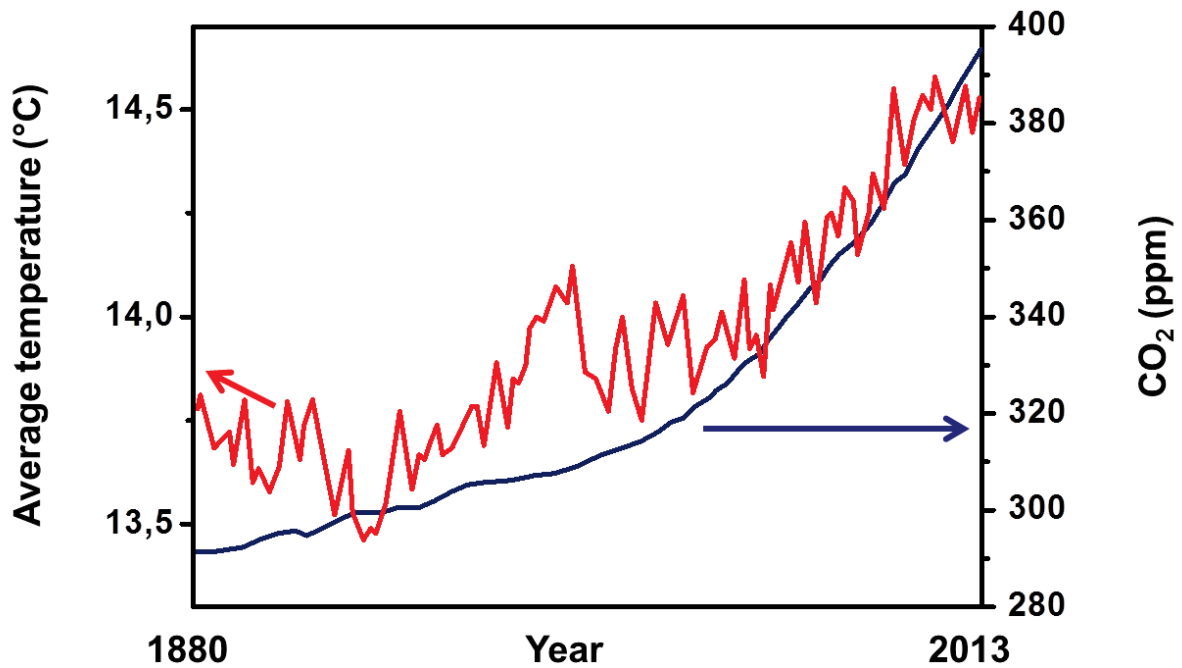


Figure 3 – Although the scientific community is not yet thoroughly convinced of the causal relation between the increase of atmospheric CO₂ and global warming, these two phenomena seems linearly correlated (Adapted from [3])

Global warming involves dramatic changes of all ecosystems, with important consequences for most living organisms. Although the increase of the greenhouse effect is not universally recognized as the main culprit of the raised average temperature, many countries have implemented politics targeting the progressive reduction of CO₂ emission. This involves not only the rationalization of manufacturing processes, but also energy production with limited CO₂ emissions, reducing the amount of electricity produced from fossil sources.

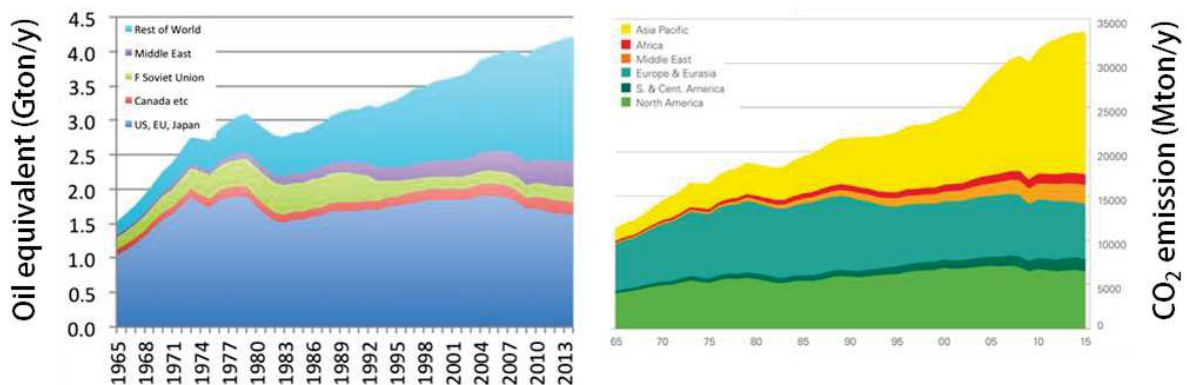


Figure 4 – Left: while US, EU and Japan oil consumption decreased during last 5 years, China, India, Brazil emerging economies show an unceasing augmentation in the use of fossil fuels, with consequent high CO₂ emission rates (Right – Reproduction from [2])

On the other hand, most developing countries are more reluctant and insist on feeding their “industrial revolution” with relatively cheap and easy-to-get fuels (Figure 4).

Western countries compensate the reduced power supply from fossil fuels by looking toward renewable energy sources, allowing the conversion of energy provided by potentially perennial sources, such as solar radiation, wind, water motion, etc., into electricity. Exploitation of such sources has a minor impact on the environment, since is not accompanied by the formation of hazardous/pollutant by-products, is generally scalable, allows local production, thus bringing power in region or zones that are not connected to major power grids.

However, the major drawback in energy production by renewable sources is represented by their intermittent character. This condition is not compatible with the current use of electricity, which can be demanded any time and in a very oscillating fashion. In order to overcome this issue, it is necessary to couple the renewable energy source to an energy storage system, able to store the possible surplus of energy when the production exceeds the demand and to eventually release it when the opposition condition arises. At present, one of the systems used to store this energy is pumping a mass of water from a low to a high reservoir, increasing its potential energy and reconvert it by letting water fall down back through a turbine. As it can be argued, this method is relatively expensive, has a low global efficiency and needs a parallel installation that can be complicated to realize, especially where water is scarce. A more efficient storage system is represented by the use of batteries, which allows the storage of the electrical energy produced by renewable sources, transforming it into chemical energy and reconvert it back into electricity when is necessary. The improvement of efficiency and cost reduction of energy storage devices is a crucial point for the further development and market penetration of sustainable energy production.

Limitation of the use of fossil fuels and consequent CO₂ release, with the abovementioned environment benefits, can also be achieved by drastically reducing fossil fuel driven transportation. The use of fossil fuels for automotive traction accounts for 72% of the total oil consumption and a huge increase is forecasted for the next decades, especially in non-OECD countries (Figure 5).

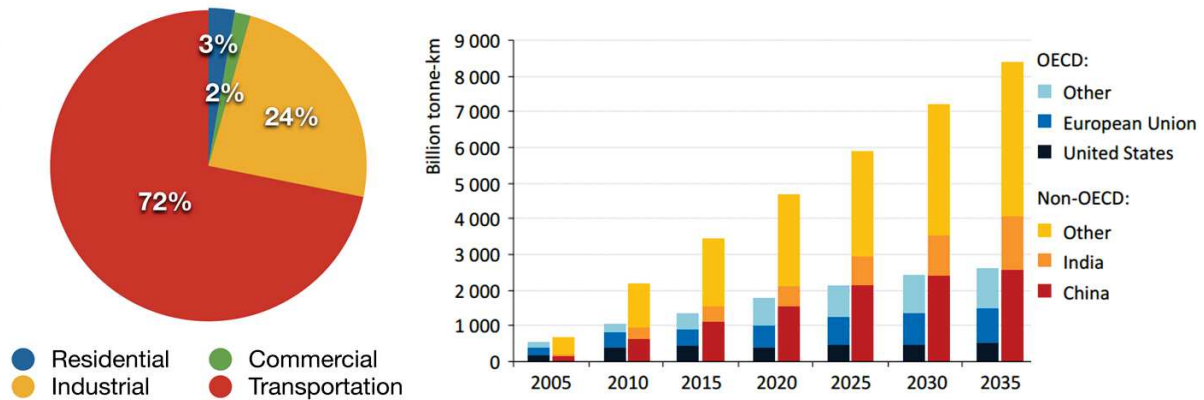


Figure 5 – Use of fossil fuels for transportation accounts for 72% of total production (Left). The absolute demand for automotive use will increase in next decades, especially in developing countries (Right – Reproduction from [1])

In the first decade of the 21st century, hydrogen was targeted as promising alternative energy vector for automotive applications, but several major hurdles, (safety issues related to gaseous or liquid H₂ tanking, poor performance on solid state storage) have hampered the possible worldwide diffusion of this technology. Partial and full electrification of vehicles have been deeply investigated by major car producers and have boomed in the last years when performance has approached that of internal combustion engines. Hybrid, Plug-in hybrid, and fully electric vehicles (HEVs, PHEVs, EVs, respectively) cannot be considered, at present, as a perfectly interchangeable alternative to combustion engine cars, since a gap in terms of cost, performance and power supply still endures. However, under particular conditions such as urban mobility, where conventional engine's efficiency falls, where the driving range is not a major issue and emission reduction is mandatory, electric mobility becomes competitive. Beside these particular applications, partially/fully electric car's alimentation is becoming nowadays a credible alternative for generic automotive purpose (Figure 6).



Figure 6 – Some examples of performing electric vehicles, from left to right: Tesla 3, a fully-electric four-door automobile with a range of 345 km at a cost of 35000 US\$ (2017);[4] BMW i3 (160 km range, 180 expected in 2017 new version, 41000 US\$, produced since 2013);[5] first fully-electric truck by Mercedes-Benz with 200 km of range and a maximum load of 26 tonnes (2016).[6]

In conclusion, the future development of modern society in a dramatic energy-consuming scenario has to face several challenging issues, such as the sustainability of energy supply for many purposes (automotive transportation, electricity production, etc.), which can be achieved by shifting from polluting fossil fuels toward renewable energy harvesting sources. One of the keys for succeeding in this conversion is the possibility to store and eventually move the energy in an easy fashion and at reduced costs with an improved environmental protection. Electrochemical storage devices are targeted as credible candidates to support this shift; better understanding their working mechanisms, improving their performance and reducing their cost are crucial goals to achieve in order to support this new energy revolution.

1.2. Batteries' overview

An electrochemical cell is a simple device that allows converting chemical energy into electricity. It consists of three main parts, a *negative* and a *positive electrode* (that are also improperly called *anode* and *cathode*, respectively) and an *electrolyte* (Figure 7). Each electrode exhibits its own electrochemical potential¹[7] that depends on its physicochemical nature. If the two electrodes are allowed to exchange electrons through an external circuit, the system reacts spontaneously to reach the equilibrium, *i.e.*, to minimise its free energy. The redox (half) reactions occurring at the electrodes produce a spontaneous electrons flow from the negative side to the positive one. This

¹ The standard potential of an electrode is defined as follows: electromotive force of a cell in which one electrode is a standard hydrogen electrode and the other one is the electrode in question, with the activity of all the species involved in the reaction equal to 1. The tabulated values are usually given at 298 K.

electric current is confined in the external circuit by the presence of the electrolyte, which is an electron insulator. In order to ensure the electroneutrality of the system, however, the electron's flow must correspond to an ion transfer in the electrolyte, which has to be therefore an ionic conductor. When the reactants at both sides are completely consumed by the electrochemical reactions,² the electrons' flow stops, *i.e.*, the system has reached the equilibrium and the cell is *discharged*. Such electrochemical devices can be considered as power supplies that end their activity after the first discharge and should be therefore replaced by new *charged* cells. In some cases, depending on the chemistry of the system, the reactions leading to the discharge of the cell can be reversed by applying an opposite current from the exterior, and the cell can be thus brought back to its initial state. The first irreversible devices are also called *primary cells*, whilst the rechargeable ones are named *secondary cells*. Secondary cells can be used not only as power supplies, but they can also play the role of current tanks. Unlike primary cells, they can be in principle built in their discharged state.

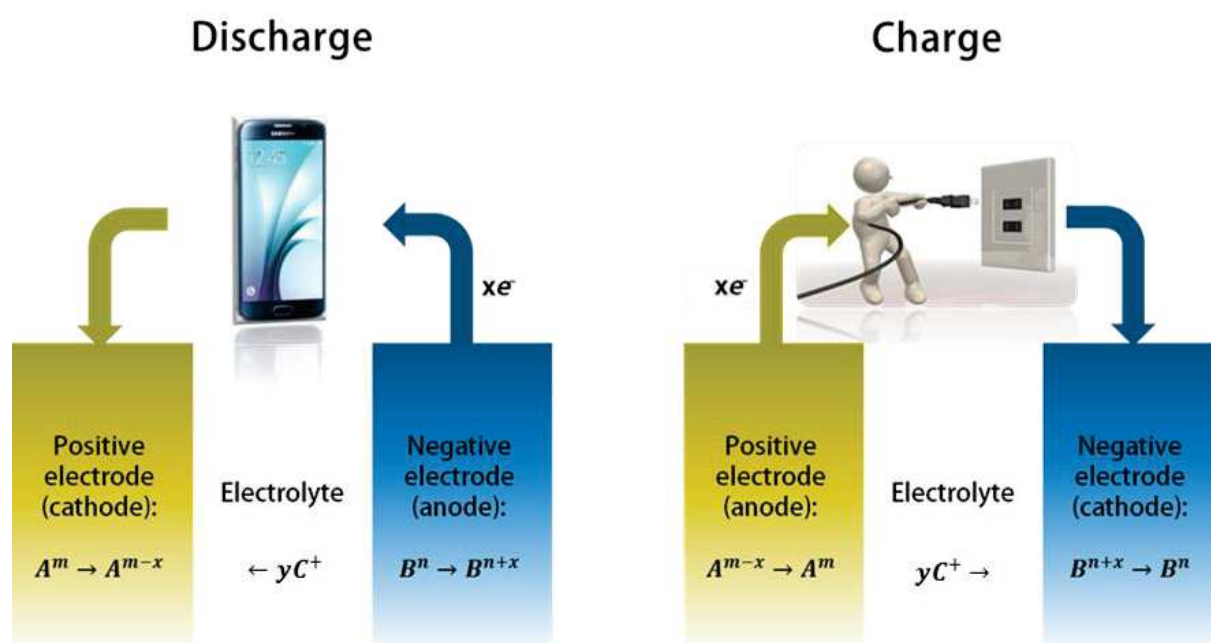


Figure 7 – Schematic representation of the discharge and charge process in a secondary cell.

By stacking, in series or in parallel, two or more electrochemical cells it is possible to increase either the voltage or the capacity, respectively, of the resulting system, which should be called *battery*. It is worth mentioning that nowadays the words *cell*

² Assuming that the reactants are present in stoichiometric ratio, with no limiting species in the system.

and *battery* can both be referred to a closed electrochemical power source, with no distinction between one or more connected electrochemical cells.

The energy ε that can be stored in a battery can be calculated according to the next equation:

$$\varepsilon_{cell} = E \cdot C$$

Where E is the cell potential and C is the capacity.

The whole potential of the cell can be obtained by the following expression:

$$E = E_{red} - E_{ox}$$

Here E_{red} and E_{ox} are the potentials where, respectively, the reduction and oxidation reactions take place. In a general fashion, the electrode potential can be calculated using the Nernst equation:

$$E_{el.} = E_{el.}^0 + \frac{RT}{nF} \ln \prod_i a_i^{\nu_i}$$

Where R is the gas constant, T the absolute temperature, n the number of transferred electrons, F is the Faraday constant, a is the activity³ of the i^{th} species, ν is its stoichiometric coefficient and E^0 is the standard electrode potential. If the electrode is coupled to a hydrogen standard electrode, the standard electrode potential E^0 can be related to the Gibbs free energy of the cell reaction via the following equation:

$$E_{el.}^0 = -\frac{\Delta G^0}{nF}$$

The capacity, C , represents the quantity of charge stored into the battery, and is defined according to the following equation:

$$C = \int_0^t I(t) dt$$

Where I is the current intensity flowed at the time t .

For practical applications, it is more useful to calculate it from the single electrode capacities[8]:

³ Activity, a , is used instead the concentration of a species in non-ideal conditions, as can be argued by its definition: $a = e^{\frac{\mu - \mu^0}{RT}}$, where μ is the chemical potential and μ^0 is the standard chemical potential.[7]

$$C = \frac{C_+ C_-}{C_+ + C_-}$$

According to the Faraday's law, electrode capacity can be expressed as follow:

$$C_x = \frac{mzF}{M}$$

Where m is the mass of the electrochemical active material and M is its molecular weight, z is number of transferred electrons per ion, F is the Faraday constant. In order to compare the capacities of different materials, it is common to adopt the gravimetric specific capacity, thus dividing last equation for the mass m . The gravimetric specific capacity, commonly expressed in mAh g⁻¹, is therefore one of the crucial parameter when considering the choice of a potential electrode material. Another key factor is the operating voltage, which should be the lowest for a negative electrode and the highest for the positive one, in order to maximise the overall energy of the cell. It is worth noting that this is an ideal approach that does not take into account neither the non-active materials that reduce the capacity nor the limitation on the voltage window imposed by the electrolyte stability.

1.3.Li-ion technology

A modern “energy revolution” was provided by the discovery and the subsequent commercialization of Lithium-based Batteries, which dramatically changed communications, work, mobility and lifestyle of western society in last 25 years. They stem from the pioneering studies on the reversible intercalation of Li into host materials. During the 70's, layered TiS₂ was found to reversibly insert Li⁺ and hence was proposed as a possible positive electrode in LB in a working prototype by Whittingham.[9] Beside this pioneering work, more studies were performed in order to get insight into their mechanism. One of the most important contributions was provided by Peled and co-workers, which demonstrated the *in situ* formation of a solid-electrolyte interphase (SEI), due to parasite reactions between Li metal and the electrolyte.[10] Unfortunately, SEI on the surface of the Li metal negative electrode hinders uniform Li plating during charge, thus leading to the formation of dendrites. Along subsequent cycles dendrites may grow and create internal short circuits in the battery, with consequent risk of overheating and explosions.[11] The way to circumvent this major issue was the replacement of the metallic Li negative electrode with another material able to insert Li ions at relatively low potential. Yazami and

Touzain observed that Li ions can be reversibly inserted into graphite (0.2 V *vs.* Li⁺/Li) without forming dendrites.[12] In parallel, Mizushima and co-workers tried to reversibly remove Li from several layered LiMO₂ (M = Cr, Co, Ni). In particular, LiCoO₂ allows reversible Li extraction at 4 V *vs.* Li⁺/Li, opening the gates for high potential positive electrodes.[13] These two major findings paved the way for the further realization and commercialization by Sony in 1991 of the so-called Li-ion battery (LIB). A general scheme of a typical LIB is presented in Figure 8:

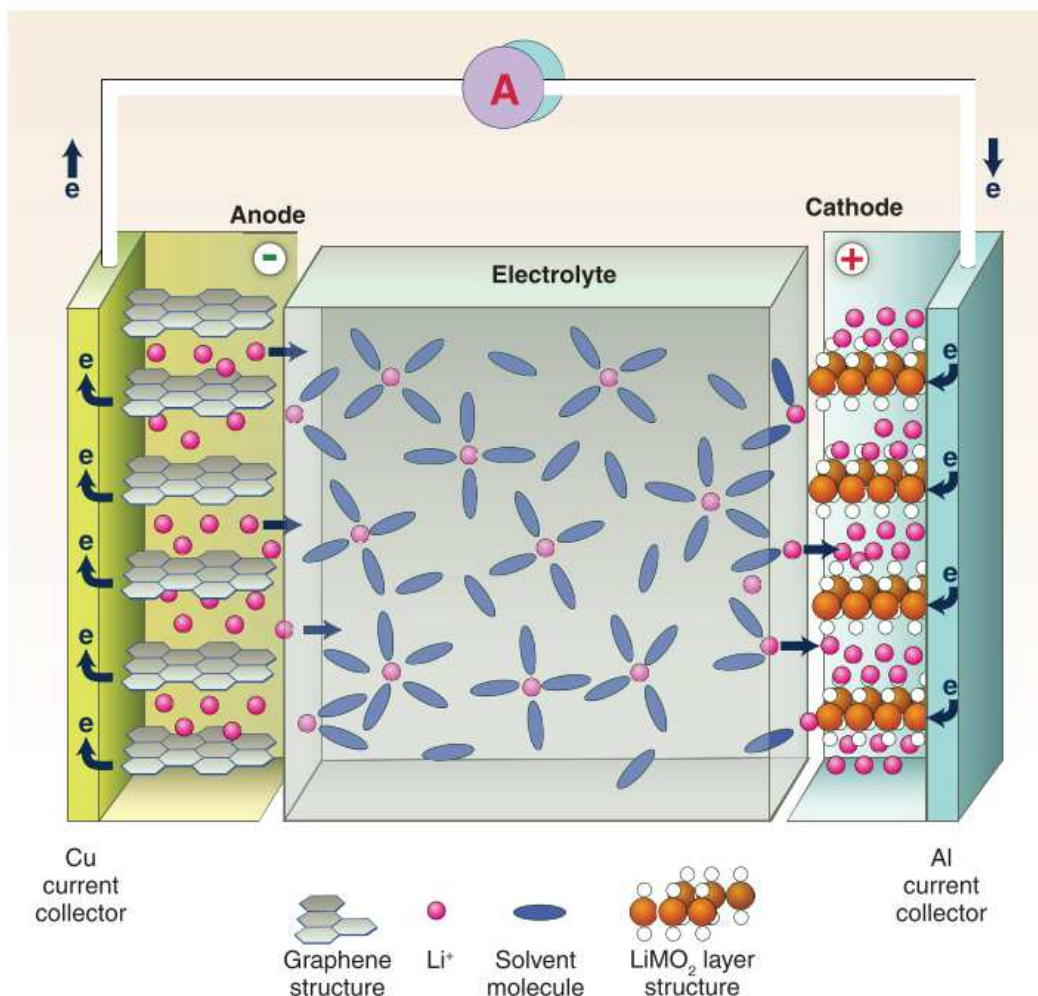


Figure 8 – A schematic representation of the discharge of a Li-ion battery. The graphite-based negative electrode undergoes Li⁺ de-intercalation, according to the following equation:



Li⁺ migrates toward the positive Li_{1-x}CoO₂ in order to obtain the reduced LiCoO₂:



Electrolyte features a lithium salt (*e.g.*, LiPF₆) dissolved in a mixture of liquid carbonates (Ethylene carbonate, propylene carbonate, etc.) Reproduction from [14]

Since their appearance, LIBs have widely penetrated the market as power supplies for electronic portable devices, thanks to their higher power density compared to other types of batteries, such as Nickel Metal Hydride (Ni-MH) or Nickel Cadmium (Figure 9 - a). Nowadays they represent 75% of the whole market (Figure 9 - b).

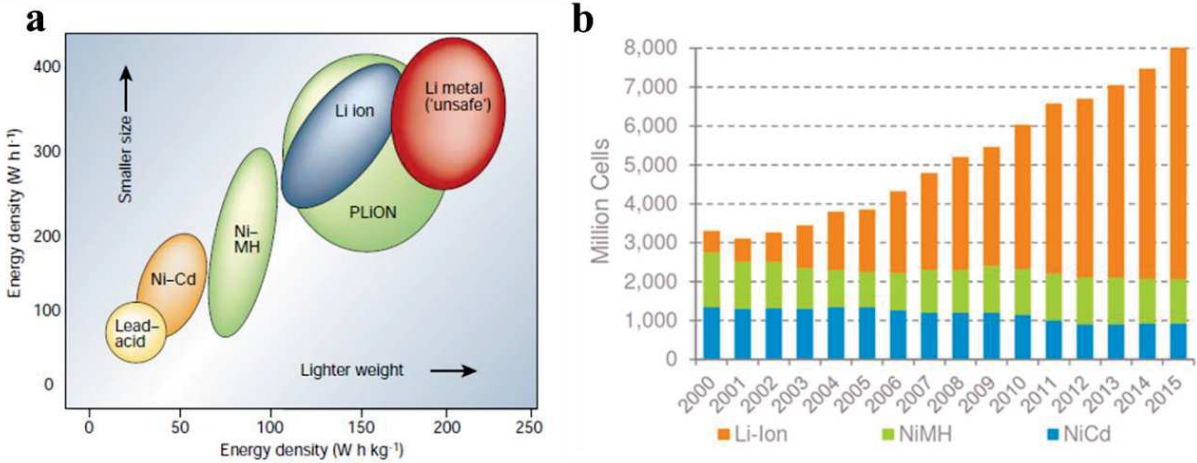


Figure 9 –Among different energy storage technologies, Li-ion batteries provide the highest specific energy per kilogram and per litre (a – Reproduction from [15]). Such elevate performance not only ensured to LIBs the leadership on the market of portable power supplies, but also contributed to its unceasing expansion (b – Reproduction from [16]).

1.4.Beyond Li-ion? Resources, consumption, forecasts

The evolution on the performance of portable electronics is directly linked to the huge progresses in the technology of power supplies. The benefits provided by the so-called “Li-ion revolution” have not stopped with their application in pocket devices, but can be extended toward other more challenging applications, such as the alimentation of new-generation plugin hybrid (PHEVs), hybrid (HEVs) and electric vehicles (EVs). This shift can be considered very challenging, since the requirements needed for automotive traction involve elevate power densities, but also a tanked energy that can compete with that of current fossil fuel-based vehicles.[17] From the first commercialized LIB to the present day, constant improvements have led to systems which can store more than twice of the initial energy. However, rather than from pure electrochemical aspects, many upgrades came from engineer tailoring, and the Li-ion technology seems to have almost attained its limits (Figure 10).[17][18]

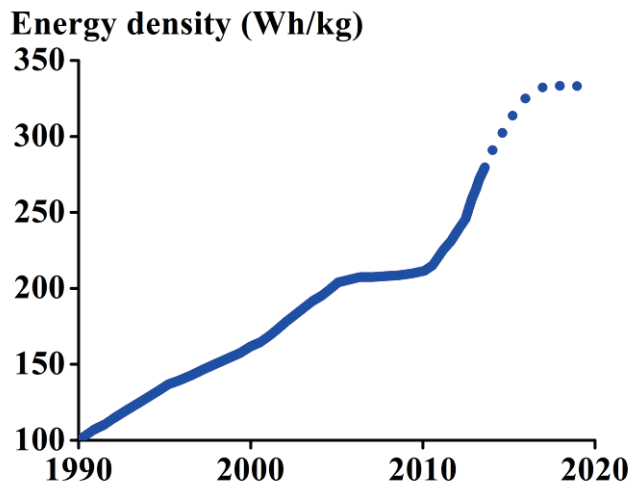


Figure 10 – Although the performance of LIBs has been greatly improved since their first commercialization, they may have reached their intrinsic limits and cannot meet the request of higher-demanding applications (Adapted from [17]).

Despite these considerations, HEVs and EVs were introduced in the market and some of these vehicles offer performance and autonomies that can challenge combustion engine ones. For this reason, they are expected to flank or even replace the current car fleet in the next decades. Such huge development has been recently questioned because of a major issue concerning Li availability. Li, indeed, is a relatively rare metal and is not uniformly spread on Earth’s crust. It is usually extracted from brines, and the largest natural reservoirs of Li-rich minerals are located in South America, and more precisely, in a desert region shared by Chili, Bolivia and Argentina.

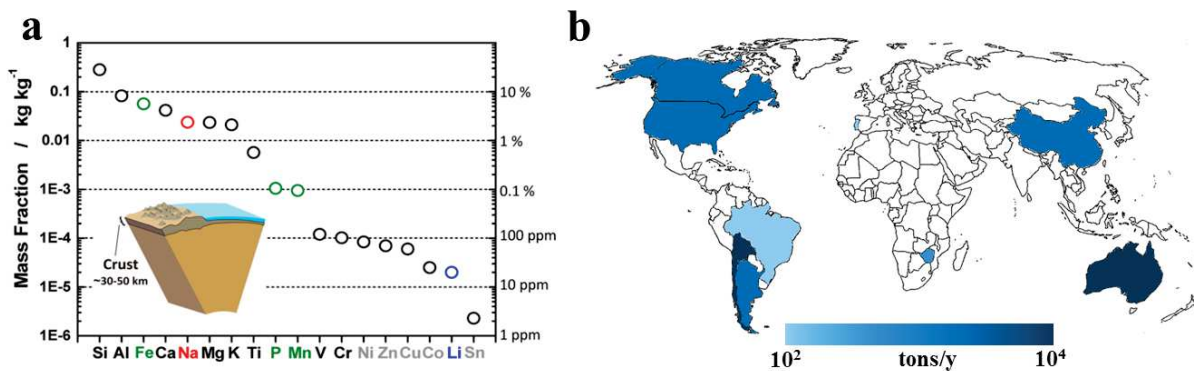


Figure 11 – Li can be considered a rare element, with an average concentration of 20 ppm on the Earth’s crust, far less than other alkali and alkaline-earth elements (a – Reproduced from [19]). Furthermore is not uniformly spread, and the largest reservoirs are located in South America, where there is the highest extraction activity. (b – Adapted from [20]).

Other important reservoirs are located in Australia, which in last years increased its extraction of Li. Smaller productions can be found in the USA, Canada China and Zimbabwe (Figure 11).

Is it difficult to estimate whether the available Li amount on known reservoirs can fulfil the forecasted demand.[21][22] Several scenarios have been thus elaborated, taking into accounts many parameters, such as different penetration levels of EV technology, recycling programs, upgrade in the Li extraction techniques, and so on.[23] However, even in the case of relatively pessimistic diffusion of Li-ion technology, there is a concrete possibility that Li might become a key resource, leading to a situation analogous to that underwent for oil, the price of which is unstable and mainly dependent on strategic choices of the producing countries.[24]

The challenge of cheap and efficient energy storage shall not be exhausted with “mobile” applications but will face to the urgent need of large-scale installation in tandem with renewable energy generators. Aimed at reducing the dependence on fossil fuels – with the associated production of CO₂ contributing to the increase of the greenhouse effect – the development of alternative energy production sources was boosted during last decades. Solar, wind, sea waves, waterfalls, etc. are unlimited and clean source of energy that can be harvested and converted into electricity. Unlike gas, coal or nuclear power plants, whose energy production is stable and can be tuned on demand, electricity production from renewable installation depends on the presence of the primary energetic source and is therefore intermittent. This major hurdle can only be tackled by coupling some energy storage devices to renewable plants. However, one of the challenges of this application lies in the possibility of realising batteries exhibiting huge capacities and long lifetimes with limited costs. Although several companies have developed LIBs with MWh scale,[14] the possibility that current Li-based technologies fulfil the growing demand of such installation is also questioned and the scientific community tries to look toward alternative systems, based on cheaper, more abundant and more performant ion vectors.[17] In the following section of this thesis, several alternatives to LIBs will presented. Some of them have been investigated more in details, and hence can represent a near-term alternative to Li. Others, more cutting-edge, such as magnesium-based ones, still deserve researcher’s attention.

1.5. Na-ion technology

The most logical candidate to replace Li as ion carrier in energy storage device is Na. Belonging to the same group of the periodic table, it is expected that Li and Na exhibit similar chemistry. Na is the second lightest alkali metal and the couple Na^+/Na offers a highly negative reduction potential (-2.71 V vs. SHE). The development of Li- and Na-based energy storage systems have started almost in parallel, but the latter was rapidly abandoned in favour of the former, which was more promising in terms of specific capacities and operating voltage. However, during last years, Na came back in the spotlight, since unlike Li, it can be considered almost an unlimited and ubiquitous element, with less production costs.

At this stage it is worth mentioning that Na-ion batteries (NIBs) are targeted to be the nearest-term replacing technology of LIBs and therefore similar performance, *i.e.*, an operating voltage of more than 3 V, is expected. Several advanced prototypes were recently proposed by the RS2E - CNRS, France (18650 battery)[25] and Faradion, UK (first Na-ion plugged vehicle).[26] However, the less negative redox potential and the higher atomic weight of Na may represent a non-negligible gap between the two technologies.[27] Bearing in mind the similitudes between Li and Na, the research on Na-ion batteries (NIBs) tried to translate the background achieved after 30 years of experience in LIBs and applicate it with “just” changing the ion carrier. On positive electrode side, the reversible de-intercalation from layered Na_xCoO_2 polytypes was demonstrated since the 80’s. However, the negative electrode cannot be represented by graphite, which is electrochemically inactive toward Na^+ insertion using carbonates as electrolyte solvents.[28] Hard carbon was instead successfully employed as negative electrode in NIBs, since it delivers more than 300 mAh g^{-1} at low operating voltage. Nowadays, many insertion positive electrodes have been tested, such as layered and tunnel-type TMOs, transition metal sulphides and fluorides, layered polyanionic compounds (NVPF for instance), Prussian blue analogous and organic polymers and more details on such materials can be found in recent reviews.[29][19][30] Interestingly, insertion positive electrodes for Na batteries exhibits better performance with respect to the corresponding Li ones. This behaviour has been attributed to the low solvation energy of Na^+ (a weaker Lewis acid than Li^+) that strongly influences cation kinetics.[19]

Regarding the research on negative electrodes for NIB, four main directions are currently followed, in analogy with these on LIBs:

- Carbonaceous materials
- Oxides and polyanionic compounds behaving as Na-topotactic insertion materials
- Oxides and sulphides for conversion reactions
- Single or combined *p*-block elements forming reversible alloys with Na

This last category will be discussed in more detail, since the active materials studied in this thesis belong to it. On the other hand, the first three types are described in the review of Yabuuchi and co-workers.[19] A Ragone plot summarising most negative electrodes for NIBs is presented in Figure 12:

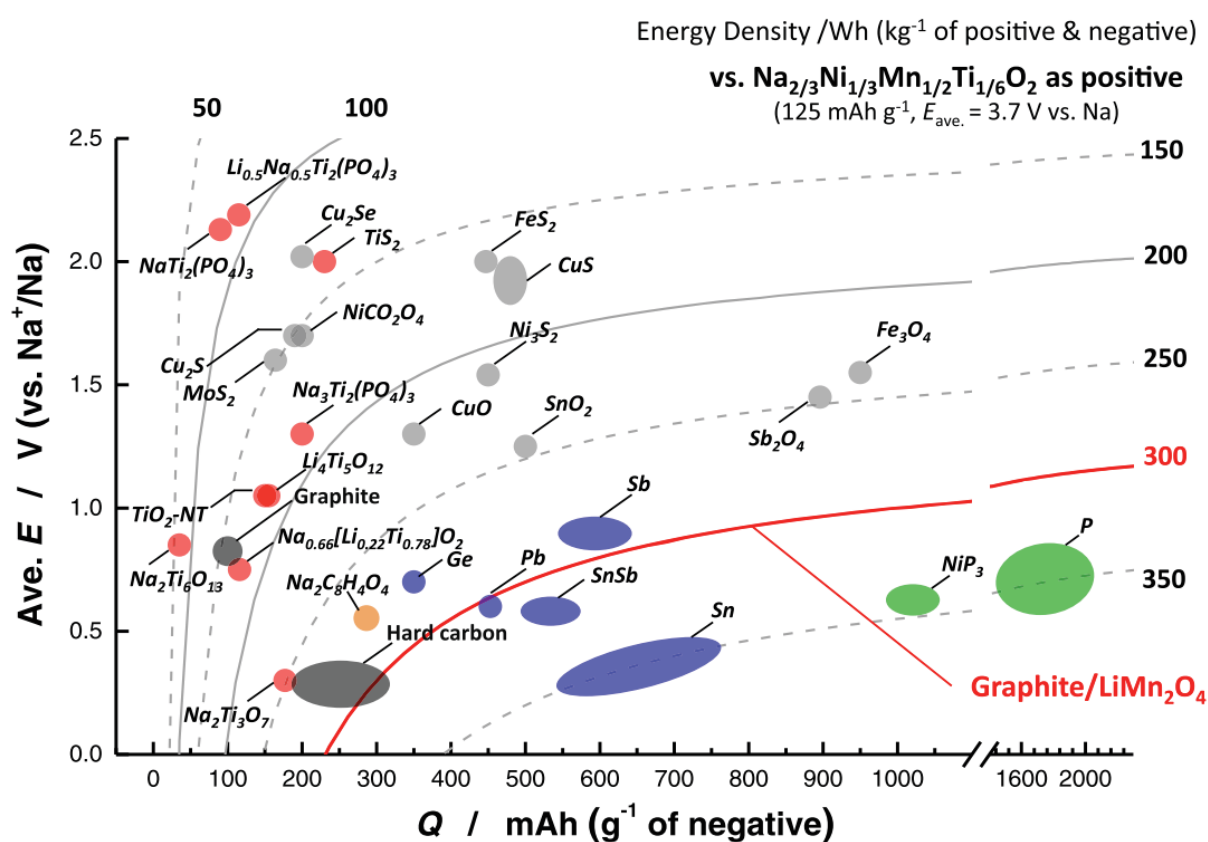


Figure 12 – The Ragone plot of several possible electrode negative electrodes in NIBs. Average voltage (V) and energy density (Wh Kg⁻¹) vs. gravimetric capacity are presented. Black circles: carbonaceous materials; red circles: oxides and phosphates (insertion materials); purple and green circles: *p*-block – based materials; grey circles: oxides and sulphides for conversion reactions (Reproduction from [19]).

1.5.1. Alloy - type negative electrodes for NIBs

Several *p*-block elements are able to electrochemically alloy with Na. As can be seen from Figure 12, the interest in studying such compounds lies both on their low alloying voltage but also on the elevated gravimetric capacities that the associated reactions can theoretically provide. Nevertheless, such alloying/de-alloying reactions are associated to important volume changes that are responsible of the reduced cycle life of alloy-type electrodes. This major issue already observed in analogous Li-based systems, is even more crippling in the case of NIBs, since the volume variations are twice as high for the same alloying element. Interestingly it has been also found that the volume occupied by Na atoms is independent of the alloying element, excepting for the surprising case of P.[31]

Despite this drawback, several strategies can be adopted in order to mitigate the volume expansion, such as the use of electrolyte additives for the control of the SEI or the choice of the polymeric binder in the electrode formulation. For instance, Jow and co-workers demonstrated that the addition of a poly(*p*-phenylene) in a Pb-based electrode (Pb exhibits a volume expansion of 400% during electrochemical alloying with Na) resulted in noteworthy stable cycle numbers (>300).[32] On the basis of this encouraging result, other elements were further tested, such Sn and Sb. In particular, Sn potentially offers a very low alloying potential, which is desirable in order to enhance the overall energy density of the battery. Baggetto *et al.* demonstrated that reversible electrochemical alloying between Na and Sn occurs in subsequent steps until achieving the Na₁₅Sn₄ phase (874 mAh g⁻¹).[33] Even in this case, the reversibility of the alloying/de-alloying process was increased by the introduction in the electrode formulation of specific polymeric binders.[34]

Sb-based electrodes were proposed by Quian and co-workers, who realized by high-energy ball-milling a Sb/C composite exhibiting a specific capacity of 610 mAh g⁻¹. Cycling performance was proved to be dramatically influenced by specific electrolyte formulations. Indeed, the addition of 5% fluoroethylene carbonate (FEC) led to a capacity retention of 94% after 100 cycles.[35] The reaction mechanism was further elucidated by our group through an *operando* X-ray diffraction (XRD) study. Starting from bulk crystalline Sb, Na_xSb amorphous phases are formed along the alloy process until achieving a Na₃Sb hexagonal lattice, which appears in competition with the metastable cubic Na₃Sb phase.[36] The SnSb alloy was also tested *vs.* Na, in a

nanocomposite SnSb/C prepared by high-energy ball-milling.[37] Such electrode material exhibits good initial specific capacity (540 mAh g⁻¹) and a capacity retention of 80% after 50 cycles. Although no elucidation of the reaction mechanism has been provided yet, the analysis of the galvanostatic profile let one suppose a difference between the electrochemical reaction of the elements alone and the SnSb phase. A further work by our group provided a more performing SnSb electrode *vs.* Na but also pointed out that, unlike the same system *vs.* Li, the reaction mechanism of SnSb is more complex and cannot be explained by the simple sum of the mechanisms of the two single metals.[38]

As a summary of this section, alloy-type negative electrodes represent a promising alternative to carbonaceous materials in NIB, in particular for the high specific capacities that can be potentially achieved. Further developments must be directed to limit or contain the large volume expansion during the alloying/de-alloying process, thus allowing a higher capacity retention for a larger number of cycles. In a wider perspective, the development of the Na-ion technology is related to understanding the differences between Li and Na chemistry, keeping in mind that the approach to this research field imposes stricter working and testing conditions, because of the more reactive nature of Na with respect to Li.

1.6.Punching more electrons per cation: multivalent elements

As stated above, enhancing the capacity of the positive electrode in LIBs is considered one of the key factors for a new breakthrough in Li-based energy storage technology, and is highly expected in order to meet the requirement demanded by new huge energy-consuming applications. In this regard, achieving two-electron reduction for each metal centre in Li positive electrode has been intensely investigated.[39] Such a redox mechanism might allow doubling the nominal capacity of an electrode, but is difficult to obtain in practice due to the volume expansion associated with the insertion of two Li⁺ for each redox site.[40] Besides this approach, is it possible to achieve the same goal by replacing Li⁺ or Na⁺ by

multivalent⁴ cations with similar ionic radii (Figure 13).

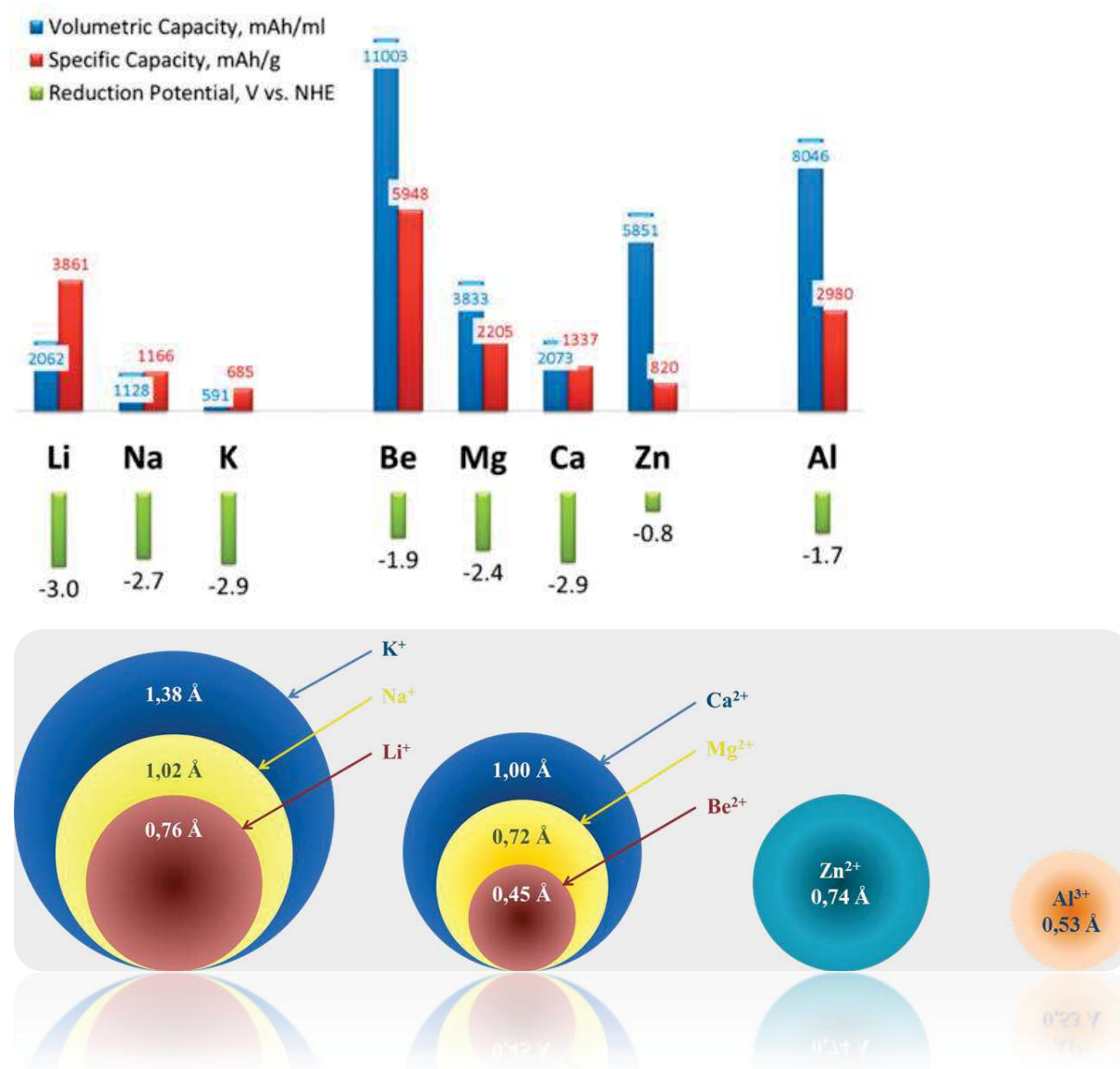


Figure 13 – Top: multivalent elements offer higher volumetric and gravimetric capacities with respect to their monovalent neighbours of the same period, with in general sufficiently low standard redox potential (Reproduction from [40]). Bottom: comparison between Shannon’s ionic radii for mono- and multivalent ions (Adapted from [41]).

Nevertheless, it should be noted that the elevated charge density on small cations represents a hurdle for their solid-state diffusion into hosting materials. In this section the properties of several promising elements for multivalent-based energy storage systems will be briefly discussed, with more detail for magnesium.

⁴ Even though the word “multivalent” could lead to ambiguity, in this case is employed to define the elements that have a cation which carries a fixed charge $n \neq 1$, and not an element that can exist in multiple oxidation states. In the community of electrochemical energy storage this word is employed to emphasize the difference between the emerging system based on multiple-charge carriers and the state-of-the-art Li-ion technology. However, to avoid this misunderstanding, it could be replaced by the more precise “supervalent”. [40][46][50]

1.6.1. Calcium

Ca belongs to alkaline-earth metals and despite its tendency to react with O_2 and H_2O to form CaO and $Ca(OH)_2$, it is less dangerous than metallic Li. It is the fifth most abundant element on Earth's crust and can be found in many compounds such as calcite and aragonite ($CaCO_3$), which is the main component of marble, and gypsum ($CaSO_4 \cdot 2H_2O$). Regarding the electrochemical performance, it exhibits a highly negative reduction potential, -2.87 V vs. SHE , which is only 0.17 V higher than that of the Li^+/Li couple. Moreover, its ionic radius is 1.00 \AA , only 24% larger than that of Li^+ . As stated above, elevated charge density could lead to sluggish insertion/de-insertion kinetics and Ca^{2+} represents a good compromise between size and carried charge. Unlike magnesium, aluminium or zinc, calcium did not benefit of basic studies on electroplating and therefore, despite its interesting properties, the development of Ca-based system has received less attention by the scientific community.

A primary battery based on $Ca/SOCl_2$ was proposed in the 80's for application under severe temperature conditions, such as for drilling rigs operating at temperatures as high as $200\text{ }^\circ\text{C}$. In these conditions, the use of Li becomes extremely dangerous because of its low melting temperature (m_p is $180\text{ }^\circ\text{C}$), which may cause explosions.[42] Even though no prototype could be realized due to the rapid corrosion, a novel interest in exploring more accurately Ca electrochemistry had started. In particular, the interaction between Ca and inorganic polar aprotic solvents was investigated and the formation of SEI layers in such systems was reported.[43] However, the SEI formed on Ca exhibits a higher ionic resistivity than that generated by analogous Li-based compounds, likely due to the less ionic character of the formed Ca-containing species.[44] Besides these investigations which date back to the 80's, no other studies are reported to our knowledge since the work of Aurbach *et al.*, which deals with the chemical composition of calcium electrodes *vs.* different electrolyte formulations.[45] Interestingly, they reported that BF_4^- is stable against reduction, opening for the use of $Ca(BF_4)_2$ as active metal salt in Ca electrolytes. However, the first report of reversible Ca plating/stripping was provided only in late 2015 by Ponrouch *et al.* They demonstrated the reversible deposition and stripping of Ca^{2+} on calcium metal using a $Ca(BF_4)_2/EC:PC$ electrolyte at $100\text{ }^\circ\text{C}$., and showed that both temperature and salt concentration dramatically influence the electrochemical behaviour.[46] The main hurdle for achieving a Ca rechargeable

battery is the lack of suitable electrolytes that are still stable down to the very low reduction potential of Ca^{2+} . Similarly to Mg, the development of new classes of electrolytes was directed toward the so-called heavy Grignard compounds (RCaX). Unlike Mg, the synthesis of such class of compounds shows major issues, especially for the potentially effective PhCaCl . [40]

In parallel with the development of a rechargeable Ca battery, it is worth mentioning the alternative process proposed by Lipson *et al.* in 2015, who suggested replacing the negative electrode of Ca metal, therefore moving toward a Ca-ion system. They demonstrated the reversible Ca electrochemical intercalation into $\text{Na}_x\text{MnFe}(\text{CN}_6)$ (MFCN). Moreover, a complete rechargeable Ca-ion cell was presented with the use of a “pre-calciated” tin negative electrode and a dry non-aqueous electrolyte, $\text{Ca}(\text{PF}_6)_2/\text{EC}:\text{PC}$ 3:7 v/v (Figure 14). Unfortunately, there was no information on the real chemical nature of the “calciated tin”. [47]

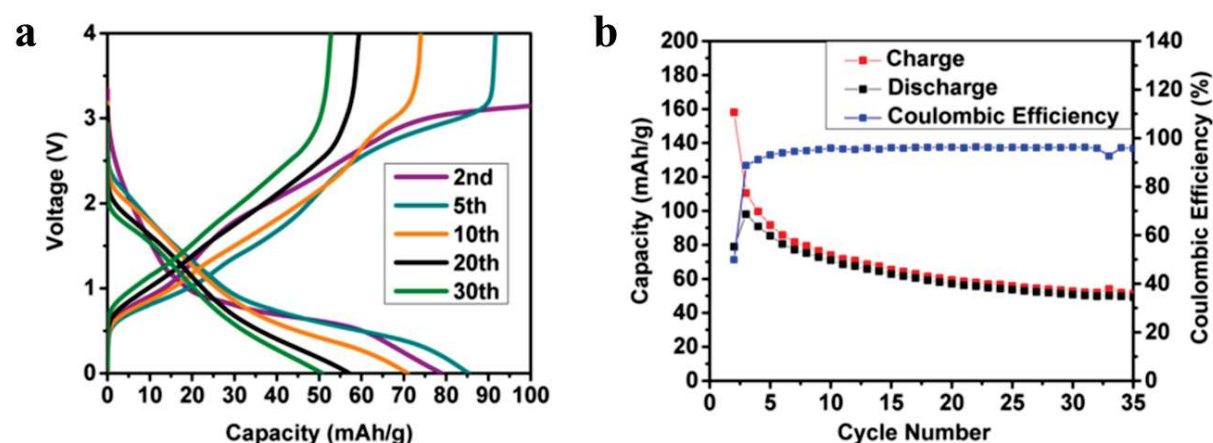


Figure 14 – Galvanostatic cycling of the Ca-ion first prototype battery, equipped with a desodiated MFCN positive electrode, calciated tin negative electrode and 0.2 M $\text{Ca}(\text{PF}_6)_2$ in 3:7 EC:PC v/v (a) and capacity with the corresponding coulombic efficiency (b – Reproduction from [47]).

More recently in 2016, another Ca-ion prototype was proposed by Cabello and co-workers. It was realized with layered CaCo_2O_4 as the positive electrode, in analogy to LiCoO_2 in Li-ion batteries, and a V_2O_5 as intercalation negative electrode (Ca intercalation into V_2O_5 was already studied in 2001 by Amatucci and co-workers). [48] Although the rechargeable behaviour of the battery was clearly demonstrated, the authors stated that only low specific capacities can be achieved using an intercalation negative electrode such as V_2O_5 . [49]

1.6.2. Zinc

At present, excepting one report on a Ni-based system,[50] the only element considered as possible active material and charge carrier for rechargeable batteries belonging to the *d*-block is Zn. It is by far the less abundant element among those presented in this literature overview. Nevertheless, it gained the attention of the scientific community since it exhibits elevate theoretical volumetric energy density (5851 mAh cm⁻³). Moreover, it is non-toxic, easy-to-process and has a high electronic conductivity. Its cation is divalent and the ionic radius (0.74 Å) is similar to Li⁺. The standard potential of the Zn²⁺/Zn redox couple is -0.78 V vs. SHE. This value, which at a first glance could be considered too positive for a negative electrode, is very interesting for aqueous systems.[51] Indeed, examples of aqueous Zn-containing batteries can be found all along the history of batteries, and among them can be mentioned the Zn-carbon (developed from Léclanché cells, they actually feature a MnO₂ positive electrode material) or the more recent Zn-Ni systems. More recently, theoretical studies were undertaken to investigate Zn²⁺ mobility in different intercalating host, such as spinel Mn₂O₄, FePO₄, NiO₂, and δ-V₂O₅, compared to other cations.[52] Electrochemical studies proved the intercalation of Zn²⁺ in α-MnO₂,[50] and Na₃V₂(PO₄)₃ NASICON.[51] In parallel to these developments, non-aqueous Zn electrochemistry was also investigated by Han and co-workers, who pointed out the excellent oxidation stability of water-free Zn electrolytes, associated to good ionic conductivity.[53] Zn is a versatile element in energy storage systems and its possible use in Zn-air⁵ primary and rechargeable batteries was recently discussed.[54]

1.6.3. Aluminium

Al is the third most abundant element on Earth's crust, just after oxygen and silicon. Its lightness (26.98 g mol⁻¹), density (2.7 g cm⁻³) and multivalent nature (the cation is Al³⁺) lead to the outstanding volumetric capacity value of 8040 mAh g⁻¹. Nevertheless, the redox potential of the Al³⁺/Al couple is -1.67 V vs. SHE, which is by far more positive than that of Li⁺/Li. Al can boast a long history in electrochemistry, since its first use in a battery dates back to the middle of 19th century, when it was set as positive electrode toward a zinc plate.[40] A century later, Al was used as negative

⁵ Metal-air batteries generate electricity through a redox reaction between metal and the oxygen of the atmosphere. They generally feature a metal negative electrode, a separator soaked in a metal-ion conducting electrolyte and at the positive side, an air-electrode.[228]

electrode *vs.* MnO₂ in aqueous environment, which led to the formation of an ion-blocking layer upon the Al metal. Particular attention was furthermore given to Al for its possible use in Al-air primary batteries but no reports of rechargeable Al-based systems were provided until the work of Jayaprakash *et al.* in 2011. [55] They realized an Al battery featuring a positive electrode based on V₂O₅ nanowires and an electrolyte based on the (1-ethyl-3-methylimidazolium chloride) ionic liquid. The electrochemical performance of this system is encouraging, *i.e.*, a 20-cycles stable specific capacity of 270 mAh g⁻¹ was observed. A more recent work reported the use of graphite as intercalation positive electrode, exhibiting the high intercalation potential of 1.8 V *vs.* Al³⁺/Al.[56] Chevrel Phase (CP) Mo₆S₈ was also tested,[57] but a real improvement was provided in 2015 by Lin and co-workers, who proposed an Al battery featuring graphite as positive electrode and AlCl₃/1-ethyl-3-methylimidazolium chloride as electrolyte. Despite the relatively low specific capacity (less than 60 mAh g⁻¹), this prototype exhibited an impressive cycle life (7500 cycles) at the elevated current density of 4000 mAh g⁻¹. [58]

1.7. Magnesium

Mg is the 7th -8th most abundant element on the Earth's crust (depending on the estimation and on the related error)[59][60] and unlike Li is uniformly spread. It does not occur uncombined, but is mainly found in large deposits of magnesite (MgCO₃), dolomite (MgCO₃ · MgCO₃) brucite (Mg(OH)₂).[59] Despite this, Mg is mostly obtained from sea water, in which it becomes the third most abundant elements (1.3 Kg of Mg/m³).[61] As a direct consequence, Mg precursors are cheaper than corresponding Li ones and prices can be further reduced if Mg arises as a key component on next-generation of energy storage devices. Furthermore Mg is not toxic, but rather has crucial importance for living organisms, since it is a component of chlorophyll in green plants and is an essential cofactor in enzymes activity.[60]

Regarding the physical properties, it exhibits a melting point of 650 °C and is far less air- and moisture-sensitive than alkali metals. In addition, is light but denser than Li (1.74 g cm⁻³ towards 0.53 cm⁻³), its cation is divalent and consequently is capable of providing high volumetric energy density (3837 mAh cm⁻³), which is approximately twice as high as that of Li metal and fivefold that of graphite in LiBs.[62] However, it is worth noting that the reduction potential of the couple

Mg^{2+}/Mg is -2.36 V toward SHE, i.e. 680 mV less negative than Li^+/Li . Voltage is a crucial parameter for the overall energy density of the battery (cf. 1.2) and this important gap between Li- and Mg-based systems could let one think that latter are not suitable for portable devices but are more useful for stationary energy storage. Nevertheless, as underlined by Muldoon and Gregory in a recent review,[40] an elevated volumetric capacity is of capital importance for all the applications in which the smallest room should be dedicated to the alimentation pack, such as personal electronic, but also cars, assistive robots, etc. Hence, despite the voltage gap between the two systems, and considering all the interesting features above described, Mg batteries can be taken into account as a credible alternative for next-generation storage systems.[61][62][63] As summary of this section, next table offers a comparison between the principal physical and electrochemical properties of the alkali and alkaline-earth metals for energy storage applications:

M^{z+}	Abundance on Earth's crust (ppm)[59]	Price (US\$/tonne)	M_p (°C)	E^0 (V vs. SHE)	g/mol e^-	Shannon Ionic radius (Å)[41]	Theoretical capacities[40]	
							(mAh g ⁻¹)	(mAh cm ⁻³)
Li ⁺	2	6400 ^a	180	-3.04	6.941	0.76	3800	2060
Na ⁺	23600	250 ^a	98	-2.71	22.99	1.02	1160	1140
Mg²⁺	23300	1990	650	-2.37	12.15	0.72	2200	3800
Ca ²⁺	41500	160 ^a	851	-2.87	20.04	1.00	1340	2060
Zn ²⁺	70	2280	420	-0.76	32.69	0.74	820	5851
Al ³⁺	80000	1635	660	-1.67	8.99	0.53	2980	8046

Table 1 – Summary of availability, cost, physical and electrochemical properties of different element that are either in use or could be used as main component in energy storage devices. ^a: price per tonne of M-carbonate.

1.7.1. Stripping/plating on Mg metal

As stated in the previous paragraph, Mg has been targeted not only as a possible alternative charge carrier to replace Li in energy storage systems, but also to be directly employed as negative electrode in MBs, in a similar fashion as it was done in the 80's for LBs. Unfortunately, LBs were short-lived since Li anodes are plagued by dendritic formation during plating, leading to short-circuits and explosions.[64] This major issue, combined with the high reactivity of Li metal towards air and moisture, contributed to the breakthrough of LIB. Mg metal, however, is not plagued by dendrite formation during plating, as shown by Matsui (Figure 15).[65]

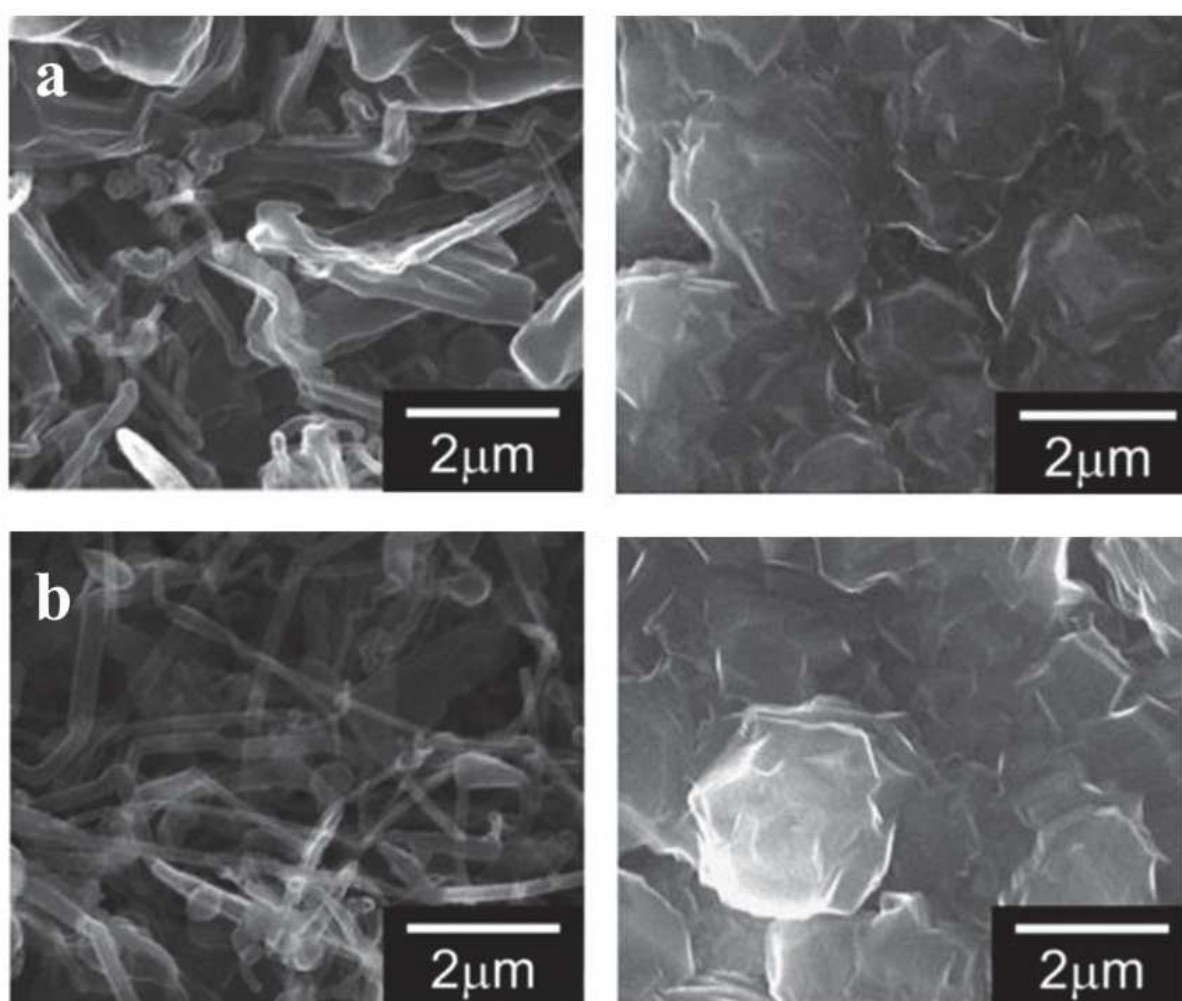


Figure 15 – The direct comparison with SEM images of electrodeposited Li (left column) and Mg (right column) at current densities of 2500 mA cm⁻² (line a) and 5000 mA cm⁻² (line b). Such a huge difference is explained by the fact that SEI formation during Li plating may occur not in a homogeneous fashion, thus favouring the growth of dendrites.[65] In the case of Mg deposition, on the contrary, no SEI formation was reported.[66] (Adapted from [65]).

In addition to all the features presented in the previous section, also for this reason it has been considered as a promising alternative in energy storage systems.

Despite this encouraging background, the realization of a MB was not a trivial task. In the case of Li-based systems (cf. 1.3), the partial decomposition of the electrolyte occurring at the surface of the negative electrode produces an interphase layer between the metal and the solution with the properties of a solid electrolyte with a relatively high electronic resistivity. For this reason it was called a “solid-electrolyte interphase” (SEI), by Peled and co-workers.[10] In this study, that can be considered a milestone in battery electrochemistry, the authors proposed a model valid for all alkali metals in non-aqueous battery systems, and SEI was subsequently recognized as a key-factor in the definition of safety, power capability, morphology of lithium deposits, shelf life, and cycle life of the battery.[67] Curiously, these conclusions were drawn from prior studies devoted to magnesium electrodes.[68] Indeed it was stated that, in thionyl chloride (TC) solutions, the migration of Mg^{2+} ions through the formed passivating layer was the limiting factor in the overall magnesium deposition/dissolution rate. Moreover, it was observed that the deposition of magnesium on an inert nickel cathode begins only after nickel is covered by a passivating layer ($MgCl_2$) that blocks the electronic current and enables only ionic current to pass.

Li- and Mg-based systems present different ionic conductivities at their interfaces. It has been proved that Li rapidly reacts with both electrolyte solvents (mostly carbonates) and with the herein dissolved salt anions, such as ClO_4^- , PF_6^- , BF_4^- , etc. These reactions form insoluble Li salts, such as Li_2CO_3 , Li_2O , LiF , etc. that allow Li-ion diffusion. On the surface of Mg metal, analogous electrolyte formulations lead to the same reactions observed in the case of Li but, unfortunately, Mg^{2+} is unable to diffuse through this layer.[69] Consequently, Mg electrode is “passivated” [66] and any further reversible Mg cycling is hampered. These evidences limit the choice of electrolyte solvents and Mg-based salts; electrolyte engineering is still considered one of the most challenging problems for the development of MBs.

1.7.2. Electrolytes

Despite these hurdles, a pioneering report of metallic Mg-compatible electrolytes was reported by Gregory and co-workers in 1990. Based on previous studies (one of them dating back to 1927!) they tested several classes of chemicals,

such as aminomagnesium chlorides, organoborates and alkyl-magnesium halides, better known as Grignard reagents.[70] Noteworthy, an organoborate compound, $\text{Mg}(\text{BPh}_2\text{Bu}_2)_2$, dissolved in THF/DME was employed as electrolyte in the very first rechargeable MB, equipped with a Co_3O_4 cathode. Although the proof-of-concept was given, the overall electrochemical properties were limited by the low oxidative stability of $\text{Mg}(\text{BPh}_2\text{Bu}_2)_2$ (less than 2 V vs. Mg^{2+}/Mg).

Another important section of this pioneering work was devoted to Grignard reagents. Such compounds were discovered by the French chemist François Auguste Victor Grignard who received the Nobel Prize in Chemistry in 1912. Because of their strong nucleophilic character, they are widely used in organic chemistry, especially for the alkylation of aldehydes and ketones.[71] In this case, it has been proved that they allow effective Mg reversible deposition if a small amount of aluminium halides is added to the electrolyte. In particular, the electrolyte formulated with EtMgCl 1.5 M/ AlCl_3 0.1 M in THF shows 99.5% of anodic current efficiency with a non-dendritic deposition, as shown by the SEM image in Figure 16:

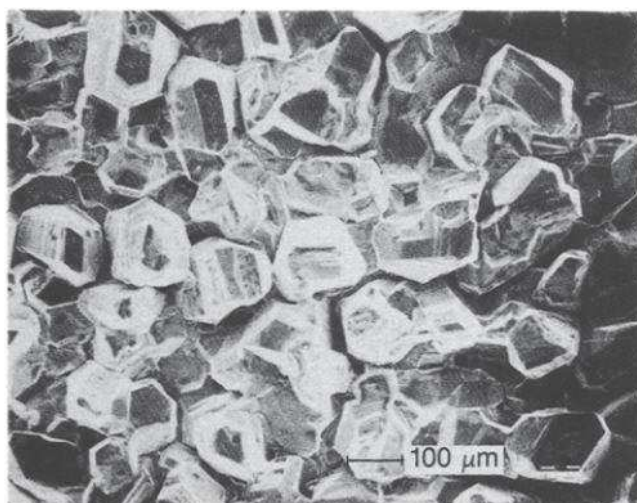


Figure 16 – SEM image on deposited Mg from a EtMgCl 1.5 M/ AlCl_3 0.1 M/THF solution. Is it worth noting the regular hexagonal structure of Mg crystallites, without any dendrite formation (Reproduced from [70]).

The reactions to which the electrolyte undergoes during plating are complex, but two major observations can be made:

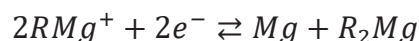
- A Grignard reagent (RMgX in a general formula) does not exist in solution as a single species but reacts according to the following equilibrium reaction:



- When an aluminium halide is added, a second reaction occurs:



Both equations evidence the presence of Mg in cationic species, which are expected to react with the cathode, thus resulting in the deposition of Mg metal:



As it is possible to argue from the second equation, the presence of AlX_3 (a Lewis acid) shifts the equilibrium toward the Mg-containing cation. On this intuition lies the basis of one of the fundamental breakthroughs in MBs and of the following research on electrolyte formulation.

Indeed, in 2000, Aurbach and co-workers reported a prototype of rechargeable MB able to deliver a stable capacity of 60 mAh g⁻¹ for almost 600 cycles at a current density of 0.3 mA cm⁻². [72]

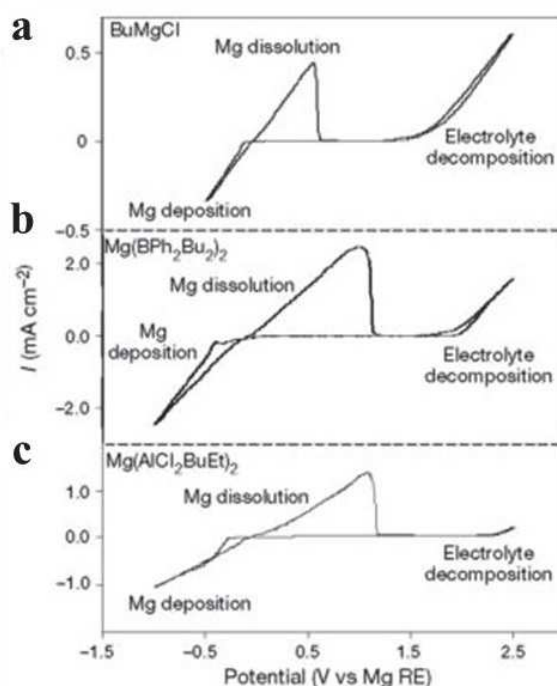


Figure 17 – Comparison between the cyclic voltammetry (CV) of Aurbach’s electrolyte, (c) Gregory’s electrolyte (b) and BuMgCl (a). The first offers the widest electrochemical window, (i.e. the stability before decomposition) among the three formulations. The enhanced oxidative stability is not just a key parameter for increase cycling properties but also allows using high-voltage working cathode, such as Mo₆S₈. All the CVs were measured in a three-electrode cell, with Pt as working electrode, Mg strip and Mg wire as counter and reference electrode, respectively. The potential scan rate was 5 mV s⁻¹ (Reproduction from [72]).

Lewis base	Lewis acid	Acid/base ratio	Mg cycling efficiency (%)	Electrolyte decomposition (V)
Bu₂Mg	AlCl ₂ Et	1:2.00	95	2.10
Bu₂Mg	AlCl ₂ Et	1:1.75	95	2.05
Bu₂Mg	AlCl ₂ Et	1:1.50	97	2.00
Bu₂Mg	AlCl ₂ Et	1:1.25	94	1.90
Bu₂Mg	AlCl ₂ Et	1:1.00	96	1.80
Bu₂Mg	AlCl ₂ Et	1:0.75	95	1.65
Et₂Mg	AlCl ₂ Et	1:2.00	92	2.25
Ph₂Mg	AlCl ₂ Et	1:2.00	80	2.08
Bz₂Mg	AlCl ₂ Et	1:2.00	88	2.15
Bu₂Mg	AlCl ₃	1:2.00	75	2.40
Bu₂Mg	AlCl ₃	1:1.75	74	2.30
Bu₂Mg	AlCl ₃	1:1.50	74	2.25
Bu₂Mg	AlCl ₃	1:1.25	83	2.15
Bu₂Mg	AlCl ₃	1:1.00	86	2.10
Bu₂Mg	AlCl ₃	1:0.75	92	2.00
Bu₂Mg	BPh ₃	1:1.50	86	1.77
Bu₂Mg	BPh ₃	1:1.00	68	1.60
Bu₂Mg	BPh ₃	1:0.66	91	1.40
Bu₂Mg	BPh ₃	1:0.50	93	1.30
Bu₂Mg	BCl ₃	1:1.00	80	1.20
Bu₂Mg	BCl ₃	1:0.50	93	1.75
Bu₂Mg	BCl ₃	1:0.20	71	1.50

Table 2 – Cycling efficiency and decomposition voltage for a wide series of Lewis base-acid combination. Oxidative stability decreases with the base-acid ratio (Reproduced from [66]).

Another critical point influencing the electrochemical stability of DCC electrolytes was identified in the relatively labile Al-C bond, which breaks via β -elimination. In order to avoid this reaction, Aurbach and co-worker proposed an electrolyte in which alkyl groups of both Lewis base and acid were fully replaced by either Cl⁻ or phenyl groups. In particular, a 0.4 M solution in THF of the reaction product between AlCl₃ and PhMgCl leading to the formation of the all-phenyl complex (APC) shows superior oxidative stability, exceeding 3 V vs. Mg²⁺/Mg (Figure 19). Moreover, it allows faster Mg deposition and exhibits a very high ionic conductivity.[75] [76]

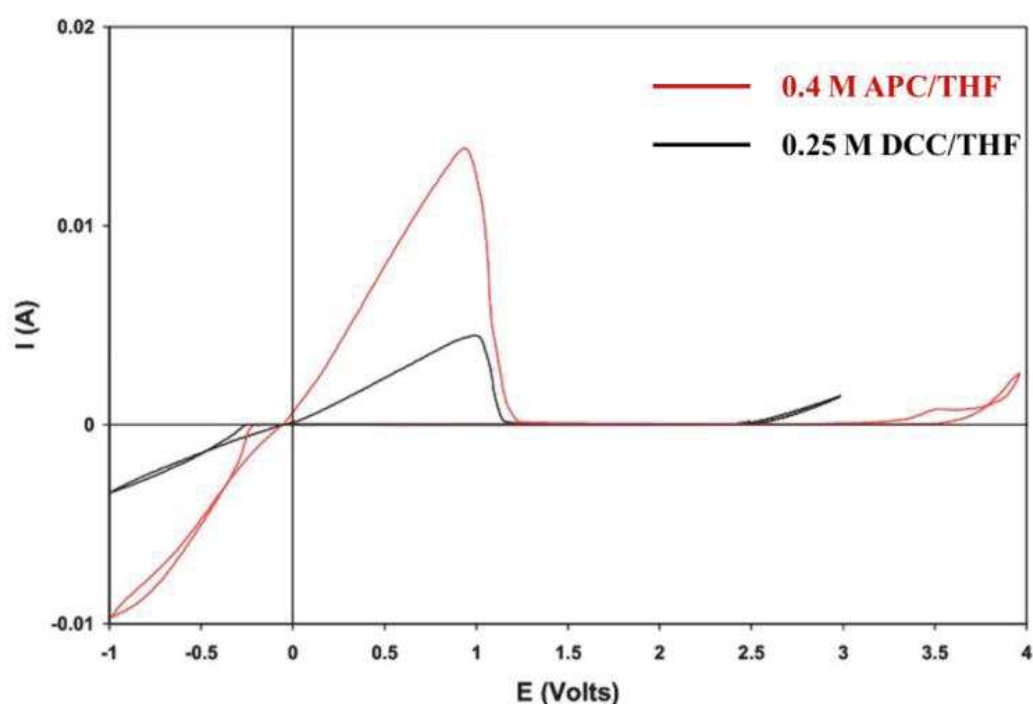


Figure 19 – Comparison between CVs obtained with all-phenyl complex (APC, red line) and DCC (black lines). The former shows a noticeably higher oxidative stability (by about 1 V) with faster Mg deposition than the latter. Both CVs were performed at 25 °C in a three-electrode configuration cell, using Pt wire as working electrode, Mg for both counter and reference electrode. Scan speed was set to 25 mV s⁻¹ (Adapted from [75]).

APC-based electrolyte have become a benchmark in MB's research, since it was successfully employed in many reports dealing with Mg-based energy storage systems.[77][78] Despite these noticeable improvements, Grignard-based electrolytes should not be considered as practical electrolytes for MBs for two main reasons: i) they are strong nucleophiles and have the tendency to react with many cathode materials and ii) the complex equilibria dominating the reduction reactions lead to a relatively poor control on the electrolyte composition, which represents a hurdle for

further optimization.[63] Therefore, other groups proposed alternative electrolyte formulations in order to enhance the stability of the complex. For instance, Kim and co-workers replaced the Grignard reagent with the less nucleophilic Hauser base⁶ hexamethyldisilazide magnesium chloride (HMDSMgCl), in combination with AlCl₃. [79] Surprisingly, they found that the re-crystallized salt outperformed the *in situ* product, with an oxidative stability of 3.2 V (Figure 20 - b).

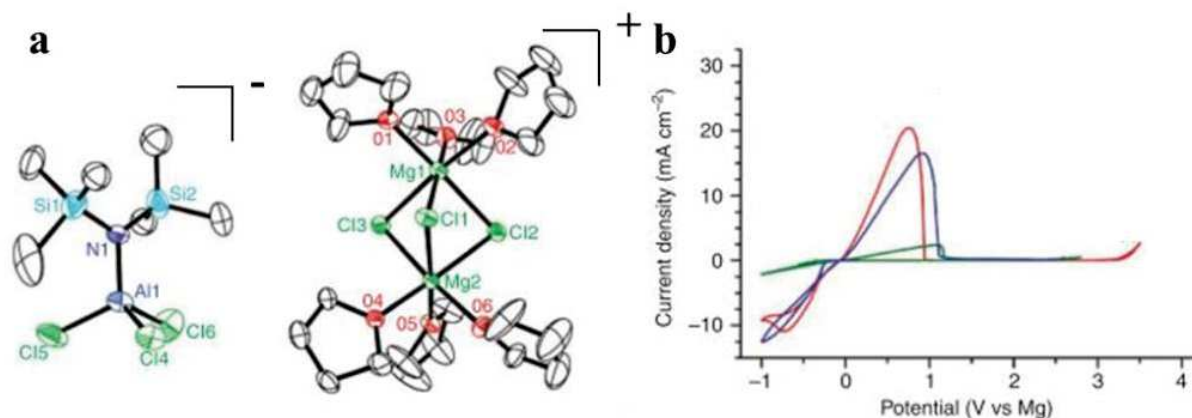


Figure 20 – (a) Oak Ridge Thermal Ellipsoid Plot (ORTEP) view of the crystallized product $[\text{Mg}_2(\mu\text{-Cl})_3\cdot 6\text{THF}]^+[\text{HMDSAICl}_3]$; (b) CVs of HMDSMgCl (green line), *in situ* product (blue line) and re-crystallized $[\text{Mg}_2(\mu\text{-Cl})_3\cdot 6\text{THF}]^+[\text{HMDSAICl}_3]$, which exhibits the highest oxidative stability. CVs were obtained using a 3-electrode cell with a Pt disk working electrode, a Mg wire reference electrode, and a Mg ribbon counter electrode at a scan rate of 25 mV s^{-1} (Adapted from [79]).

It is also worth noting that unlike Grignard-based formulations, this electrolyte was found to be compatible with a sulphur cathode. Lewis base phenolate-[80][81] and thiolate-based[82] electrolytes were also reported. Other approaches involved the replacement of the Lewis acid: Muldoon *et al.* tested a combination of phenylmagnesium chloride and of a boron-based Lewis acid in THF (tris(pentafluorophenyl)borane), obtaining an oxidative stability of 3.7 V.[83]

However, all the above-described electrolytes share two principal drawbacks: i) the presence of chloride, which is considered the culprit of the corrosion of several battery's components [84] and ii) the use of THF, which is relatively volatile and tends to form peroxides.[85] For these reasons, the most recent research on electrolytes for MBs was focused in shifting from organohalo-aluinate/organoborate-

⁶ A Hauser base is the product of the reaction between a secondary amine, R₂NH and a Grignard reagent R'MgX. [229]

based systems to other safer and more performant formulations. Mohtadi and co-workers, for instance, developed an electrolyte based on $\text{LiBH}_4/\text{Mg}(\text{BH}_4)_2$ in DME, showing a good coulombic efficiency (94%), high current densities and low deposition overpotential.[86] Although the electrochemical stability *vs.* Pt is not outstanding (1.7 V), it rises towards stainless steel and glassy carbon (2.2 and 2.3 V, respectively). This trend is opposed to Grignard-based formulations, thus confirming the noncorrosive behaviour of this borohydrides-based electrolyte. A combination of LiBH_4 and $\text{Mg}(\text{BH}_4)_2$ was also tested with other solvents, such as diglyme (DGM) and DME, in comparison to THF, evaluating how the electrochemical performance can be influenced by the choice of the solvent.[87]

Another important effort in replacing Grignard reagents was made in 2014 by Doe and co-workers. They achieved the full substitution of organic groups by chlorine in both Lewis base and acid, using MgCl_2 and AlCl_3 in 1:2 ratio, solved in various organic liquids, such as THF, 1,2-dimethoxyethane (monoglyme, DME) and tetraglyme. Similarly to DCC and APC, the *in situ* formed complex was called magnesium aluminium chloride complex (MACC). MACC-based electrolytes exhibit oxidative stability up to 3.1 V and a coulombic efficiency of almost 100%.[88]

As stated above, the second main hurdle for the further improvement of Mg electrolytes is the volatility of solvent. As already did for Li-ion technology, gel electrolytes have been explored. For instance, Chusid and co-workers impregnated a magnesium organohalo-aluminate salt, dissolved in THF, in both polyethylene oxide (PEO) and polyvinylidene fluoride (PVdF).[89] Other gel polymer electrolytes were reported but their composing magnesium salts are known to be not compatible with Mg metal.[85] MOFs were also proposed as nanometric media wherein immobilize magnesium phenolate or magnesium bis(trifluoromethane sulfonyl)imide ($\text{Mg}(\text{TFSI})_2$) in triglyme.[90] Lastly, the solvent can be directly removed using inorganic solid state electrolytes. Higashi and co-workers investigated the ionic conductivity of both $\text{Mg}(\text{BH}_4)_2$ and $\text{Mg}(\text{BH}_4)(\text{NH}_2)$. The latter exhibited good ionic conductivity and oxidative stability exceeding 3 V (at 150 °C).[91] Table 3 summarizes all the electrolytes cited in this section, and provides a direct comparison of their principal features.

electrolyte type	Composition	E_{ox} on Pt vs. Mg^{2+}/Mg	solvent	Remarks
Liquid State				
organo/organo-halo				
Organo borates	Mg(BPh ₂ Bu ₂) ₂ 2:1 PhMgCl:	1.9	THF	
	Me ₃ B	3.5	THF	$E_{ox} = 2.2$ V on SS
	(Mg ₂ (μ-Cl) ₃ ·6THF)[B(C ₆ F ₅) ₃ Ph]	3.7	THF	$E_{ox} = 2.2$ V on SS
		2.2	THF/glymes	optimum in THF
		3.2	THF/glymes	$E_{ox} = 2.2$ V on SS
Grignard halo-aluminate	Mg(AlCl ₃ -nRnR') ₂ R, R' = alkyl or aryl 2:1 RMgCl:AlCl ₃ R = phenyl			
inorganic ionic salts non-halide based				
borohydrides	1:x Mg(BH ₄) ₂ :LiBH ₄ , x = 0–6	1.7	Monoglyme/ DGM	non-corrosive $E_{ox} = 2.2$ on SS
non-Grignard halo-aluminates				
phenolates & aloxides	2:1 ROMgCl:AlCl ₃ R = phenyl alkyl	2.6	THF	
	R = phenyl fluoroalkyl	2.9	THF	
Amido based	3:1 (HMDS)MgCl:AlCl ₃	3.2	THF	$E_{ox} = 2.2$ V on SS
Inorganic halide based	2:1 MgCl ₂ :AlCl ₃	3.1	monoglyme	
Solid state				
Gel polymer	Mg(AlCl ₂ EtBu) ₂	2.5	Tetraglyme/ PVdF	3.7 mS cm ⁻¹ at 25 °C
Inorganic salts	Mg(BH ₄)(NH ₂)	>3.0	none	10–3 mS cm ⁻¹ at 150 °C, coulombic efficiency <50%

Table 3 – Summary of the more significant electrolytes for MB that were developed, featuring composition, solvent and marking electrochemical properties.

In conclusion, finding stable, safe and Mg-compatible electrolytes with also high electrochemical performance represents a real challenge, since electrolytes based on conventional Mg salts are not compatible with metallic Mg. In addition, Mg-metal compatible electrolytes suffer poor electrochemical stability or irreversibly react with many positive electrodes, thus limiting the choice of materials that can be employed. A solid understanding of the anode/electrolyte/cathode interface reactions and the search of novel tuned active Mg-species (also involving computational studies) could give a new breakthrough on electrolyte for MB. However, not using Mg metal as the negative electrode, and replacing it with other materials compatible with classical electrolyte formulations has been discussed and represents the principal subject of the present thesis (cf. 1.7.4).

1.7.3. Positive electrodes

Positive electrodes for Mg batteries have been widely investigated during the last decades. Many challenges need to be faced in order to develop viable materials providing fast Mg^{2+} kinetics (*i.e.*, fast Mg^{2+} insertion), high energy density (high redox potential vs. Mg^{2+}/Mg and low molecular weight) and elevate compatibility with electrolytes.

Indeed, one of the main hurdles in the development of positive electrodes for Mg-based systems is the sluggish solid-state diffusion of Mg^{2+} , mainly due to its elevate charge/radius ratio, and the consequent difficulty to redistribute the divalent charge into the hosting framework. [92][93] A wide variety of intercalation materials have been tested during the last 25 years, such as oxides, sulphides and phosphates. Most of them, however, exhibited poor electrochemical activity characterised by reduced Mg intercalation and/or elevate polarizations.[70][94] Nevertheless, some of these results should be reviewed since the poor activity can be ascribed also to less-performing or corrosive electrolytes. However, interesting electrochemical behaviour *vs.* Mg has been shown by a class of molybdenum chalcogenures, also known as “Chevrel Phases”. In particular, Mo_6S_8 was employed in the first Mg-battery prototype and nowadays is, by far, the most studied positive electrode for Mg-based storage systems, becoming the reference materials for complete cells. For its importance, this material will be discussed in detail in the next section, followed by a rapid overview of other alternative positive electrode materials. Since Mg-positive electrodes were not the main scope of this thesis, only their most relevant aspect will

be highlighted. A more complete picture of these materials can be found in several detailed reviews.[85][95][96]

1.7.3.1. Chevrel phases

In 1971 Roger Chevrel and co-workers synthesized for the first time a family of ternary molybdenum chalcogenides $M_xMo_6T_8$, in which M is a mono-, di- or trivalent element (x can range from 0 to 4) and T is a chalcogen (S, Se or Te).[97] Their crystal structure can be depicted as a 3D array of T_8 chalcogen cubes encompassing a distorted Mo_6 octahedron, while M cations may occupy the three-dimensional open frameworks.[98] More precisely, 3 different types of cavities are present but only type-1 and -2 allow M insertion (Figure 21). Indeed, type-3 cavities are characterised by a strong repulsion between Mo atoms, which hinders further cation accommodation.[99]

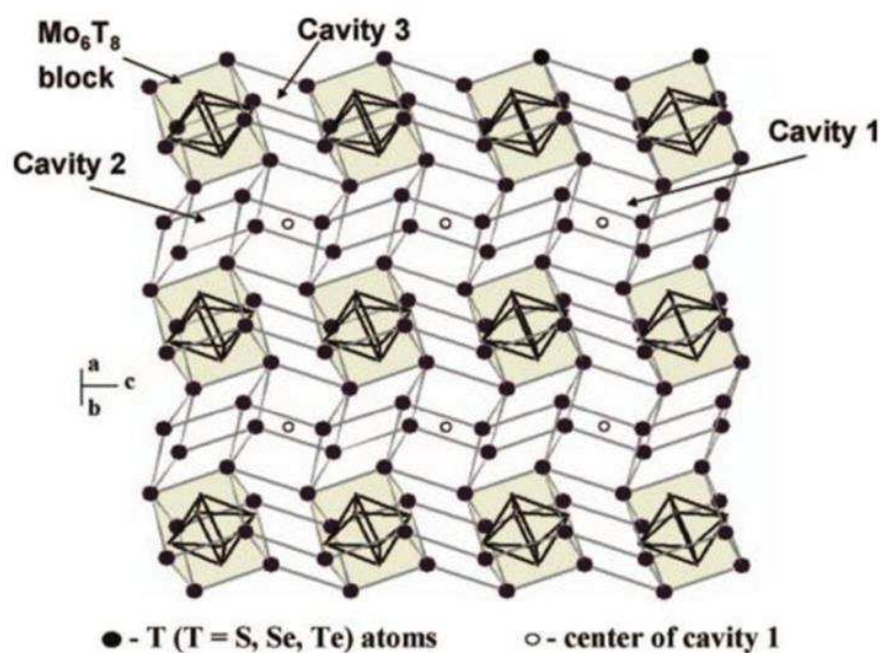


Figure 21 – The general structure of a ternary Chevrel phase. Distorted Mo_6 octahedra are encased in T_8 cubes. Therefore, 3 different types of cavity can be obtained, but only type-1 and -2 can accommodate M atoms (Reproduction from [99]).

Chevrel phases (CPs) have attracted the interest of the scientific community for two major and interconnected reasons: i) they offer a noteworthy richness of chemical compositions (more than 100 compounds have been synthesized) and ii) they exhibit outstanding properties with a wide range of applications. Indeed, several CPs, such as $PbMo_6S_8$, have been deeply investigated due to their remarkable

superconductivity behaviour.[100][101] Moreover, sulphur-based CPs were used as promising catalyst for the hydrodesulfurization of thiophene at low temperature,[102] whereas the thermoelectric properties of several $M_xMo_6S_8$ ($M = Cr, Mn, Fe, Ni; x = 1.3, 2$) compounds were recently tested.[103]

Another key property of CPs is their inclination to accommodate various elements.[101][104][105] Indeed, the high mobility of the guest atoms M in the open framework structure enables synthesizing new metastable compositions via low-temperature chemical or electrochemical reactions.[106] Consequently, ternary CPs with intermediate compositions ($M_xMo_6T_8$) and the corresponding binary Mo_6T_8 have been widely investigated as electrode materials in rechargeable lithium and sodium batteries (Figure 22).[107][108][109][110]

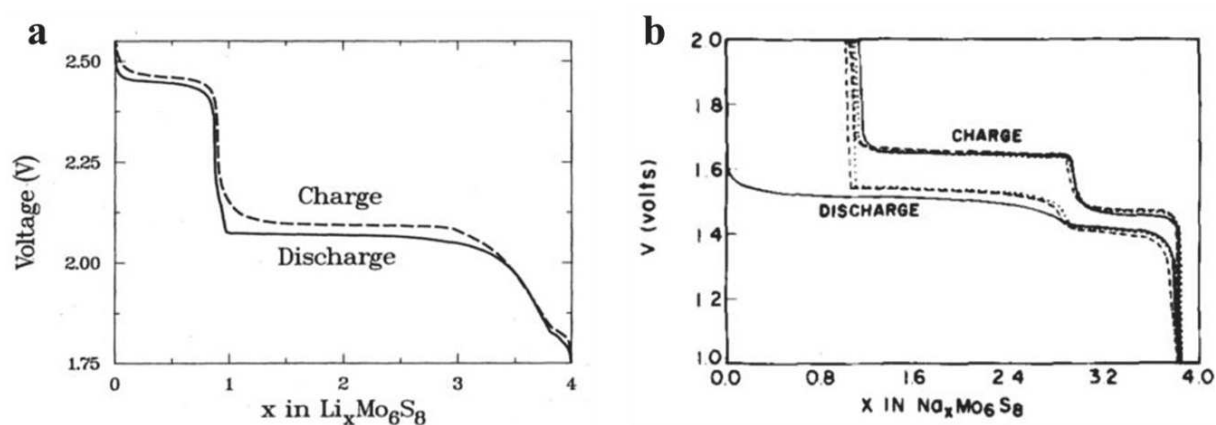
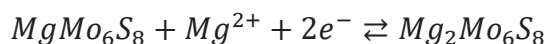


Figure 22 – Galvanostatic profiles of Li (a: current density of $C/12.5$, solid and dashed lines represent discharge and charge, respectively) and Na (b: $100 \mu A cm^{-2}$, solid, dotted and dashed lines represent 1st, 2nd and 3rd cycles) insertion /de-insertion into Mo_6S_8 CP. It is worth noting that M^+ insertion occurs according to the subsequent occupancy of the two available cavities. In effect, in the case of Li, two steady plateaus, at 2.45 V and 2.07 V, respectively, were found. Last part of Li insertion involves changes in crystallographic structure, with consequent different electrochemical signature (sloppy plateaus). Even if less immediate from the analysis of the galvanostatic curve, Na insertion occurs in a similar fashion. The type-1 cavity is occupied by 1 equivalent of Na^+ per equivalent of CP and can be confirmed by the irreversible capacity exhibited during the subsequent charge. Indeed, it was found that the electrochemical formation of $NaMo_6S_8$ is irreversible. [110] (Reproduction from [108] (a) and [110] (b)).

However, their relatively low operating voltages and reduced specific capacities have prevented their use as positive electrode materials in commercial cells, as they cannot compete with layered or polyanionic compounds.[19] Chevrel phases were put back on stage as positive electrode materials of the first prototype of rechargeable magnesium battery (MB) by Aurbach and co-workers. In this pioneering work, Mo_6S_8 showed a stable capacity during reversible Mg^{2+} ions intercalation

(60 mAh/g for almost 600 cycles of discharge/charge).[72] As it can be seen from Figure 23, Mg insertion occurs in two stages, according to the following equations:



that correspond to the magnesianation of sites A and B, respectively.[111] It is important mentioning that during the insertion of small cation (Cu^+ , Li^+ , Mg^{2+}) into the CP, a deformation of the cubic S_8 network occurs. This leads to an important difference between the cation occupying the type-1 and the type-2 cavity: indeed, the former realizes a plated ring (inner positions, site A), whilst the latter, more mobile, presents a quasi-octaedral arrangement (outer positions, site B).[112]

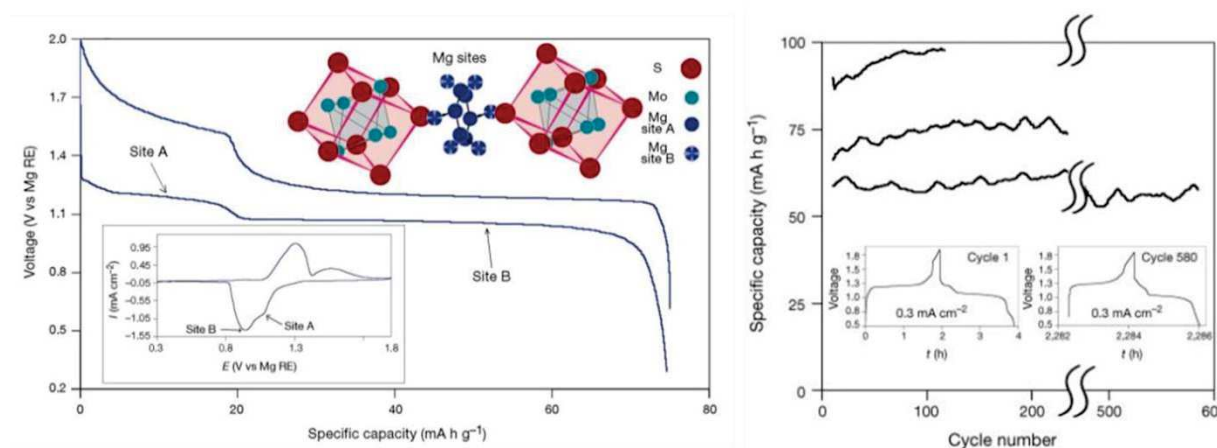


Figure 23 – The prototype MB by Aurbach and co-workers. As previously seen for Li- and Na-based battery, Mg^{2+} is galvanostatically intercalated into the two well-known sites, called A and B (current density: 0.3 mA cm^{-2} , left), also confirmed by the CV (scan rate: 0.05 mV s^{-1} , left – inset). This material has become a benchmark positive electrode for MB also thanks to the outstanding number of reversible cycles exhibited by the optimized MB (straight lines, top right), which kept good performance after almost 600 discharges/charges, right – inset. Reproduction from [72]).

However, Mg trapping into the Mo_6S_8 host was noticed,[113] and was recognized to be the major cause of the sluggish diffusion of Mg^{2+} cations. In particular, Levi and co-workers identified in the first reaction between Mg and Mo_6S_8 the limiting process in Mg^{2+} insertion, which is much slower with respect to Li^+ .[114][115] Interestingly, the same group found no Mg-trapping in analogous Mo_6Se_8 , likely due to a minor ionicity of the anionic framework, with the consequence of more stable intercalation compounds.[116] However, Se is heavier than S, thus leading to an electrode with a very low specific capacity (88.8 mAh g⁻¹) Mg-trapping can also be avoided by increasing

the working temperature of the battery. Indeed, full Mg insertion/extraction was achieved at 60 °C.[111]

In spite of the well-known problem of capacity loss discussed above, of the relatively low specific capacity and of the low value of the Mg-insertion potential, Mo₆S₈, still remains the benchmark for cathode materials in MBs and Magnesium-ion batteries (MIBs) prototypes,[95] and also starts to be pointed out for calcium- and aluminium-ion cells.[57][117] A deep understanding of the intercalation mechanism into the Chevrel phases might help in designing new cluster-containing intercalation compounds with higher capacity and energy density.

Modified CPs: the complete replacement of S by Se discussed above is definitely more interesting from a fundamental point of view than for practical purposes. Nevertheless, partial replacement was proposed by Aurbach and co-workers, who synthesized nanometric Cu_{2.5}Mo₆S_{8-y}Se_y (y = 0, 1, 2) phases. They observed only a 10% capacity loss for mixed phases instead of 50% for pure sulphide CPs, at C rate and room temperature.[75] Despite this encouraging benefit, it is worth mentioning that long synthesis time (7 days), involving heating steps at elevated temperatures may represent a major hurdle for practical applications. Mitelman and co-worker also showed that Mg²⁺ trapping can be avoided using partially leached ternary CP Cu_xMo₆S₈ (x ~ 1).[118]

1.7.3.2. Other positive electrodes

In the quest for more performing positive electrodes, many other compounds have been tested. Most materials allow Mg²⁺ intercalation, but a few of them directly react with Mg to form Mg salts. A brief presentation of the most promising strategies for replacing Mo₆S₈ is given hereafter. The materials are further summarised in Table 4.

Oxides: first attempts to electrochemically intercalate Mg²⁺ into oxides were provided by the pioneering work of Gregory and co-workers, who tested various compounds such as Co₃O₄, Mn₂O₃, Mn₃O₄, MoO₃, PbO₂, Pb₃O₄, RuO₂, V₂O₅ and WO₃. Even though most of them did not show further Mg²⁺ de-intercalation, Co₃O₄ was successfully used in a rechargeable MB prototype proposed in the same paper.[70]

γ - V_2O_5 : it is a layered compound containing V^{5+} in a square-pyramidal coordination with 5 oxide neighbours and a weak V-O interaction with the 6th oxide ion (Figure 24).

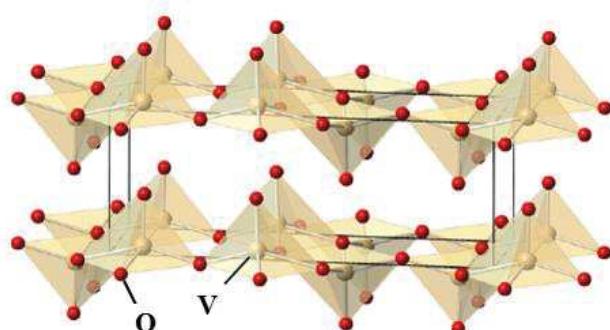


Figure 24 – Schematic representation of γ - V_2O_5 crystal structure. Cation insertion is possible in the cleavage parallel to the basal plane of the square pyramids.

Pereira-Ramos and co-workers reported reversible Mg intercalation at 150 °C.[119] Interestingly, Novák and Desilvestro found that the presence of water dramatically enhances the Mg^{2+} reversible insertion, since it acts as solvating agent.[120] Moreover, even hydrated $Mg(V_3O_8)_2$ showed enhanced mobility with respect to the corresponding dry phase.[121] Unfortunately, the addition of water to non-aqueous electrolytes is not compatible with both the Mg negative electrode and the active solvated species into the electrolyte. Indeed, it is known that even minor traces of water lead to the formation of passivating species on the surface of metallic Mg.[95] However, reversible Mg^{2+} intercalation into thin film layered V_2O_5 was recently shown by Gershinsky and co-workers. This electrode provides a specific capacity of 150 mAh g^{-1} at the current density of 0.5 $\mu A cm^{-2}$ in a cell completely free from water.[122] Superior kinetic was also proved for both amorphous powders, (ball-milled V_2O_5 - P_2O_5)[123] and nanometric materials (V_2O_5 nanocluster embedded in a carbon matrix).[124]

MnO_2 : Manganese dioxide is a widely studied material for LIB positive electrodes, because of the large availability and the environmentally benign properties of Mn. MnO_2 exists in several polymorphs and α - MnO_2 hollandite,[125] λ - MnO_2 spinel [126] and δ - MnO_2 birnessite [127] were tested toward Mg. Hollandite prepared from K- α - MnO_2 showed the most promising initial specific capacity of 282 mAh g^{-1} . However a rapid capacity fading was observed after few cycles, due to

the partial collapse of the α - MnO_2 structure. For K- α - MnO_2 a more complex mechanism was proposed, involving conversion pathways.[128] A recent work by Ling *et al.* indicated that conversion reactions are more thermodynamically favourable compared to the intercalation even for α - MnO_2 . [129]

Transition metal oxides (TMOs): The possibility of intercalating Mg^{2+} into TMOs has been reported and several MgTMOs, such MgCo_2O_4 and $\text{Mg}_{0.67}\text{Ni}_{1.33}\text{O}_2$, were successfully synthesized.[130] They showed appreciable room temperature electrical conductivity and an open circuit voltage between 3 and 3.5 V *vs.* Mg^{2+}/Mg . Unfortunately, there is a lack of stable electrolyte formulation around these voltage values which dramatically limits the actual development of such class of materials.

Polyanionic compounds: this group includes a wide variety of materials, such as phosphates, silicates, sulphates, etc. that are characterised by a tridimensional anionic framework in which cation intercalation is possible. Although they were extensively studied as positive electrodes for LIBs and NIBs, only few reports of their activity in Mg-based system can be found, mainly due to their high potential toward Mg^{2+}/Mg . Among them, it is worth mentioning the studies carried by NuLi's group on a series of MgMSiO_4 olivine compounds.[131][132] In particular, mesoporous $\text{Mg}_{1.03}\text{Mn}_{0.97}\text{SiO}_4$ showed a specific capacity along several cycles between 150 to 225 mAh g^{-1} . [133] Reversible Mg intercalation was also achieved in $\text{Li}_2\text{FeSiO}_4$, in which Li was electrochemically leached and replaced by Mg.[134] These results are however more than questionable as no other research groups were able to reproduce them.

Unlike LIBs, where LiFePO_4 represents a benchmark positive electrode, few studies deal with the possible application of phosphates on Mg-based batteries, such as the theoretical investigation on MgVPO_4 [135] or the electrochemical test of MgFePO_4F . The latter exhibits an operating voltage of 2.6 V and a good cyclability. However, the specific capacity remains relatively low (60 mAh g^{-1}). [136] Amorphous FePO_4 was also tested toward Mg, exhibiting a specific capacity of 130 mAh g^{-1} , which corresponds to insertion of 0.37 Mg per formula unit. Although an electrochemical magnesianation appeared from the galvanostatic signature, authors did neither comment the specific shape of the subsequent charge, which should correspond to Mg de-intercalation, nor provided further data on subsequent cycling.[137]

Other chalcogenides: as stated above, one of the major advantages provided by CPs is represented by the relatively fast kinetics of Mg^{2+} intercalation/de-intercalation, which is mainly due to the lower electronegativity of the S_8 (or Se_8) anionic framework, compared to an analogous O_8 cube.[138] Consequently, TiS_2 nanotubes were tested by Tao and co-workers. Such electrode delivers the specific capacity of 236 mAh g^{-1} , which corresponds to a 0.49 Mg inserted per formula unit, but is plagued by rapid capacity fading.[139] More recently, the cubic thiospinel Ti_2S_4 tested by Sun and co-workers in 2016 showed a specific capacity between 160 and 130 mAh g^{-1} from the 2nd and the 40th cycle at the C/10 rate, working at $60 \text{ }^\circ\text{C}$.[138] Micrometric TiS_3 was also reported, with good cycling behaviour and capacity values comparable to those of CPs.[140] As already shown for CPs, better overall performance can be achieved by replacing S by Se. It is noteworthy the report of Liu and co-workers, on WSe_2 nanowires, which exhibit a stable capacity of 200 mAh g^{-1} at the current density of 50 mA g^{-1} for 160 cycles. Moreover, excellent capacity retention was shown even at fast current rates, with a 17.5% of capacity loss at 800 mA g^{-1} .[141]

Chalcogens for direct reactions: Unlike intercalation processes, such direct reactions enable achieving more elevated energy densities (up to one order of magnitude) because of the high number of Mg which can react with the active material. For instance, the reaction between Mg and S to form MgS can theoretically deliver 1670 mAh g^{-1} , compared to the 140 mA g^{-1} practically provided by LiCoO_2 in LIBs. However, the major hurdle for developing such electrodes is represented by the nucleophilic character exhibited by most Mg-electrolytes, which irreversibly damage sulphur positive electrodes. Nevertheless, thanks to the work of Muldoon and co-workers on non-nucleophilic electrolytes (cf.1.7.2), rechargeable magnesium-sulphur cells delivering 1200 mAh g^{-1} during the first discharge were developed.[79] Although a capacity loss was observed, likely due to sulphur dissolution, this work paved the way to further developments in this field. Indeed, it is worth mentioning the paper of Zhao-Krager *et al.*, who confined Se and SeS_2 into a mesoporous-carbon CMK-3 matrix, and tested them *vs.* Mg. Se-based positive electrodes showed a reversible capacity of 480 mAh g^{-1} after 50 cycles at 2C rate.[142]

Organic compounds: organic molecules may represent a competitive alternative to inorganic materials in terms of costs and environmental impact. Indeed, they start to be considered as viable electrode materials in LIBs.[143] Only

few works, however, deal with their use as positive electrode materials in Mg-based systems. In one of the most promising reports, Bitenc and co-workers investigated poly(antraquinoyl) sulphide (PAQS) and poly(hydroquinonyl-benzoquinonyl) sulphide (PHBQS) that exhibited capacities between 150 and 200 mAh g⁻¹ at an operating voltage of 1.7-1.5 V.[144][145]:

Compound	Working potential (V vs. Mg ²⁺ /Mg)	Theoretical energy density (mAh g ⁻¹)	Sp. Capacity (mAh g ⁻¹)	Remarks
Insertion mechanism				
Oxides				
Co ₃ O ₄	2.28	222 (MgCo ₃ O ₄)	147	1 st complete MB [70]
V _x O _y	2.40	294 (MgV ₂ O ₅)	150, 0.1 mA	At 150 °C [119]
		190 (Mg(V ₃ O ₈) ₂ ·xH ₂ O)	160 – 60 (50 CV cycles)	H ₂ O needed for enhanced Mg ²⁺ intercalation [121]
		294 (MgV ₂ O ₅)	190 – 150 (35 cycles)	Thin film layered V ₂ O ₅ ; H ₂ O-free cell [122]
		Depending on the molar V ₂ O ₅ :P ₂ O ₅	120 – 60 (5 cycles at 5 mA g ⁻¹)	Amorphous 0.75 mol V ₂ O ₅ ; 0.25 mol P ₂ O ₅ [123]
		273 (MgV ₂ O ₅ 45 wt.% into C matrix)	120 – 80 (100 cycles at 320 mA g ⁻¹)	[124]
MnO ₂	Sloppy plateaus	616 (MgMnO ₂)	240 – 75 (6 cycles at 36 μA cm ⁻²)	α-MnO ₂ , rapid capacity fading [125]
		“	330 – 180 (5 cycles at 60 mA g ⁻¹)	λ-MnO ₂ [126]
		“	65 – 50 (10 cycles at 100 mA g ⁻¹)	δ-MnO ₂ [127]
		“	282 (1 st discharge)	K-α-MnO ₂ , conversion mechanism? [128]
TMOs (MgCo ₂ O ₄ and Mg _{0.67} Ni _{1.33} O ₂)	3.5 – 3.8 (OCV)	295 and 326, respectively	-	Too high potential for Mg electrolytes [130]
Polyanionic compounds				
Mg _{1.03} Mn _{0.97} SiO ₄	1.6	380	130 – 110 (80)	Mg _{1.03} Mn _{0.97} SiO ₄

			cycles at 62.9 mA g ⁻¹	nanoparticles [131]
			300 – 200 (20 cycles at 62.8 mA g ⁻¹)	Mesoporous Mg _{1.03} Mn _{0.97} SiO ₄ from SBA- 15 template [133]
MgCoSiO₄	1.6 – 1.3	306	270 -120 (200 cycles, C/4)	3D hierarchically porous structure [132]
Li₂FeSiO₄	2.3 – 1.9	362 (MgFeSiO ₄)	340 (5 cycles at 6.62 mA g ⁻¹)	Electrochemical Li replacing, 55°C, tested in MB [134]
MgVPO₄F	2.6 and 1.5 (theoretical)	312	-	First principles calculation [135]
MgFePO₄F	Sloppy plateau	316	50 – 35 (10 cycles, C/20)	[136]
FePO₄	1.5 – 0.9	178 (Mg _{0.5} FePO ₄)	130 (1 st discharge)	Reversible process? [137]

Other chalcogenides

TiS₂	1.6 – 1.1	239 (Mg _{0.5} TiS ₂)	230 – 185 (80 cycles at 10 mA g ⁻¹)	TiS ₂ nanotubes [139]
Ti₂S₄	1.5 – 1	239 (MgTi ₂ S ₄)	200 – 140 (40 cycles, C/10)	At 60 °C
TiS₃	Sloppy plateau		140 – 80 (50 cycles at 10 mA g ⁻¹)	Micrometric Ti ₃
WSe₂	1.7 – 1.2		200	WSe ₂ nanowires

Modified CPs

Mo₆S_{8-y}Se_y	1.2 and 1.1	Depending on S – Se ratio	105 (for Mo ₆ S ₆ Se ₈ , 100 cycles, C/8)	7-days synthesis [75]
CuMo₆S₈	1.25, 1.15 and 1.07	60	-	No Mg ²⁺ trapping [118]

Direct reaction

S	Tested in MB	1670 (MgS)	1200 (1 st discharge), 816 (2 nd discharge)	Mg/S battery with non- nucleophilic Lewis base HMDSMgCl + AlCl ₃ as electrolyte [79]
Se	1.4 – 1.2	678 (MgSe)	500 – 180 (10 cycles at	Se – CMK-3 composite [142]

			135 mA g ⁻¹)	
SeS_n	1.46 and 1.18	Depending on Se – S ratio	600 (1 st discharge at 40 mA g ⁻¹), 380 (2 nd discharge)	SeS ₂ – CMK-3 composite [142]

Organic compounds

PAQS	1.7 – 1.5	225	From 205 (1 st cycle at 50 mA g ⁻¹) to 100 ((1 st cycle at 500 mA g ⁻¹)	Results depending on electrolyte employed. [144]
PHBQS	2.0	382	From 60 to 155 (after 20 cycles at 50 mA g ⁻¹)	Performance influenced by the electrolyte. Several current densities tested. [145]

Table 4 – Positive electrode materials for Mg-based system cited in this thesis.

1.7.4. Negative electrodes

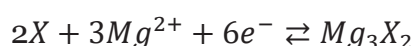
The use of the Mg as negative electrode can offer an outstanding theoretical capacity but, as discussed before, is not actually compatible with stable and thus safe electrolyte formulations. From this crucial point, the interest in seeking possible alternative materials that can replace metallic Mg arose in the last five years, similarly to the well-known evolution from LB to LIB. The attention of the scientific community has been mainly focused on *p*-block elements, but more recently an insertion electrode material, Li₄Ti₅O₁₂, was also proposed.[146] *p*-block elements have been extensively studied (alone or combined) as possible electrode materials for LIB, and more recently even for NIB, but they are also able to alloy with Mg.

In 2013, at the beginning of this thesis, only few articles were known in the literature and others came out during these last three years. The following section summarizes all works concerning the *p*-block elements as alloy materials for MIBs.

1.7.4.1. Sb and Bi

The very first study on Sb and Bi was presented by Arthur and co-workers in 2011.[147] They electrodeposited nano-sized particles of Bi and Sb in a three-electrode cell. Bi-containing phases were deposited on a copper-alumina-platinum substrate starting from solutions of Bi(NO₃)₃ · 5H₂O and SbCl₃ in DMSO . Nano-Sb

was deposited on a copper-titanium-platinum substrate starting from Sb_2O_3 dissolved in an aqueous solution of citric acid. All cells were equipped with a platinum-based working electrode and Ag/AgCl as the reference one. The electrodes were electrochemically tested *vs.* Mg using an organohaloaluminate-based electrolyte. The comparison of the first discharge (corresponding to the magnesiation) of the studied systems (Figure 25) shows that Sb delivers the highest capacity among all the tested materials and is very close to the theoretical value of 660 mAh g^{-1} . Sb-Mg and Bi-Mg alloying reactions are in agreement with the generic following equation:



Where X is either Sb or Bi.

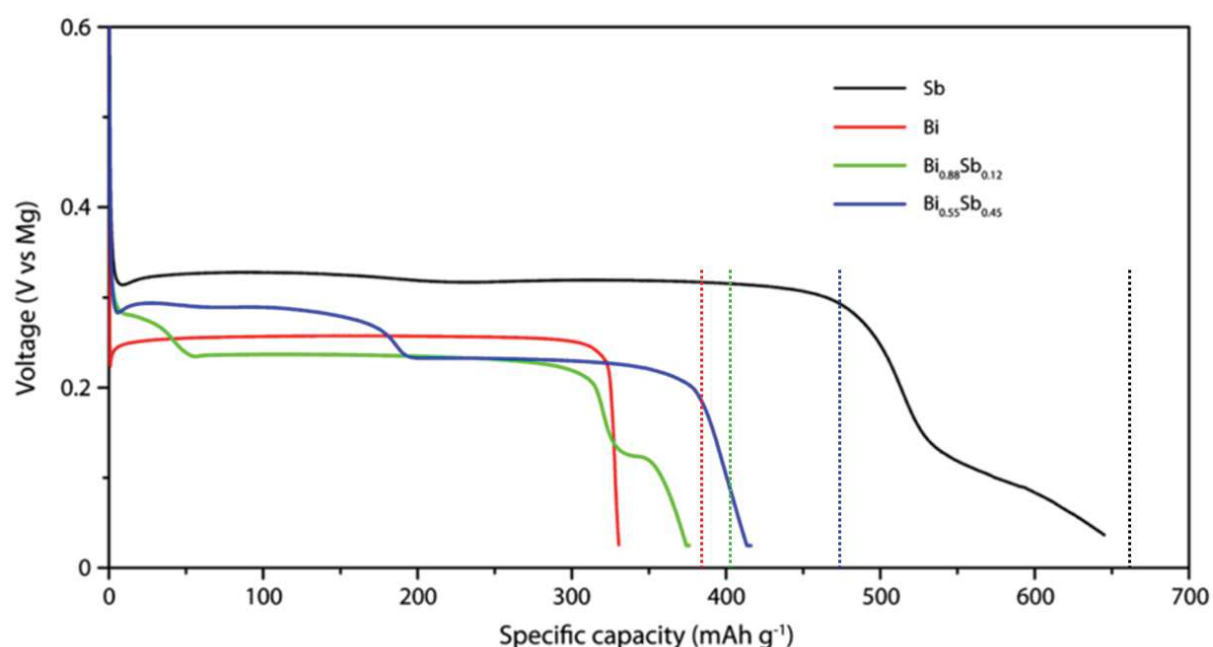


Figure 25 – Galvanostatic profile of the first magnesiation for electrodeposited Sb- (black), Bi- (red), Bi_{0.88}Sb_{0.12}- (green) and Bi_{0.55}Sb_{0.45}- (blue) based electrodes, at C/100 current rate, as a function of the specific capacity. Vertical dotted lines provide the theoretical specific capacity values for each material (Adapted from [147]).

Both Bi and Sb exhibit almost straight, well-defined alloying plateaus, at 0.25 and 0.32 V, respectively. However, it is interesting to observe a major difference in the final part of the curves: in fact, while the alloying plateau of Bi sharply ends in correspondence to the specific capacity of 330 mAh g^{-1} , the profile of Sb starts decreasing around 460 mAh g^{-1} and exhibits a second sloppy plateau between 0.12 and 0.05 V. Unfortunately, the authors neither comment this difference (possible

electrolyte degradation?), nor provided any study on the mechanism. Even though no *ex situ* XRD was performed on the Sb-based electrode, it seems possible that the obtained capacity values were overrated due to parasite reactions responsible of the second plateau.

Specific capacities of the Bi-Sb intermediate compositions lie between those of the pure metals, as it can be expected, and are proportional to the Sb-Bi ratio. It is worth noting that the higher is the Sb-Bi ratio, the highest the gap between the practical and the theoretical value of the specific capacity. Indeed, the authors observed that the capacity retention decreases with increasing the Sb-Bi ratio after the first cycle, as resumed in the Table 5.

Electrode	Sp. capacity (1 st discharge) mAh g ⁻¹	Capacity retention (2 nd disch.)
Bi	330	98 %
Bi _{0.88} Sb _{0.12}	375	94 %
Bi _{0.55} Sb _{0.45}	410	82 %
Sb	650	55 %

Table 5 – Summary of the gravimetric capacities measured after the first discharge and of the capacity retention after the second discharge for Bi, Sb and Bi-Sb solid solutions at C/100.

The cycling performance of each material, recorded at C rate, confirmed the very poor activity of the Sb in contrast with the interesting cyclability of pure Bi (Figure 26).

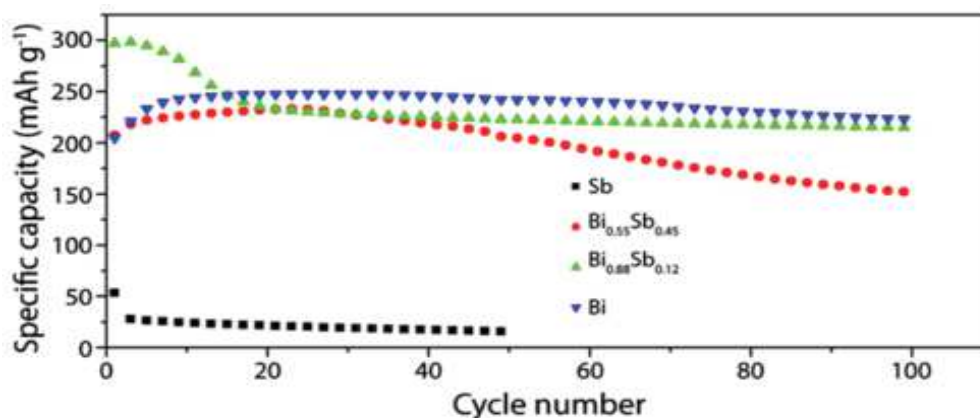


Figure 26 – Cycling behaviour of Sb- (black dots), Bi_{0.55}Sb_{0.45}- (red circles), Bi_{0.88}Sb_{0.12}- (green triangles) and Bi- (blue triangles) based electrodes at C current rate. Despite its relatively low theoretical capacity, Bi is a promising candidate for negative electrodes in MIB because of its high capacity retention even at elevated current densities. (Reproduced from [147]).

From these evidences, the study of Sb as possible negative electrode was put aside whilst the promising results on Bi encouraged further investigations. In 2013, Shao and co-workers proposed the use of Bi nanotubes (Bi NTs, prepared by hydrothermal synthesis) claiming that superior electrochemical performance can be achieved with this specific morphology.[78] In particular, electrochemical performance of micrometric Bi particles and Bi NTs were compared. The use of Bi nanotubes results in a lower polarization between discharge and charge, a higher capacity at fast current rates, and an overall better cycling stability (Figure 27).

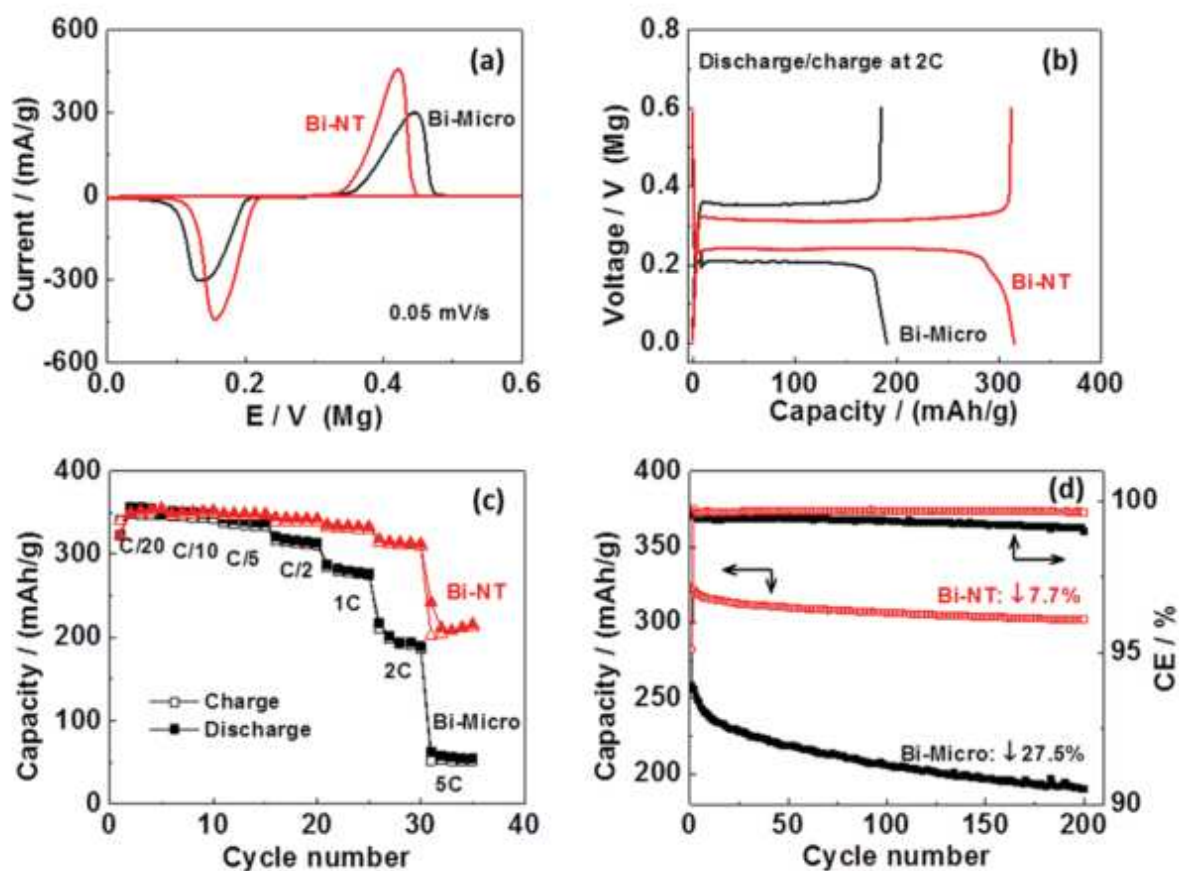


Figure 27 – A comparison between the cyclic voltammetry on Bi nanotubes- (red) and micrometric Bi- (black) based electrodes shows a reduced polarization for the former (a), also visible in the galvanostatic profile (b). Moreover, Bi-NT deliver higher specific capacity, compared to the Bi-micro at elevated current densities (b), show better capacity retention (c) with a steady coulombic efficiency (d) (Adapted from [78]).

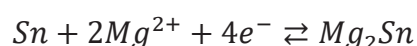
According to these data, the authors concluded that the enhanced performance of Bi nanotubes arise from the *in situ* formation of interconnected Bi nanoparticles allowing fast ion mobility during cycling. Another Bi-based electrode was proposed

by DiLeo and co-workers, which realized Bi - carbon nanotubes composite electrodes, with a tuned electrochemical deposition of a Bi precursor[148]

Despite these interesting results, it is important to notice that the proposed syntheses are laborious and would not sit well with upscaling, thus limiting possible future applications. Indeed, industrials prefer to look towards simpler production ways. To confirm this, Toyota Motor patented in 2014 a Mg_3Bi_2/C composite obtained by high-energy ball-milling as the negative electrode for MIB.[149]

1.7.4.2. Sn

Tin is an element that has been extensively studied during the last 15 years as a negative electrode for LIB since it can form Li-rich alloys, thus achieving elevate theoretical capacities. However, during the alloying/de-alloying process, a dramatic volume change occurs (300%), with consequent fracturing and isolation of the electrode particles and finally rapid capacity fading.[150][151] Despite the efforts made to accommodate this volume expansion,[152][153][154] and an attempt made by Sony, which produced 10 years ago a battery containing Sn in the negative electrode,[155] Sn is still far from a possible profitable use in LIBs.[152][156] Nevertheless, it was tested as a possible negative electrode in Mg-ion batteries by Singh and co-workers in 2012.[77] They conditioned Sn nanoparticles with carbon black and PVdF in electrodes that were electrochemically tested *vs.* electrodeposited Mg (Figure 28). During the first discharge, Mg electrochemically alloys with Sn to form Mg_2Sn , according to the following equation:



The theoretical specific capacity is 911 mAh g^{-1} . Mg_2Sn formation occurs with a steady plateau at 0.15 V and it was confirmed by *ex situ* XRD. Even if the theoretical capacity is almost reached during the first discharge, an important capacity loss is observed during the following charge, explained by the authors by the high volume expansion (more than 200%) occurring during magnesiation. Formed Mg_2Sn undergoes pulverization during the subsequent charge and isolated particles cannot be further demagnesiated. Although a lower hysteresis than Bi (50 mV *vs.* 90 mV) is observed between discharge and charge, Sn seems to suffer of poorer kinetics, as it can be seen from the direct comparison shown in Figure 28: indeed, at a moderate

current rate (C/20) the discharge and charge specific capacity values are slightly higher for Bi.

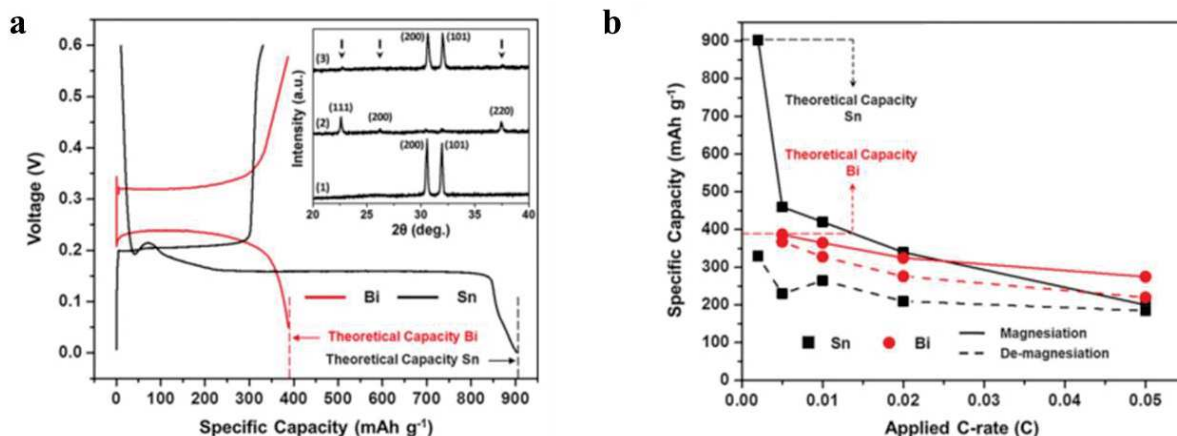


Figure 28 – Magnesian and demagnesian of nano-Sn (black lines) and Bi (red lines) (a) at C/50. Sn achieves almost the theoretical specific capacity during the first discharge with the formation of Mg₂Sn, confirmed by *ex situ* XRD (a, inset (2)). On the subsequent charge, only 30% of the previous capacity was retained. Poor capacity retention was also observed for several current densities (b) (Reproduction from [77]).

Finally, a Mg ion battery with a positive electrode of Mo₆S₈ and a 0.5M Mg(N(SO₂CF₃)₂)₂/DME electrolyte was tested. This work anticipated by few weeks the computational study of Malyi *et al.*, who focused on seeking possible high-performance negative electrodes in Mg-ion batteries.[157] Alloying voltage, volume expansion and Mg diffusion into the lattice of Sn were calculated, not for the common tetragonal β -Sn but for the cubic polymorph α -Sn. The authors found that Sn electrochemically alloys with Mg at 0.184 V, which is close to the experimental value, and also evidenced the low activation barrier for Mg diffusion into the α -Sn lattice.

In the aim of enhancing the cycling performance of Sn, in 2014 Parent and co-workers reported the use of a composite of graphene and β -SnSb.[158] SnSb was thoroughly investigated as possible negative electrode in Li- and more recently Na-ion batteries, with a particular interest devoted to the comprehension of the alloying/dealloying mechanism.[159] In this case, the authors stated that during the first magnesian/demagnesian cycles, the electrode undergoes a sort of conditioning that leads to the formation of a porous network of Sn nanoparticles (<33±20 nm) allowing highly reversible Mg-storage. However, Sb domains suffer Mg trapping and thus do not substantially contribute to the overall performance. The specific capacity lies between 300 and 350 mAh g⁻¹ for the first 100 cycles, which is

far from the theoretical value of 780 mAh g^{-1} . Moreover, after a maximum reached around the 15th cycle, a slow but steady capacity fading is observed all along the subsequent cycles (Figure 29).

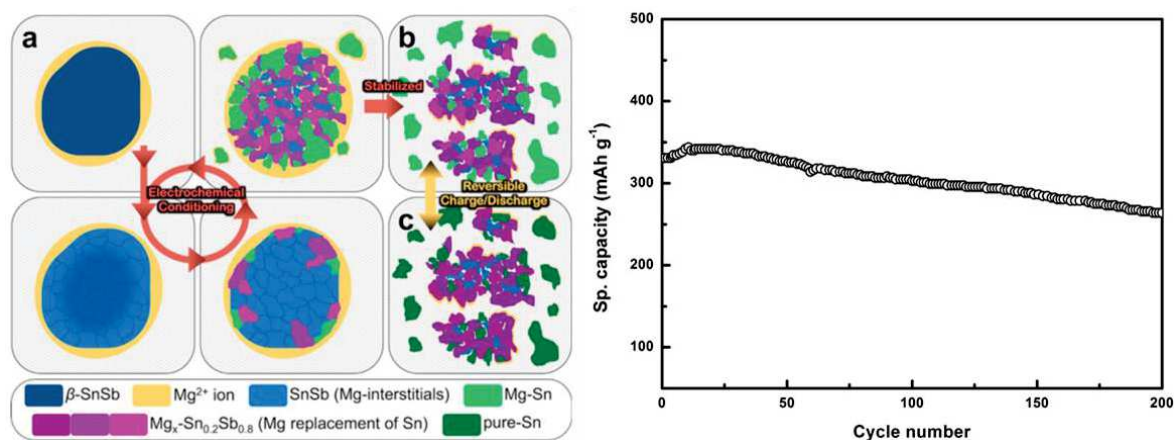


Figure 29 – Left: Mechanism involving the reversible magnesiation of SnSb-based electrodes. Mg-ions (yellow) first intercalate into tetrahedral interstitial sites (light blue) and then continue insertion by substituting for Sn atoms in lattice sites (purple). The process produces large lattice strains and the ejection of Sn atoms (green) from the Mg–Sn–Sb alloy, leading to the formation of small compositionally segregated subparticles. (b) Magnesiated SnSb electrode that has stabilized after initial conditioning. (c) During subsequent cycles, there is no change on the morphology but only in the Mg loading, which mainly alloys with Sn. Sb-rich domains suffer from significant Mg-trapping and poor reversible storage capacity. Right: Despite the relatively high number of cycles, the specific capacity of nano-SnSb electrode is far from the theoretical value of 780 mAh g^{-1} and constantly fades after reaching a maximum of 350 mAh g^{-1} at the 15th cycle (Reproduction from [158]).

In conclusion, these works demonstrate the promising potential in the use of Sn-based negative electrodes, but also show the difficulty related to an opportune conditioning of the Sn particles, underlying the need of stable nanoscale morphology. A second study by the same group thoroughly investigated the interfacial phenomena during magnesiation, stating that the first formation of Mg_3Sb_2 can have a strong influence on the crystallization form of the Sn, which shows lower barrier for Mg diffusion when the lattice is cubic rather than tetragonal.[160]

More recently, in 2015, Balinska and co-workers proposed the use of Sn in combination with a *d*-block metal, Zr, in the Zr_5Sn_3 alloy,[161] Such combination between *p*- and *d*-block elements was already widely studied for the Li-ion technology.[162][163] Indeed, crystalline structures containing a large atom (rare-earth metals, Zr, Hf, etc.) could provide a sufficiently large interatomic void, which is

favourable for cation intercalation. However, the overall electrochemical performance are very poor.

1.7.4.3. Pb

The reversible magnesiation of another *p*-block element, lead, was achieved by Periyapperuma *et al.* in 2015.[164] Very honestly, the authors reported that the first magnesiation of a Pb film sputtered on a stainless steel support results in an unexpectedly long alloying plateau, which exceeds the theoretical capacity (Figure 30). This was attributed to the possible catalytic activity of Pb that decomposes the electrolyte. To avoid this effect, a high initial current pulse was applied to the cell (5 mV for 3 minutes), which caused the formation of a thin passivation layer on the metal surface which deactivates it.

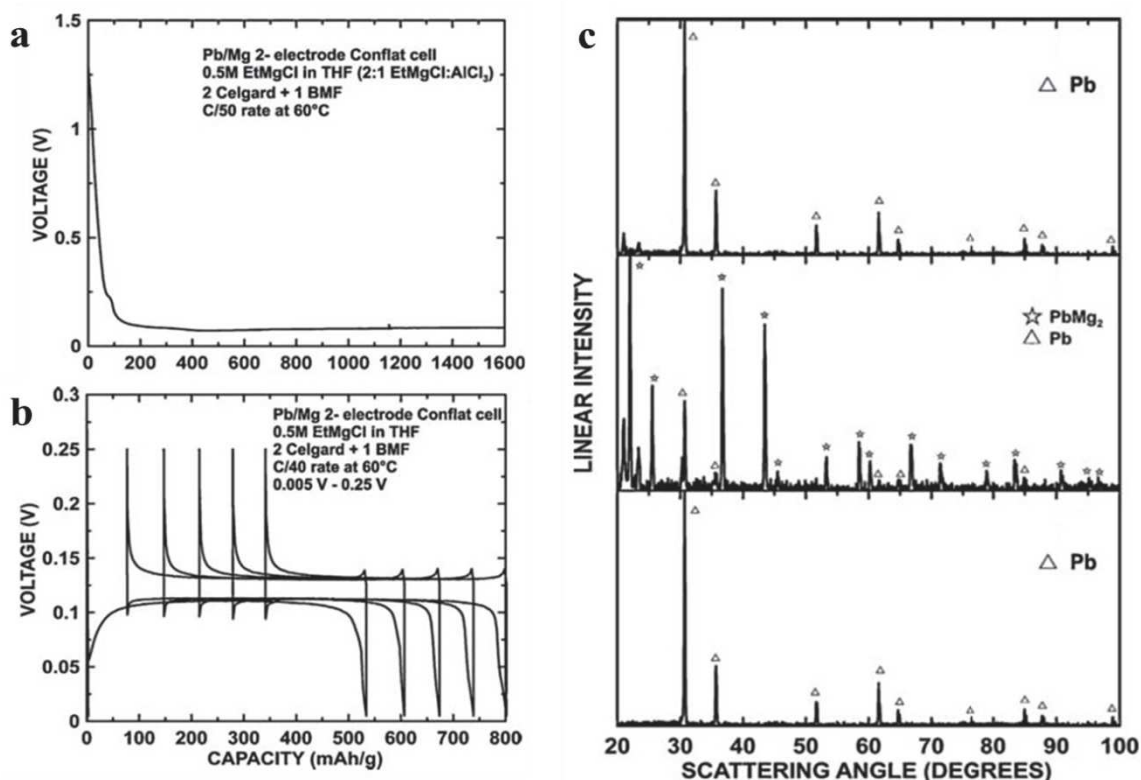
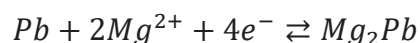


Figure 30 – First attempt for the electrochemical magnesiation of Pb. The obtained plateau largely exceeds the theoretical capacity and is mainly due to the catalytic effect of Pb that decomposes the electrolyte (a). In order to overcome this problem, the half-cell underwent a current pulse of 5 mV for 3 minutes, which allows forming a passivation layer on the surface of the electrode. The authors claimed that Pb has the lowest average voltage value ever reported in literature (0.125 V). However, a significant shift of the cycles can be also noticed, explained by parasite electrochemical phenomena (b). *Ex situ* XRD analyses confirmed the formation of the cubic Mg₂Pb (*Fm* -3 *m*) after the first discharge and the demagnesiation upon a complete cycle (C, from bottom to top – Reproduction from [164]).

Thanks to this treatment reversible cycling was possible, but with a constant shift on subsequent cycles, due to electrolyte decomposition (Figure 30 - b). *Ex situ* XRD confirmed the formation of the magnesiated phase Mg_2Pb , according to the equation below:



It is worth mentioning that these electrochemical tests were not run at room temperature but at 60°C. The authors emphasize the very low value of the magnesiation potential which can lead to elevate energy density, but also considered the very poor coulombic efficiency as a limiting factor for the possible use of Pb-based electrodes.

1.7.4.4. Other elements

To the best of our knowledge, there is no report in the literature on the magnesiation of other elements other groups than ours. However, in 2013, the above-mentioned work of Malyi *et al.* studied structures, energetics and diffusion properties of Mg in lighter elements such Si and Ge.[157] Particular attention was put on the alloying voltage and on the volume expansion, as reported on the Table 6 (below):

Element	Sp. Capacity (mAh g ⁻¹)	% Vol. expansion	Voltage (V)
Ge	1476	178	0.241
Si	3817	216	0.151

Table 6 – The interest on studying lighter p-block elements, such as Si and Ge, lies on the elevate theoretical capacities that they can provide but also on the low (theoretical) alloying potential vs. Mg^{2+}/Mg as shown from the work of Malyi *et al.*[157] Nevertheless, also the volume expansion should be taken into account since it has a negative effect on overall battery life.

Si can be attractive because of its high specific capacity and low alloying voltage, but the authors questioned the possibility of its further application because of both its high volume expansion and the low Mg diffusivity in structure of Si, which is a crucial parameter in bulk storage applications.

1.8. Conclusion and aim of the work

In conclusion of the previous section, all the *p*-block elements proposed as possible negative electrodes for MIBs are summarized in the Table 7 with their principal features.

Element	Magnesiated compound	Mg _a X _b sp. group	% Vol. expansion	Magnesium voltage (V)	Sp. capacity (mAh g ⁻¹)
Si	Mg ₂ Si	F m -3 m	216	0.151 (theor.)	3817
Ge	Mg ₂ Ge	F m -3 m	178	0.241 (theor.)	1476
Sn	Mg ₂ Sn	F m -3 m	120	0.15	911
Sb	Mg ₃ Sb ₂	P -3 m 1	118	0.32	660
Pb	Mg ₂ Pb	F m -3 m	160	0.11	518
Bi	Mg ₃ Bi ₂	P -3 m 1	98	0.25	382

Table 7 – Main features of the *p*-block elements proposed in the literature as negative electrode materials in MIBs.

It is necessary to stress that the replacement of Mg metal as the negative electrode cancels some of the crucial benefits of Mg-based batteries compared to other technologies, especially in terms of volumetric capacity and ease of electrode conditioning. However, the actual lack of marketable electrolytes represents a severe hurdle for a possible large scale development of the Mg-based energy storage. Similarly to the case of Li, therefore, the possible switch from Mg to Mg-ion system needs to be taken into account and is still investigated as a credible option for next-generation energy batteries. Indeed, a strong interest is actually growing in this field, as evidenced from the review presented in the previous section. At the same time, it is also important to underline most of these studies are only preliminary, generally presenting complex synthetic pathways that could hardly match with a large-scale production. Moreover, most of the electrochemical reactions are often presented without a thorough analysis on the alloying/de-alloying mechanism. On the basis of these considerations, we can draw the following goals for this thesis:

- studying possible alternative negative electrodes for Mg-ion batteries, starting from simple and upscalable synthetic routes and checking their electrochemical behaviour;

- increasing the electrochemical performance, seeking for other *p*-block elements, but also looking for possible synergetic effects rising from the combination of different elements;
- elucidating the mechanism of magnesianation/demagnesianation for the proposed active materials with the systematic use of combined electrochemical-structural investigation techniques applied *in situ* under reaction conditions (*operando* mode).

The Chapter II will deal with the synthesis of the electroactive materials and the experimental procedures for the electrode and the electrolyte preparations. Furthermore, the characterization techniques will be discussed, with brief reminds to their theoretical background. In the last section, the description of the performed electrochemical tests, whereas the different cell setups will be discussed

In the Chapter III will be exposed and analysed the results of both electrochemical tests and structural characterizations for each *p*-block element as a single electroactive element, whilst in the Chapter IV a similar schema will be followed for selected combination of the above mentioned elements.

The thesis will be concluded by the Chapter V, where the most promising Mg-alloy negative electrode will be implemented in a full MIB with a conventional electrolyte, confirming the interest of our research strategy. Moreover, a new and efficient synthetic protocol for the main precursor of the reference positive electrode Mo_6S_8 , i.e. $\text{Cu}_2\text{Mo}_6\text{S}_8$ will be presented.

II Experimental section: methods and characterizations

2.1. Mechanical milling and alloying

As briefly introduced at the end of the previous Chapter, several *p*-block elements are considered as favourable candidates for negative electrode in Mg-ion batteries. In our work, the interest was firstly focused on the behaviour of the single elements such as Sn, Sb, Bi, In (Chapter III). In a second time, several promising combinations of them, including intermetallics, solid solutions and composite materials have been also evaluated (Chapter IV). In the aim of proposing economic, tuneable and upscalable preparation methods for a further possible development of this technology, it has been decided to prepare them by mechanochemical routes.

A process involving a mechanical action of a grinding medium in a high-energy ball-mill can induce severe physical and chemical transformation on a solid. Depending on different parameters (milling time, type of mill, materials, number of balls, etc.) it is possible to tune the amount of energy transmitted to the system, which is a key factor for the results of the mechanical process (Figure 31).[165] Indeed, many effects can be obtained on the starting powder(s), such as a simple size reduction, amorphisation or solid solution, stable and metastable alloy formation and even multiphase chemical transformations, such as solid-gas reactions.[166] When the milling process does not require a material homogenization but only a size reduction (for a single powder) or an intimate mix of powders with a uniform composition, it is commonly referred to as Mechanical Milling (MM). However, if the conditions allow the material transfer between two (or more) starting reagents in order to form alloy(s) or solid solution(s), the process is named Mechanical Alloying (MA). In MA, the continuous sphere-sphere and sphere-jar collisions lead to repeated fracturing and cold welding of the starting material(s), thus inducing the creation of structural defects, such as vacancies, dislocations and grain boundaries.[167] The formation of these point defects enhances the reactivity of the milled solid(s) and, in opportune conditions, leads to mechano-chemical reactions.[7]

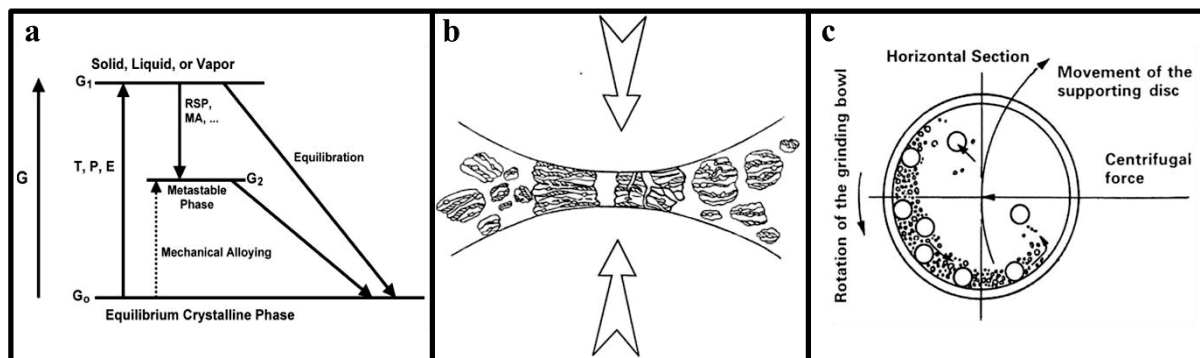


Figure 31 – a: Schematic representation of the “energize and quenching” techniques to achieve metastable phases. MA provides enough energy to move the reactants into a higher-energy state (G_1). When the milling is ended, a new, metastable phase is obtained (G_2). b: Schematic representation of a powder trapped between two spheres in a ball-milling. Depending on the stage of the process, either fracturing or cold welding is favoured. c: Outline of the milling process in a two-dimension mill (Reproduced from [168]).

Mechanical treatment on solids has been initially developed in the middle of the 60’s for the production of nickel-based superalloys intended for gas turbines.[169] Subsequently, other dispersion strengthened alloys were prepared for applications that required severe working conditions, such as heat resistant materials, even employed in aerospace industry.[170] MA was extended for the synthesis of a wide range of materials, such as amorphous,[171] nanocrystalline [172] and quasicrystalline solids,[173] with a particular attention to the production of intermetallic, metastable phases otherwise non achievable with more conventional synthesis routes.[174] Nowadays, mechanochemistry is successfully employed in a large number of different fields,[175] such as organic chemistry,[176] pharmaceutical synthesis,[177] organometallics,[178] etc.

The equipment needed for the mechanical treatment of the powders is relatively simple and it consists of a jar, usually made of stainless steel (SS), with several spheres of the same material as grinding media. However, SS is not the only available material, and can be replaced for instance by zirconium(IV) oxide or tungsten carbide, depending on the type of powder that is going to be milled. For instance, Sn powder has the tendency to stick on the walls of a SS jars, with the consequence that a high amount of powder is lost, influencing the yield or the stoichiometry of the synthesized compound. Moreover, some powders may be air sensitive and oxidise during the synthesis, also influencing the reaction yield. In our case, the powders were always accommodated inside the jar into an Ar-filled glove box, in order to

ensure an inert atmosphere during milling. Two different types of mills were employed: a planetary ball-mill (Pulverisette 7 - Fritsch) or a 3-D rotational mill (3D Mix/Miller 8000 – SPEX - Figure 32).



Figure 32 – Two different mills were employed in order to synthesize active electrode materials. The first is a 3D Spex 8000M Mixer/Mill working at a constant rate of 875 cycles per minute. (a) Ball-milling is generally performed using a stainless steel jar, but other materials can be also employed, such as zirconia; (b) grinding spheres are made of the same material. In alternative, a planetary ball-mill can be used, such as the Fritsch Pulverisette 7 that allows tuning the speed rate from 100 to 1100 rides per minute; (c) stainless steel jar and spheres were employed; (d).

In the present thesis, the study of several pure elements belonging to the *p*-block has been undertaken. The materials were in general used as received (after characterising them by XRD in order to ensure their purity), with the exception of Bi, which was previously ball-milled for 10 minutes in the 3D ball-mill because obtained in the form of large chunks. The characteristics of the pristine elements are listed in Table 8.

Reagent	Supplier	Purity stated	Particle size (μm)
Sn	Aldrich	$\geq 99\%$	150
Sb	Alfa-Aesar	99.5%	50
Bi	Aldrich	$\geq 99.99\%$	Chunks
In	Aldrich	99.98%	100

Table 8 - Purchased pristine *p*-block elements with their corresponding purity's statements.

Moreover, several powders with various chemical natures, such as Sn-Bi (composite), $\text{Bi}_{1-x}\text{Sb}_x$ (solid solution), InBi (intermetallic) were successfully prepared by MA and investigated as possible negative electrodes for Mg-based rechargeable system. Magnesiated phases of the single elements (such as Mg_2Sn , Mg_3Sb_2 , Mg_3Bi_2 , MgIn) were also synthesized as reference compounds for the study of the magnesiation of their de-magnesiated counterparts (cf. Chapter III). Table 9 summarizes the synthesis conditions for each compound.

Parameter	Sn-Bi	Bi _x Sb _{1-x}	InBi	Mg ₂ Sn	Mg ₃ Sb ₂	Mg ₃ Bi ₂	Mg ₃ BiSb	MgIn
Type of mill	SPEX (3D)	P7 (2D)	P7 (2D)	SPEX (3D)	SPEX (3D)	SPEX (3D)	SPEX (3D)	SPEX (3D)
Milling container	ZrO ₂	SS	SS	ZrO ₂	SS	SS	SS	SS
Milling speed (rpm)	875	600	600	875	875	875	875	875
Overall milling time	5 hours	24 hours	24 hours	5 hours	5 hours	5 hours	5 hours	5 hours
Rest time	/	10' after each 10' milling stint	10' after each 10' milling stint	/	/	/	/	/
Grinding medium	ZrO ₂	SS	SS	ZrO ₂	SS	SS	SS	SS
Ball/powder weight	6	20	20	16	24	16 – 24	24	24
Milling atmosphere	Ar	Ar	Ar	Ar	Ar	Ar	Ar	Ar
Milling temperature	25 °C	25 °C	25 °C	25 °C	25 °C	25 °C	25 °C	25 °C
Notes				10 wt.% Mg excess	10 wt.% Mg excess	10 wt.% Mg excess	10 wt.% Mg excess	

Table 9 - Summary of the chosen setup for each BM synthesis.

It is worth noting that, in spite of the wide range of synthesized compounds, there are recurrent analogies concerning milling conditions. In fact, it is important to stress that the optimization of such conditions for each compound was not the main purpose of our study. The strategy was rather to find an acceptable milling setup for the first prepared powders, *i.e.*, allowing the preparation of the pure phase in the shortest time, and then to extend it to the other syntheses. Sometimes minor changes on the initial protocols were necessary in order to achieve the desired product, such as the addition of an excess of Mg (10%) for some magnesiated compounds, or the use of a ZrO₂ jar in presence of Sn. Concerning the choice of one mill instead of the other, in some cases it was possible to synthesize the same compound with either 2D or 3D setup. For instance, Bi_xSb_{1-x} was successfully prepared with both mills, and finally the 3D mill was chosen since it allows a faster synthesis. In conclusion, the choice of the milling conditions for the preparation of the studied powders has proved to be effective (cf. Chapter III and IV) even though the milling conditions should be considered neither univocal nor optimized.

2.2. Characterization techniques

2.2.1. X-rays diffraction (XRD)

XRD analysis represents by far the main characterization technique used in this thesis. It was employed for the following purposes:

- checking the presence of impurities in commercial, as received powders (metals for electrode preparation or salts for electrolytes);
- verifying the effective formation of the expected compounds after mechanochemical syntheses;
- performing *ex situ* and *in situ* analyses on electrodes after electrochemical cycling.

XRD patterns were collected with both Empyrean and X'pert (PANalytical) diffractometers in $\theta/2\theta$ configuration, equipped with the Cu K α radiation without monochromator ($\lambda_{\text{mean}} = 1.5418 \text{ \AA}$); Both X-rays tubes operated at 45 kV and 30 mA. A special sample holder equipped with a 4,4'-oxydiphenylene-pyromellitimide (Kapton, DuPont) window allowing the protection of air-sensitive samples from oxygen and moisture was used. The obtained diffraction data were compared with the

patterns contained into the ICDD (International Centre for Diffraction Data) and COD (Crystallographic Open Database) using the software HighScore Plus for phase identification (and check the presence of possible impurities). Full pattern matching was carried out using the software FullProf, according to the Le Bail method.[179] Fitting of a XRD pattern, *i.e.*, a set of collected diffraction points, means finding a function that can interpolate these points and minimize the sum of the square difference between the observed points and the calculated ones:

$$\sum_i w_i (I_{meas,i} - I_{calc,i})^2$$

The observed peak shapes on an XRD pattern can be described by the so-called peak-shape function (PSF), which results in a convolution of instrumental and sample contributions. The intensity $I_{meas,i}$ of the powder diffraction pattern of each phase is the sum of the contribution y_k , from all the overlapped individual Bragg peaks and the background, as showed on the following equation:

$$I_{calc,i} = \sum_h S(k) |F(k)|^2 y_k (2\theta_i - 2\theta(h)) + b_i$$

Where:

- $S(k)$ is the scale factor
- $F(k)$ is the structure factor, which contains the crystallographic information (Miller indices), as stated in the :

$$F(k) = \sum_k f_k e^{2\pi i(ha_k + kb_k + lc_k)}$$

In the Le Bail method, the intensities are not refined directly. Instead, the partitioning scheme of overlapping reflections is optimized iteratively in analogy to the Rietveld algorithm,[180] but without refining the atomic positions in the lattice. The starting “calculated” intensity values are set to arbitrary identical quantities, typically units. The number of the refinement cycles can be chosen by changing the parameter NCY. It is worth noting that in Le Bail’s method only peak shape, lattice parameters and background are refined during each least squares cycle.

- y_k is the peak-shape function (PSF). Among the most common used PSFs, the Pseudo-Voigt (PV) was chosen for all the refined patterns. It consists of a linear combination of a Gauss function and a Lorentz function, as described by the :

$$y_k = PV = \eta \frac{C_G^{0.5}}{\sqrt{\pi}H} e^{-C_G x^2} + (1 - \eta) \frac{C_L^{0.5}}{\pi H'} (1 + C_L x^2)^{-1}$$

Where:

- η ($0 \leq \eta \leq 1$) is the fractional contribution of the Gauss function into the linear combination, that corresponds to the parameter “Shape” on FullProf
- H is the full width at half maximum as a function of θ for the Gauss function (Cagliotti formula):

$$H = \sqrt{U \tan^2 \theta + V \tan \theta + W}$$

- H' is the full width at half maximum as a function of θ for the Lorentz function:

$$H' = \frac{X}{\cos \theta} + \frac{Y}{\tan \theta}$$

- C_G and C_L are both constant; $\frac{C_G^{0.5}}{\sqrt{\pi}H}$ and $\frac{C_L^{0.5}}{\pi H'}$ are the normalization factor for Gauss and Lorentz functions, respectively such that their definite integral from negative to positive infinity are equal to 1.

- x , which is equal to $\frac{2\theta_i - 2\theta_k}{H_k}$, is essentially the Bragg angle of the i th point in the powder diffraction pattern with its origin in the position of the k th peak, divided by the same peak's full width at half maximum.

PV is a centrosymmetric function with respect to its argument x and could not perfectly match with the possible asymmetry of some peaks, especially at low angles. Correction to the asymmetry can be made adding on the parameters “Asy1” and “Asy2”. The background is represented by an interpolation made by the user and is generally different for each pattern. Background points can be set to refined parameters in FullProf.

2.2.2. Scanning electronic microscopy (SEM) and elemental mapping with energy-dispersive X-ray spectroscopy (EDX)

The morphology of pristine and synthesized powders was mainly investigated by scanning electronic microscopy (SEM) using a Hitachi S-4800 microscope equipped with a field emission gun. All the powders were deposited on a C-based conductive tape. The powders were in general analysed without any other treatment. However, for some less-conducting powders, a rapid metallization (15 seconds) with a Pt source was performed. Mapping EDX analysis was also performed in the case of the Sn-Bi composite in order to investigate on the homogeneity of the composition of the samples (cf. 4.1) on a Hitachi S-4500 microscope fitted with a Thermofisher EDX detector. Since one of the goals of this thesis was testing easily-prepared active materials not having any particular morphology, SEM was not used as a main characterization technique but rather as a complementary tool that was helpful for determining the grain size of such powders and for providing and checking the homogeneity of the electrode formulations.

2.3. Electrode formulation

As already stated on the Chapter I, an opportune conditioning of the active electrode material is crucial to improve the electrical conduction and the mechanical strength of the electrode during the severe volume changes upon alloying/dealloying reactions. Depending on the needs of a specific experiment, it is possible to choose between supported and non-supported electrodes. The following section describes the preparation, the positive features and the drawbacks of both electrode formulations.

2.3.1. Self-supported electrode

The active material, a carbonaceous additive - carbon black (CB, Y50A, Saft) - and a polymeric binder - poly-tetrafluoroethylene (PTFE, 6N, DuPont - Figure 34) - were mixed and manually pressed in an agate mortar in order to get a compact film. Disks of the opportune diameter to fit into the Swagelok cell (11 mm) were cut and subsequently stored in glove box.



Figure 34 – Self-supported electrode formulation (left), with the corresponding SEM image (right).

From one active material to another it was necessary to tune the active mass/CB/PVdF ratios in order to improve the mechanical properties of the so-obtained film. The Table 10 (below) summarizes all the ratios of the various components for each self-supported electrode:

	% Active material	% CB	% PTFE
Bi	70-80	20-10	10
In	50	38	12
InBi	60-80	30-10	10
Bi_xSb_{1-x}	60-80	30-10	10
Sn-Bi	60	30	10

Table 10 – Composition of various self-supported electrodes in terms of active material, carbonaceous additive and polymeric binder. It is worth noting that in several cases a range of active material is provided, instead of a single value, since different tests were performed.

In general, the mass of the electrodes ranges from 20 to 40 mg, but if needed it can be higher (for *operando* tests, cf. 2.5) or lower.

The self-supported formulation allows a good mass control and is necessary for all the characterization techniques in which the presence of an additional layer (*e.g.*, the current collector) could hamper the measurement (cf. 2.5). However, is not suitable for large-scale electrode production, and in spite of the presence of the polymeric binder, sometimes offers unsatisfactory mechanical properties. Finally the relatively high thickness may represent an obstacle for the complete electrochemical reaction with Mg, resulting in elevated polarization and in a severe electrochemical pulverisation resulting from volume expansion and shrinking of the electrode

material during magnesianation and de-magnesianation, respectively, leading to fractures and hence loss of the electrical contact.

2.3.2. Electrodes casted on metallic current collectors

In this case, the active material (70 wt.%) was mixed with two carbonaceous additives, CB (9 wt.%) and vapour-ground carbon fibres (VGCF, VGCF-H, Showa Denko K.K. – 9 wt.%); polyvinylidene difluoride (PVdF, Solef 5130, Solvay 12 wt.%) was added as the binder and N-methyl-2-pyrrolidone (NMP, 99%, Sigma-Aldrich) as the solvent. The so-obtained slurry was homogenized in a planetary ball-mill for 1 hour, and subsequently casted onto a metallic support, in general a 17.5 mm Cu foil (99.9%, Goodfellow), then dried at room temperature for 24 hours and finally kept 2 hours more in a vacuum flask at 80 °C. Disks of this film were cut out and stored in glove box. The final mass of the active material was precisely measured in the glove box and was found in the range 1–2 mg cm⁻².



Figure 35 – Cu-supported film from which several disks were punched (left) and corresponding SEM image, where it is possible to visualise the micrometric particles of the active material in a carbonaceous matrix.

Such electrode formulation is based on a well-established protocol of the ICGM – AIME laboratory, mainly used for preparing negative electrodes for Li-ion (and recently Na-ion) batteries [36][181] and was slightly adapted to the electrode herein tested. It allows getting a higher and a more uniform number of electrodes compared to the method presented in the previous paragraph, and is preferable for the

evaluation of performance as well as for long cycling tests. The use of Cu as the current collector is the most adopted since it is electrochemically inert in the usual working range of negative electrodes (reduction potential of 0.34 V *vs.* SHE). Nevertheless, the limited thickness of the casted film and hence the resulting low amount of active material leads to a bad control of the mass of the latter. Insertion/de-insertion and consequently discharge/charge capacity values can be influenced by this incertitude, and the replication of the same electrochemical test on two or more identical batteries becomes important to minimize this potential source of error. Indeed, the scale used to weigh the electrodes has an accuracy of ± 0.1 mg. Is not all rare to find electrodes that weight around 1 mg and hence it is possible to have an error of 10% on the mass, which has an impact in the determination of capacity, current rate and number of cations electrochemically inserted/de-inserted.

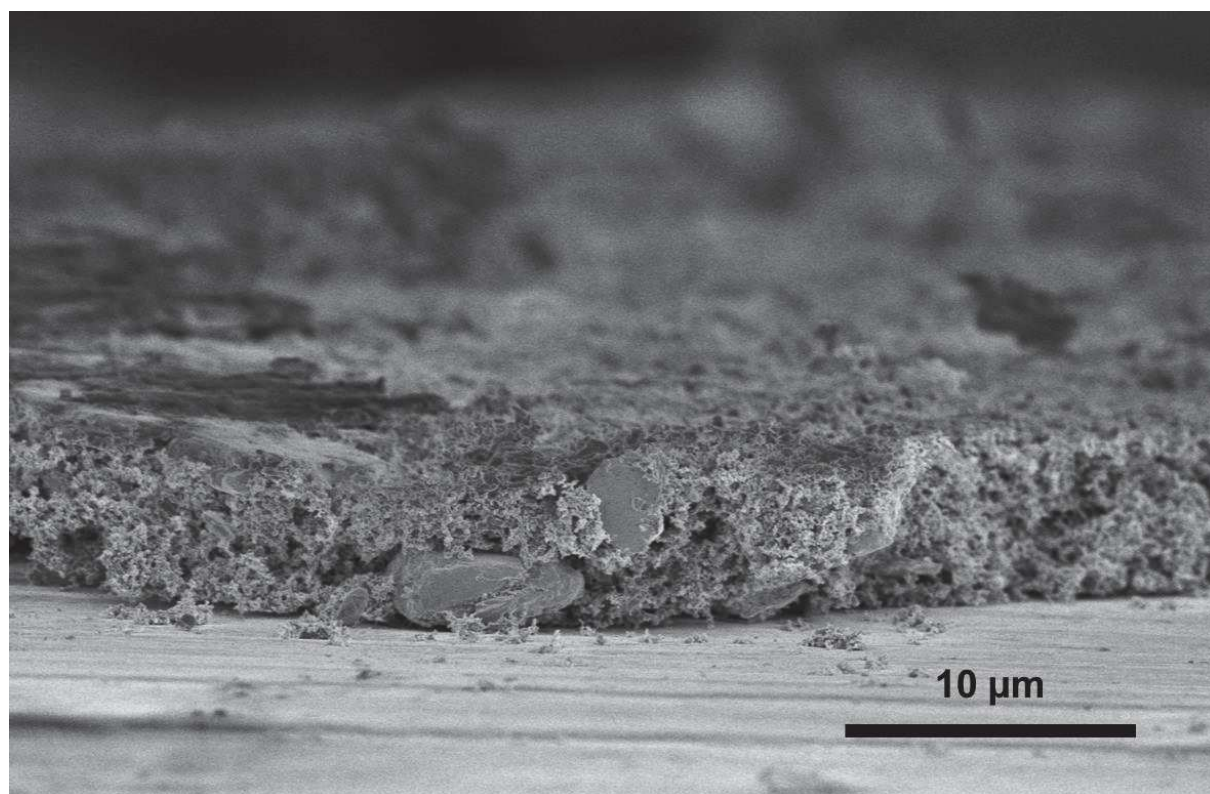


Figure 36 – SEM image of a typical self-supported electrode film. The slurry is casted on the metallic foil (Cu, in general) and is it possible to see the micrometric particles of active material surrounded by carbonaceous additives and polymeric binder. Here final thickness of the electrode is around 5 μm.

2.3.3. Preparation of the electrolytes

As discussed in Chapter I, Mg-based energy storage still represents an emerging technology that does not have yet any reference electrolyte. Finding Mg-metal compatible electrolytes has been recognised as one of the main hurdles for the development of Mg batteries and still represents one of the more investigated aspects on this field. Even though it was not one the goals of this thesis, a minor part of this work was devoted to the preparation and subsequent testing of several electrolytes in order to check the compatibility with the studied electrode materials and then, try to obtain the best possible electrochemical performance. This step was necessary since, before the beginning of this thesis, no Mg electrolyte had ever been used in our laboratory. The electrolyte formulations adopted were mainly taken from the literature, but in some cases they were slightly modified.

2.3.3.1. EtMgCl/2Et₂AlCl in THF

The first electrolyte that was employed for the electrochemical tests was prepared following the protocol proposed on the paper of Arthur et. al.[147] Similarly to most electrolytes belonging to the first generation, it consists in a mix of a Lewis base (ethylmagnesium chloride, EtMgCl) and a Lewis acid (diethylaluminum chloride, Et₂AlCl) that react together to form an organohaloaluminate complex (cf. 1.7.2) the 2:1 molar ratio between the two components has a positive effect on the oxidation stability of these electrolytes, as it was proved for several similar formulations.[66] Firstly, this electrolyte was synthesized following the same protocol proposed on the paper, but poor electrochemical cycling was observed. Hence it was decided to raise the concentration of the active species by doubling and finally increasing fourfold their starting value. With the increased concentration, the first promising results on electrochemical tests were achieved and hence this formulation was taken as a reference for almost all electrochemical tests presented in this thesis (Chapters III and IV). Table 12 summarize the different reagents employed for the preparation of the electrolyte.

Product	Supplier	Declared purity	Quantity
EtMgCl	Sigma-Aldrich	2.0 M in THF	4 ml
Et ₂ AlCl	Sigma-Aldrich	97%	2 ml
THF	Sigma-Aldrich	≥ 99.9%	6.5 ml

Table 11 – Components of the EtMgCl/2Et₂AlCl in THF electrolyte.

The final concentration of the *in situ* formed complex “[$(\mu\text{-Cl})_3\text{Mg}_2(\text{THF})_6$]AlEt_xCl_{4-x}” is 0.35 M. Both EtMgCl and Et₂AlCl are extremely air-sensitive and the reaction between them is highly exothermic. Therefore the preparation of the electrolyte was carried out in the glove box, with a careful and dropwise mixing of the two species. Moreover, it was noticed that even minor differences in the partial pressure of O₂ or H₂O in the glove box impact the quality of the synthesized electrolyte, leading to the formation of a dark precipitate or to the gelification of the solution. It was thus decided to prepare the electrolyte in small batches of 10 ml, and to restrict its shelf life to two months.

2.3.3.2. Other formulations

All Phenyl Complex (APC) in THF: as showed by Aurbach and co-workers, the poor oxidative stability of the organohaloaluminate complex electrolytes may lie in the occurrence of parasite β -elimination reactions in the alkyl chains of the Grignard reagent.[182] In order to overcome this issue, the use of the phenylmagnesium chloride was proposed, in combination with the organic chain-free AlCl₃ as the Lewis acid.[75] The reagents used in our work to prepare such electrolyte are summarised in Table 13.

Products	Supplier	Declared purity	Quantity
PhMgCl	Sigma-Aldrich	2.0 M in THF	10 ml
AlCl ₃	Sigma-Aldrich	99.999%	0.334 g
THF	Sigma-Aldrich	≥ 99.9%	10 ml

Table 12 – Components of the APC electrolyte.

Following the same protocol of the paper of Aurbach *et al.* cited above,, solid AlCl₃ was added to the THF and stirred until achieving the complete dissolution. Subsequently, PhMgCl was added dropwise to the THF solution. The mix was stirred

for 16 additional hours before use. The final concentration of the *in situ* formed complex is 0.25 M. Although the use of this electrolyte has recently spread in the literature, poorer electrochemical results were achieved for our systems. This formulation was thus only scarcely used.

MgCl₂/AlCl₃ in THF: in order to enhance the oxidative stability of Mg electrolytes, the first fully inorganic magnesium salt solution was proposed in 2014 by Doe and co-workers, termed magnesium aluminium chloride complex (MACC).[88] This formulation is based on the same idea of the Lewis acid-base reaction, but in this case by simply dissolving MgCl₂ and AlCl₃, in the usual 2:1 ratio, in anhydrous THF. The reagents used to prepare such electrolyte are summarised in Table 14.

Products	Supplier	Declared purity	Quantity
MgCl ₂	Sigma-Aldrich	≥ 98%	0.508 g
AlCl ₃	Sigma-Aldrich	99.999%	0.356 g
THF	Sigma-Aldrich	≥ 99.9%	11 mL

Table 13 – Components of the MgCl₂/AlCl₃ in THF electrolyte.

Even after a slight optimization of the formulation in order to completely solubilise the two inorganic salts with a final concentration of 0.24 M, no electrochemical activity has been observed with the tested materials. The use of this electrolyte was therefore abandoned.

2.4. Electrochemical tests

This section is devoted to the description of the preparation of the cells containing the prepared materials and their subsequent electrochemical testing. Most electrochemical tests were performed in the “half-cell” configuration in which the electrode containing the active material was set as working electrode (WE), opposed to a pure Mg disk (99.9%, 0.25 mm - Goodfellow) as counter and reference electrode (CE and RE, respectively). At this stage, it is important to underline that the tested material always plays the role of the positive electrode in the half-cell, even though its low working voltage *vs.* Mg²⁺/Mg makes it a possible negative electrode in the Mg-ion full cell configuration.

2.4.1. Cell preparation

Most electrochemical tests were performed using a Swagelok-type cell. It consists of a two-side open cylindrical SS body in which is possible to insert two SS plungers. Between them are placed the two electrodes, separated by two Whatman GF/A borosilicate glass fibre sheets soaked with the electrolyte. A stainless-steel spring ensures a uniform pressure inside the cell. In order to avoid any short circuit, plungers are separated from the cell body by a polyethylene terephthalate sheet (Mylar - Figure 37). All the assembly operations were carried out in an Ar-filled glove box.

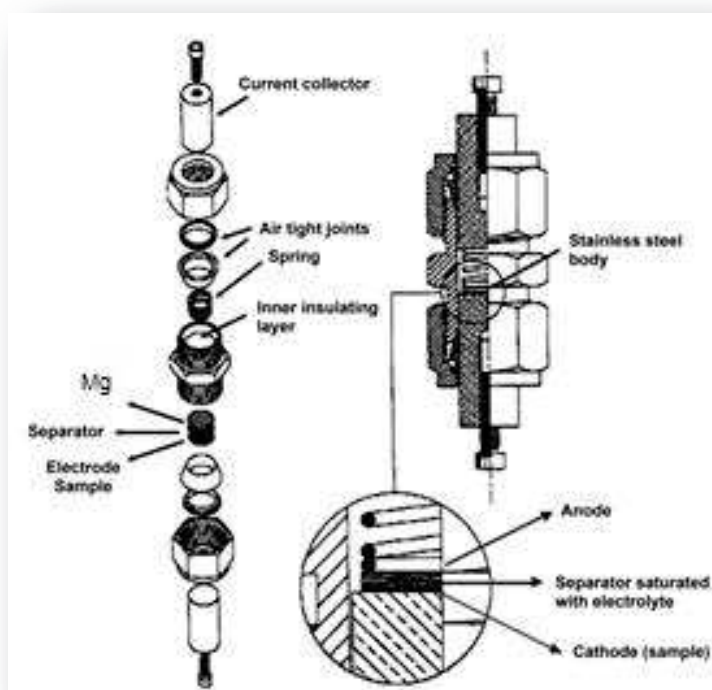


Figure 37 – A schematic view of a Swagelok cell and of its components.

Is it worth mentioning that nowadays, the most adopted configuration for battery testing at ICGM – AIME is the coin cell, which allows testing the electrode material with a setup similar to commercial cells. Moreover, the internal diameter of the coin cell is larger than that of Swagelok cells, and heavier electrodes can thus be tested, with a better control of the mass of active material. Nevertheless, the Swagelok setup was preferred in our work mainly because it is easier to disassemble, thus allowing the recovery of the Mg disk that, unlike Li and Na batteries, is reused in new batteries.

Electrochemical tests were performed using both MacPile (BioLogic) and VMP/MPG2 (BioLogic) research-grade battery testers, placed in a controlled-temperature room kept at 20°C. After preliminary tests but also following the literature on analogous systems, cycling voltage limits were set between 0.8 V and 0.0 V *vs.* Mg²⁺/Mg, since all the electrochemical reactions of our active materials *vs.* magnesium occur in this electrochemical window.[147][78] The upper voltage limit was chosen in order to minimize possible parasite reactions due to the relatively poor oxidation stability of Mg-organoalohaluminat based electrolytes (cf. 1.7.2).

2.4.1.1. Cyclic voltammetry

Cyclic voltammetry (CV) is a potentiodynamic technique that is widely used in battery analysis in order to test the voltage window of the electrolytes (*i.e.*, the potential range in which they do not undergo degradation) but also for a preliminary test on the electrochemical behaviour of the active materials. In a typical experience, a starting voltage V is imposed to the cell and is constantly varied (as a function of time) until achieving a final voltage value V' . When this value is reached the potential is again linearly swept in order to come back to the initial potential V . During these voltage sweeps, the current flux is monitored. When the voltage reaches a point at which a reduction/oxidation is induced, current begins to flow and a peak is detected. CV analysis can provide information on the occurrence and the eventual reversibility of an electrochemical process. During this thesis, CV was mostly employed to test electrolytes. Indeed, in a 3-electrode setup with a gold plate as working electrode and a magnesium disc as both counter and reference electrode, CV enables evaluating the ability of Mg deposition, Mg stripping as well as the oxidative stability of the electrolyte (Figure 38):

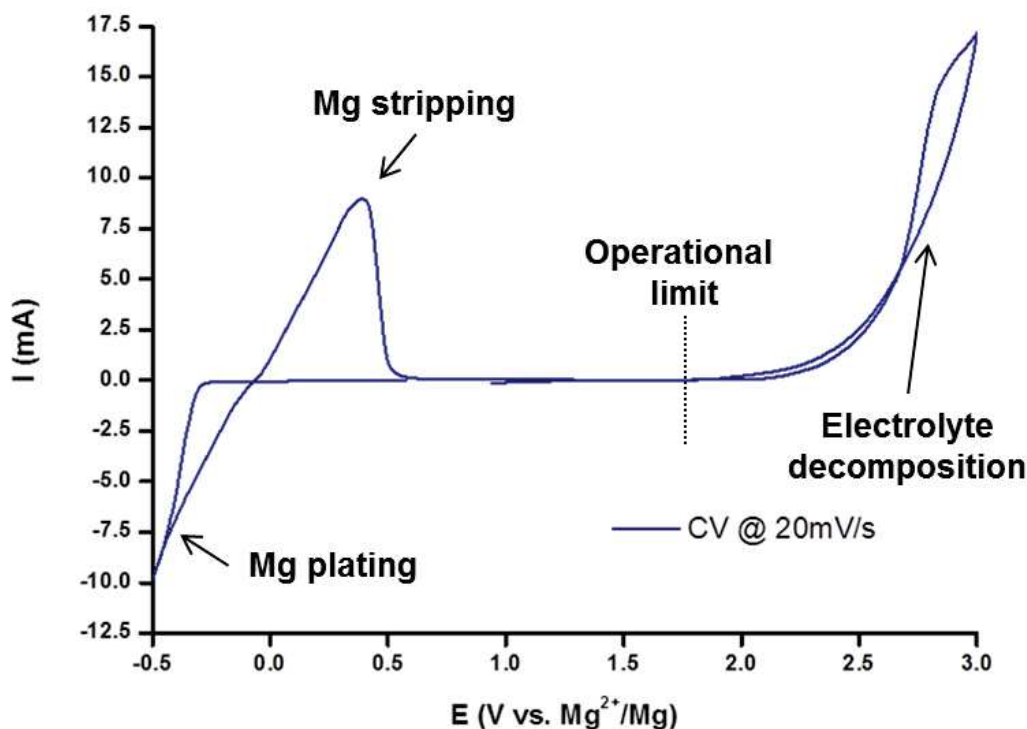


Figure 38 – A typical CV on $EtMgCl:2Et_2AlCl$ in THF electrolyte, where it is possible to observe Mg plating (negative I peak) and subsequent stripping (positive I peak). Electrolyte decomposition occurs above 2 V. CV was performed in a three-electrode Swagelok cell with Au foil as working electrode and two Mg discs as counter and reference electrode, respectively; scan rate was 20 mV s^{-1} .

An adequate scan rate must be chosen in order to fit with the kinetics of the studied reactions: if the scan rate is too fast, the reaction may not have the time to take place and hence no current flux is detected. Indeed, CV gives information on the electrochemical reactions that occur in a cell but does not allow quantifying the amount of reacting species, since the voltage varies at regular time steps and hence the reaction might be not complete. Therefore, more complete analytical methods were preferred to CV to study the electrode materials.

2.4.1.2. Galvanostatic Cycling with Potential Limitation

Galvanostatic Cycling with Potential Limitation (GCPL) is a routine analysis in battery testing and is by far the most employed electrochemical technique in this thesis.[183] Unlike CV, a constant current density value is set for the tested cell and the voltage variation is measured as a function of time. In our work, the

current rate is indicated by the C/n value, where n corresponds to the number of hours necessary for the reaction of 1 mole of Mg²⁺ per mole of active material.⁷

In some cases, instead of using the C/n current rate, it was decided to fix the current density in order to compare similar materials with slightly different molecular weight.

Figure 39 shows a discharge profile measured during a GCPL analysis. The cell voltage is plotted as a function of the number of moles of the inserted/de-inserted cation, which is proportional to the time at constant current as stated by Faraday laws, resumed by the following relation:

$$n = \frac{It}{zF}$$

Where *I* is the applied current for the time *t*, *z* is the number of charge shifted by the Mg²⁺ and *F* is the Faraday constant.

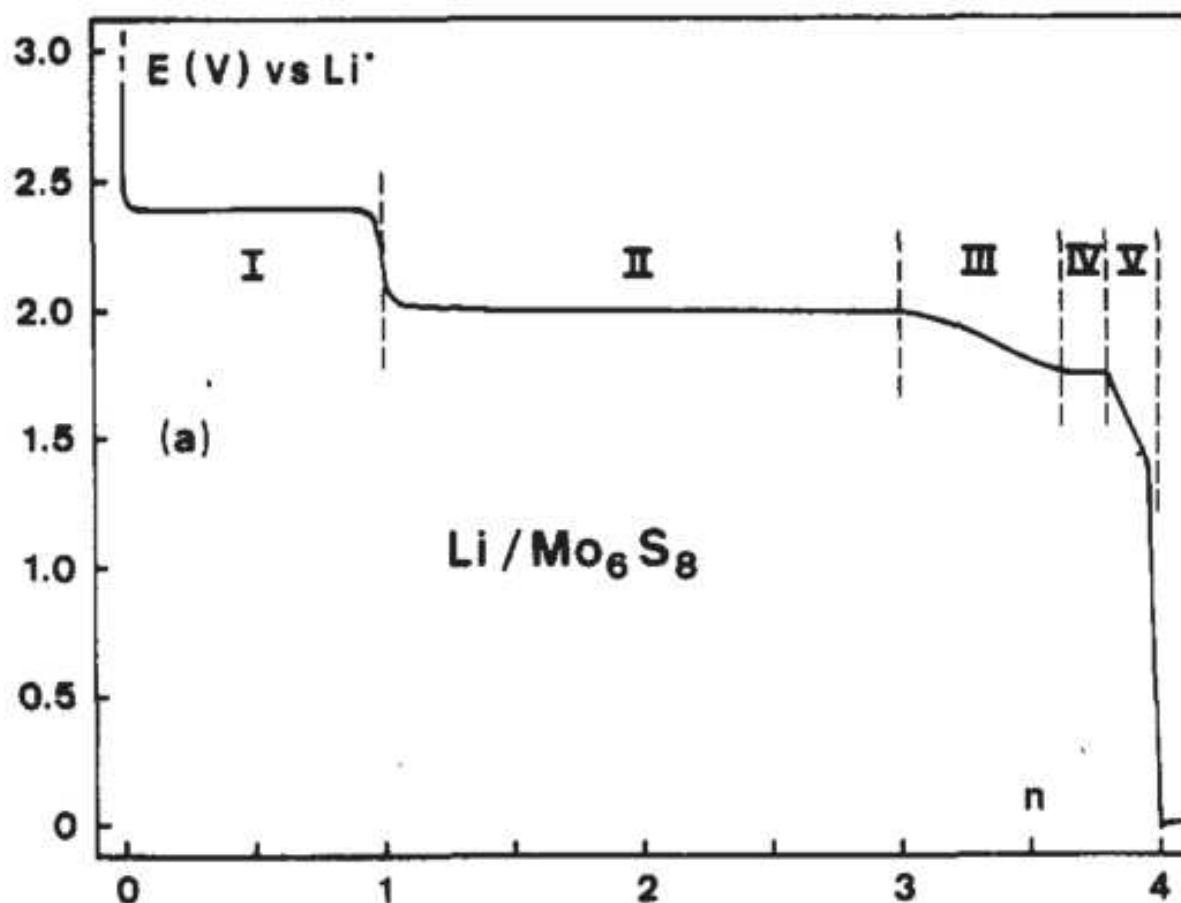


Figure 39 – Discharge profile of a GCPL where is possible to observe five different electrochemical processes, represented by five plateaus. I,II and IV are typical of a biphasic process, whilst III and V are monophasic (Reproduction from [109]).

⁷ This is the common definition employed in the fundamental research. However, in the field of the industry, C/n is the current rate that should be provided in order to achieve the complete discharge (or charge) of the battery in *n* hours.

For example, several regions are evidenced during the galvanostatic sweep shown in Figure 39, corresponding to the discharge of Mo_6S_8 vs Li. The regions where the potential varies very little are called “plateaus” and are the main evidence that an electrochemical process is ongoing. Depending on the different tested materials and on the electrochemical reactions occurring is it possible to have sloppy plateaus – for a single-phase process, III and V – or steady plateaus – biphasic process, I,II and IV.[109] Furthermore, in order to obtain more precise information on the potentials of the ongoing electrochemical process, is it possible to use the GCPL data to simulate a curve which has almost the shape of a CV by differentiating the insertion value x with respect to the cell voltage V , and then plotting it as a function of V .

Even though GCPL is generally performed at constant current density, it is sometimes interesting to evaluate the response of the electrode at various C/n values. This experiment, also known as rate-capability test, consists on a series of GCPL on the same battery at increasing C/n values, and allows the evaluation of the capacity retention of the studied electrode.

2.4.1.3. Galvanostatic Intermittent Titration Technique

The voltage values of the electrochemical phenomena evidenced by the GCPL techniques are strongly influenced by kinetics effects, principally dependent on the imposed current rate. To measure the real thermodynamic potentials of a reaction, it is necessary to let the system relax, opening the circuit for a period of time. In a Galvanostatic Intermittent Titration Technique (GITT) a current is imposed to the cell for a relatively short period of time (Closed Circuit Voltage, CCV), followed by a longer stint in open circuit voltage (OCV). This sequence is repeated until achieving the complete Mg^{2+} insertion/de-insertion. By analysing the time necessary for achieving the plateaus in OCV and even the shape of the curve during these periods, is it possible to gather information on the kinetics of the electrochemical reactions, as it will be detailed in Chapter III. However, it is worth mentioning that this technique is very time-consuming, since the relax voltage could be achieved after long OCV stints, thus increasing the related problems typical of long-time cycling, such as electrolyte aging, possible loss of electrical contact, etc.

2.5. Coupled analyses

For a thorough understanding of the electrochemical behaviour of the tested active materials, it is necessary to investigate in detail the alloying/de-alloying reaction mechanisms. Coupled analyses allow performing a non-electrochemical characterization on the working electrode while the cell is cycling, in the so-called *operando* mode. In the present work *operando* XRD was employed

2.5.1. *Operando* XRD

Operando XRD analyses were performed using the Empyrean 2theta/omega diffractometer (PANalytical) with a modified support that allows accommodating a specifically tuned *in situ* electrochemical cell, inspired by the work of Leriche *et al.*[184] A picture and a schematic representation of the *in situ* cell are shown in Figure 40.

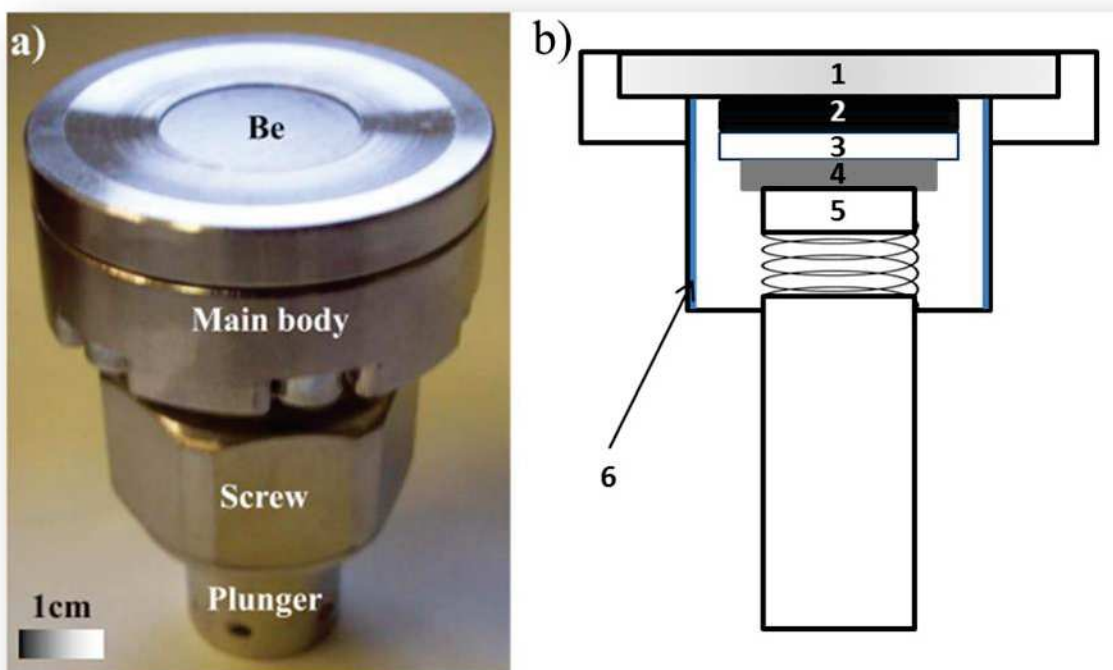


Figure 40 – a: picture of the *operando* cell (Reproduction from [184]) and b: schematic representation of the setup: 1 – Be window; 2 – working electrode; 3 – separator; 4 – Mg disc; 5 – stainless-steel plunger; 6 – Mylar foil.

The main difference between this setup and the Swagelok configuration is the presence of a beryllium window in contact with the working electrode, instead of the

SS plunger. Despite its toxicity, Be is employed since is electrochemically inert, it is an electrical conductor and especially because it is almost transparent to X-rays. Moreover, even though it is crystalline, it does not show any diffraction peaks in the region between 0 and 45°,[185] which is the most interesting angular domain for studying the different phases evolving during the electrochemical reaction of the active materials presented in our work. Moreover, the relatively large diameter of the window was conceived to present a high electrode surface to the incident X-ray beam, and thus for enhancing the overall quality of the XRD acquisitions. Compared to the setup proposed by Leriche *et al.*, this cell does not feature any Be window in the plunger, which is a simple SS rod.

III Screening on *p*-block elements

This Chapter features the study of the pure elements studied as possible candidates for negative electrodes in MIBs. These studies will be presented in a chronological fashion: in fact, the screening started with tin and antimony, mainly for two reasons: i) they offer elevate theoretical capacities when alloying with Mg and ii) they have been extensively studied in the ICGM – AIME team in the last years as active materials for negative electrodes in LIBs and NIBs. In fact, it must be stressed that this thesis has been the first pioneer study carried out in our team on Mg-based batteries. Therefore, the preliminary part of the work was focused on the optimization of the various components of the test cells, such as the electrolyte, discussed in the previous Chapter, and the electrode formulation. Therefore, most of these tests were performed on Sn-based films already optimised for the other technologies. This preliminary work laid the foundations for the study of the others materials presented in the following chapters, such Bi and In that offer a better electrochemical activity with Mg.

3.1.Sn

The Mg – Sn binary phase diagram shown in Figure 44 contains only one intermetallic phase, *i.e.*, Mg₂Sn.

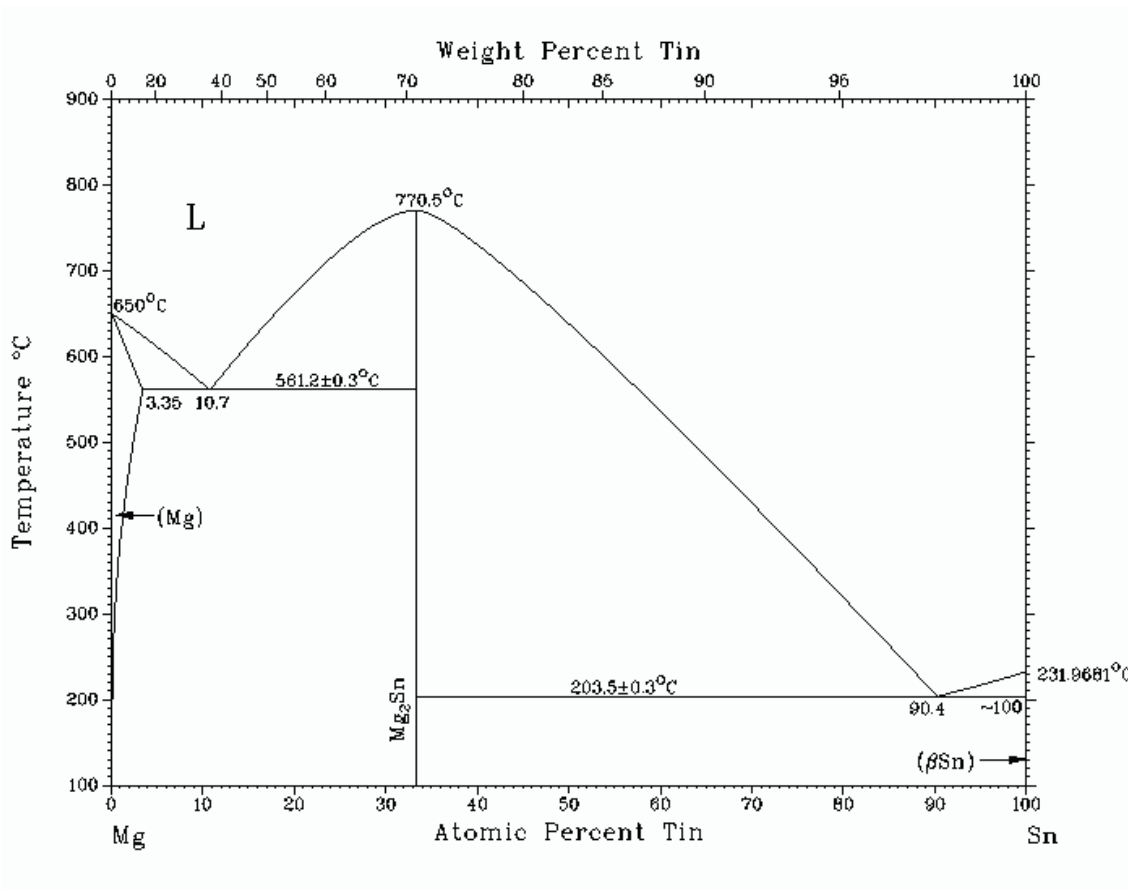
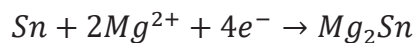


Figure 41 – Binary Mg-Sn phase diagram (Reproduction from [186]).

The complete magnesiation of Sn should therefore allow inserting two moles of Mg per mole of Sn, according to the following equation:



This reaction provides the specific capacity of 903 mAh g⁻¹.

In Figure 42 is represented the first galvanostatic cycling of a Sn-based electrode toward Mg.

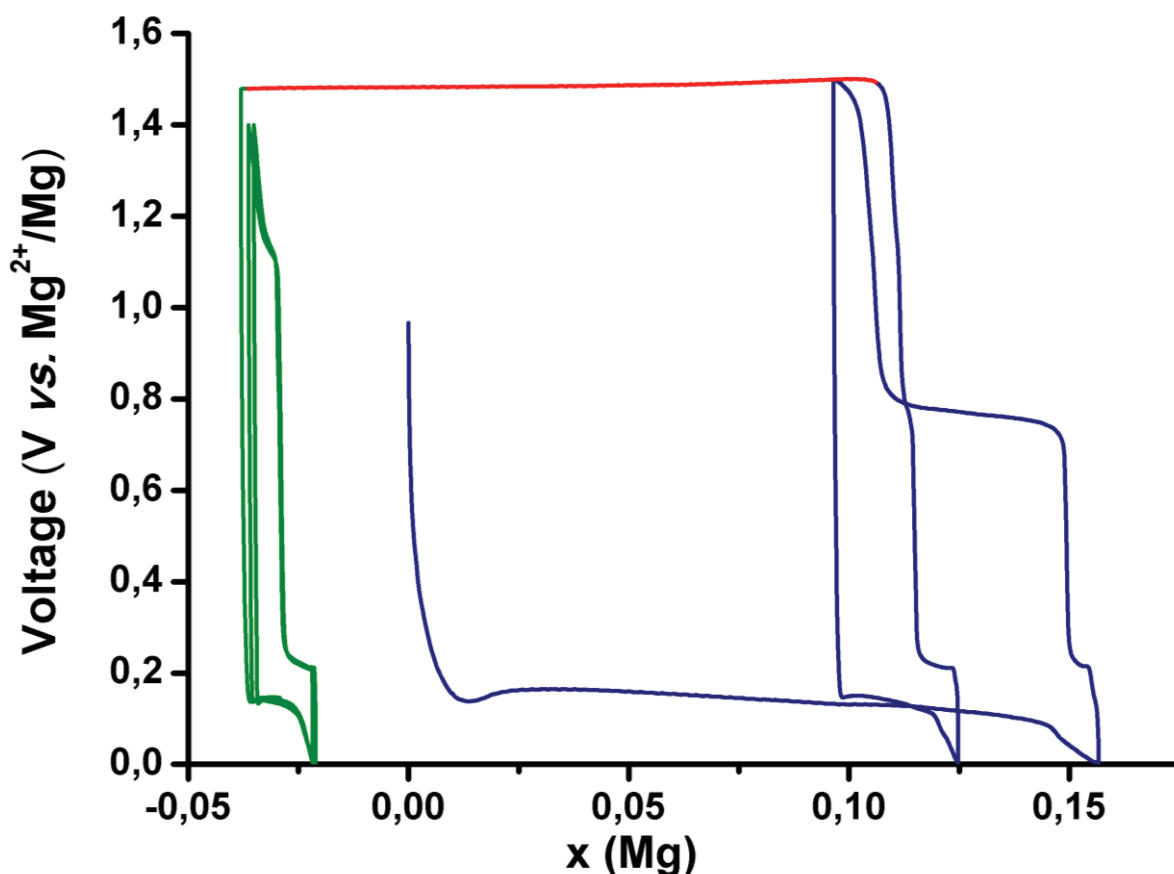


Figure 42 – GCPL Sn-based electrode vs. Mg. Electrolyte EtMgCl:2Et₂AlCl in THF. Current rate: C/100; electrode supported on Cu; a Cu current collector was also used to support the Mg disc.

The cell exhibits a OCV of ~ 1 V and when the current flow starts, the potential rapidly drops and almost reaches 0.13 V. During the discharge, the potential should normally decrease in a monotonic fashion but here it reaches a lower limit value and then slightly increases up to 0.17 V. This “potential drop” is not a specific feature of Sn-based electrodes but it has been found in all the cells tested along this thesis, as it will be presented later. This phenomenon was already observed in the literature[147][148][77][164], and is likely due to a kinetic balance between the nucleation of Mg₂Sn particles and their subsequent growth or to the resistance offered by the thin oxide film that easily recover Sn particles.

Subsequently, the alloying reaction between Mg and Sn proceeds along a plateau that exhibits a slight but continuous potential decrease. Unfortunately, Sn magnesianation rapidly ends at the value of 0.16 moles of Mg reacted with Sn, far from the theoretical value of 2. Successive charge shows a first short plateau (0.215 V), which can be ascribed to a very partial demagnesianation, rapidly followed by a longer plateau at 0.8 V. Based on the study of Singh and co-workers, two first plateaus values (0.17 and

0.215 V, respectively) are in good agreement with Mg-alloying and de-alloying reaction.[77] The plateau at 0.8 V was not observed and can be therefore due to a parasite reaction, probably connected to electrolyte decomposition. The first cycle is therefore characterized by a poor Sn magnesiation that also appears to be highly irreversible.

During the following cycle it is possible to observe the alloying plateau at the same potential, but Mg insertion is only 16% of that obtained during the first discharge. Interestingly, the second demagnesiation appears more reversible - 28% of capacity retention - compared to only 2.5% during first cycle. Moreover, the plateau at 0.8 V observed during first charge is here almost vanished. This may be due to an irreversible degradation of the electrolyte during the first cycle that influences the following ones. Another clue of an irreversible change of the composition of the electrolyte is testified by the following phenomenon (red line) that was not observed during first cycle, i.e., the complete degradation of the electrolyte. It is worth noting that the oxidative stability of Grignard-based electrolytes was previously checked by CV (cf. 2.4.1.1), and was found to be stable up to 2.2 V. The current was therefore manually stopped during the charge and the cycling resumed with a new discharge. The cell then underwent further cycling (green line), but with only very poor Mg insertion/de-insertion.

The result of a galvanostatic cycling on Sn-based electrode provided in the next section comes from several attempt in the optimization of different sector of the cell:

- Electrolyte formulation
- Metallic foil supporting the electrode formulation
- Metallic current collector between the Mg disc and the stainless-steel plunger

Figure 43 gathers the GCPL cycling of a Sn-based electrode with a DDC electrolyte.

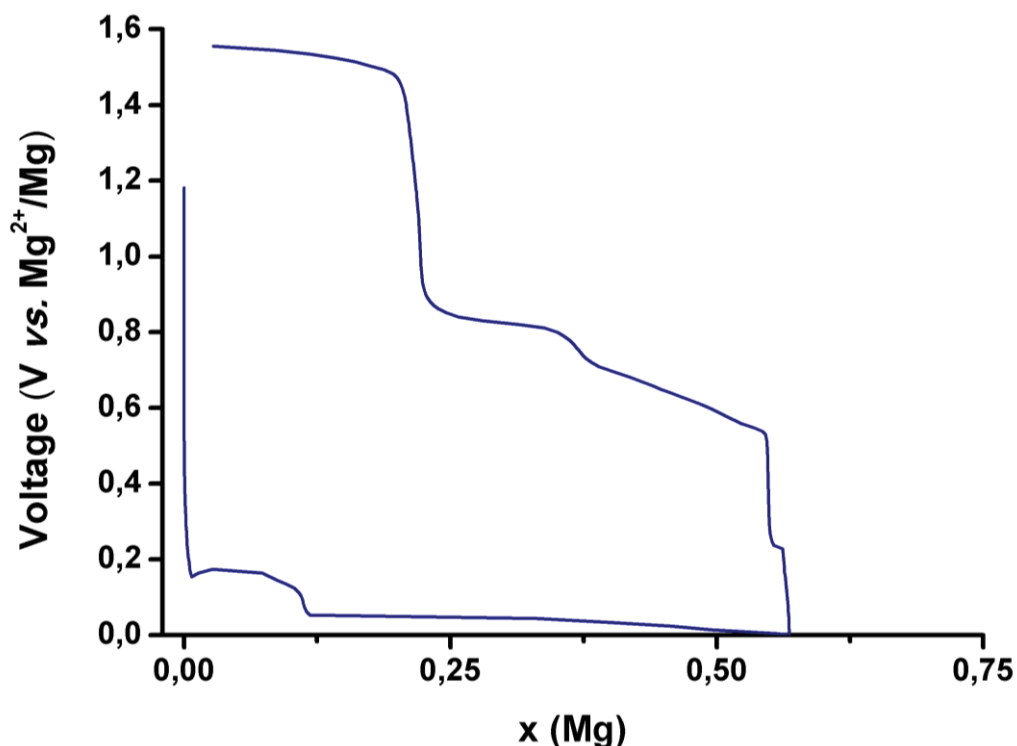


Figure 43 - Sn vs. Mg with $\text{MgCl}_2\text{-AlCl}_3$ in THF. Current rate: C/100; electrode supported on Cu; a Cu current collector was also used to support the Mg disc.

Also in this case, the galvanostatic profile exhibits the typical plateau of Mg alloying. Even though the electrolyte was changed, the amount of inserted Mg is similar to that observed in the first GCPL. In this case, however, a second plateau at lower potential (0.05 V) appears, which cannot be ascribed to further Sn magnesiation. During the following charge, a very short plateau is visible at 0.23 V, indicating the poor reversibility of the alloying reaction. Interestingly, three other plateaus are observed at higher potentials, a first one from 0.6 to 0.75 V, a second one at 0.8 V (similar to the one observed during the first GCPL) and a third one above 1.5 V, likely due to the oxidation of the electrolyte. In this case, no further cycling was observed. Even if the change of the electrolyte did not allow achieving better performance, it was helpful to understand that the relatively poor Mg insertion during the first discharge is not simply affected by the choice of the electrolyte, and that other parameters can be changed in order to improve the overall performance.

Among these parameters influencing the occurring of possible parasite reactions, there is also the choice of the adequate current collector. Indeed, opening the cell after cycling revealed corrosion upon the Cu disk placed between the Mg and the SS plunger. We thus decided to replace the Cu disk used as current collector for the Mg electrode with an Al disc (Figure 44).

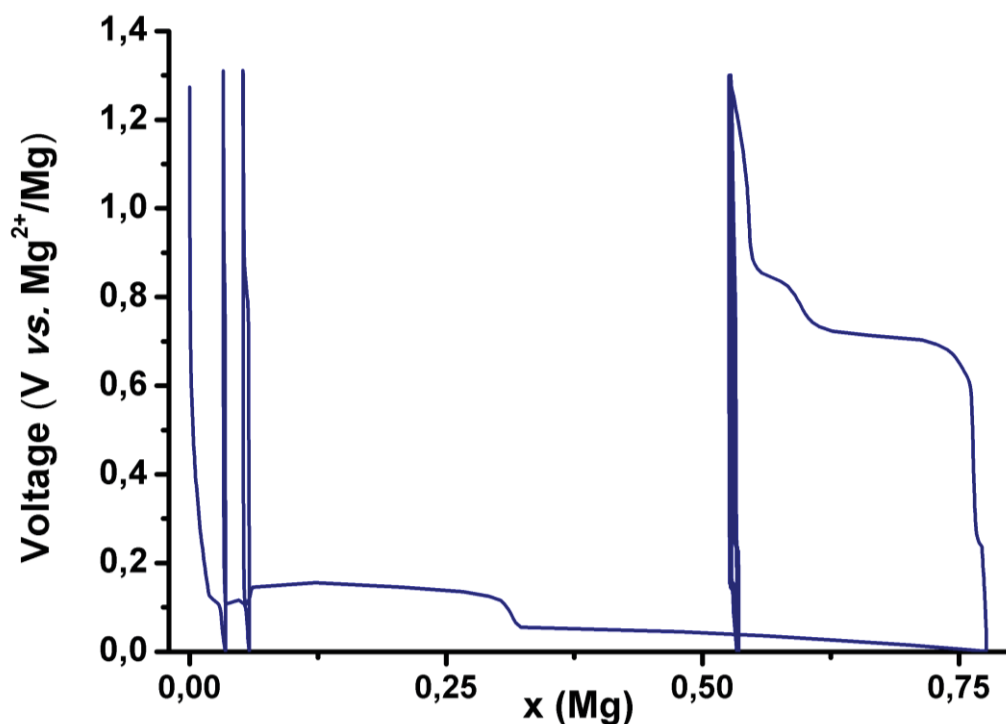


Figure 44 – Sn vs. Mg with an Al current collector. Electrolyte: EtMgCl:2Et₂AlCl in THF; current rate: C/100; electrode supported on a Cu disk; the Mg disc was supported on an Al current collector.

The galvanostatic profile shows two initial very short “cycles” that can be considered as a conditioning of the electrode materials, followed by a sensibly longer alloying process during the third discharge. This cell exhibits the highest Mg insertion value (0.32 x at 0.17 V), but this is followed by an undesired reaction, as can be argued by the apparition of a second plateau at lower potential. The following charge again offers a very poor reversibility, followed by two high voltage plateaus, at 0.70 and 0.83 V, respectively. In order to prevent further oxidation of the electrolyte, the upper limit of the voltage window was decreased to 1.3 V compared to the two previous tests.

Following the strategy of complete removal of Cu from the testing cell, the electrode slurry was tape casted onto an Al foil instead of the usual Cu one (Figure 45). This GCPL shows a longer alloying plateau during the first discharge (0.35 Mg moles at 0.18 V), which is however not followed by any de-alloying reaction during charge. A very small plateau at 0.8 V is observed. Unlike previous cells, further discharging processes are observed during the following discharges, with a noticeable gradual decrease of the length of the alloying plateau until the battery fails. Moreover, the upper limit of the potential window was again lowered to 1.2 V.

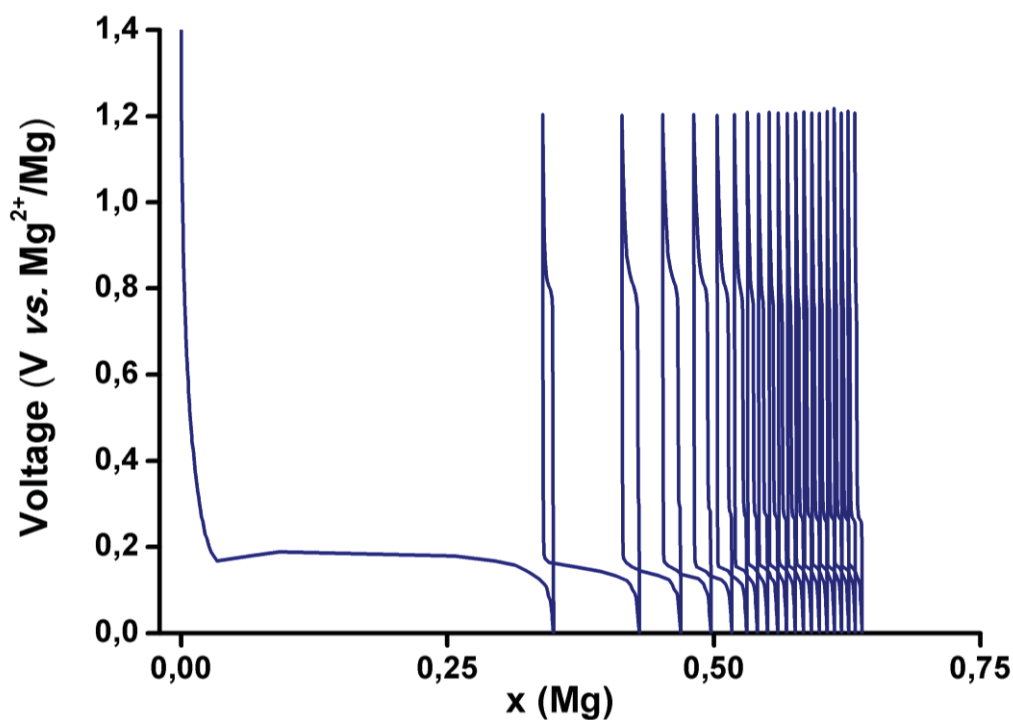


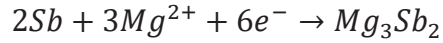
Figure 45 –Sn vs. Mg electrode supported on Al film. Electrolyte: EtMgCl:2Et₂AlCl in THF; current rate: C/100; electrode support: Al; the Mg disc was supported on an Al current collector.

In summary, these first tests allowed a first evaluation of the feasibility of a reversible magnesiumation of Sn-based electrodes. Although Mg₂Sn can be found in the phase diagram, Mg alloying on μ -Sn particles seems difficult, with initial capacity far from the theoretical value and with scarce reversibility. Even if several optimizations of the cell configuration were tested, only a limited improvement was finally achieved. These results should be also analysed bearing in mind those reported by Singh and co-workers that obtained partially reversible cycling with rapid capacity fading, only starting from nanometric Sn particles at the very low current rate of C/500.[77] Nevertheless, our preliminary work on electrolytes, current collectors and electrode formulation have been useful for creating more performing protocols for the realisation of Mg-based system.

From the example of Sn, one can appreciate the strategy that was used to tackle, one by one, the different obstacles hindering the optimal operation of our Mg cells. However, such way of proceeding, even though necessary for the prosecution of the thesis, has been quite time consuming and needed many repeated tests before being sure of the outcome.

3.2. Sb

Antimony is the second *p*-block element tested during this thesis. Despite its toxicity, it is still investigated as possible electrode material because of its relative lightness and ability to reversibly alloy with alkali and alkaline-earth metals. From the Mg-Sb binary phase diagram is it possible to see a stable Mg_3Sb_2 phase (Figure 46). The alloying reaction is provided by the following equation:



The theoretical capacity provided is 660 mAh g⁻¹.

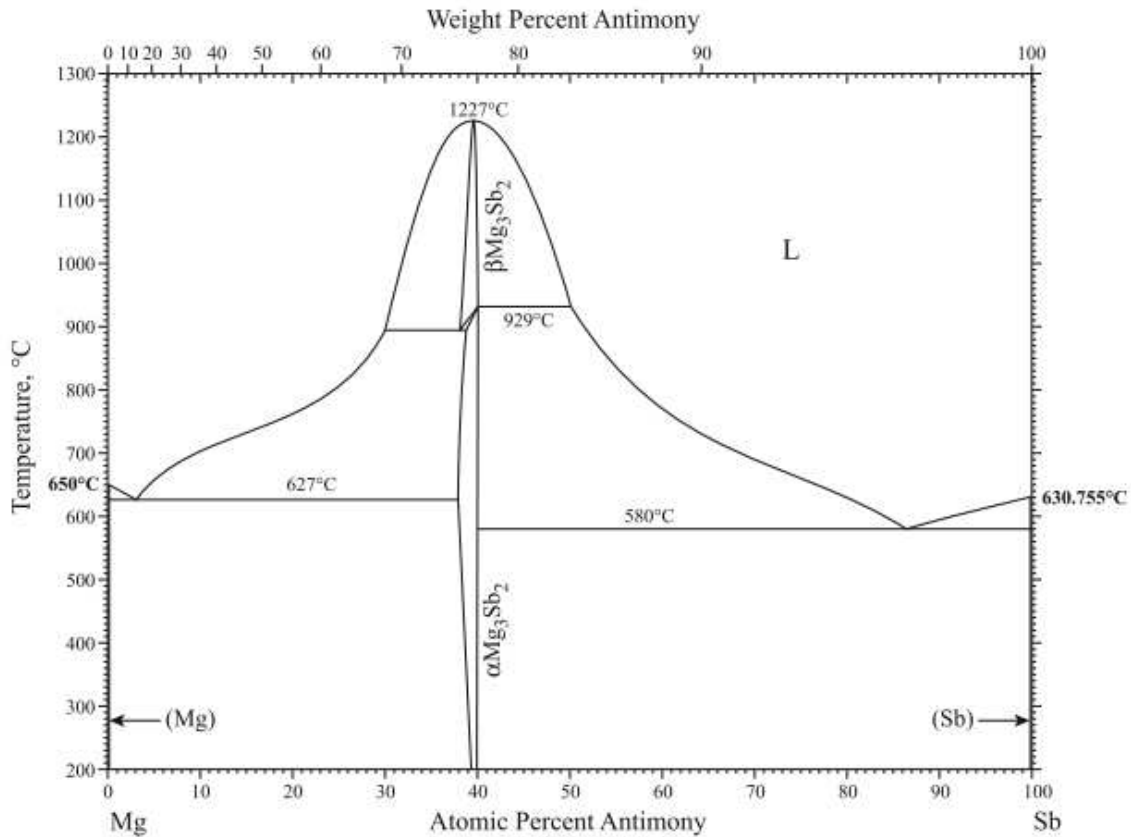


Figure 46 – Mg – Sb phase diagram (Reproduction from [187]).

However, all cycling test of electrodes based on micrometric Sb (μ -Sb) vs. Mg metal was very unsuccessful, independent of the electrolyte and of the cycling conditions. Unlike Sn, where limited alloying reaction was achieved, micrometric Sb seems completely inactive toward magnesiation, as can be seen from Figure 47:

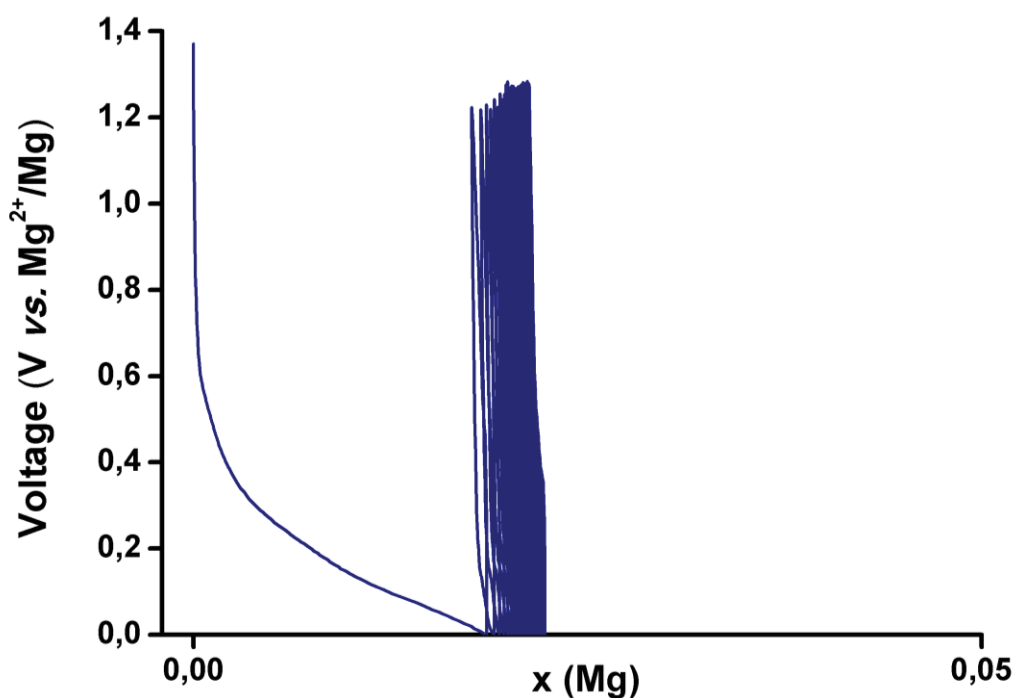


Figure 47 – No cyclation was observed for Sb-based electrodes. Sb vs. Mg. Electrolyte: EtMgCl:2Et₂AlCl in THF; current rate: C/100; electrode supported on an Al disk; current collector used for the Mg disc: Cu.

The very poor performance of Sb-based electrode toward Mg is rather surprising, if compared to the good behaviour exhibited by the same element vs. both Li and Na. [36][188]

3.3. Bi

Bismuth is the heaviest element of group 15, and because of its high atomic mass, it can offer only limited theoretical capacity – 385 mAh g⁻¹. However, considering its elevate density (9.78 g cm⁻³) it can provide a volumetric capacity of 3763 mAh cm⁻³, which is almost fivefold higher than graphite (818 mAh cm⁻³; $\rho_{\text{graphite}}=2.23 \text{ g cm}^{-3}$). Moreover, according to the work of Arthur *et al.*, Bi exhibits a very interesting cycling stability.[147] In the Mg-Bi phase diagram, only a single alloy is reported, with composition Mg₃Bi₂, similarly to the case of Sb which belongs to the same group in the periodic table (Figure 48).

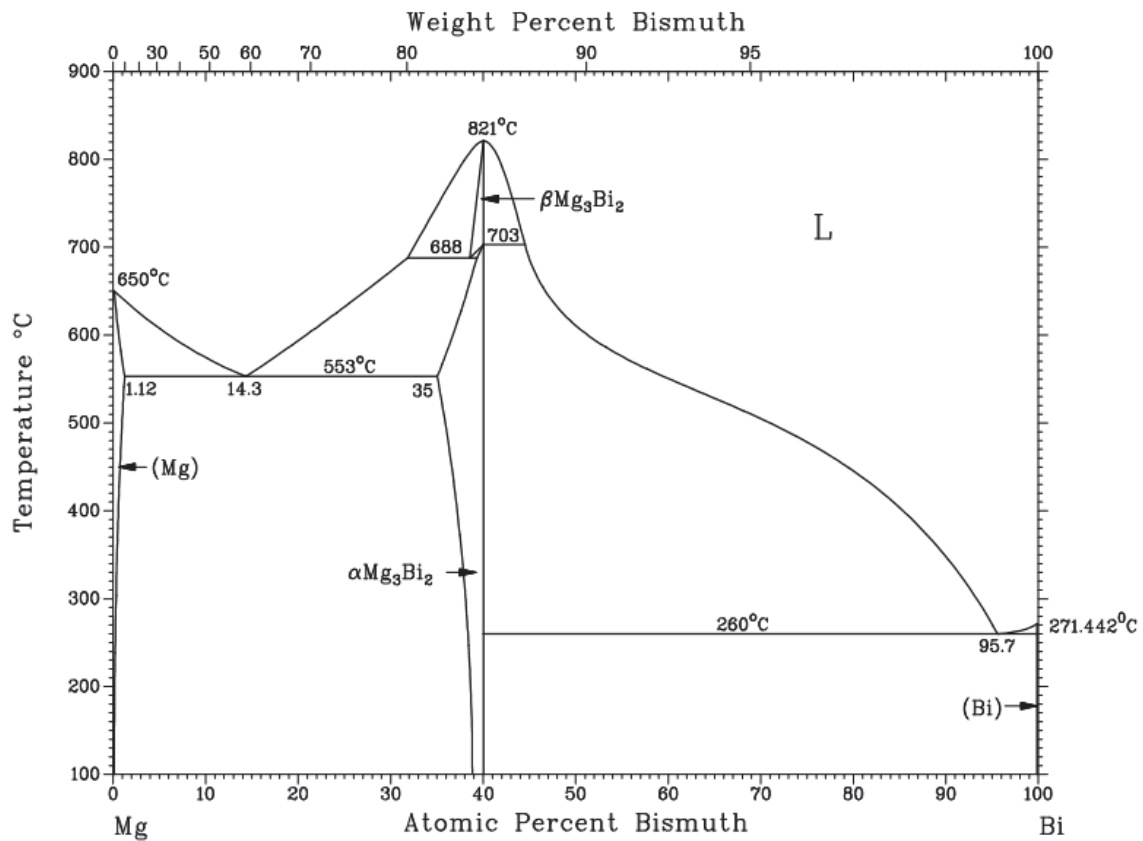


Figure 48 – Bi – Mg binary phase diagram (Reproduction from [189]).

As stated in the previous chapter, Bi is usually obtained commercially in the form of large chunks, and must be therefore reduced to a fine powder before preparing the electrodes. Figure 49 shows the SEM images at different magnifications of a Bi powder obtained after 5 minutes of high-energy ball-milling. It mainly consist of micrometric aggregates (50 – 100 μm average size) of smaller particles compacted by the ball-milling procedure.

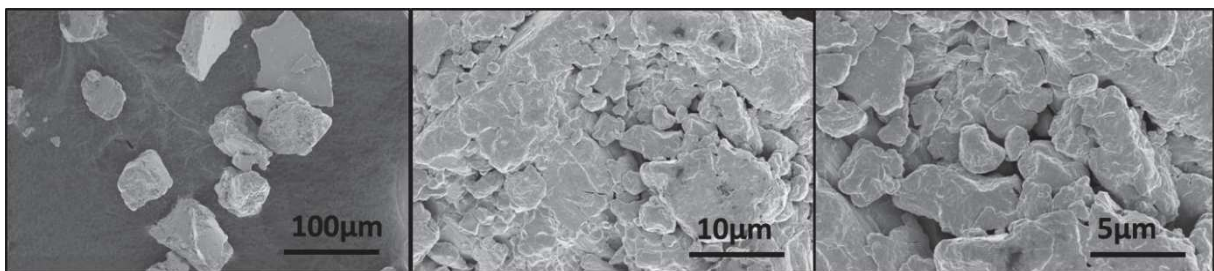
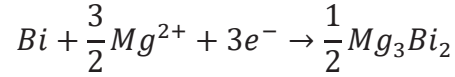


Figure 49 – From left to right, micrometric aggregates of Bi made up of smaller particles obtained by high-energy ball-milling of commercial Bi chunks (Adapted from [190]).

3.3.1. Bi-Mg reversible alloying reaction

A typical GCPL profile of a Bi-based electrode *vs.* Mg is depicted in Figure 50 – a. For more clarity only the first 1.5 cycle is shown. During the first discharge, a single plateau occurs at 0.23 V, corresponding to the reaction of 1.53 mole of Mg, likely through the alloying with Bi, according to the equation:



This reaction is highly reversible: the de-insertion of Mg occurs at 0.32 V during charge and the system shows a very limited polarization of about 90 mV. Even in this case, at the very beginning of the first discharge, a rapid potential drops occurs (around 0.11 V), before reaching the alloying plateau at 0.23 V. It is worth noting that electrochemical potential of Mg-Bi alloying is extremely stable until achieving the theoretical capacity of 385 mA h g⁻¹ (3763 mAh cm⁻³). Subsequent charge exhibits another steady and stable plateau at 0.32 V. Voltage cell rapidly raise when all the accessible Mg₃Bi₂ is de-magnesiated. High capacity retention is observed after the first charge, since 95% of first discharge capacity is retained (1.46 Mg is electrochemically removed from Mg₃Bi₂).

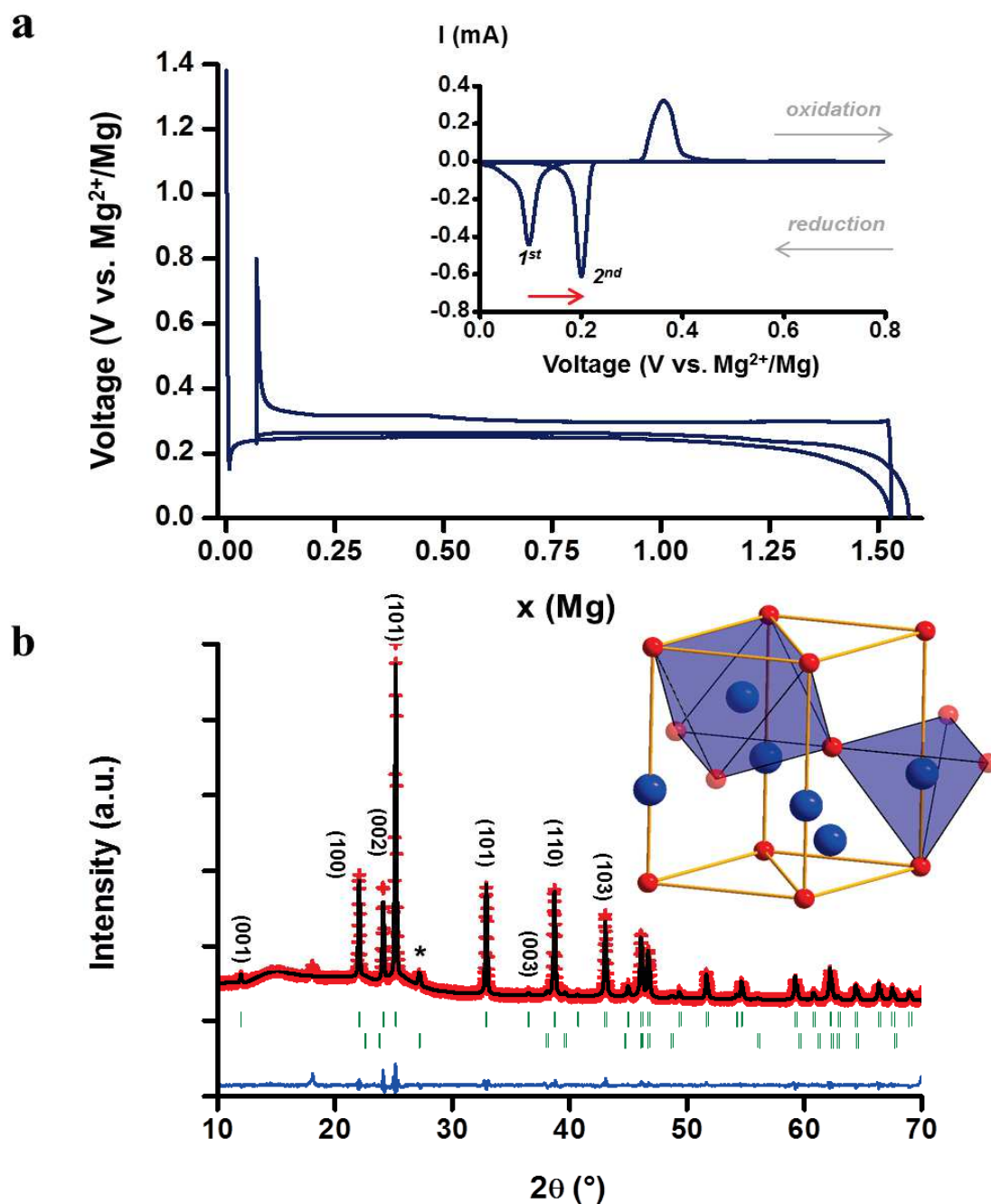


Figure 50 – a: GCPL analysis on μ -Bi-based electrode vs. Mg. Electrolyte: EtMgCl:2Et₂AlCl in THF; current rate: C/100; electrode supported on a Cu disk; current collector for the Mg disc: Cu. The theoretical reaction of 1.5 Mg is achieved (and slightly overcome) during the first discharge. The process is highly reversible, with a capacity loss of 5%. The following discharge occurs at a higher voltage than the first one. The decrease of the polarization is probably caused by the reduction of the size of the Bi particles during the first full alloying/dealloying process (electrochemical grinding). The derivative of the potential is shown in the Inset. b: The full profile matching of the *ex situ* XRD of a Bi electrode at the end of the first discharge (measured on a self-supported electrode) confirms the formation of Mg₃Bi₂. The refined cell parameters are in agreement with the literature^[191] Minor amounts of unreacted Bi metal are still visible in the XRD pattern. Red crosses, black line and green strokes represent observed XRD points, interpolation and peak positions; blue line represents the difference between the observed values and the fit (Adapted from ^[190]).

The *ex situ* XRD pattern of a self-supported electrode recovered at the end of the first discharge confirms the quasi-complete magnesianation of the pristine electrode (Figure 50 - b). Indeed a highly crystallized Mg_3Bi_2 phase is evidenced with refined cell parameters in complete agreement with the literature.[191]

The second discharge is very similar to the first one, with the exception of two significant differences. Firstly, the plateau corresponding to Mg insertion is slightly higher in potential (0.26 V). Secondly, this potential is reached more rapidly than during the first discharge, almost without the characteristic initial potential drop described above. Both effects can be explained by either an evolution of the electrolyte, or more likely assuming a modification of the morphology of the active material grains after the first discharge. Such process, that is commonly called “electrochemical grinding”, can be described as follows: the electrochemical alloying reaction of Bi with Mg during the first discharge involves a strong expansion of the initial micrometric Bi particles; during the following charge, the removal of Mg provokes a strong decrease of the volume of the particles, which tend to crack and fractionate. The initial size is thus not recovered upon removal of Mg, leading to the formation of Bi particles smaller than the initial ones. In subsequent cycles, the particles reactivity is therefore improved due to the increase of the surface of the particles exposed to the electrolyte, and the lower energy needed for both alloying and de-alloying process is reflected in a lower polarization. This effect is clearly visible by looking at the derivative of the potential, where a potential shift is visible between the first and the second reduction (cf. Inset of Figure 50).

In parallel with continuous galvanostatic tests, a GITT analysis was performed in order to better understand the mechanism of Mg insertion/de-insertion in Bi (Figure 51).

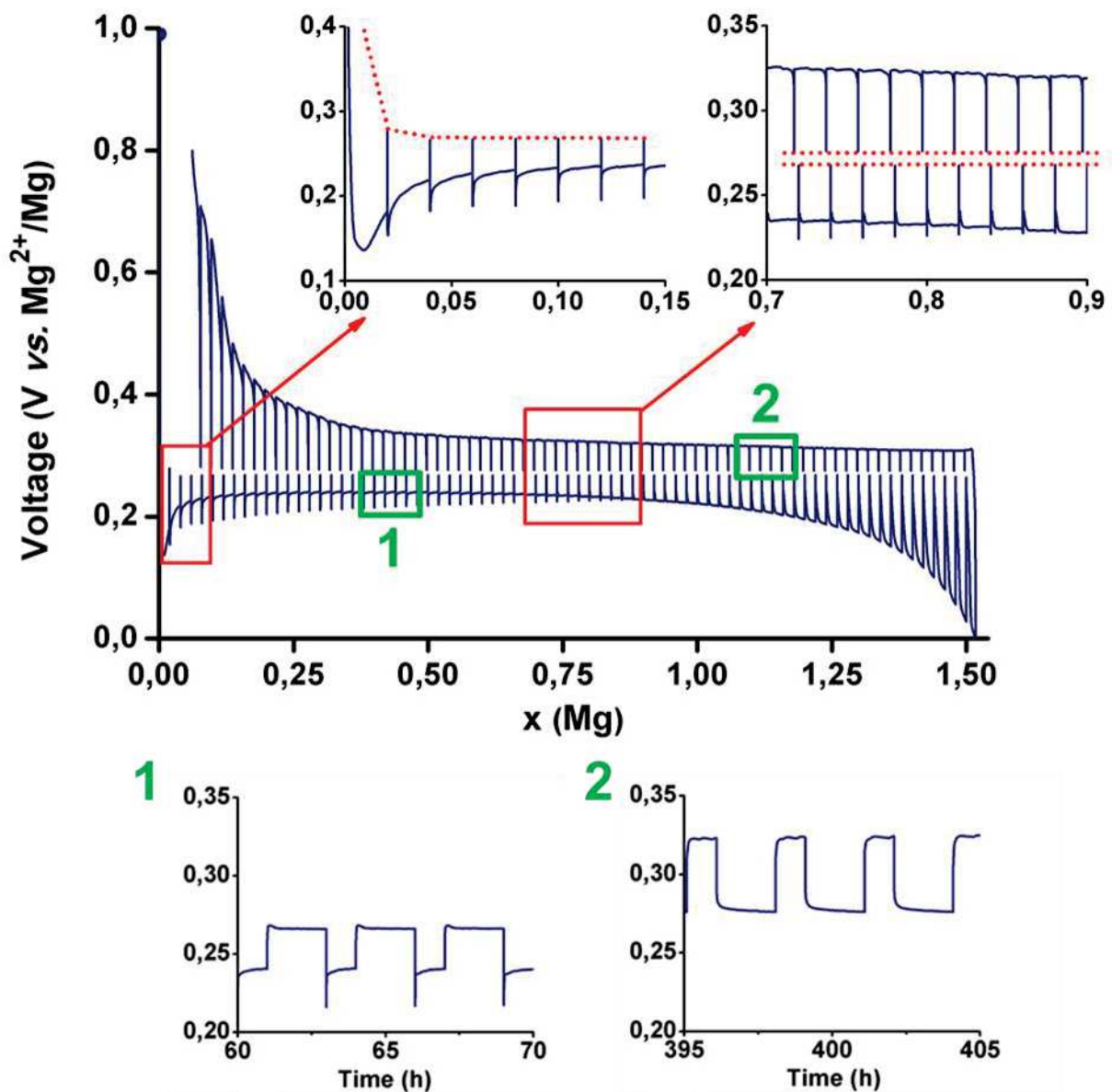


Figure 51 – GITT on μ -Bi-based electrode vs. Mg. 1 hour of reduction/oxidation at C/50, followed by 2 hours of relaxation at OCV. Other conditions are the same of the previous GCPL. GITT analysis also evidences fast relaxation kinetics, demonstrating that alloying and de-alloying reactions between Mg and μ -Bi occur with no major kinetics limitations (see zooms on regions 1 and 2, where the same curve of the main image is plotted as a function of time - Adapted from [190]).

Following the close-circuit voltage (CCV) points, it is possible to find again the same trend shown in the GCPL in both discharge and charge. Nevertheless, looking to the OCV points, during the discharge an extremely stable thermodynamic potential is achieved at ~ 0.27 V and an almost identical value can be found on the subsequent charge, showing the very high reversibility of the Mg/Bi alloying reaction. Moreover, it is possible to confirm that the characteristic potential drop during the very first

moments of the discharge should be ascribed to a kinetic effect because the OCV profile decreases directly down to the thermodynamic value without any oscillation (see Inset in Figure 51). It is also interesting to note that the difference between CCV and OCV in the plateau region is very small, and that the OCV potential is reached after an extremely fast relaxation (zooms on region 1 and 2 in the same Figure), evidencing a quasi-absence of kinetic limitation during the alloying reaction. Such observation confirms also the kinetic origin of the slightly smaller alloying potential observed during the first discharge compared to the following ones.

3.3.2. Operando XRD study

To further clarify the nature of the initial potential drop and thoroughly investigate the structural changes involved in Mg/Bi alloying/de-alloying reactions, an *operando* XRD study was performed on a self-supported electrode cycled at C/20 (12.8mA g^{-1}) over 1.5 cycles (Figure 52)

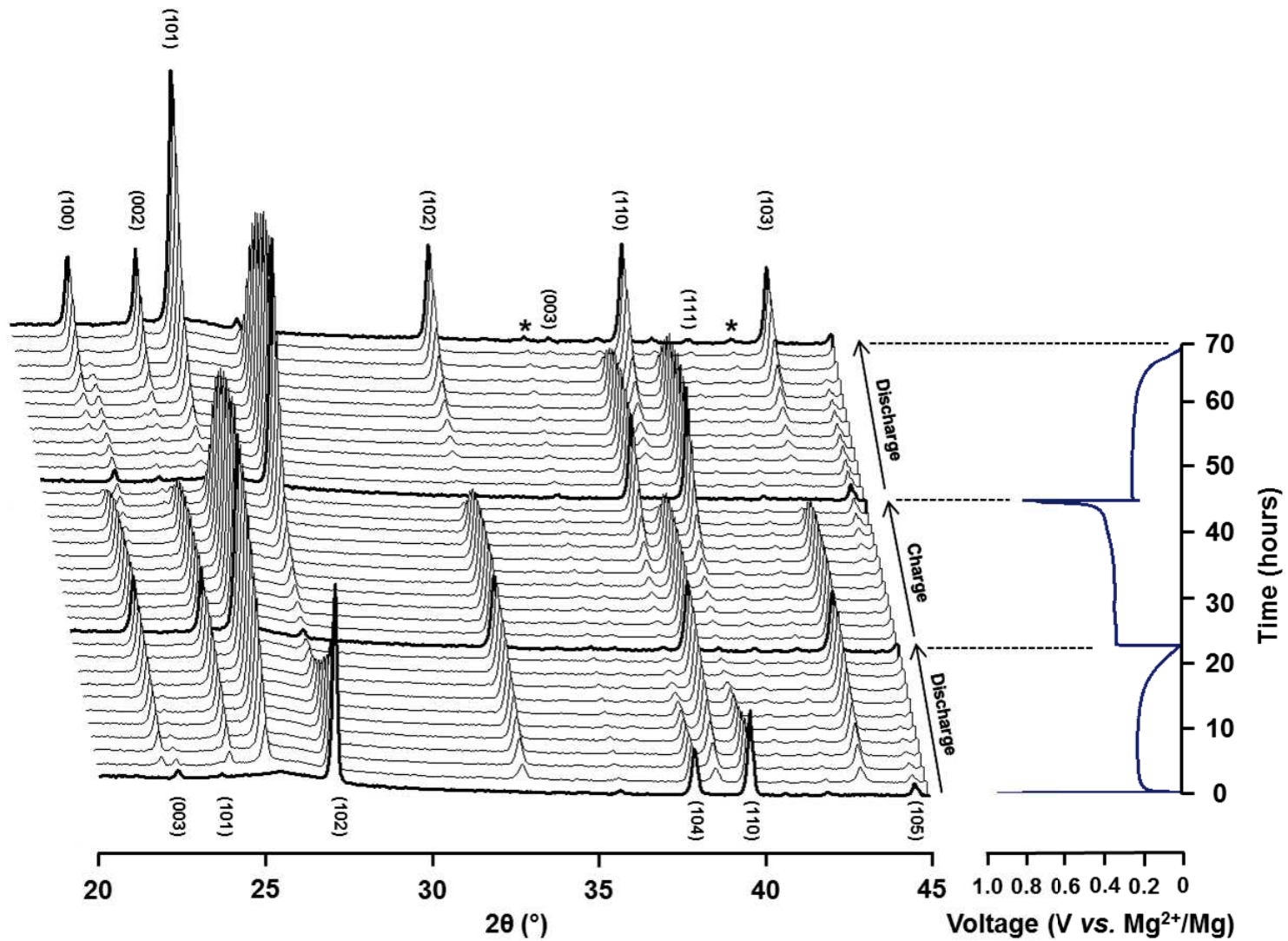


Figure 52 – First discharge, subsequent charge and second discharge of μ -Bi based electrode vs. Mg followed by operando XRD analysis. Peaks marked with * are due to the Be window (Reproduction from [190]).

As soon as the first discharge progresses, the diffraction peaks of Bi decrease in intensity, while those of Mg_3Bi_2 simultaneously grow. This effect can be evaluated pseudo-quantitatively by following the evolution of the integrated areas of the Bi (102) and Mg_3Bi_2 (102) selected diffraction peaks showing a perfect match between the maximum and minimum of each curve (Figure 53).

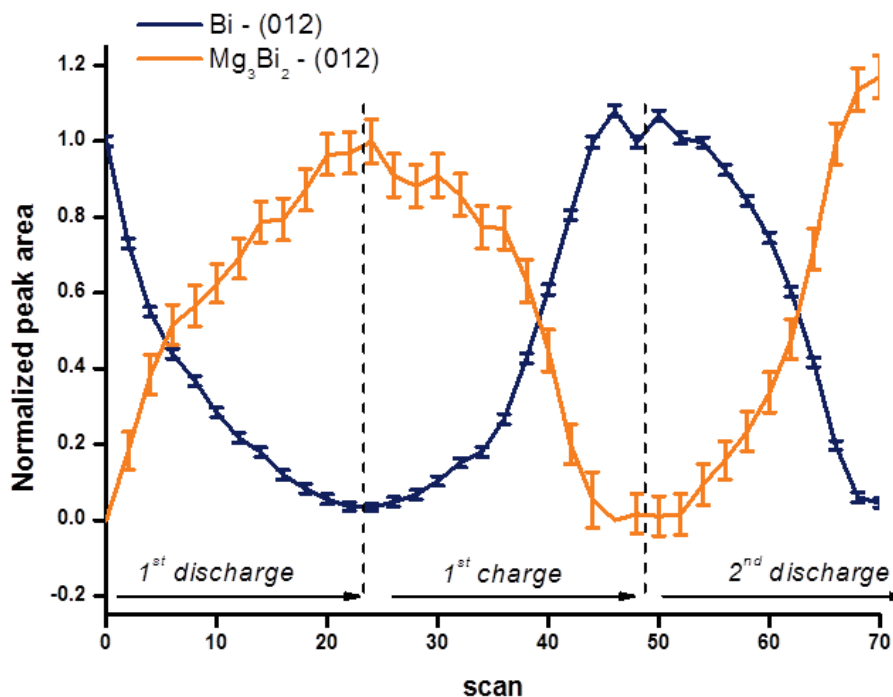


Figure 53 – Evolution of the areas below selected peaks of Bi and Mg_3Bi_2 phases (Reproduction from [190]).

It is noticeable that no delay occurs in the observation of the biphasic process as usually reported in LIBs due to the SEI formation. The reversible phenomenon is also observed during the following charge. Interestingly this biphasic transition happens without any amorphisation process, as it was previously observed for other alloy-type negative electrode materials *vs.* Li and/or Na.[159] Profile matching refinements performed on all collected XRD patterns reveal that both Bi and Mg_3Bi_2 cell parameters remain constant during the whole electrochemical cycling (Table 14).

Time (h)	Bi (s.g. <i>R-3m</i>)		Mg ₃ Bi ₂ (s.g. <i>P-3m1</i>)	
	a (Å)	c(Å)	a (Å)	c(Å)
0	4.545(2)	11.862(5)	-	-
10	4.545(3)	11.86(1)	4.654(3)	7.386(4)
20	4.549(4)	11.88(2)	4.655(1)	7.389(2)
30	4.549(3)	11.88(3)	4.653(1)	7.385(2)
40	4.547(1)	11.867(2)	4.651(1)	7.383(3)
50	4.544(1)	11.857(2)	4.656(5)	7.387(7)
60	4.544(1)	11.856(2)	4.656(1)	7.388(1)
70	-	-	4.653(4)	7.385(4)

Table 14 – Both magnesianation and de.magnesianation are complete biphasic process. No peak shift are observed for both Bi and Mg₃Bi₂ selected peaks; “ - ” means no phase or not enough to perform reliable 2-phase full pattern refinement.

This confirms that even at very low Mg insertion values, there is no Mg-solubility in the Bi matrix, in total agreement with the Bi-Mg phase diagram.[189] All the diffraction peaks of Mg₃Bi₂ follow exactly the same trend either during discharge or charge process. This indicates that the Mg atoms occupying the two Mg sites in Mg₃Bi₂ react at the same time, and do not follow distinct electrochemical pathways.

3.3.3. Performance evaluation

Besides exploring the electrochemical mechanism, it is worth trying to compare the performance of electrodes based on micrometric Bi as active material with those of the nanometric one reported in literature.[78] Electrodes prepared on Cu current collectors, shown in Figure 54, were tested at the high current rate of 2C.

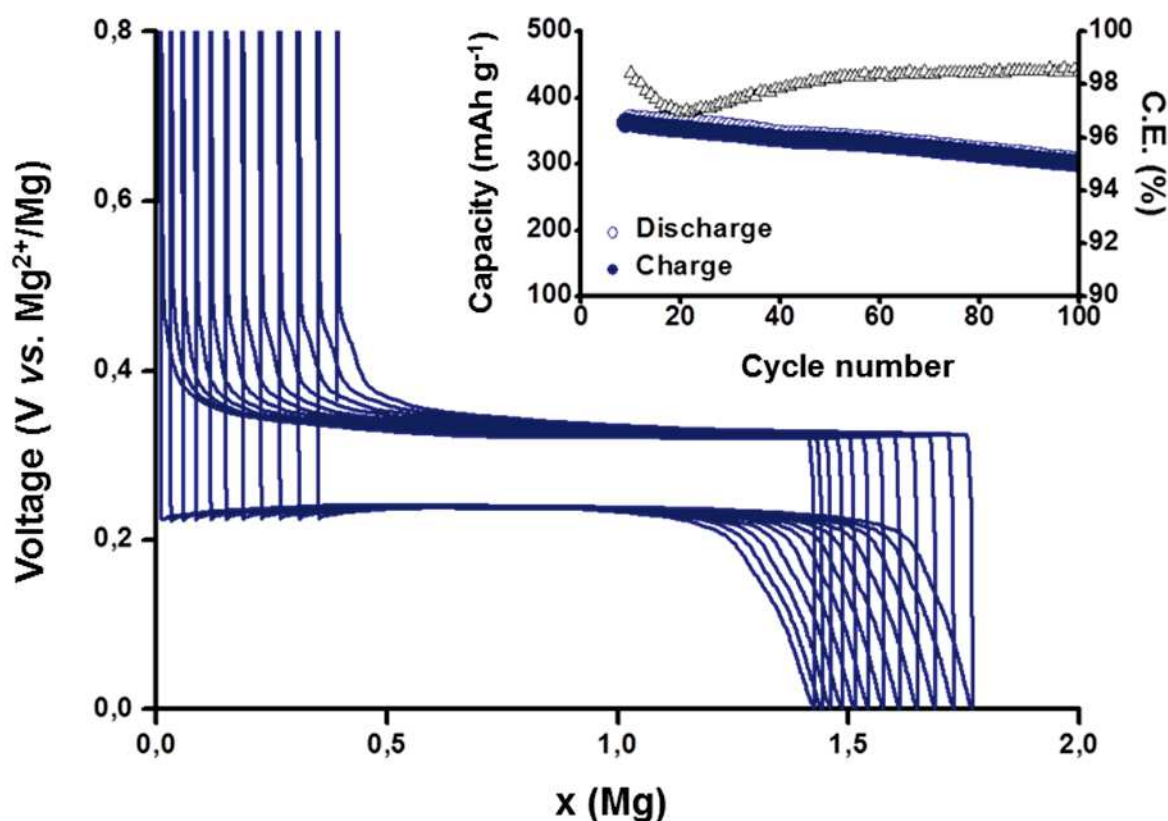


Figure 54 – Electrochemical cycles of a μ -Bi based electrode vs. Mg at the high current rate of 2C (bottom); Inset: associated specific capacity and corresponding coulombic efficiency (Adapted from [190]).

The potential drop, already observed at the beginning of the magnesiation at low rates, is more pronounced at higher current densities. Consequently, the cut-off value of 0 V vs. Mg^{2+}/Mg is sometimes directly reached and several short activation cycles are therefore necessary to overcome this potential drop and reach the alloying plateau. Nevertheless, the alloying and de-alloying processes are clearly highlighted by the usual, flat potential plateaus. The battery exhibits a mean reversible capacity of about 300 mAh g^{-1} (2933 mAh cm^{-3}), only 22% lower than the theoretical one, with a slight but steady decrease, and a coulombic efficiency stabilized around 98.5% after 50 cycles. The regular shift between each consecutive cycle testifies an irreversible Mg consumption during discharge, probably due to electrolyte degradation. The alternating high volume changes ($\sim 100\%$) during the alloying and de-alloying process might also contribute to the capacity fading with a progressive loss of electrical contact between active material grains and conductive additive. A continuous growth of the SEI might be an alternative explanation. In a Mg battery, the SEI formation at the negative electrodes materials from *p*-block elements is still a completely

unexplored domain. Surface characterization techniques, such as XPS, are needed to better understand the electrode-electrolyte interface evolution, but go beyond the scope of this thesis.

μ -Bi-based electrodes were also tested with other electrolyte formulation, i.e. the APC (cf. 2.3.3.2) but, even at lower current densities electrochemical performance appears poorer: a higher irreversible capacity after the first cycle can be noticed (25%) and a progressive fading of the discharge specific capacity. Moreover, after 20 cycles, it was observed the complete cell failure, due to a contact loss, likely caused by the electrolyte degradation (Figure 55). It is important to stress that the preparation of Mg-electrolytes requires a strict control on the purity of the reagents and any moisture contamination should be avoided.[192] However, our laboratory was not equipped to fulfil such demanding standards that can explain the unexpectedly poor electrochemical performance provided of our APC electrolyte.

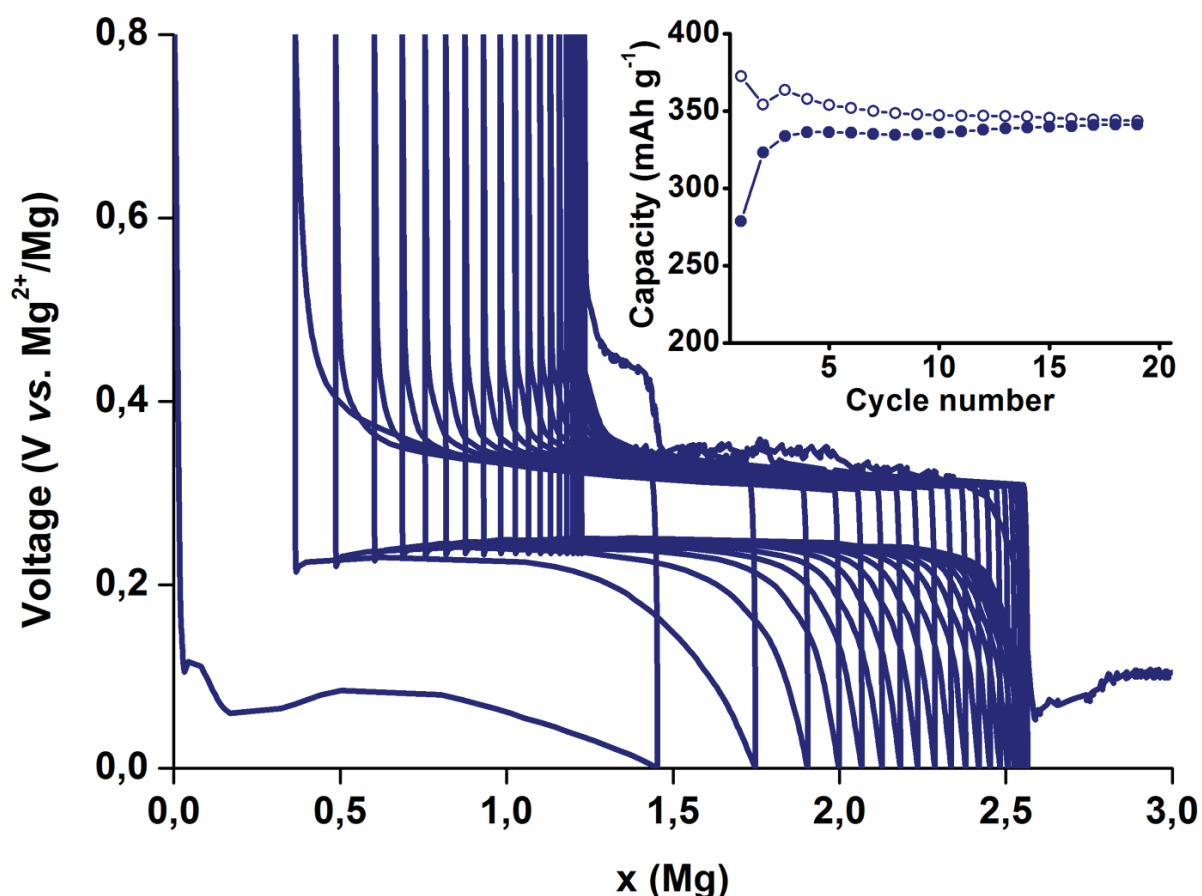


Figure 55 – GCPL on Bi-based electrode vs. Mg at C/10, with the APC electrolyte.

The electrochemical performances of the micrometric Bi-based electrode were also evaluated through rate capability tests from C/20 to 5C (Figure 56).

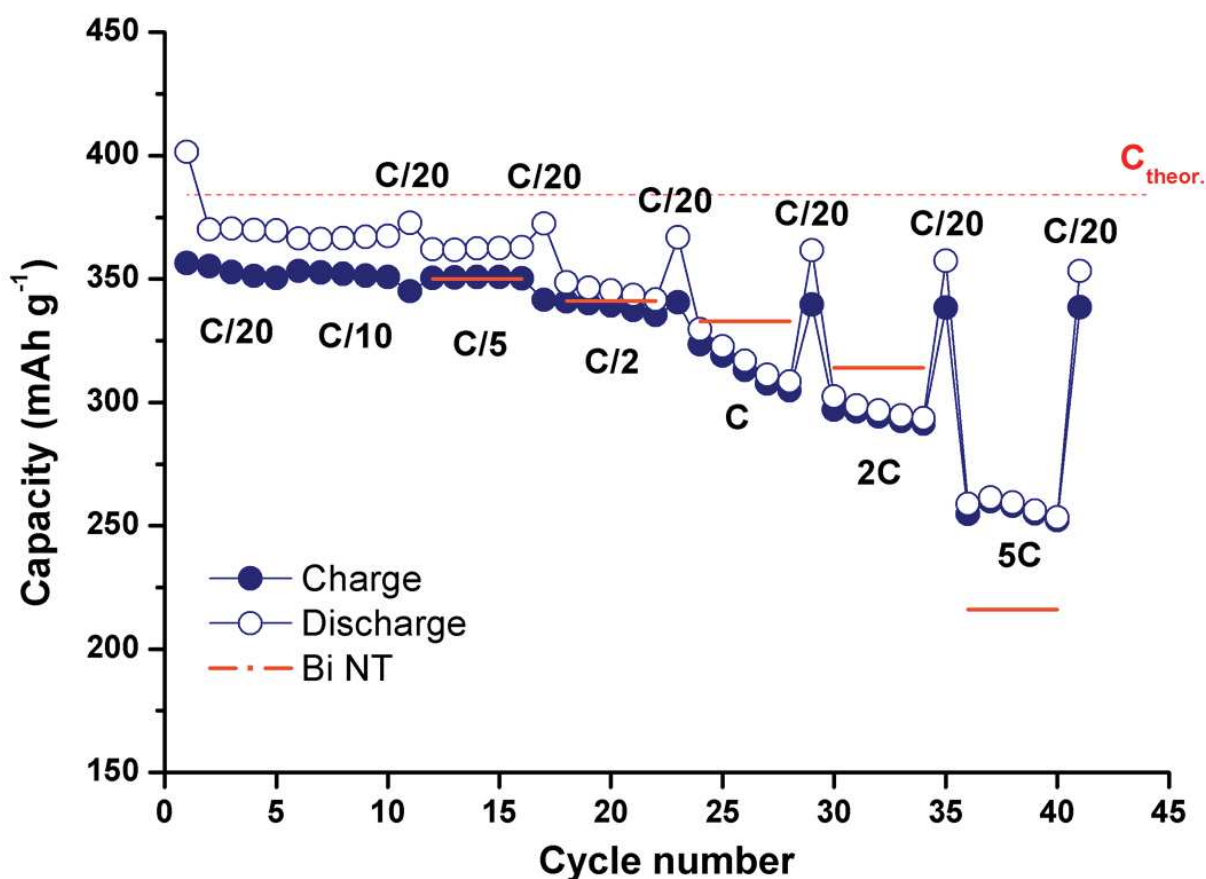


Figure 56 – Rate capability of a μ -Bi based electrode vs. Mg. Each stint features 5 cycles at the same current density, from C/20 to 5C, followed by a cycle at C/20 in order to check the resistance of the electrode at high current densities. Measured specific capacities are in line with those provided by Bi nanotubes[78] (Reproduction from [190]).

Here again, a steady decrease of the capacity with increasing current density is observed. The performance is in line with that of Bi-NT electrodes reported in the literature.[78] In addition, it is interesting to note that high capacities are obtained and remain constant for each cycle at C/20 following the five cycles at higher rates. The similarity between the rate capabilities of electrodes prepared starting from Bi nanotubes or from micrometric Bi are in line with the idea, suggested above, of electrochemical grinding of the electrode during the first cycle. In this case, the first cycle activation of micrometric Bi probably results in a veritable *in situ* nanostructuring of the metal. In summary, this study of the rate capability clearly highlights the excellent cycling properties of micrometric Bi vs. Mg, and questions the needs for nanostructured electrode materials for the particular case of Bi.

3.3.4. Mg_3Bi_2

In MIBs, which do not contain metallic Mg, a source of Mg ions is necessary either in the positive or in the negative electrode. Bi-based electrodes should be therefore associated with Mg-containing positive electrode materials (cf. 1.7.3). However, it is also very important to investigate Mg-containing negative electrodes in order to anticipate a possible next generation of Mg-free positive electrode materials.[149] For these reasons, the electrochemical behaviour of as-prepared Mg_3Bi_2 was also investigated. Micrometric Mg_3Bi_2 powder is easily obtained in only 5 hours by high-energy ball-milling (cf. 1), as evidenced by XRD analysis (Figure 57).

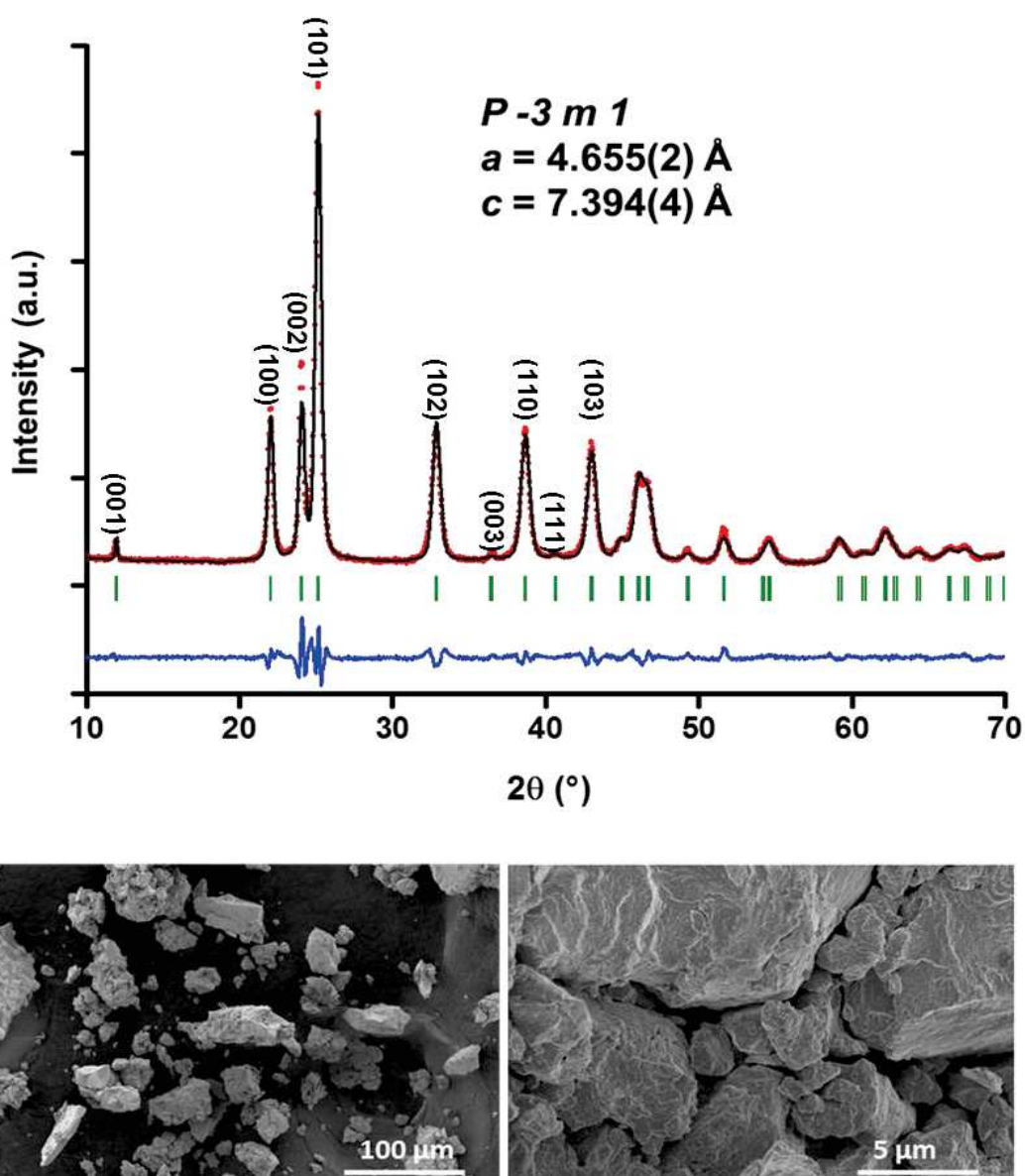


Figure 57 – Top: XRD confirms the formation of the pure phase Mg_3Bi_2 by 5 hours ball-milling. Bottom: SEM images shows that the as-prepared powder is composed of micrometric particles with a wide range of sizes (Reproduction from [190])

The two first galvanostatic and CV cycling with Mg_3Bi_2 -based electrodes are presented in Figure 58.

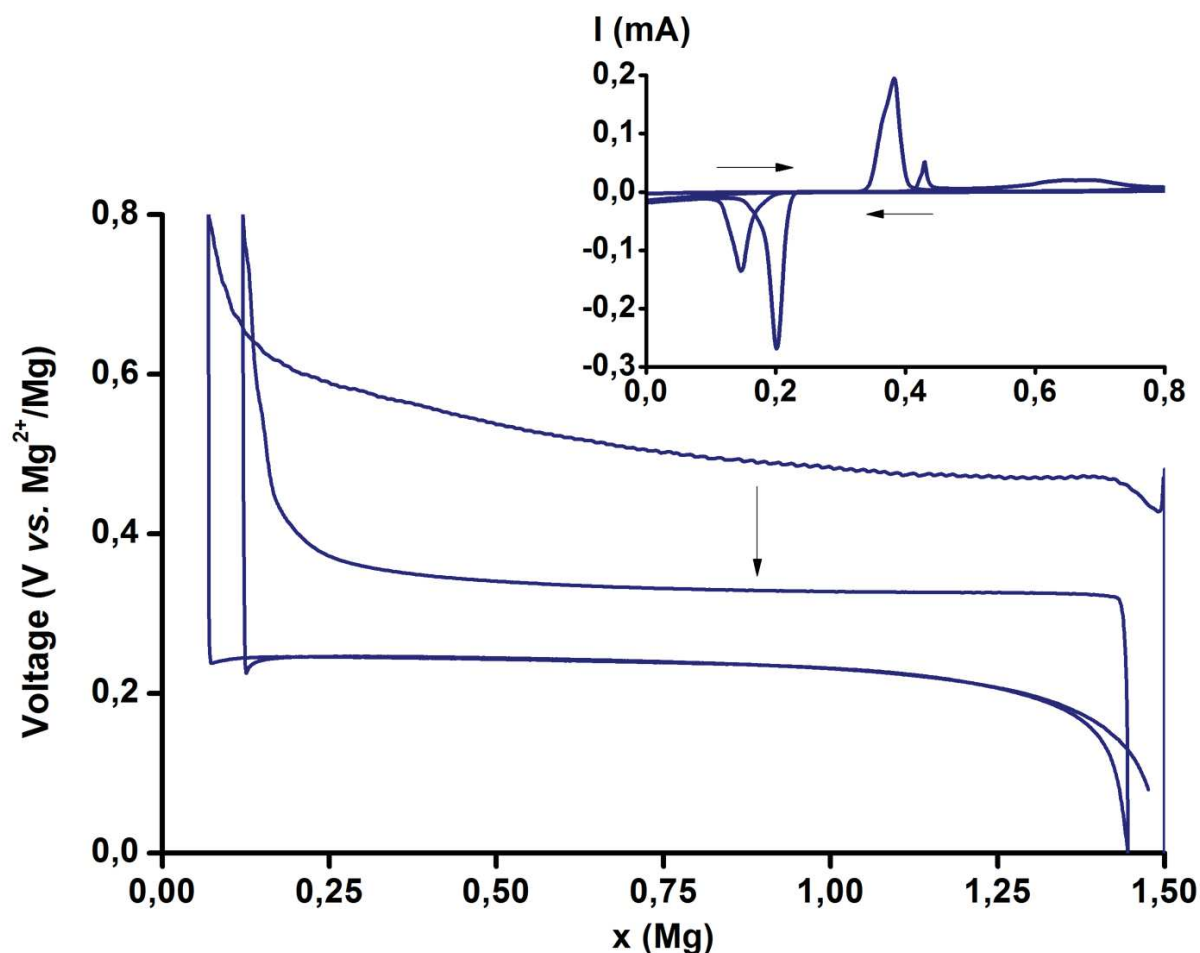


Figure 58 – With the exception of the first oxidation process, where the nanostructuring of Mg_3Bi_2 occurs, identical potentials are observed during de-magnesiumation and magnesiumation of Mg_3Bi_2 prepared by ball milling (Reproduction from [190]).

The first current value was intentionally set as negative (reduction process) in order to check whether any amount of Bi, issue of the Mg_3Bi_2 synthesis and undetectable by XRD was still present. However the cell voltage instantaneously reached the lower voltage limit (set to 0 V) and immediately started the oxidation process. This evidence confirms that no further Bi is present in the electrode or is not accessible for electrochemical magnesiumation. Almost complete electrochemical Mg de-alloying reaction is obtained, with a highly reversible capacity (95% retention in the following discharge). During the first charge, the de-alloying process occurs at about 0.5 V after a potential fluctuation analogous to that observed before the very first alloying plateau in Bi-based electrodes. The strong polarization, once compared to the value observed during charge when starting from micrometric Bi electrodes, can be

attributed to the higher energy needed for de-alloying micrometric particles of Mg_3Bi_2 . In fact, after this first process, the following discharge and charge plateaus occur at the same potential than those observed for the Bi based electrodes (cf. Figure 50). Similarly to Bi electrodes, the charge/discharge process was also followed by *operando* XRD. The biphasic mechanism is clearly evidenced by the disappearance/appearance of the diffraction peaks of both Mg_3Bi_2 and Bi, as well as by their constant cell parameters (Figure 59 and Figure 60).

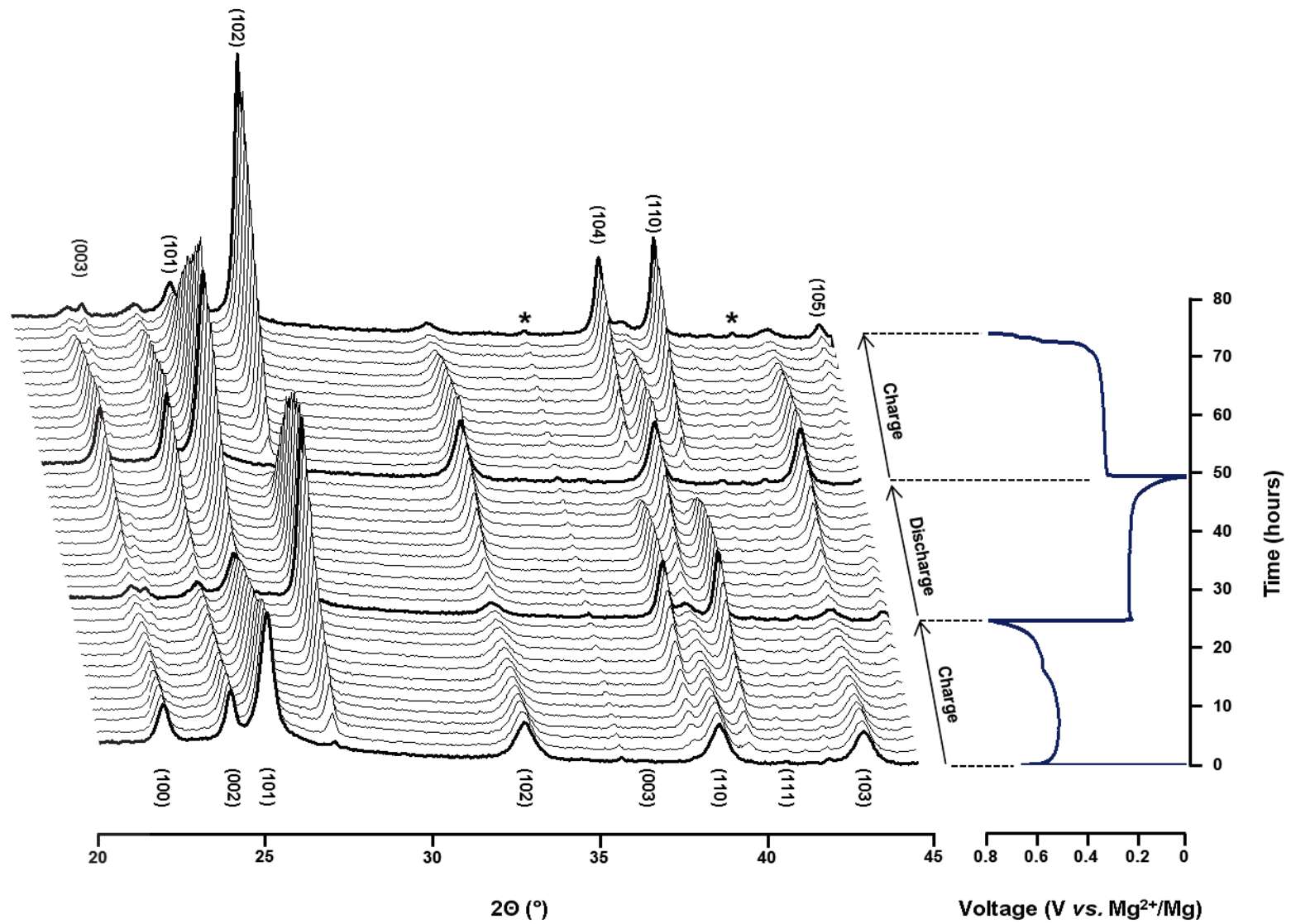


Figure 59 – Operando XRD of Mg_3Bi_2 -based electrode vs. Mg. Peaks marked with * are due to Be window of the *in situ* cell (Reproduction from [190]).

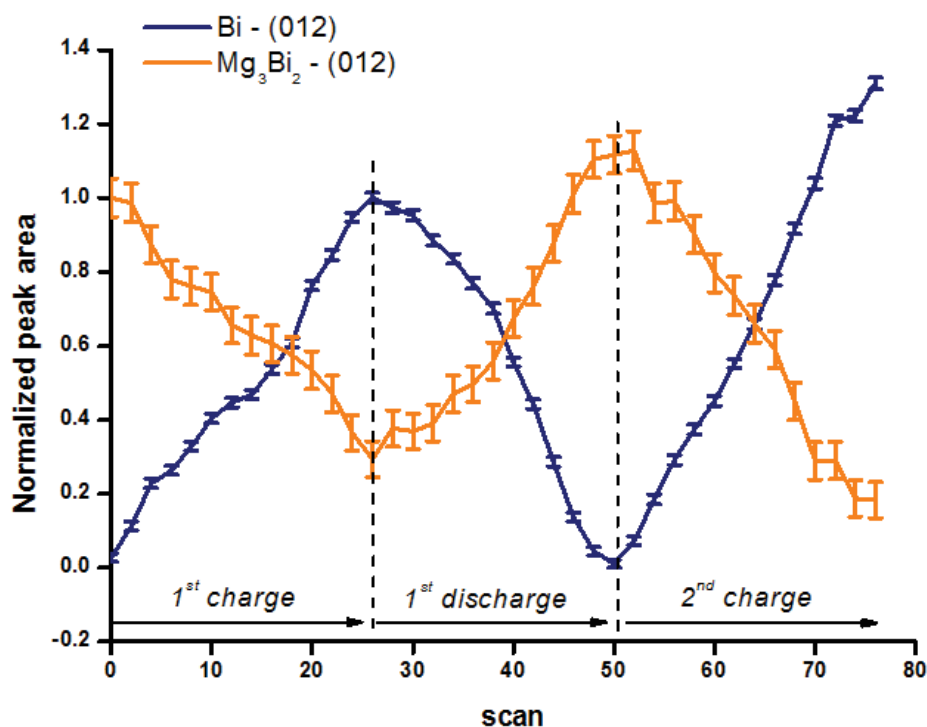


Figure 60 – Evolution of the areas of selected peaks of Mg_3Bi_2 and Bi phases (Reproduction from [190]).

In summary, it was confirmed that micrometric Bi electrochemically alloys/de-alloys rather easily to Mg. *Operando* XRD confirms that such processes are purely biphasic in the whole reaction range. This result is in agreement with the thermodynamic Bi-Mg phase diagram, which shows no Mg solubility in Bi and no binary compounds other than Mg_3Bi_2 . While intermediate amorphisation and solid solutions are commonly observed in other alloy-type electrodes, in the specific case of Bi and Mg_3Bi_2 , both phases remain highly crystallized during both the charge and the discharge. Electrochemical performance was found to be in line with those reported in literature for nanostructured electrodes, questioning the need of elaborated and difficult to upscale synthesis's techniques. Moreover, in order to foresee a more concrete application, binary Mg_3Bi_2 phase was prepared by mechanochemistry and tested. Its electrochemical properties were found to be comparable with those of pure Bi.

Although Bi was the first element studied in this work that offered reversible cycling *vs.* Mg and exhibited good electrochemical properties even in its magnesiated counterpart Mg_3Bi_2 , it is worth underlying that its theoretical specific capacity is the lowest achievable from *p*-block elements. It is therefore necessary to explore the

electrochemical performance on lighter but also more abundant elements in order to both find possible more performing electrode materials at an affordable price.

3.4. Indium

In is the 68th element on Earth's crust and can be therefore considered a relative rare metal. However this study was undertaken since it is lighter than Bi and, unlike the elements investigated above, it shows a wide variety of Mg-rich phases, as can be seen from the phase diagram shown in Figure 61. To the best of our knowledge, there was no investigation on the electrochemical behaviour of In electrode in Mg battery. The only interesting report so far is a patent from Toyota Motors, dealing with In-Sn composite materials prepared by mechanical alloying. The In activity was barely noticed, with an alloying voltage close to 0 V. However, no further details on the magnesian process were provided.[193] The employ of pure In as negative electrode in Mg-based batteries was never reported before 2015.[194]

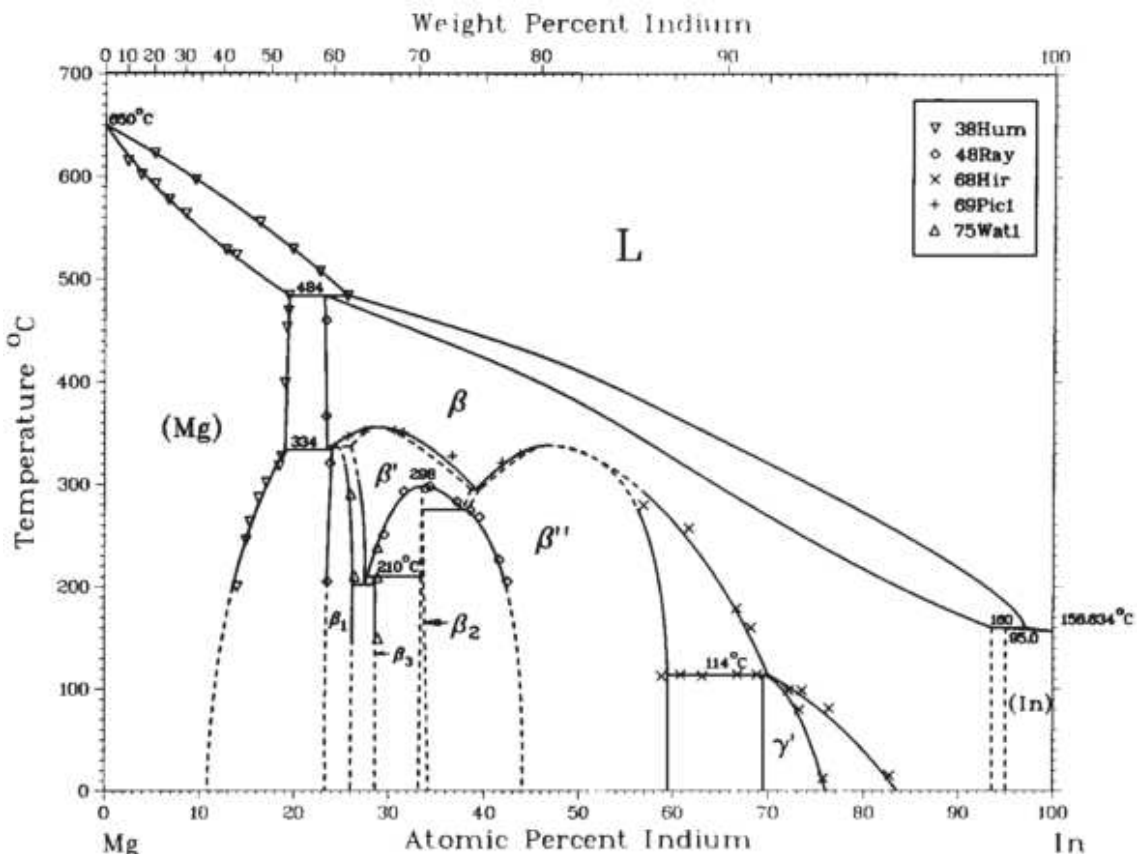


Figure 61 – The Mg-In binary phase diagram is very complex and gathers several Mg-rich phases, such as $\beta_1 \approx \text{Mg}_3\text{In}$ and $\beta_2 \approx \text{Mg}_2\text{In}$ (Reproduction from [195]).

Unlike Bi, In-based electrodes were prepared using commercial In powder without any further treatments. SEM images were collected in order to check the morphology of the pristine metal particles (Figure 62).

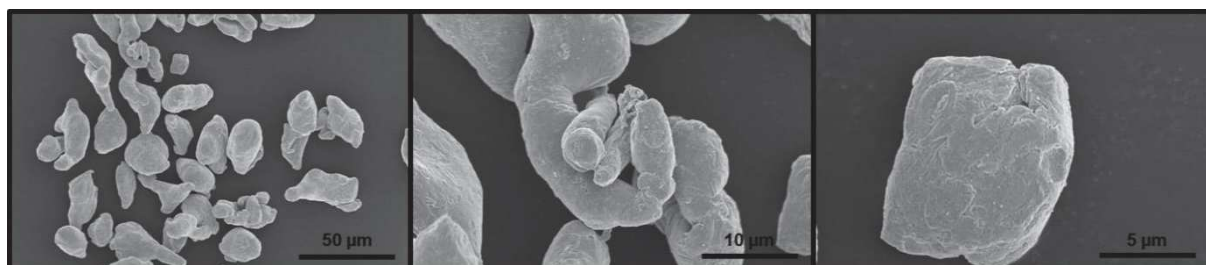
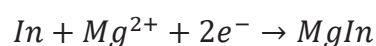


Figure 62 – SEM images at different magnification of commercial In particles, showing a relatively wide size distribution (10 – 50 μm). In is a soft metal and this feature is also testified by the lengthened shape and smoothed edges of the metal particles (Adapted from [194]).

According to the GCPL, Mg reacts with In during the discharge at a very low alloying potential (0.06 V). The electrochemical reversible alloying of μ -In-based electrodes with Mg could be thus demonstrated for the first time. Although several highly-Mg rich binary phases are present in the Mg-In phase diagram, a magnesian value of 0.92 mol (per In mole) was achieved, which provides a specific capacity around 425 mAh g⁻¹ (3107 mAh cm⁻³). *Ex situ* XRD collected at the end of the first discharge shows the formation of MgIn, as described by the following equation:



The theoretical specific capacity provided is 467 mAh g⁻¹ (3414 mAh cm⁻³).

MgIn corresponds to the average composition of the solid solution β'' in the phase diagram shown in Figure 61. The refined cell parameters of MgIn are in good agreement with the literature.[196][197] the first time during this thesis (Figure 63):

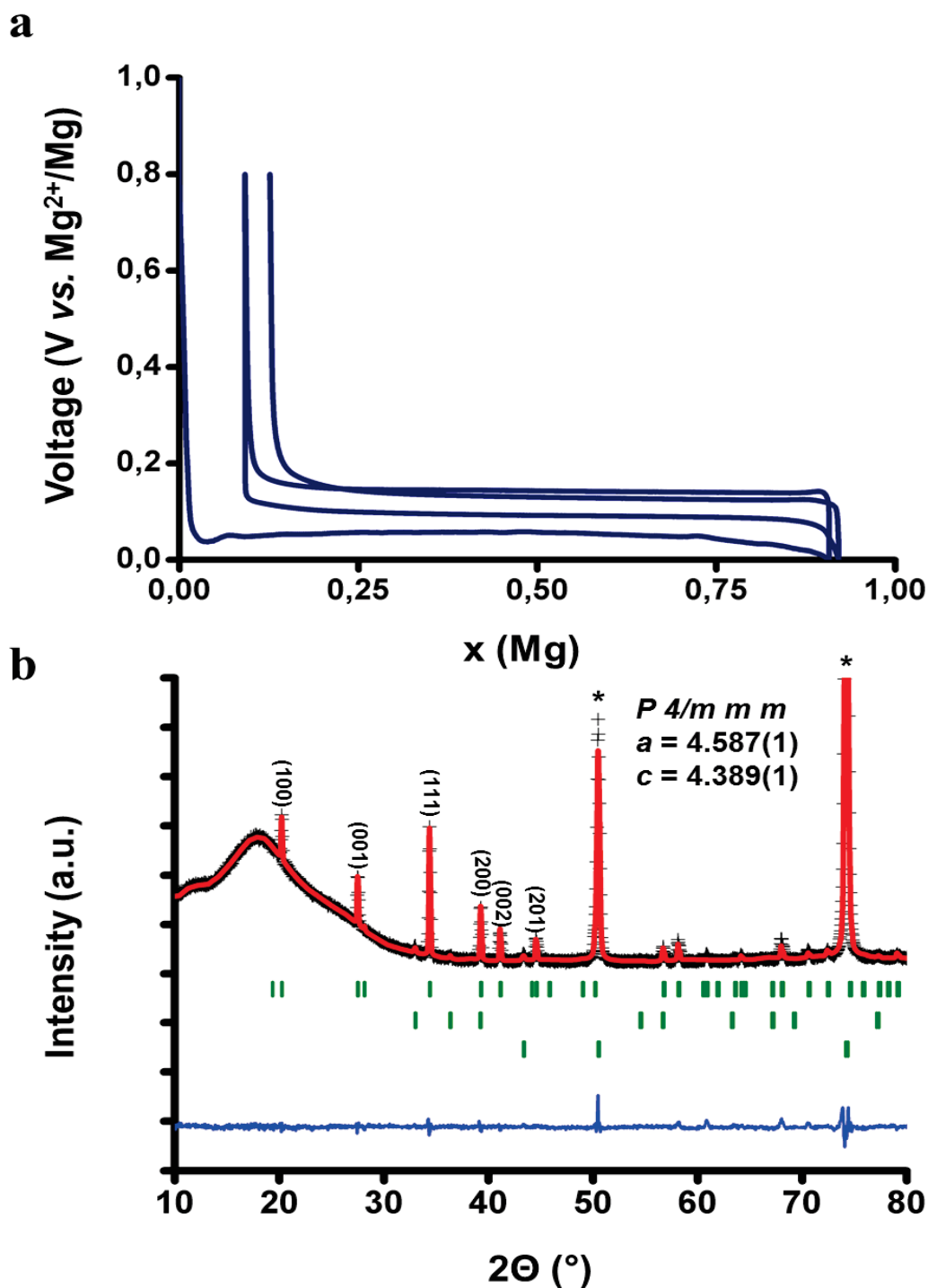


Figure 63 – a: GCPL analysis of μ -In-based electrode vs. Mg. Electrolyte: EtMgCl:2Et₂AlCl in THF; current rate: C/100; electrodes supported on Cu discs; current collector of the Mg disc: Cu. The theoretical alloying of 1.5 Mg is achieved (and slightly overcome) during the first discharge. The process is highly reversible, with a capacity loss of 5%. The following discharge occurs at a higher potential than the first one. The decrease of the polarization is due to the electrochemical grinding of In during the first cycle. b: The full profile matching of the *ex situ* XRD pattern of an In self-supported electrode collected at the end of the first discharge clearly demonstrates the formation of Mg₃Bi₂. Refined cell parameters are in agreement with the literature.[191] First phase: Mg₃Bi₂, Second phase: Bi; the peaks labelled with a * are due to the Cu electrode-supporting foil (Adapted from [190]).

The electrochemical reaction is highly reversible, as more than 90% of the Mg is recovered during the following charge, which occurs at 0.15 V. The electrochemical grinding observed during the first cycle then influences the following alloying and de-alloying potentials, with a slight decrease of the polarization. Stable plateaus of 0.09 and 0.13 V, respectively, in discharge and charge, rank In as the negative electrode material alternative to Mg metal with the lowest potential ever reported in literature up to date.[194] Unfortunately, the electrochemical driving force seems not sufficient to form phases richer in Mg, which would have been very interesting in terms of specific capacity (up to 1400 mAh g⁻¹ in the case of theoretical formation of Mg₃In).

3.4.1. Operando XRD analysis

As already done in the case of Bi-based electrodes, In magnesianation was also followed by *operando* XRD (Figure 64).

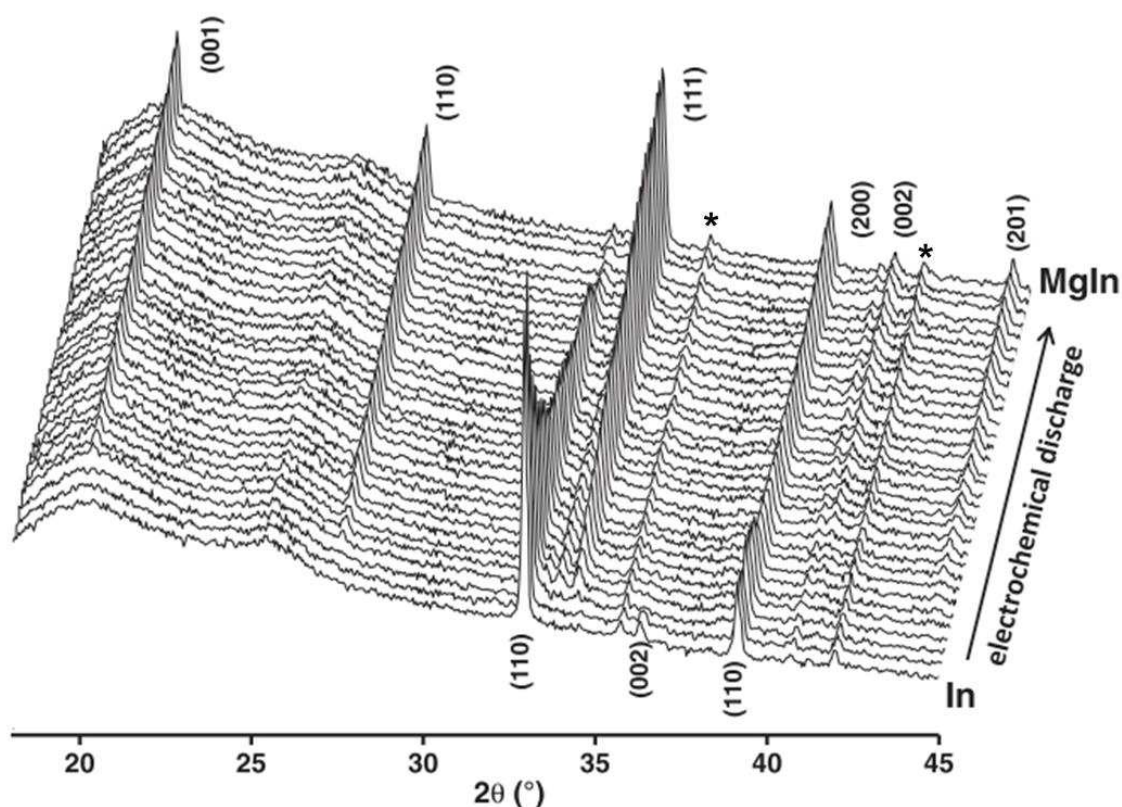


Figure 64 – *Operando* XRD of a μ -In-self-supported electrode vs. Mg. Peaks marked with * are due to Be window (Adapted from [194]).

Unlike Bi, where the formation of magnesianated phase can be observed at the very beginning of the discharge, there is no evidence of MgIn diffraction peaks in the first collected patterns (corresponding to the reaction of the first 0.1 Mg). This delay might

be attributed to the formation of nanometric MgIn domains undetectable by XRD. The Mg consumption of small amounts of Mg with the formation of a solid electrolyte interface (SEI) cannot also be completely discarded. Another possible reason is the insertion of small amounts of Mg into In metal, in agreement with the Mg–In phase diagram exhibiting a In(Mg) solid solution domain allowing the insertion of up to 5-6% Mg in In. For more clarity, the Table 15 gathers the shifts on the In lattice parameters as a function of the Mg insertion amount:

Composition		Lattice parameters (nm)		Tetragonality
at.% In	at.% Mg	<i>a</i>	<i>c</i>	<i>c/a</i>
100	0	0.4594	0.4943	1.076
99.1	0.9	0.4598	0.4929	1.072
98.2	1.8	0.4606	0.4911	1.066
97.3	2.7	0.4621	0.4864	1.052
96.5	3.5	0.4623	0.4858	1.057
96.2	3.8	0.4627	0.4845	1.047

Table 15 – Summary of the In cell parameter variation as a function of low Mg insertion (solid solution – Adapted from [195]).

Unfortunately, the structural modifications involved in this limited solid solution are too small and cannot be detected by the modification of cell parameters in the XRD pattern. Once MgIn peaks appear, they regularly grow as long as the reduction progresses, confirming the biphasic process already evidenced by the potential plateau in the galvanostatic curve. As the β'' phase exists in a relatively large domain of compositions, there is a doubt concerning the exact chemical composition of the alloy, especially at the beginning of the magnesiumation. It is reasonable to assume an initial Mg-deficient composition (41 at.%) which progressively increases before reaching a Mg-rich threshold (56 at.%). In the literature, it is reported that the cell parameters of MgIn vary with the Mg content.[196] However, here again these modifications are too small to be detected by routine XRD analyses. This is also the case of *operando* XRD performed on ordinary lab-scale instruments, where a short measuring time is imposed by the cycling conditions and the signal-to-noise ratio cannot be further improved. Electrochemical alloying occurs without any

amorphisation process, as it was already seen for Bi, and no intermediate phase between In and MgIn is observed.

3.4.2. Performance evaluation

In parallel to the electrochemical mechanism, cycling performance of In-based formulated electrode was evaluated with higher current rates or during low cycling. A very stable capacity in both discharge and charge was observed at C/50 for 10 cycles (Figure 65).

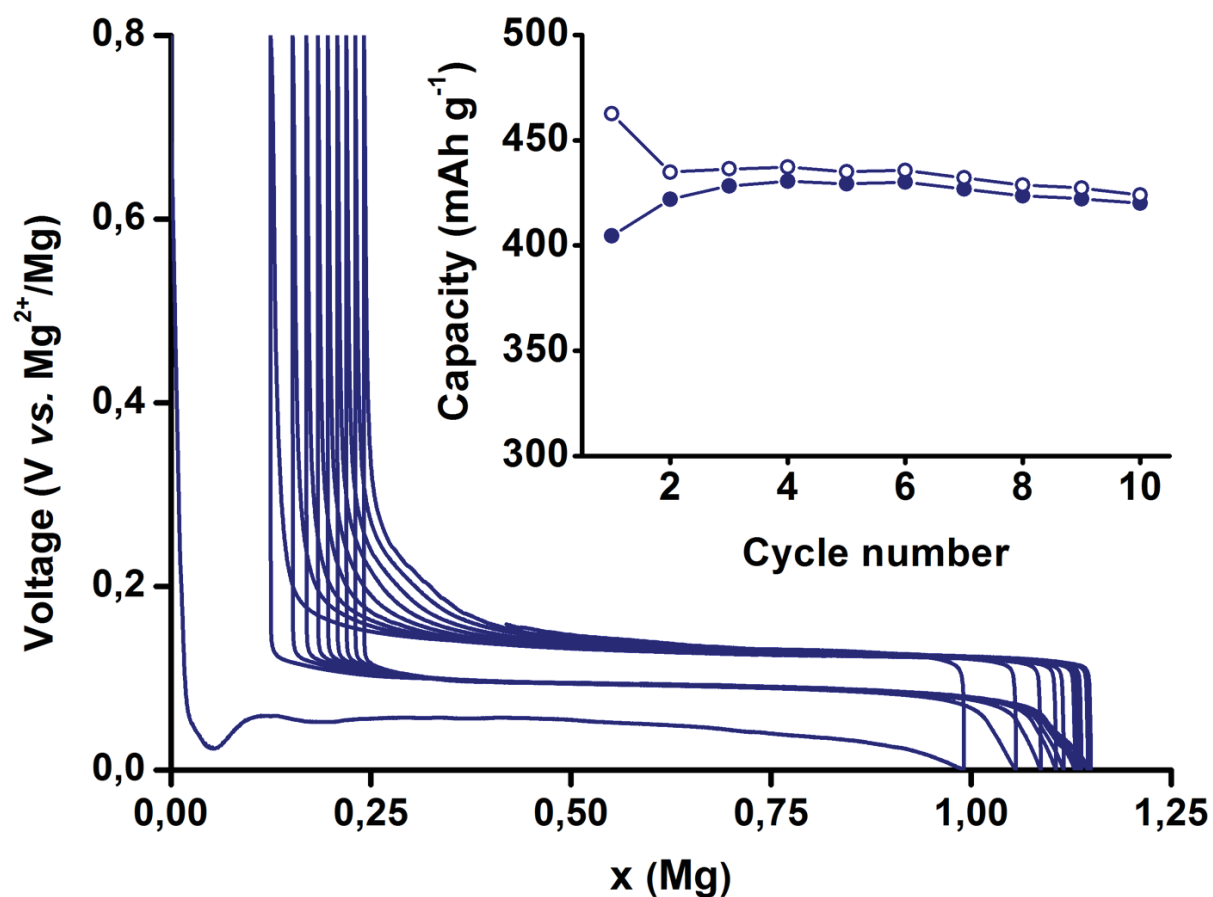


Figure 65 – GCPL cycling at C/50 of a In-based electrode. Inset: associated specific capacity (solid symbols: charge specific capacity, hollow symbols: discharge specific capacity - adapted from [194]).

The small but regular shift of the electrochemical cycles observed at C/50 should be explained by some electrolyte degradation during each cycle. Moreover, it is possible to notice a further reduction of the charge plateaus, where the end of the de-magnesiumation becomes progressively less straightforward. Tests performed at higher rates C/20 or C/10, (not shown here) presented a rapid first discharge with a rapid potential fading to 0 V. Therefore, it was impossible to investigate further

magnesiumation at such rates. Even though the electrochemical performance at moderate and high current rate is unsatisfactory, a rate capability test with a progressive increase of the current rate was carried out (Figure 66).

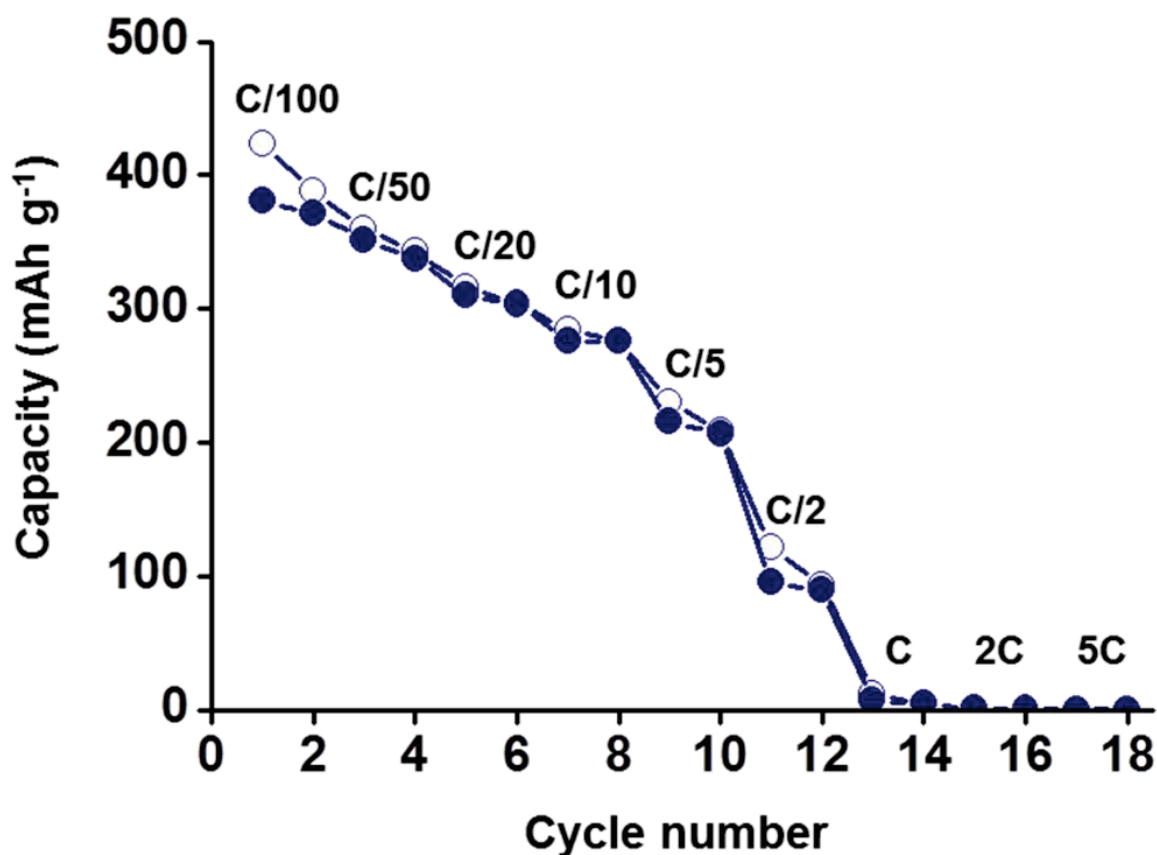


Figure 66 – Rate capability test on μ -In based electrode shows a 34% of capacity fading when current rate increases from C/100 to C/10. The capacity completely vanishes at current densities superior to C/2 (Adapted from [194]).

The reversible capacity slowly decreases from 425 to 280 mAh g⁻¹ with increasing the rate to C/10, then rapidly fades and vanishes at C. Interestingly, in contrast to the unsuccessful above mentioned tests at C/20 and C/10, the nanostructuring of the electrode during the first discharge enables here a reversible magnesiumation at these elevate rates (around 280 – 300 mAh g⁻¹, respectively). These results clearly demonstrate that In alloying/de-alloying process is thermodynamically favourable but suffers from kinetics limitations.

3.4.3. MgIn

Following the same strategy of realizing Mg alloys for potential MIBs, it was decided to evaluate the possible differences when starting from its magnesiated counterpart MgIn.

In this thesis high-energy mechanical alloying was proposed in order to form MgIn. Its large existence domain is undoubtedly helpful for the synthesis, which is achieved after 5 hours of milling from stoichiometric amounts of In and Mg (no Mg excess was needed). A single crystalline phase is clearly evidenced on the resulting XRD pattern (Figure 67):

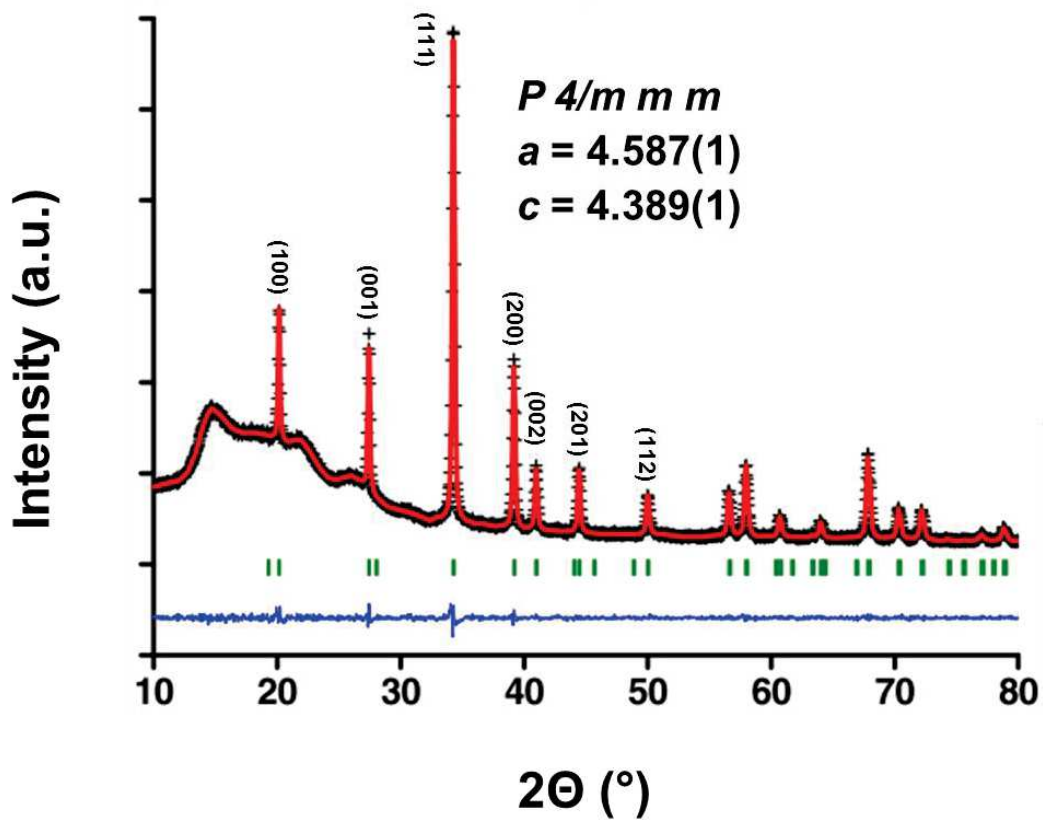


Figure 67 – XRD pattern of MgIn synthesized by high-energy ball-milling. Full profile matching evidences the presence of a single phase in the $P 4/m m m$ space group. Refined cell parameters are in good agreement with the literature.[191] Black crosses, red line and green strokes represent observed XRD points, interpolation and peak positions; blue line represents the difference between the observed values and the fit (Adapted from [194]).

The refined cell parameters confirm the formation of MgIn with a 1:1 composition, in line with the literature.[196]

Since the ball milling synthesis of MgIn was relatively simple and effective, the synthesis of other Mg-richer binary phases was also tried, in order to check if starting

with a more magnesiated phase (Mg_2In or Mg_3In , for instance) could allow electrochemically re-obtaining the starting phase, thus leading to higher specific capacities. However, all attempts to form such phases were unsuccessful: the main obtained products were MgIn and Mg .

SEM images show the micrometric morphology of the powder, with a size ranging from 20 to 50 μm (Figure 68).

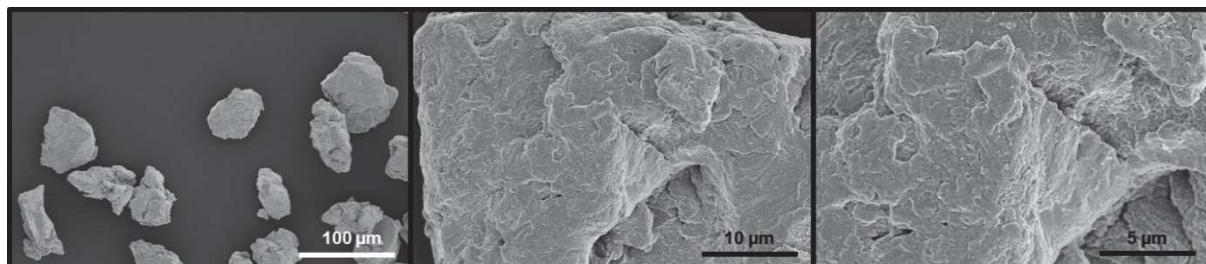


Figure 68 – SEM images of MgIn evidence a narrow size distribution (20 – 50 μm).

MgIn -based electrodes were tested with Mg metal as negative and counter electrode. The galvanostatic cycles collected at $C/100$ are presented in Figure 69.

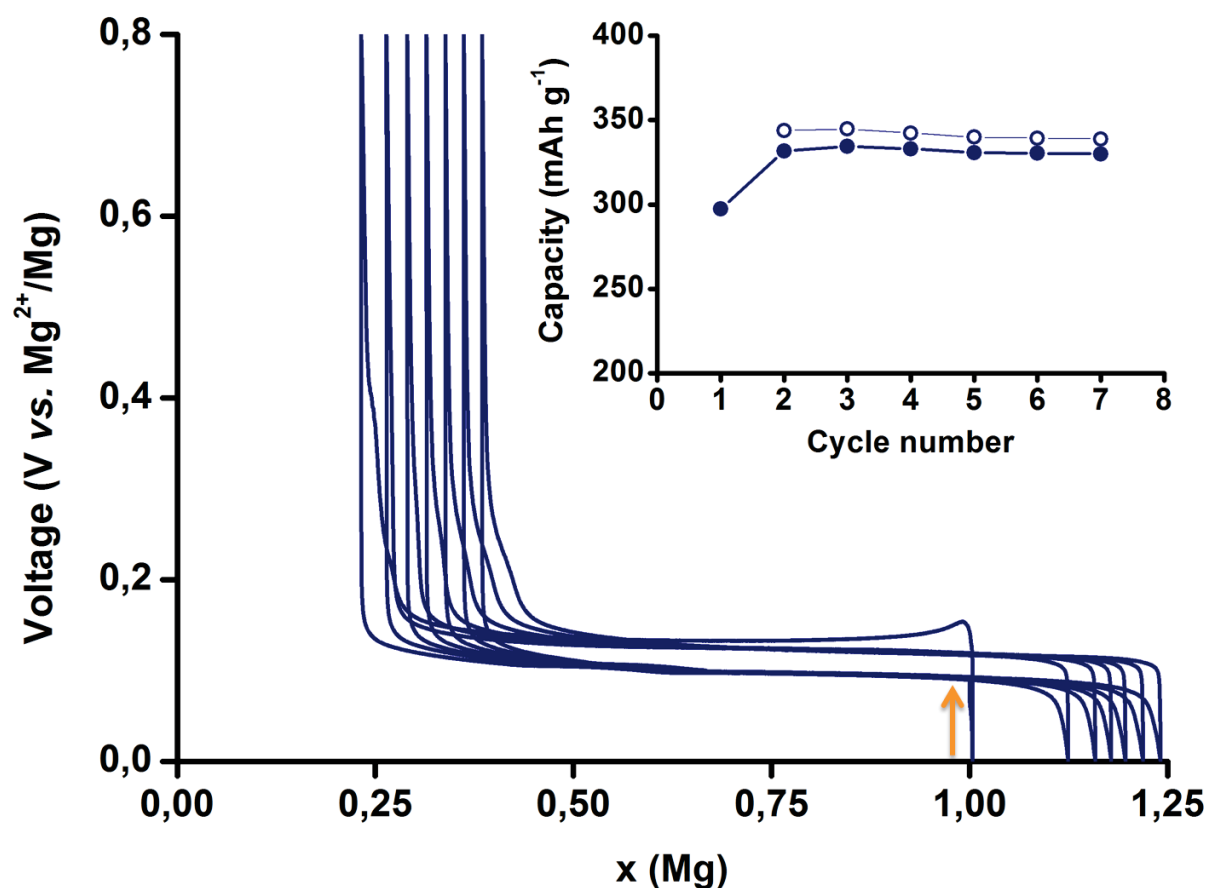


Figure 69 – GCPL at $C/100$ of the MgIn -based electrode vs. Mg ; inset: corresponding capacity evolution (solid symbols: charge specific capacity, hollow symbols: discharge specific capacity - Adapted from [194]).

Cycling is started with a very short reduction sequence where the cell voltage directly drops to 0 V. This evidences that no remained amorphous or nanosized In particles are present in the ball-milled MgIn in the initial electrode. The first oxidation enables the MgIn electrode to reach 355 mAh g⁻¹, about 76% of the theoretical capacity. The subsequent discharge evidences a high reversible reaction. Interestingly, an additional capacity is observed at the very end of the second discharge. The initial presence of an amorphous and magnesiated In-based phase could explain this additional capacity. This minor phase can be de-magnesiated during the first charge and then participates to the overall capacity. There is no capacity fading upon repeating cycling, as it is observed with In (Figure 63). Such early-stage results show that the intermetallic MgIn easily synthesized by ball-milling can be used as negative electrode of Mg-ion batteries for investigating future Mg-free positive materials.

3.5. Conclusions

In this Chapter, micrometric powders of pure *p*-block elements were investigated as electrode materials toward Mg. The more promising ones in theory (Sn and Sb) exhibited very poor activity. Bi-based electrodes, however, showed an impressively high reversible process, with very flat plateaus, low polarization and decent capacity retention at elevated current rates. For the first time, the electrochemical behaviour of In was also studied. It exhibited the lowest alloying voltage with Mg, which is a desired feature in order to enhance the overall energy in a future prototype cells.

IV Synergy between Bi and other elements

As shown in Chapter III, the micrometric powders of some *p*-block elements are able to electrochemically alloy with Mg. However, their electrochemical performance is rather heterogeneous, and Bi resulted by far the best one despite its elevated atomic weight. In this Chapter, we have concentrated our effort in seeking possible synergies in materials obtained by associating Bi with a lighter element, such as Sn, Sb or In. The idea is achieving the higher specific capacities of the latter elements with the good cycling stability provided by Bi. This strategy has already proved to be effective for other alloying systems, for instance in SnSb toward Li.[36] Herein, different associations are investigated: an intimate physical mixing in Sn-Bi composite, a chemical mixing (with shared bonds) in a solid solution fashion ($\text{Bi}_{1-x}\text{Sb}_x$) or in a particular intermetallic compound (InBi).

Different associations were investigated: an intimate physical mixing in the Sn-Bi composite, a chemical mixing (with shared bonds) in a solid solution fashion ($\text{Bi}_{1-x}\text{Sb}_x$) or in a specific intermetallic compound (InBi).

High-energy ball-milling was employed to synthesize all samples. Similarly to Chapter III, XRD has been the main characterization technique adopted to investigate the reaction mechanisms. Moreover, electrochemical performance of each active material was analysed and compared to those of the single elements, in order to understand the mutual influence of the electroactive atoms and the resulting behaviour toward reversible magnesiation.

4.1.Sn-Bi

According to the Sn-Bi binary phase diagram shown in Figure 70, there are neither stable binary phases nor miscibility domains at room temperature.

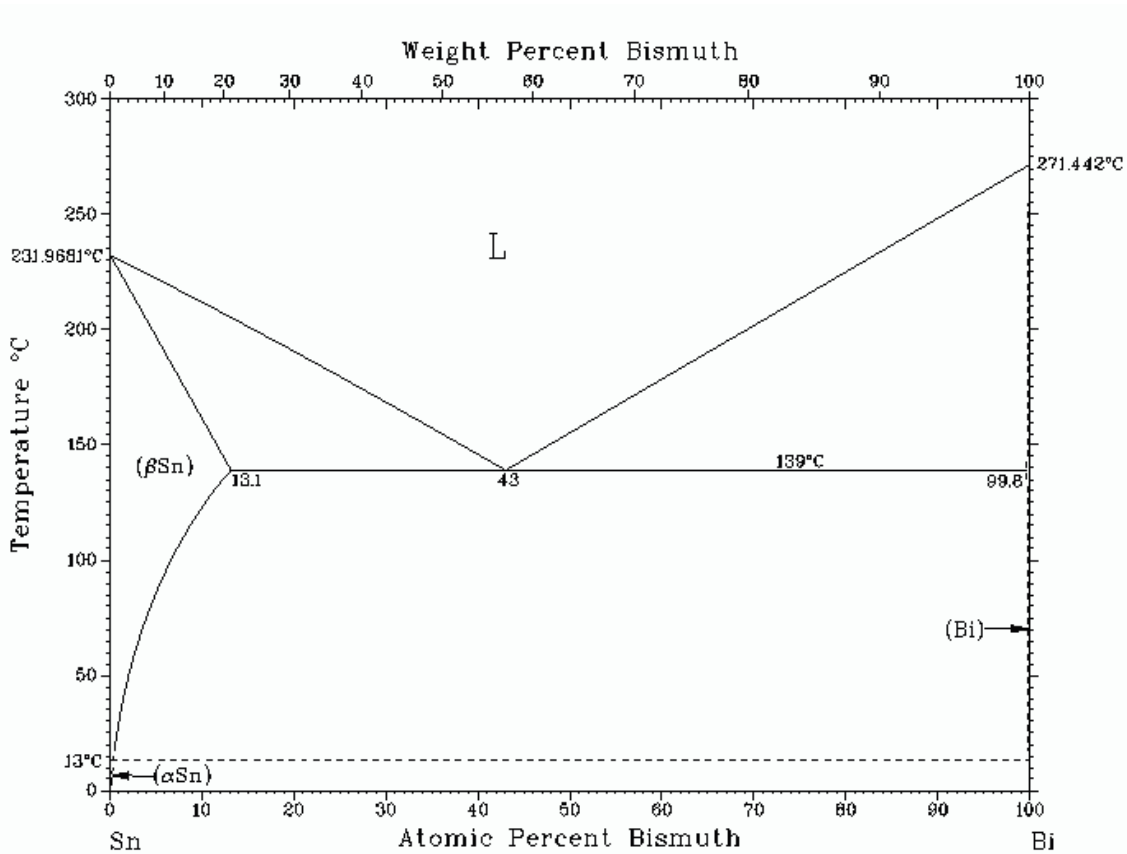


Figure 70 - Sn - Bi binary phase diagram (Reproduction from [198])

In a first attempt, a mixture with a 1:1 Sn:Bi atomic ratio was prepared by 5 hours of high-energy ball-milling. The full profile matching of the XRD pattern on the obtained powder, shown in Figure 71, evidences two distinct and well-crystallized phases. Cell parameters are in agreement with those reported for pure Bi and pure Sn, respectively.[199] The resulting intimate mixture will be hereafter considered as a composite material and labelled Sn₅₀Bi₅₀.

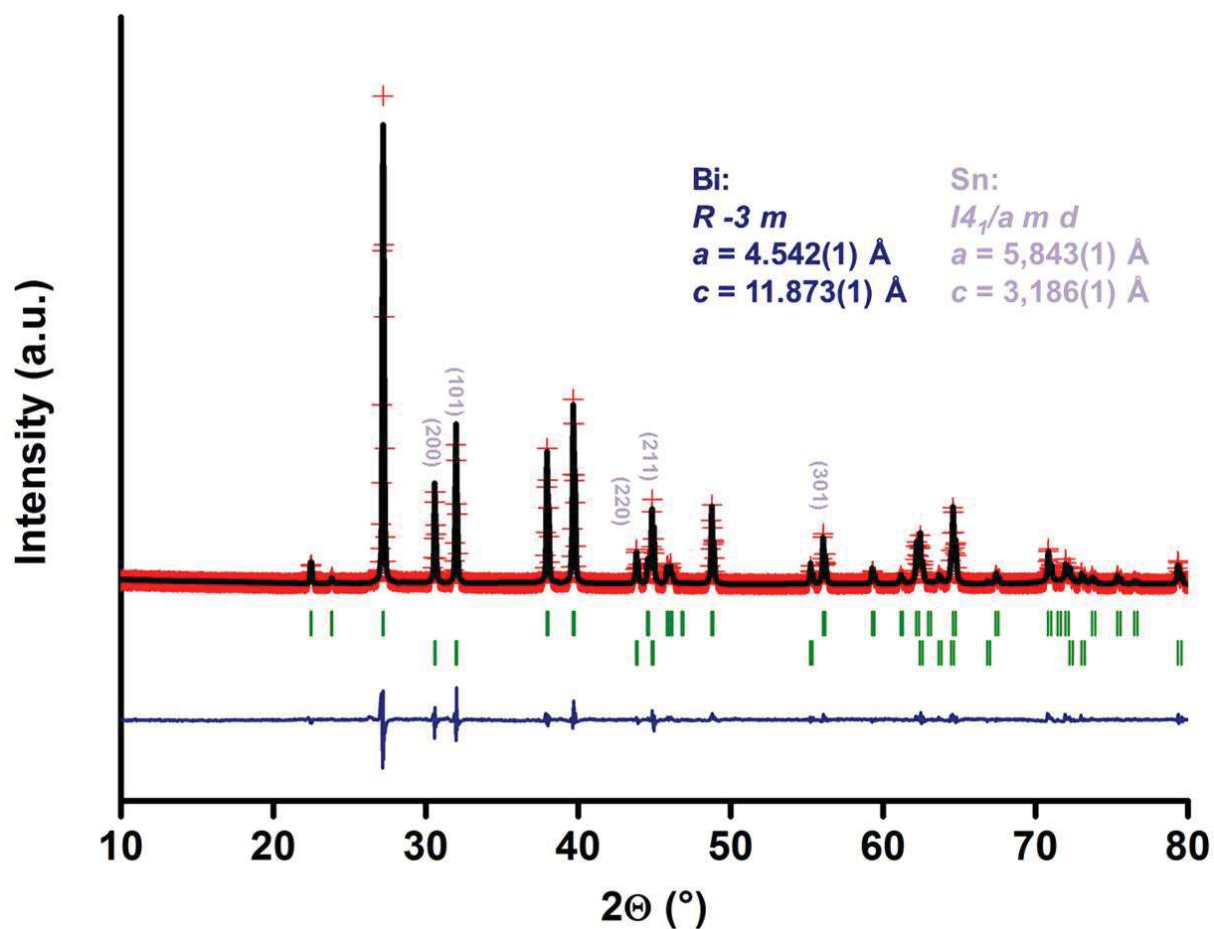
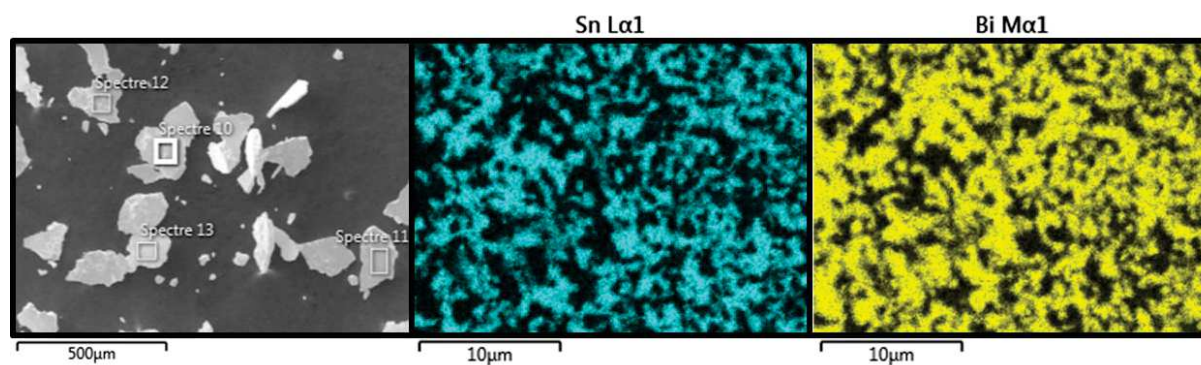


Figure 71 – XRD pattern of the powder obtained after 5 hours of high-energy ball-milling on a 1:1 molar mix of Sn and Bi powders. After the treatment, two well-distinct phases are found. Red crosses, black line and green strokes represent observed XRD points, interpolation and peak positions; blue line represents the difference between the observed values and the fit.

EDX analysis confirms that there were no major changes in the Sn/Bi molar ratio after the ball-milling. Element mapping shows a homogeneous distribution of Sn and Bi at a micrometric scale. However, local gradient of both elements can be detected at the sub-micrometric level (Figure 72).



	at.% Spectre 10	at.% Spectre 11	at.% Spectre 12	at.% Spectre 13
Sn	51	50	55	52
Bi	49	50	45	48

Figure 72 – EDX analysis on several particles of the Sn₅₀Bi₅₀ composite revealing that the ball-milling treatment has only barely modified the initial stoichiometric ratio between Sn and Bi, which are homogeneously mixed in a micrometric scale.

The electrochemical behaviour of this material toward Mg was therefore tested. On the top of the Figure 73 the first cycle of the GCPL at the current rate of C/100 is shown. During the discharge it is possible to distinguish two plateaus, the first one at 0.20 V, with some slight oscillations, and the second one, steadier, at 0.16 V (cf. derivative curve on Inset). According to the potential of each alloying reaction between the single elements and Mg (cf. 1 and 3.3.1), it is possible to ascribe the first and the second plateaus to the magnesianation of Bi and Sn, respectively. Bi particles almost completely react with Mg (1.25 Mg moles per mole of Bi) but Sn is surprisingly active, with more than 1 mole reacted per mole of Mg. Therefore the obtained specific capacity is 383 mAh g⁻¹, which is about 30% lower than the theoretic value of 573 mAh g⁻¹. Nevertheless, *ex situ* XRD collected after the first discharge clearly evidences the presence of Mg₃Bi₂ and Mg₂Sn, confirming the magnesianation of both active elements. The following charge features less well-defined electrochemical processes. However, one can still observe the de-magnesianation of Mg₂Sn occurring in the first part, between 0.26 and 0.30 V, followed by that of Mg₃Bi₂, at 0.35 V. Unfortunately, both reactions are only partial, since a significant irreversible capacity of 36% is observed. (Figure 73, bottom).

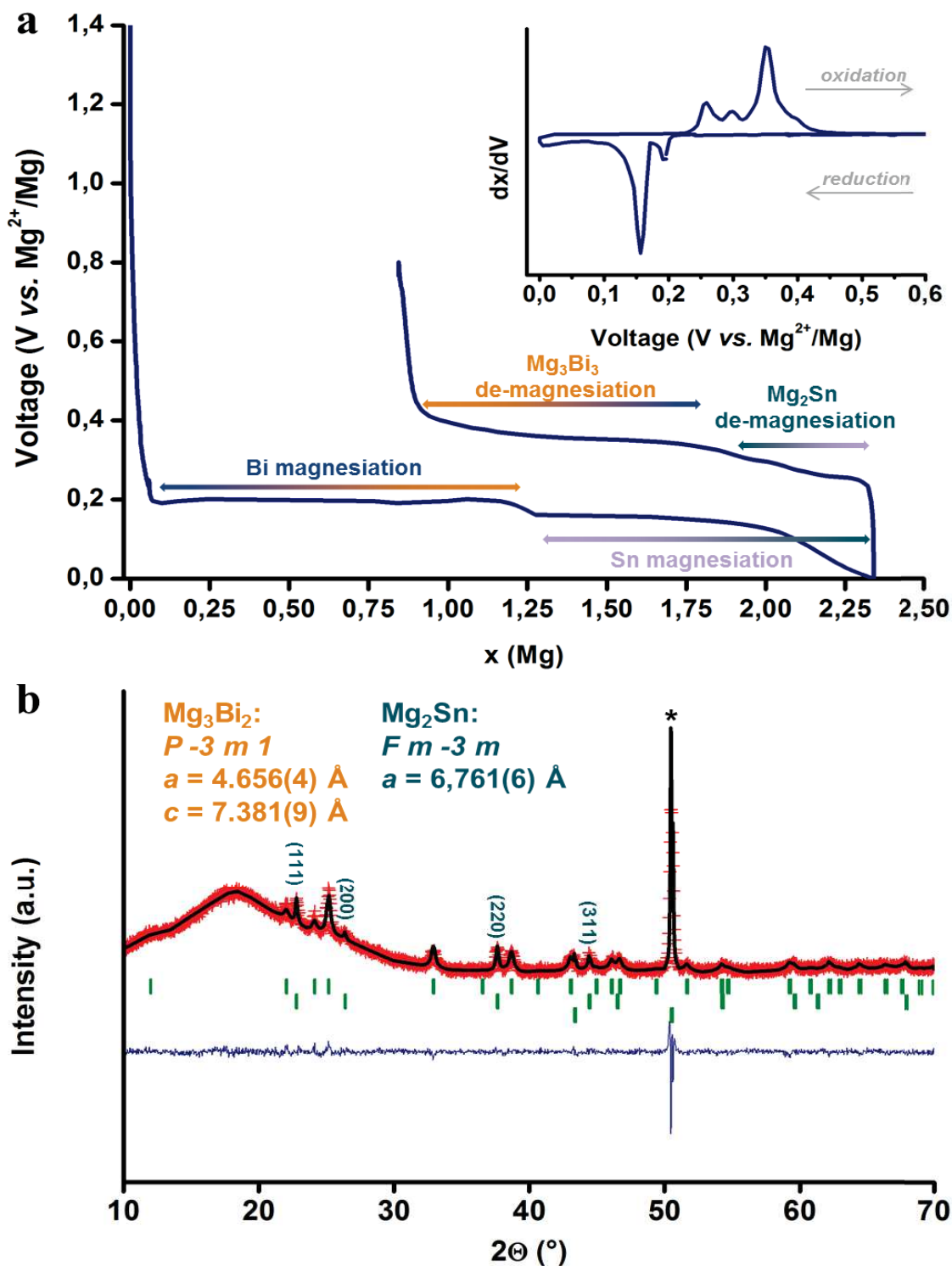


Figure 73 – a: GCPL at C/100 on micrometric Sn-Bi electrode. Unlike pure Sn-based electrodes, the intimate mix of Sn and Bi has a positive influence on Sn, which becomes electrochemical active. However, during the following charge, a dramatic capacity loss is observed, due to incomplete de-magnesianation of both Mg_2Sn and Mg_3Bi_2 ; b: *ex situ* XRD collected after first discharge shows the formation of both Mg_3Bi_2 and Mg_2Sn , thus confirming the activity of Sn toward Mg. Red crosses, black line and green strokes represent observed XRD points, interpolation and peak positions; blue line represents the difference between the observed values and the fit.

The capacity loss of each electrochemical process is reported in Table 16.

	Mg alloyed (x)	Mg de-alloyed from corresponding magnesiated composition (x)	% of capacity loss
Bi	1.12	0.89	20%
Sn	1.06	0.45	58%

Table 16 – Moles of Mg electrochemically alloyed and de-alloyed per mole of Bi and Sn, respectively. The electrochemical process involving Sn appears less reversible than these of Bi.

Even though a high capacity loss is observed at the end of the first cycle, the interesting result is that the electrochemical magnesian micrometric Sn, albeit partial, is achieved. This enhanced activity of Sn toward Mg, compared to pure Sn electrodes having the same morphology, is very likely due to the simultaneous presence of Bi. Despite the absence of any chemical interaction between the two active elements, the intimate mix created by mechanical milling seems to promote the access of Mg to the micrometric particles of Sn, perhaps by limiting the tendency of Sn to coalesce. However a part of Sn is still inaccessible and the complete magnesian is not obtained. The capacity loss observed during the following charge could be also explained by the agglomeration of Sn: de-magnesian of Mg_2Sn may in fact lead to the formation of fresh Sn that recover the particles of Mg_2Sn , limiting further de-magnesian. This hypothesis is also in line with the increase of irreversible capacity exhibited by the reaction of Bi *vs.* Mg for Sn-Bi electrodes, compared to pure Bi ones. The latter, in fact, showed excellent capacity retention and almost complete de-magnesian (cf. 3.3.1). In this case, the agglomeration of Sn formed during the first part of the charge process could partially hinder the further de-magnesian of Mg_3Bi_2 particles, thus explaining the relatively high capacity loss in the case of Bi.

4.1.1. Operando XRD

To better clarify these hypotheses, the electrochemical magnesian of the $Sn_{50}Bi_{50}$ electrode was also investigated by *operando* XRD (Figure 74). As the discharge process progresses, the intensity of the Bi pattern decreases (main peak at 27.2°), whilst its magnesian counterpart, Mg_3Bi_2 , is forming (main peak at 25.0°). As in the case of the pure Bi-based electrode, a biphasic process without the apparition of any amorphous phase is observed.

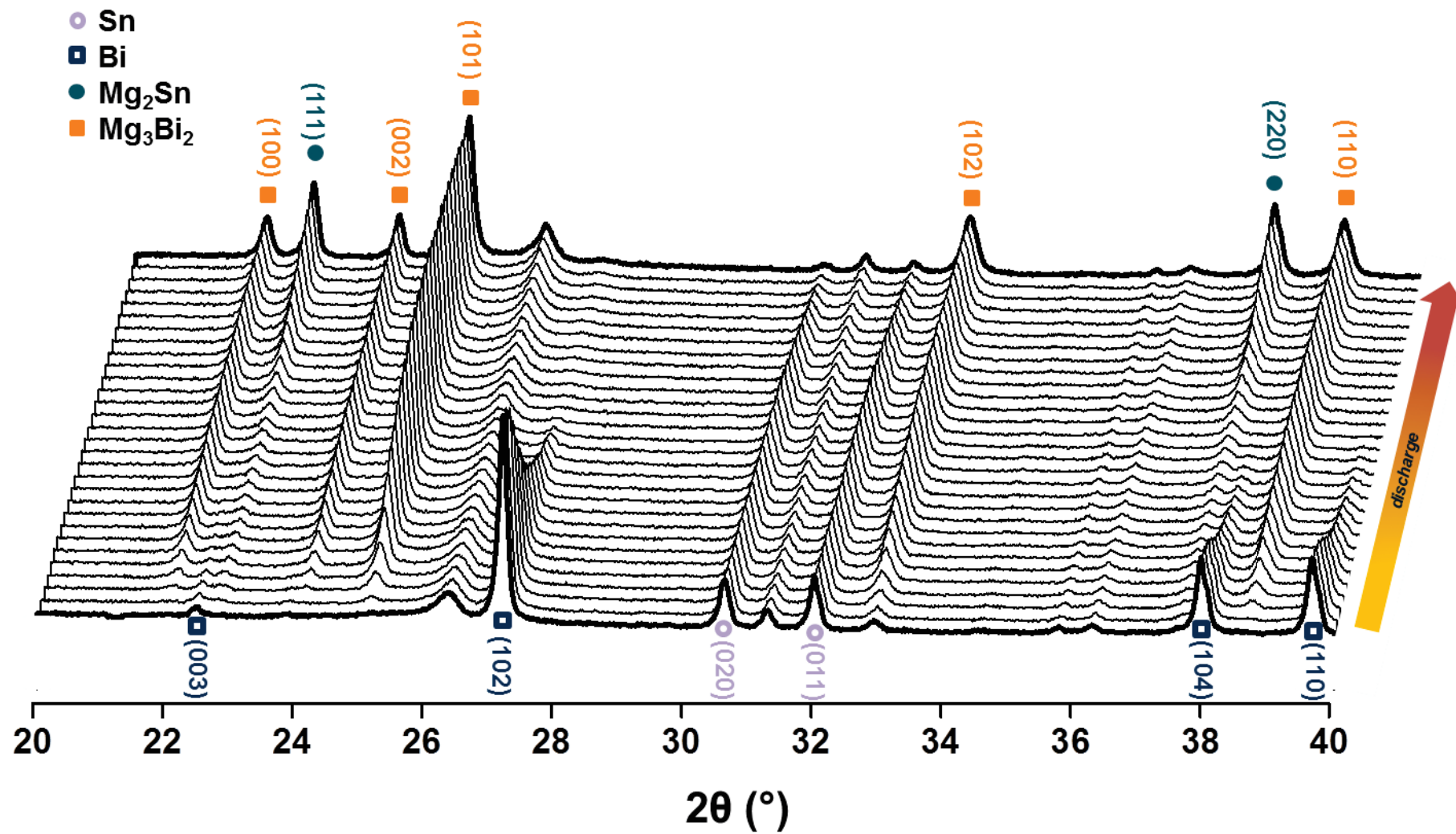


Figure 74 – Operando XRD study following the electrochemical magnesianation of the micrometric Sn₅₀Bi₅₀-based electrode at the C-rate of C/100.

At a first glance, the magnesianation of Sn takes place mainly in the second part on the discharging process, with the formation of the well-crystallized cubic phase Mg_2Sn (22.7° the main peak). Also in this case it is possible to observe a biphasic process. However, in agreement with the GCPL test, the reaction is not complete, since the main peaks of Sn (30.7 and 32.1°) are still present at the end of the discharge. A deeper insight into the pattern evolution shows that main peak of Mg_2Sn is already visible at the early stages of the discharge, even if it starts growing only after the magnesianation of Bi. The presence of both alloying reactions at the same stage of the discharge could explain the fluctuations on the first plateau that is visible in the GCPL (Figure 73 – top). Unfortunately, it was not possible to study the following charge process, due to the failure of the electrochemical cell, likely caused by the non-optimized condition of the self-supported electrode formulation.

4.1.2. Performance evaluation of different Sn-Bi mixtures

In order to better understand the mutual influence of Bi and Sn activity toward Mg, two additional Sn-Bi mixtures with different molar ratios were prepared, *i.e.* nominally $\text{Sn}_{30}\text{Bi}_{70}$ and $\text{Sn}_{70}\text{Bi}_{30}$. Since Sn has the tendency to stick to the walls of the jar during ball-milling, it is possible to obtain powders with Sn-Bi molar ratio different from the nominal one. Flame atomic absorption spectroscopy (FAAS - Figure 75)⁸ was employed in order to check the Sn-Bi ratio in each composite material. The results are shown in Figure 75 and resumed in Table 17. It is worth mentioning that the sum of the relative percentage of Sn and Bi in the 3 composites is not exactly 100%. This is likely due to a not perfect linearity of the points used for both calibration curves and even slight differences on the line's slope can be origin sensible shift on the obtained concentration values. However, they are close to the theoretical ones, and the small difference has a minor impact on the following discussion about the cycling performance of the 3 Sn-Bi mixtures.

⁸ FAAS analyses were performed on an iCE 3300 AAS Atomic Absorption Spectrometer (Thermo Fisher Scientific) equipped with both Bi and Sn lamps. Two distinct calibration curves were realized for Sn and Bi, respectively. Standard sample were prepared as follow: 1 mole of pure element was solved in 30 ml of concentrated HCL and distilled water was added until having a 1M solution. Such solution was subsequently diluted in distilled water in order to prepare 4 samples at decreasing concentration. Table 17 summarizes the corresponding concentrations in mg L^{-1} . The analyzed samples were prepared following the same protocol, starting from the ball-milled powders. Atomic absorption spectroscopy allows measuring the concentration of a given element by measuring the absorbance of a sample when it is irradiated by the wavelength of the investigated element. This is possible using the Beer-Lambert equation, given in the rearranged formula: $A = \epsilon bC$, where A is the absorbance measured by the instrument, ϵ is the molar attenuation coefficient, b is the optic path of the electromagnetic radiation and C is the concentration of the species.

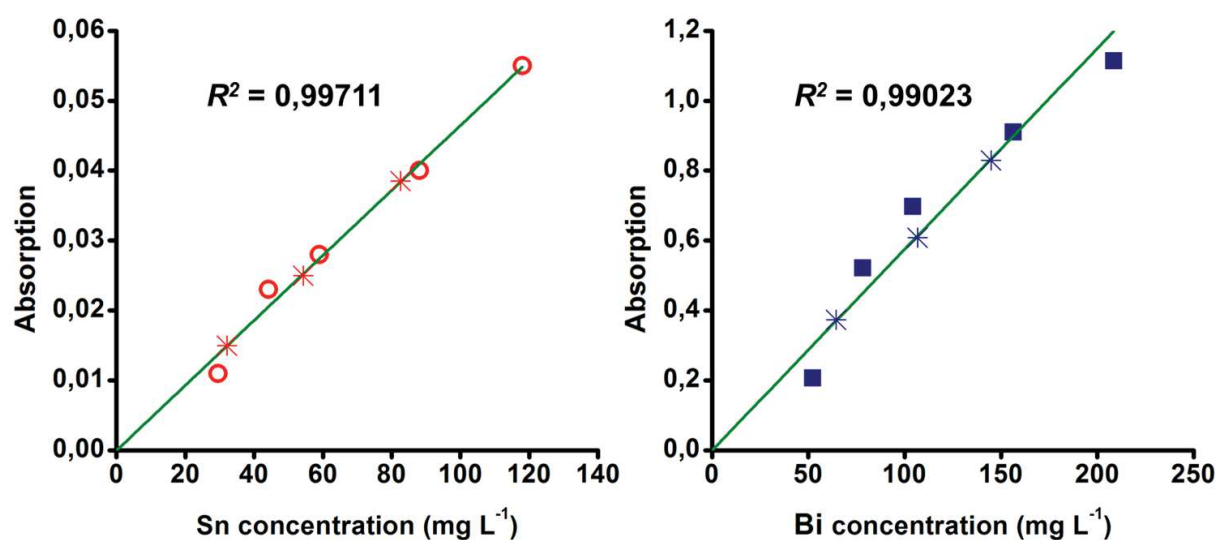


Figure 75 – Calibration lines for both Sn (left) and Bi (right) reference samples, respectively red circles and blue squares. Once the absorbance of a sample is measured, it is possible to retrieve its concentration by using the corresponding calibration line. Red and blue stars represent the concentrations of Sn and Bi, respectively, in the 3 composite materials synthesized by high-energy ball-milling.

	[Sn]from the calibration curve (mg L ⁻¹)	% Sn	%Sn (EDX)	[Bi] from the calibration curve (mg L ⁻¹)	% Bi	%Bi (EDX)
Sn₃₀Bi₇₀	32.2	27	31	144.9	69	69
Sn₅₀Bi₅₀	54.3	46	52	106.7	51	48
Sn₇₀Bi₃₀	82.6	70	74	64.4	31	26

Table 17 – Summary of the obtained concentration for both Sn and Bi, by the respective measures of FAAS and the approximate amount of each element for the 3 synthesized compositions. For comparison, EDX elemental mapping values were also provided. All the percentages are atomic ratios.

The electrochemical properties of each composite material were further evaluated with GCPL tests. The difference in the Sn-Bi ratio influences the theoretical specific capacity and hence the corresponding C/n current ratio is necessarily different. In this case, in order to obtain more comparable results, it was chosen to set the same current density value for all the tested materials, *i.e.* 0.05 mA cm⁻², which correspond to a C/10 for the Sn₅₀Bi₅₀.

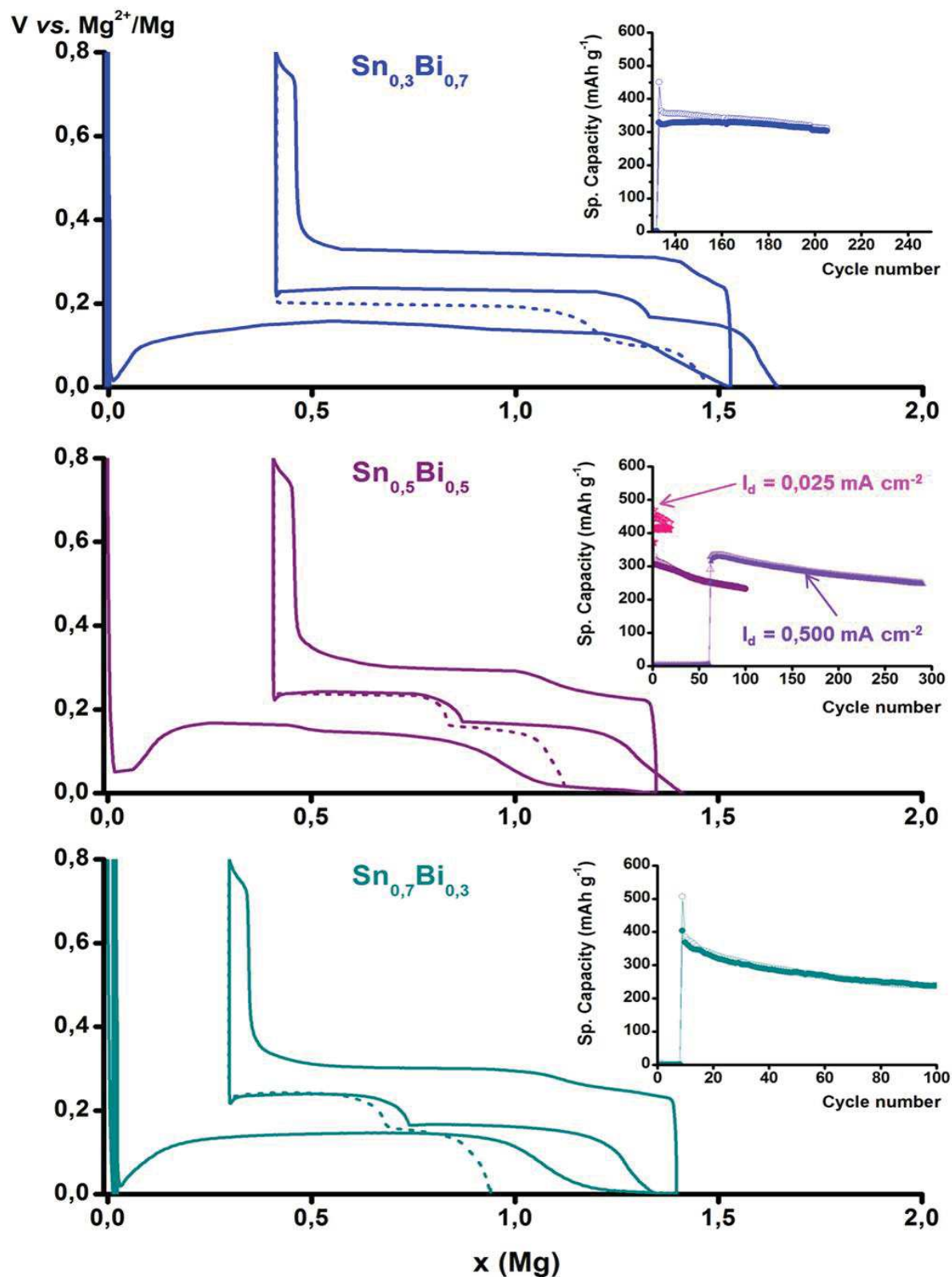


Figure 76 – Comparison between the first active cycle and the following discharge of $\text{Sn}_{30}\text{Bi}_{70}$, $\text{Sn}_{50}\text{Bi}_{50}$ and $\text{Sn}_{70}\text{Bi}_{30}$, cycled at the same current density of 0.05 mA cm^{-2} . For each composition, the 100th discharge is shown with a dashed line. Each inset gathers the capacity evolution during cycling. Hollow symbols: discharge capacity; solid symbols: charge capacity. NB: For the composition $\text{Sn}_{50}\text{Bi}_{50}$ are also reported the capacity evolution for two other cells, tested at C/20 and C, respectively.

During the first discharge a major difference between the Sn₅₀Bi₅₀ and the other two compositions can be noticed. Indeed Sn₅₀Bi₅₀, after the characteristic potential drop, rapidly reaches the first alloying plateau, whereas the other two compositions stabilize their potential less rapidly. These activation cycles are however randomly observed, regardless of the composition and the starting material and therefore should not be considered as a specific feature of one or another Sn-Bi mixture. More noteworthy is that both Sn₃₀Bi₇₀ and Sn₇₀Bi₃₀ did not exhibit two well-distinct alloying plateaus, unlike Sn₅₀Bi₅₀. Different specific capacity values are provided by the three compositions and are resumed in the Table 18, where they are compared with the theoretical ones:

Active material	Discharge. specific capacity (mAh g⁻¹)	Theoretical specific capacity (mAh g⁻¹)	% Capacity loss
Sn₃₀Bi₇₀	450	516	13%
Sn₅₀Bi₅₀	441	573	23%
Sn₇₀Bi₃₀	515	644	20%

Table 18- Comparison between theoretical and effective specific capacity after the first discharge for all the tested Sn-Bi ratios and corresponding percentage of capacity loss.

The Bi-richest phase should provide the lower specific capacity, considering the high atomic weight of Bi. However, the observed capacities are not linearly correlated to the Sn amount. Indeed, although the presence of Bi influences the electrochemical reactivity of Sn toward Mg, its activity is only partial.

For all studied compositions, well-defined plateaus are visible during the first charge. The first de-alloying reaction (de-magnesiumation of Mg₂Sn) occurs at the same potential in all the samples, with a sloppy plateau between 0.23 and 0.29 V. Is it worth noting that Mg-removal from Mg₂Sn is not proportional for the three samples. Separate alloying processes are clearly evidenced in the second discharge of all samples. The homogeneous mixture of Sn and Bi phases provided by the mechanical milling seems lost after the first magnesiumation. Interestingly, even Sn and Bi domains are well distinct, the electrochemical activity of Sn toward Mg is still present. However, the specific capacity dramatically decreases after the first cycle in all the three samples.

A longer-term performance evaluation was also realized for all the systems (cf. Insets in Figure 76) $\text{Sn}_{30}\text{Bi}_{70}$ exhibits the most important difference between discharge and charge process. While the former continuously decreases, the latter remains very stable around 320 mAh g^{-1} . This is probably due to the growing difficulty of magnesiating Sn, which tends to aggregate and becomes less and less accessible. However, the overall capacity of the cell cannot be ascribed only to the electrochemical activity of Bi, since even at the 100th cycle (dashed line), reversible Sn alloying/de-alloying plateaus are still visible and the capacity loss is about 23% of the initial practical capacity.

On the other hand, $\text{Sn}_{70}\text{Bi}_{30}$ shows more similar capacity fading both in discharge and charge, with the exception of the first 10 cycles where the two are significantly different. The cell capacity is globally reduced during the first 30 cycles, and remains almost constant on the following cycles. Even if in this case Sn is still partially active after 100 cycles, it underwent a capacity fading of 66%.

The system $\text{Sn}_{50}\text{Bi}_{50}$ shows similar behaviour with respect to the previous sample, but with better capacity retention during the first 15 cycles. The comparison between the second and the 100th discharge shows that only 44% of Sn is still electrochemically active.

Two additional cells equipped with $\text{Sn}_{50}\text{Bi}_{50}$ electrode were tested at different current densities, i.e. 0.025 mA g^{-1} and 0.5 mA g^{-1} (corresponding to C/20 and C, respectively). In the first cell the specific capacity during discharge constantly decreases, while that of charge remains constant around 415 mAh g^{-1} . This value is 12% higher than pure micrometric Bi-based electrode tested at the same current rate. The second cell, tested at C rate exhibits lower specific capacity values than the C/20, but slightly higher compared to the C/10, with a less pronounced capacity fading, for more than 300 cycles. Such high current density might kinetically limit Sn agglomeration, which is targeted to limit the reversible reaction on both Sn and Bi particles.

Although a progressive fading of the electrochemical performance was observed for all the tested composition, it is worth underlying that in all the cases the presence of Bi played a crucial role on the electrochemical activity of Sn toward Mg, bearing in mind that pure micrometric Sn-based electrodes are almost inert to electrochemical magnesiation (cf. 1). To understand how far Bi can have a positive influence on Sn, a composite containing 95% of Sn and 5% of Bi (atomic ratio) was prepared by ball-

milling. The GCPL test on this material is presented in the Figure 77. For the sake of clarity, only selected cycles are shown:

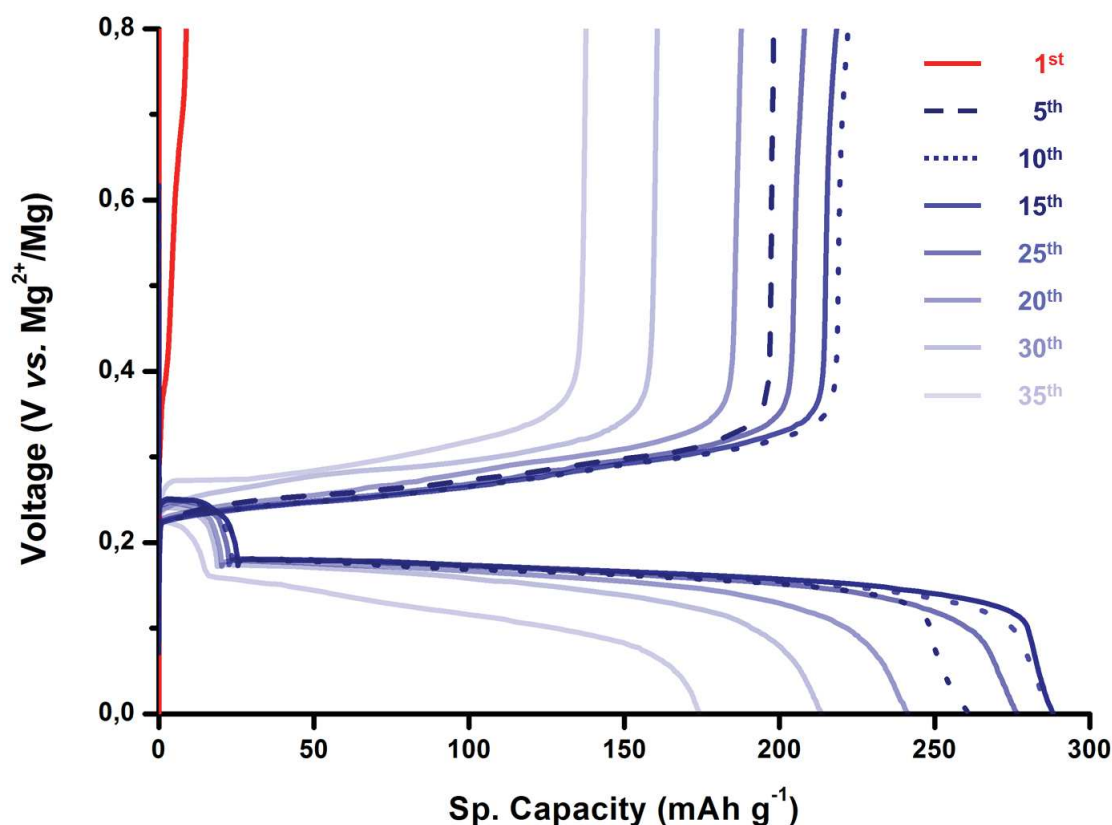


Figure 77 – Even at very low loadings (5 at.%) Bi is able to activate Sn toward reversible magnesiation. The electrode material undergoes progressive activation and reaches the maximum capacity of 288 mAh g⁻¹ at the 10th cycle, corresponding to the 32% of the theoretical value. After the 15th cycle a rapid capacity fading is observed, with a decrease of both alloying reactions. Moreover, an increased polarization between Sn-Mg alloying and de-alloying process can be noticed. The cell completely fails when Bi becomes inactive.

Even though no electrochemical reaction is observed during the very first cycle (red line), the material gradually activates toward magnesiation, in spite of the high Sn content and reaches the maximum of its capacity at the 10th cycle. As already observed for the other previously presented Sn-Bi compositions, two distinct plateaus are visible. This observation confirms that the presence of Bi, even in small amounts, has an impact on the electrochemical activity of Sn, which is dramatically enhanced compared to the pure Sn-based electrodes. Unfortunately, after the 15th cycle, a capacity fading is observed with an increased polarization of the alloying/de-alloying reaction of Sn with Mg. Moreover, it is possible to see a progressive depletion of the alloying plateau of Bi, which is gradually trapped by Sn and becomes inaccessible. Curiously, the cell suddenly fails when the Bi alloying plateau completely disappears.

In conclusion a partial synergy between Sn and Bi was demonstrated. Although the phase diagram shows neither binary phases nor solid solutions, intimate mixtures were realized *via* high-energy ball-milling of the two elements and electrochemically tested *vs.* Mg. Surprisingly, for all the tested compositions, both Bi and Sn undergo reversible magnesiation with two separated biphasic process. Moreover, Bi seems having a crucial role on the activation of Sn, even at very low concentrations. The partial replacement of Bi with a lighter and cheaper element (Sn) should provide more interesting specific capacities but, in fact, the poor cycling performance of Sn resulted in rapid capacity fading. Therefore, Sn-Bi mixtures do not allow real improvements of the performance provided by pure micrometric Bi-based electrodes.

4.2. $\text{Bi}_x\text{Sb}_{1-x}$

Bismuth and antimony belong to the same chemical group of pnictogens. They are isostructural and form a solid-solution in the whole range of compositions, as shown in the phase diagram reported in Figure 78.

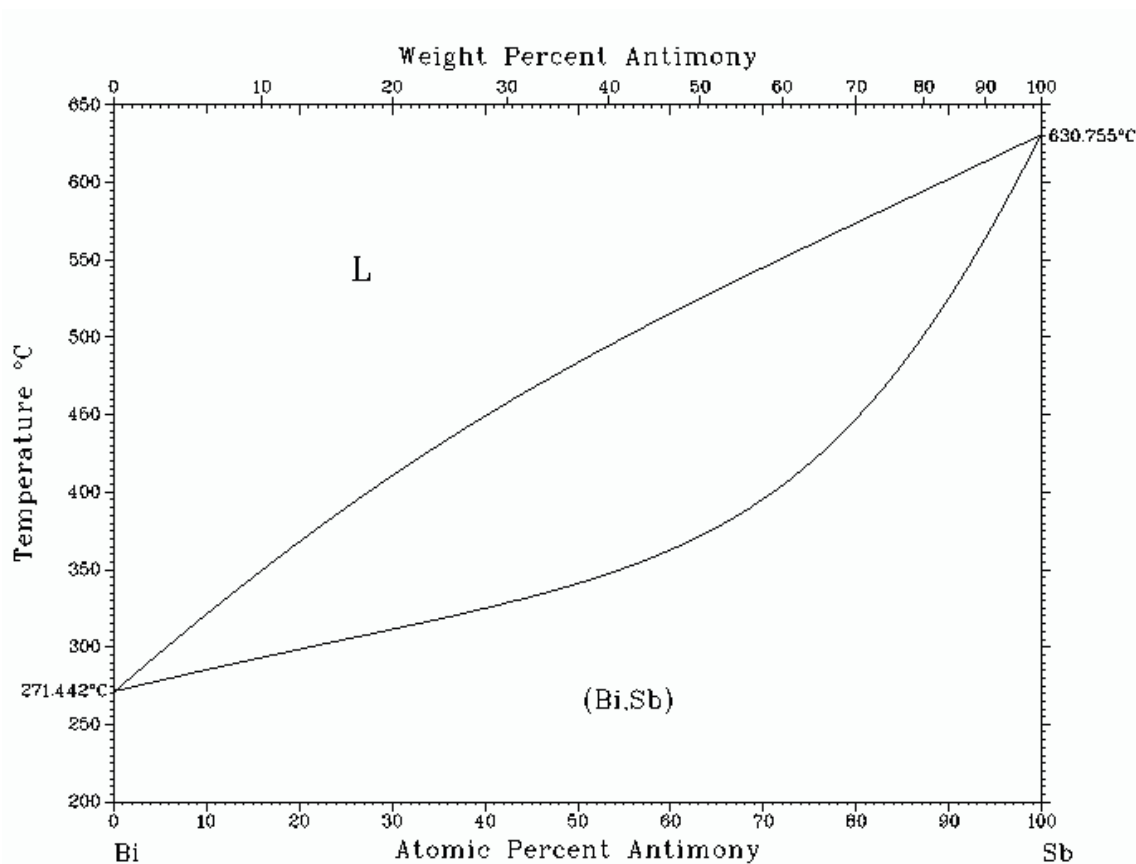


Figure 78 – Bi – Sb phase diagram evidences complete miscibility on the whole range of composition (Reproduction from [200]).

This particular feature was exploited for the realization of Bi-Sb single crystals of several compositions showing superior thermoelectric properties.[201][202][203] However the synthesis of such materials, for instance by recrystallization[204] or travelling heater method (THM)[205], is extremely time consuming (crystal growth of 4 mm/day). Therefore, alternative techniques were employed, such as mechanical alloying that generates solid solutions in the microcrystalline form.[206][207] Nevertheless, besides the structural similarities between Bi and Sb, their electrochemical properties *vs.* magnesium are inexplicably different. In order to study this phenomenon, several $\text{Bi}_x\text{Sb}_{1-x}$ compositions were prepared by high-energy ball-milling, i.e. $\text{Bi}_{0.3}\text{Sb}_{0.7}$, $\text{Bi}_{0.5}\text{Sb}_{0.5}$ and $\text{Bi}_{0.7}\text{Sb}_{0.3}$.

The XRD pattern for each composition is presented in Figure 79. They can all be indexed in the hexagonal R-3m space group. The evolution of refined cell parameters clearly follows a linear trend, as expected in a solid solution (Vegard's law) and as already observed by Cucka and Barrett.[208] This result enables to claim that the Bi/Sb nominal ratio is preserved during the mechanical alloying.

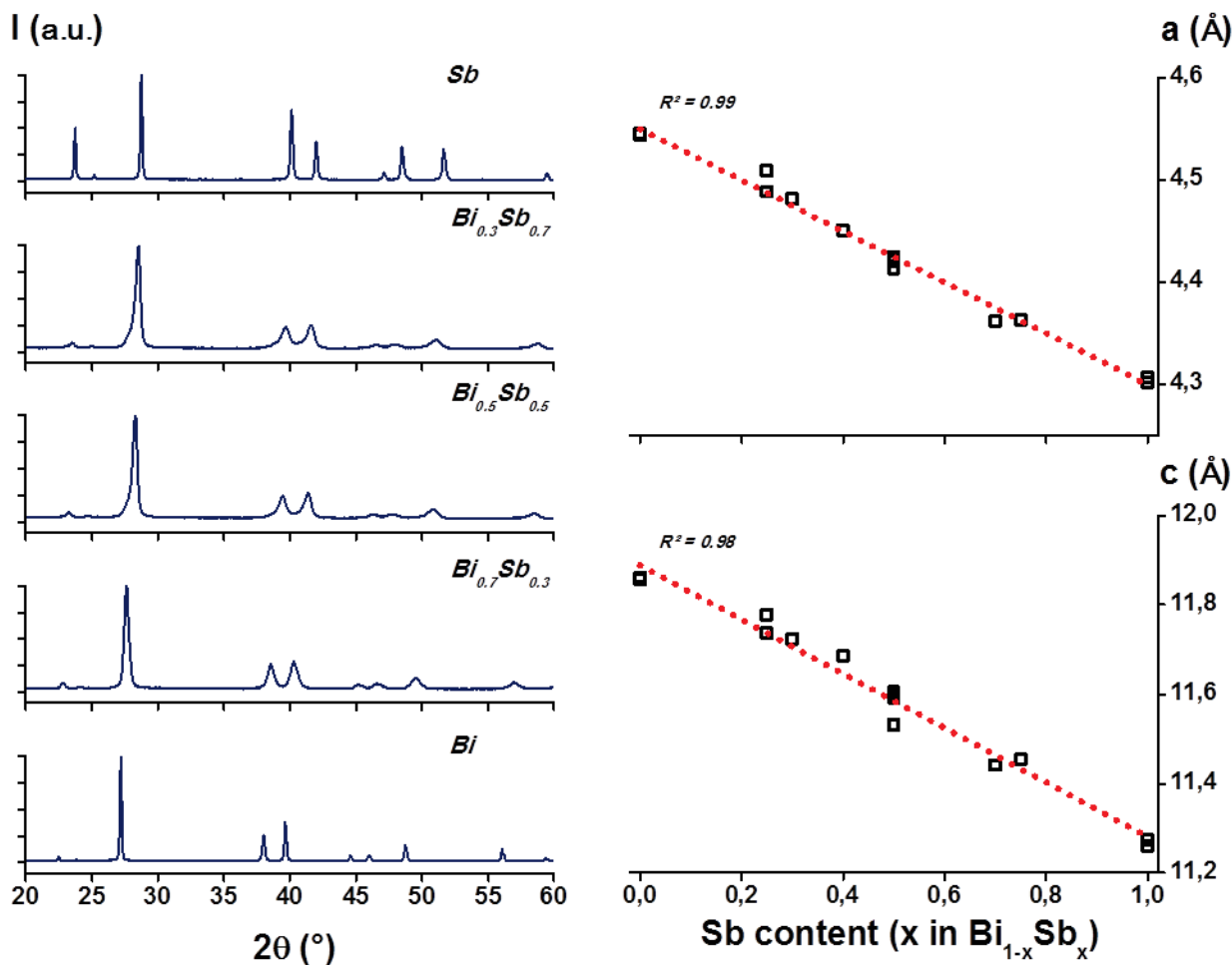


Figure 79 – Left: XRD pattern of several Bi_xSb_{1-x} solid solutions, showing the progressive shift of the peaks toward higher 2θ values; right: the variation of the lattice parameters can be related to the Sb content in the solid solution, according to Vegard's law.

The electrochemical behaviour of the electrodes was then examined; for the sake of clarity, discharge and charge profiles are compared separately in Figure 80:

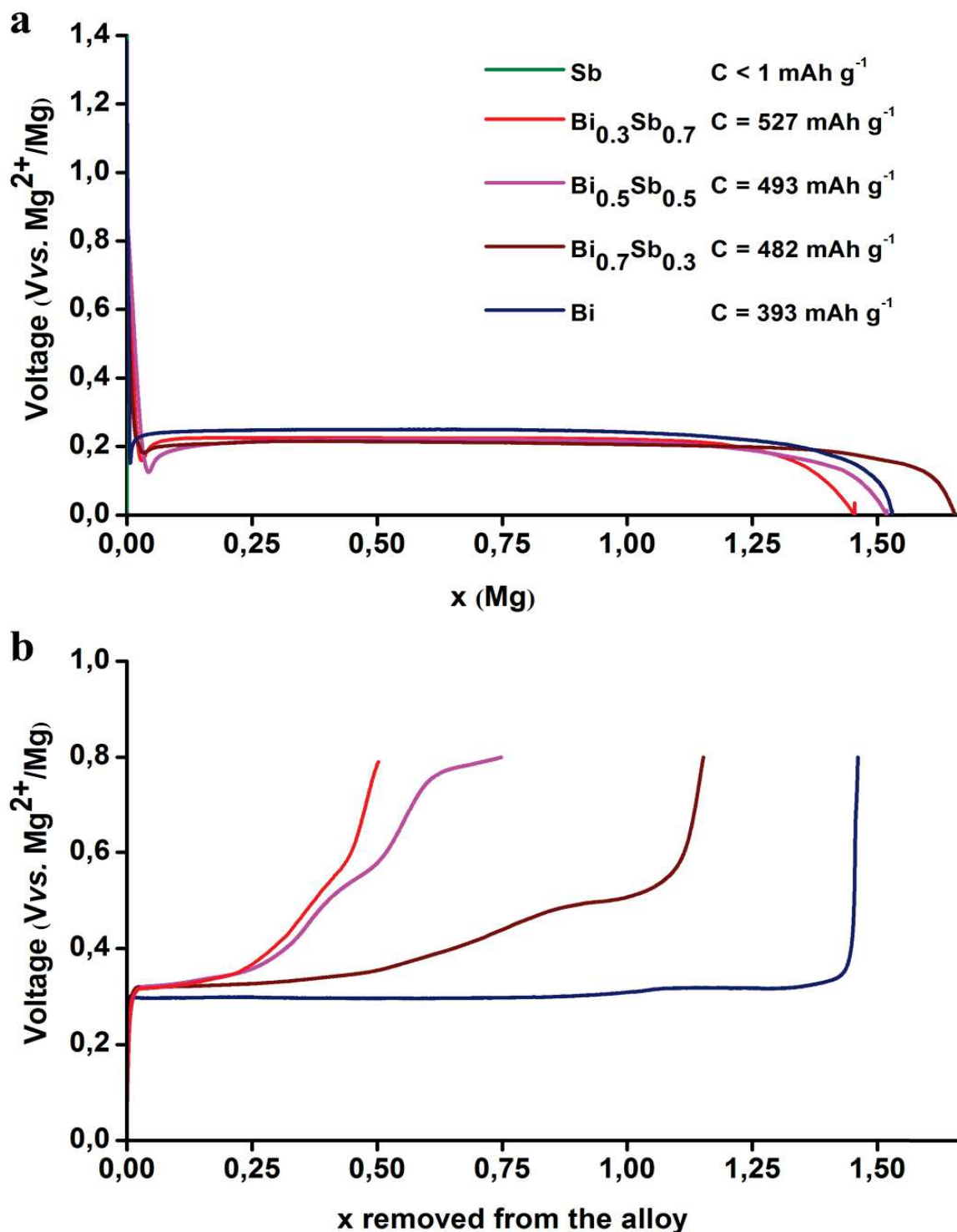


Figure 80 – a: Comparison between the first discharge of each chosen composition in the $\text{Bi}_x\text{Sb}_{1-x}$ solid solution. All samples exhibit a single alloying plateau and achieve almost complete magnesiation (1.5 moles of Mg per mole of $\text{Bi}_x\text{Sb}_{1-x}$). b: First charge for each active materials evidence a capacity fading proportional to the Sb amount. NB Unlike the results presented for Sn-Bi composites, where a single current density value was chosen, the herein presented compositions were cycled at the same current rate, which depends on the molar mass of each sample.

Analysing the discharge profiles it is worth noting that the maximum quantity of Mg (1.5 Mg moles per Bi mole) was electrochemically inserted regardless of the composition of the solid solution. Therefore, the highest specific capacity was achieved with the Sb-richest compound, $\text{Bi}_{0.3}\text{Sb}_{0.7}$ (527 mA g^{-1}). All alloying reactions occur almost at the same potential of 0.2 V, slightly lower than pure Bi, with flat plateaus. Although $\text{Bi}_{0.7}\text{Sb}_{0.3}$ exceeds the theoretical capacity (most probably because of an error in the measure of the active mass) this comparison shows that the presence of Bi plays a key role in the successful magnesiation of Sb, which is completely hampered in pure Sb-based electrodes.

Curiously, the observed discharge profiles are significantly different from those reported by Arthur *et al.*, who worked with electrodeposited $\text{Bi}_x\text{Sb}_{1-x}$. In that case, two well-distinct plateaus were reported, which suggests that their active material was not monophasic.[147]

Further de-magnesiation is more complex and appears strongly dependent on the Bi content in the active materials. Indeed, the capacity retention during the first charge decreases on increasing the Sb content. This observation suggests that separate and independent Mg_3Bi_2 and Mg_3Sb_2 domains are probably formed during the first discharge, and the synergy between Bi and Sb that allowed the activity of both elements in the Mg-alloying process is lost. As already discuss by Arthur and co-workers, the greater bond strength caused by the higher ionicity of the Mg-Sb bond in Mg_3Sb_2 compared to other pnictogenides such as Mg_3Bi_2 can have a significant impact on the electrochemical extraction of Mg^{2+} .[147] In order to verify these hypotheses and better understand the electrochemical mechanism of the BiSb-based electrode, an *operando* XRD study was performed on the intermediate composition $\text{Bi}_{0.5}\text{Sb}_{0.5}$ (Figure 81).

During discharge $\text{Bi}_{0.5}\text{Sb}_{0.5}$ reacts electrochemically with Mg, and its main peak (27.9°) rapidly decreases. The formation of a new phase can be noticed by the growth of a new peak at 25.2° , which should correspond to the formation of the magnesiated phase Mg_3X_2 (X = Bi, Sb).

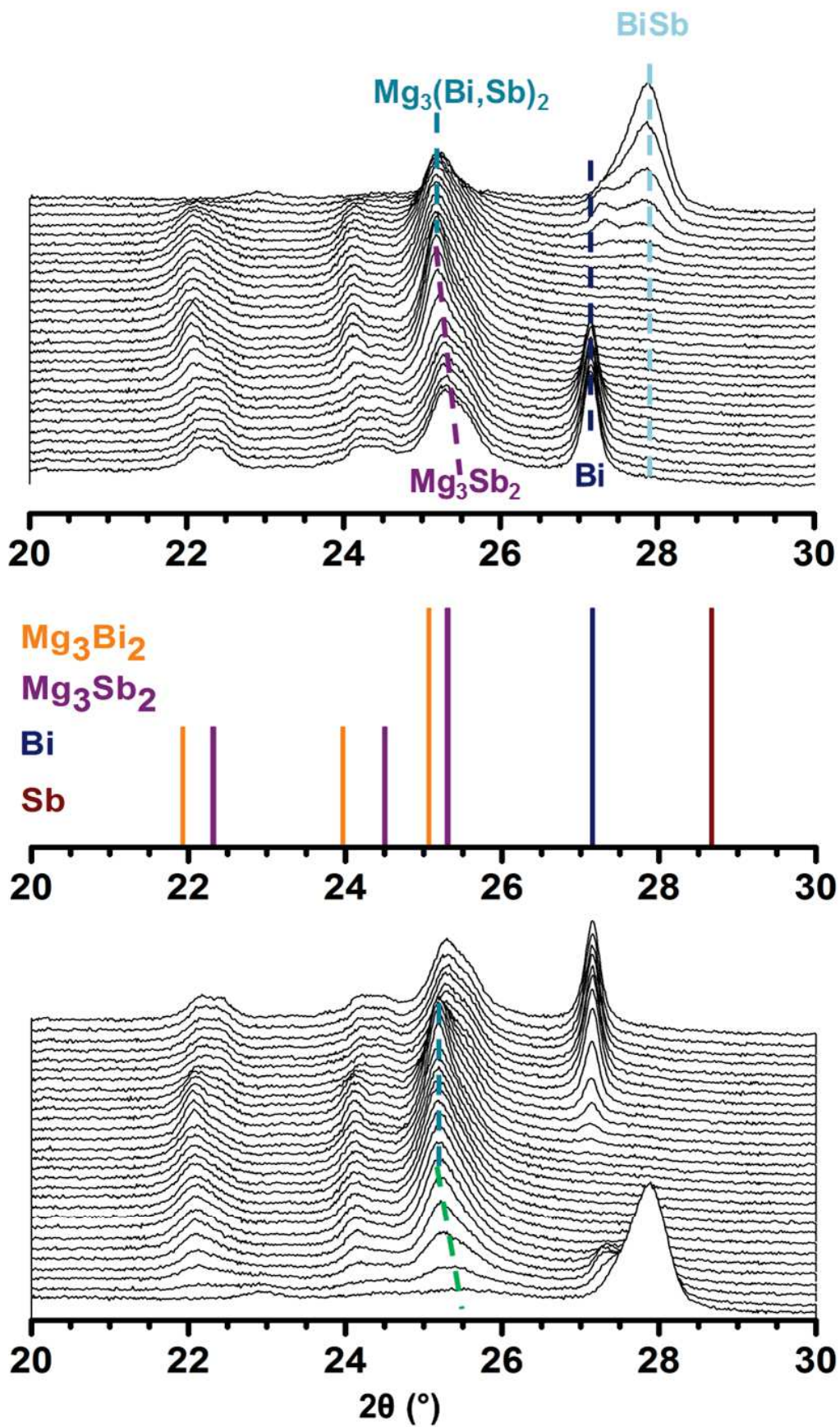


Figure 81 –Magnesiation (discharge) and subsequent de-magnesiation (charge) of a micrometric BiSb-based electrode followed by *operando* XRD.

At this stage it is worth mentioning that the magnesiated references Mg_3Sb_2 and Mg_3BiSb were both prepared via high-energy ball-milling. Their XRD patterns are shown in Figure 82. Both phases are isostructural with Mg_3Bi_2 but, their cell parameters are very similar, much closer than those of their corresponding non-magnesiated counterparts, thus making more difficult the analysis of the *operando* study.

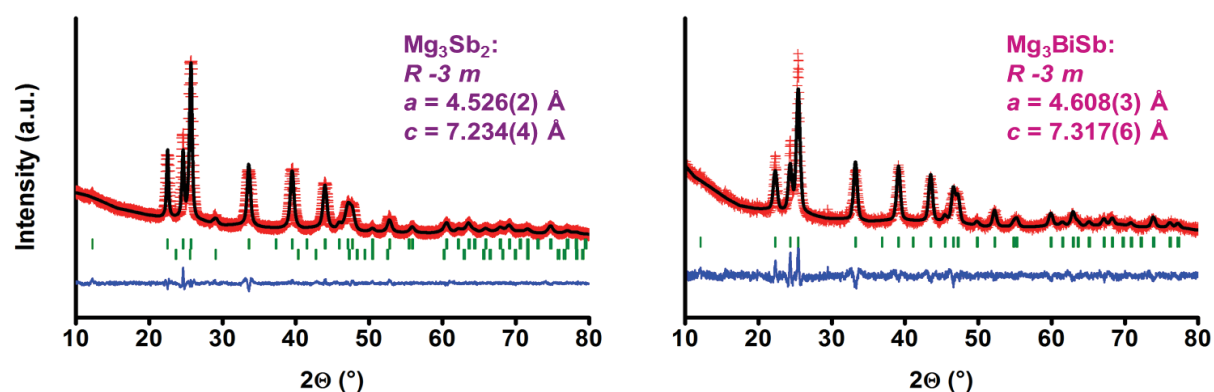
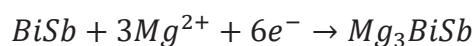


Figure 82 – XRD patterns of Mg_3Sb_2 (left) and Mg_3BiSb (right). Both structures belong to the same space group of Mg_3Bi_2 ($a = 4.655(2)$; $c = 7.394(4)$) and cell parameters are extremely close. Red crosses, black line and green strokes represent observed XRD points, interpolation and peak positions; blue line represents the difference between the observed values and the fit.

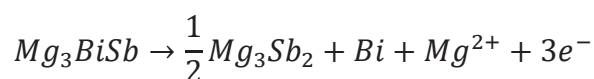
By comparing the *operando* spectra with those of the reference compounds and in particular with that of Mg_3BiSb , the peak at 25.2° might account for the formation of Mg_3BiSb . However, the patterns obtained during the *operando* study and those of the reference compounds have a quite different signal-to-noise ratio, and from the quality of the *operando* spectra an unambiguous attribution of this peak to the formation of the ternary compound Mg_3BiSb cannot be unequivocally confirmed. The formation of such ternary magnesiated phase nevertheless, is still the most probable interpretation of the *operando* patterns, and can be summarized by the following equation:



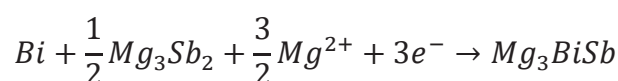
Despite the absence of any noticeable oscillation in the electrochemical profile, the formation of such a ternary phase is not straightforward. In the very early stages of the magnesiation its position of its corresponding 101 peak is slightly shifted to the right before reaching the value of 25.2° . This could be explained by assuming that Sb is preferentially magnesiated at the very beginning of the discharge, thus creating a crystallographic phase more similar to Mg_3Sb_2 . This hypothesis agrees with the

analysis of the 102 peak of BiSb that is rapidly flanked to a shoulder on its left while decreasing (Top). This result suggests that not only BiSb reacts with Mg but also that its composition shifts toward a Bi-rich solid solution.

The beginning of the following charge occurs with no major changes in the peak positions. However, as the charge proceeds, the main peak of Mg_3BiSb starts shifting to higher angles, thus toward the binary phase Mg_3Sb_2 . At the same time, a sharp peak at 27.2° starts growing. This position is not compatible with the reformation of BiSb but is undoubtedly attributed to the formation of pure crystalline Bi. Both evidences lead to conclude that the de-magnesian occurs with segregation between Bi and Sb and that electrochemical driving force is not able to de-magnesian Mg_3Sb_2 , according to the following equation:



The *operando* cell setup and the long time needed for this study (with all the consequences of rapid aging, electrolyte degradation, etc.) did not allow following the second discharge. Nevertheless, an *ex situ* XRD pattern collected at the end of the second discharge evidences again the presence of a single-phase, with diffraction peaks attributed to the ternary phase Mg_3BiSb . This result is surprising, since the presence of Mg_3Sb_2 and Bi at the end of the discharge let one suppose the formation of two distinct magnesian phases: Mg_3Sb_2 and Mg_3Bi_2 . Actually, the mechanism seems to proceed *via* a gradual enrichment in Bi of the already present Mg_3Sb_2 phase, along the electrochemical magnesian:



Thank to this *operando* experiment it is thus possible to confirm the important difference between the electrochemical performance of Bi and Sb, mostly due to the difficulty to electrochemically remove Mg from Mg_3Sb_2 .

4.3. InBi

In seeking for possible synergistic effects that allows reducing the weight of the active material and keeping high cycling performance, it was thought to combine the excellent electrochemical properties of Bi with the lightness and the low alloying potential of In (cf. o). Unlike the materials previously studied, In and Bi can form

several stable alloys at room temperature, as it possible to observe from the binary phase diagram (Figure 83):

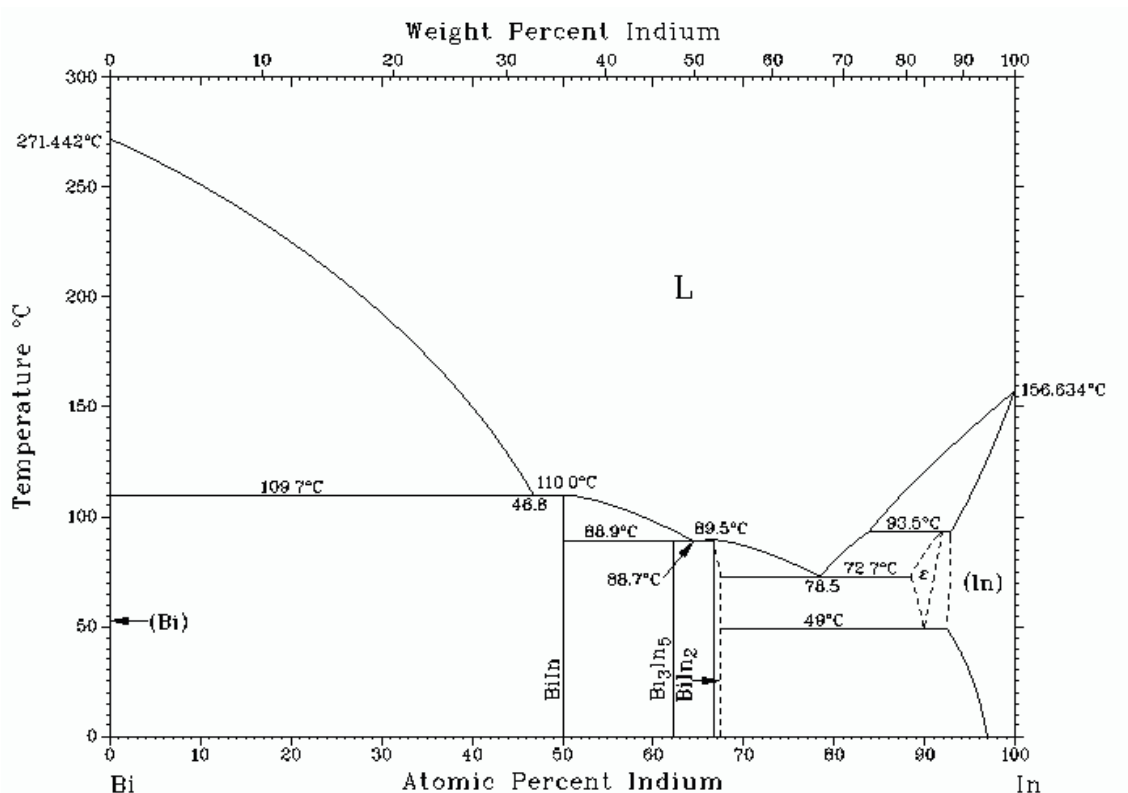


Figure 83 – Bi-In binary phase diagram (Reproduction from [198]).

It was thus tried to synthesize all the 3 stable binary composition, (InBi, In₅Bi₃ and In₂Bi), using protocols similar to those already adopted for the preparation of other intermetallic compounds, i.e. high-energy ball-milling, starting from appropriate amounts of reacting powders. However, XRD analyses on the obtained products reveal that, regardless of the starting amount of reactants, InBi was always the only crystalline phase formed. Therefore, it was decided to start the study from the intermetallic 1:1 molar compound, InBi.

According to the literature, InBi is usually obtained *via* high-temperature melting under inert atmosphere and, to the best of our knowledge, it was never synthesized by high-energy ball-milling.[209][210][211][212] In our synthesis, a stoichiometric amount of pure In and Bi powders were milled for 5 hours, obtaining a homogeneous powder. XRD pattern collected on the product evidences the formation of a tetragonal phase corresponding to the intermetallic compound InBi with crystallographic parameters in agreement with the literature (Figure 84).[199]

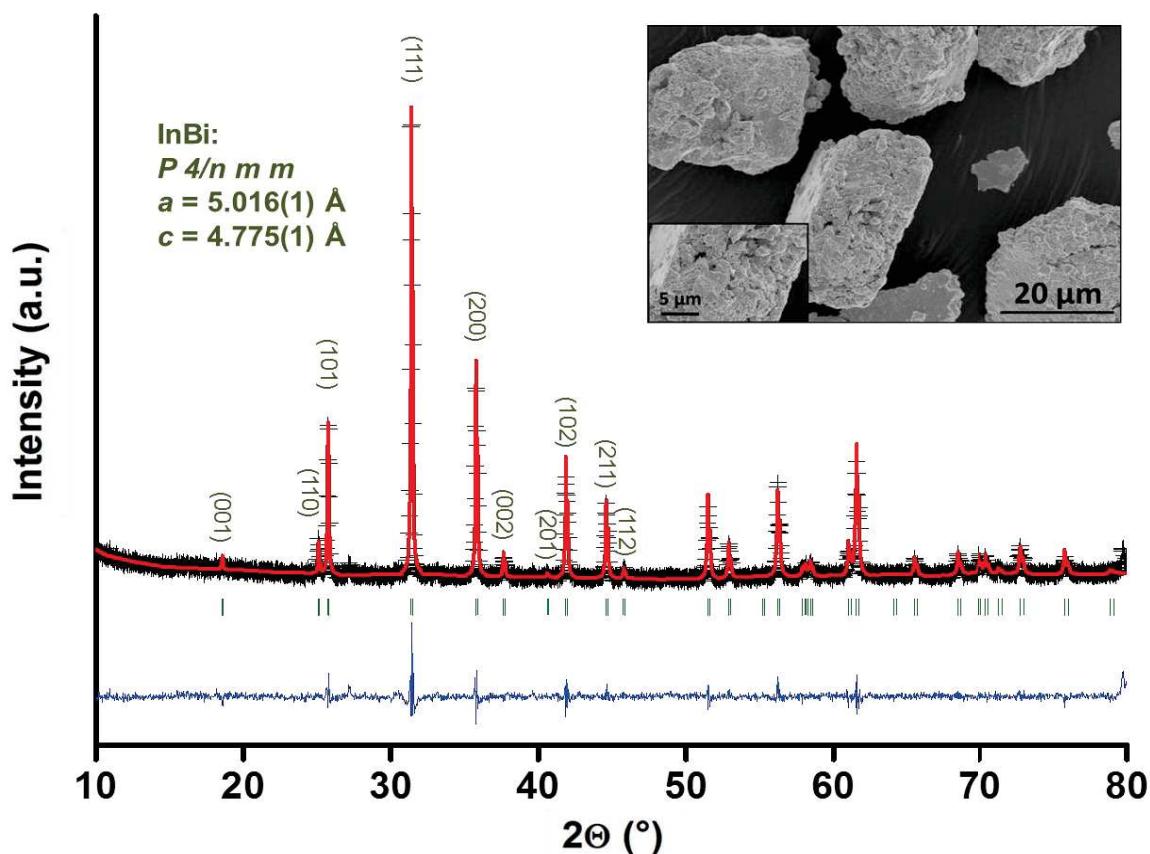


Figure 84 – XRD pattern of the powder obtained by high-energy ball-milling of a 1:1 In – Bi molar mixture. Full profile matching evidences the formation of a single crystallographic phase. Space group and cell parameters confirm the formation of InBi. Black crosses, red line and green strokes represent observed XRD points, interpolation and peak positions; blue line represents the difference between the observed values and the fit. Inset: SEM images on the InBi powder, which is formed by micrometric grains, formed by the aggregation of smaller particles. (Adapted from [213]).

From one synthesis to another, the presence of very minor residual amount of tetragonal In could be detected. SEM images at different magnifications confirm that the InBi powder consists on large aggregates (20-50 μm) of sub-micrometric particles. Electrode formulation ensures the homogeneous embedding of the micrometric active particles in a matrix formed by carbon black and the polymeric binder. The mechanochemical synthesis of InBi was hence firstly reported by our group in 2016.[213]

4.3.1. Electrochemical mechanism

The first 1.5 cycle of a InBi / Mg battery at a constant C/100 rate is presented in Figure 85. Up to 2.5 Mg per InBi react during the electrochemical reduction down to 0 V in perfect agreement with the theoretical formation of Mg₃Bi₂ and MgIn.

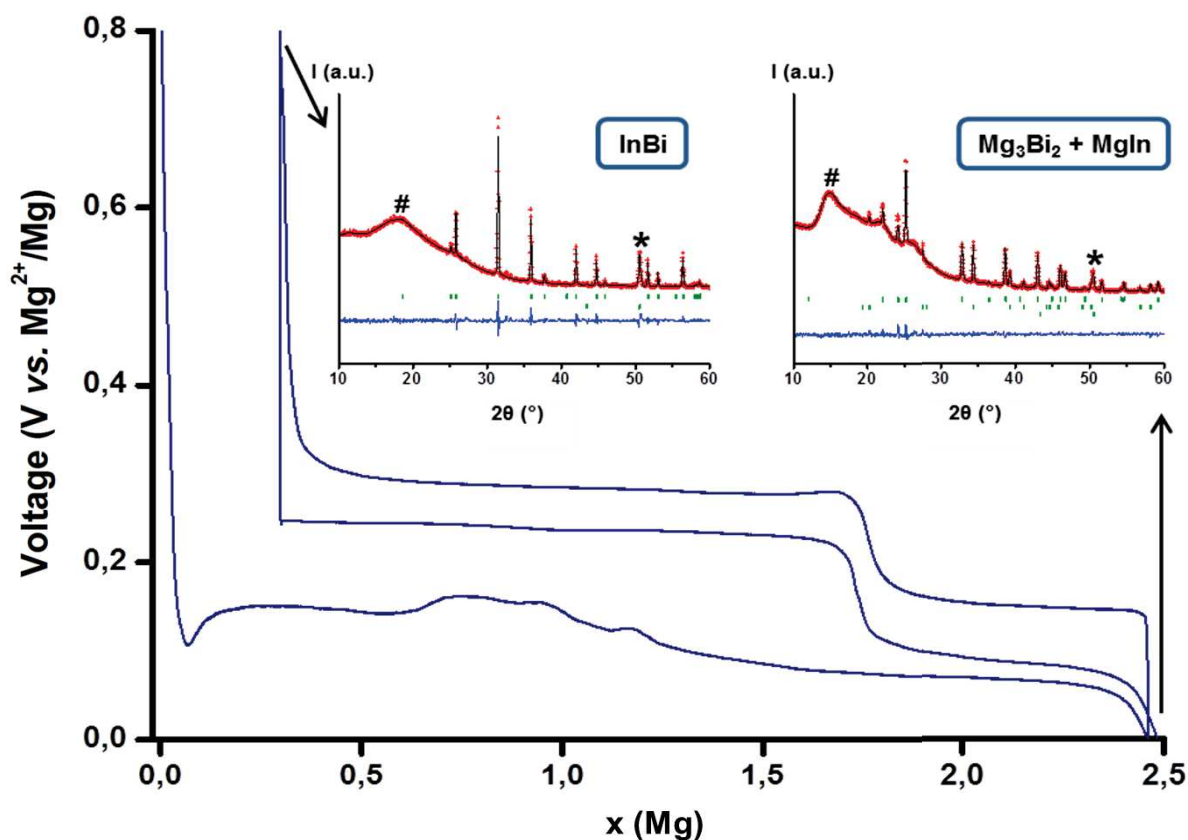
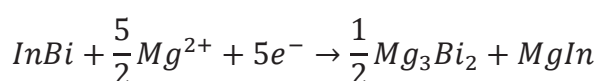


Figure 85 –GCPL analysis of micrometric InBi-based electrode gathering the first 1.5 cycle. *Ex situ* XRD performed after the first discharge confirms the formation of both magnesiated In and Bi phases. The following charge shows two well-distinct plateaus, at 0.18 V and 0.22 V, which should account for the de-magnesiation of In bi and Mg_3Bi_2 , respectively. This evidence let one think that at the end of the charge, In and Bi will be present in two separate phases. Surprisingly, *ex situ* XRD collected after the first charge shows the re-formation of the starting binary phases, InBi. During the following discharge, unlike the first one, InBi reacts via two well-distinct plateaus; the peaks marked with # are due to the polymeric binder present in the electrode formulation, whilst * are due to the Cu supporting foil (Adapted from[213]).

Ex situ XRD patterns collected at the end of the discharge confirm the formation of the two alloys. As in our previous works on Bi or In-based electrodes, they are highly-crystallized with refined cell parameters in agreement with the literature (P-3m1: $a = 4.655(1) \text{ \AA} - c = 7.390(1) \text{ \AA}$ for Mg_3Bi_2 , and P4/mmm: $a = 4.585(1) \text{ \AA} - c = 4.387(1) \text{ \AA}$ for MgIn). The combined formation of Mg_3Bi_2 and MgIn alloys is in agreement with the electrochemical behaviour of the pure elements presented in the previous chapter (cf. 3.3.1 and 3.4) and can be summarized as follows:



However, the profile of the first discharge is not a simple plateau, but exhibits a complex evolution. The early stage is characterized by significant fluctuations of the

potential. These oscillations are reproducible from one experiment to another and are maybe caused by parasite interactions at the electrode-electrolyte interface (*i.e.*, successive formation and breakdowns of unidentified solid-electrolyte interphases). Taking this into account, two principal regions can be distinguished: from 0 to 1.3 Mg, where these fluctuations are observed, and from 1.3 to 2.5 reacted Mg, where a rather flat plateau follows. According to the electrochemical tests performed on the single elements (cf. 3.3.1 and 0), Bi alloys with Mg at higher potential than In. Therefore, the alloying region below 1.3 Mg occurring at an average potential of 0.15 V should be linked to the formation of Mg_3Bi_2 , whereas the second plateau at a lower average potential around 0.09 V would correspond to the reaction of In.

The first charge shows better defined electrochemical phenomena, with two well-distinct and very flat plateaus at 0.16 and 0.29 V. Considering the de-alloying potential values of Mg_3Bi_2 and MgIn , the lowest plateau can be attributed to MgIn de-alloying, whereas the second one concerns Mg_3Bi_2 de-alloying.

The *ex situ* XRD patterns collected at the end of the charge surprisingly reveal the presence of a single major tetragonal phase with refined cell parameters that can be attributed to tetragonal InBi , even if weak variations of the cell parameters are noticed ($a = 5.002(1) \text{ \AA}$, $c = 4.769(1) \text{ \AA}$). Instead of a final coexistence of In and Bi, which was somehow expected based on the charge profile, the electrochemical driving force seems to involve a solid-state reaction leading to the reformation of the intermetallic InBi .

The voltage profile of the second discharge also exhibits two well-defined magnesiation plateaus, around 0.25 and 0.1 V, confirming the completely reversible character of the mechanism. The difference between the first and the second discharge might be attributed to a modification of the morphology of InBi . Indeed, it is known that the electrochemical reaction induces a complete disaggregation of the initial micrometric grains of active materials, which is usually reformed as particles of smaller size at the end of the first electrochemical cycle.[36]

As already seen for other studied materials, a detailed *operando* XRD study on a InBi self-supported electrode was carried out. Figure 86 gathers the XRD patterns collected during a first cycle at C/100.

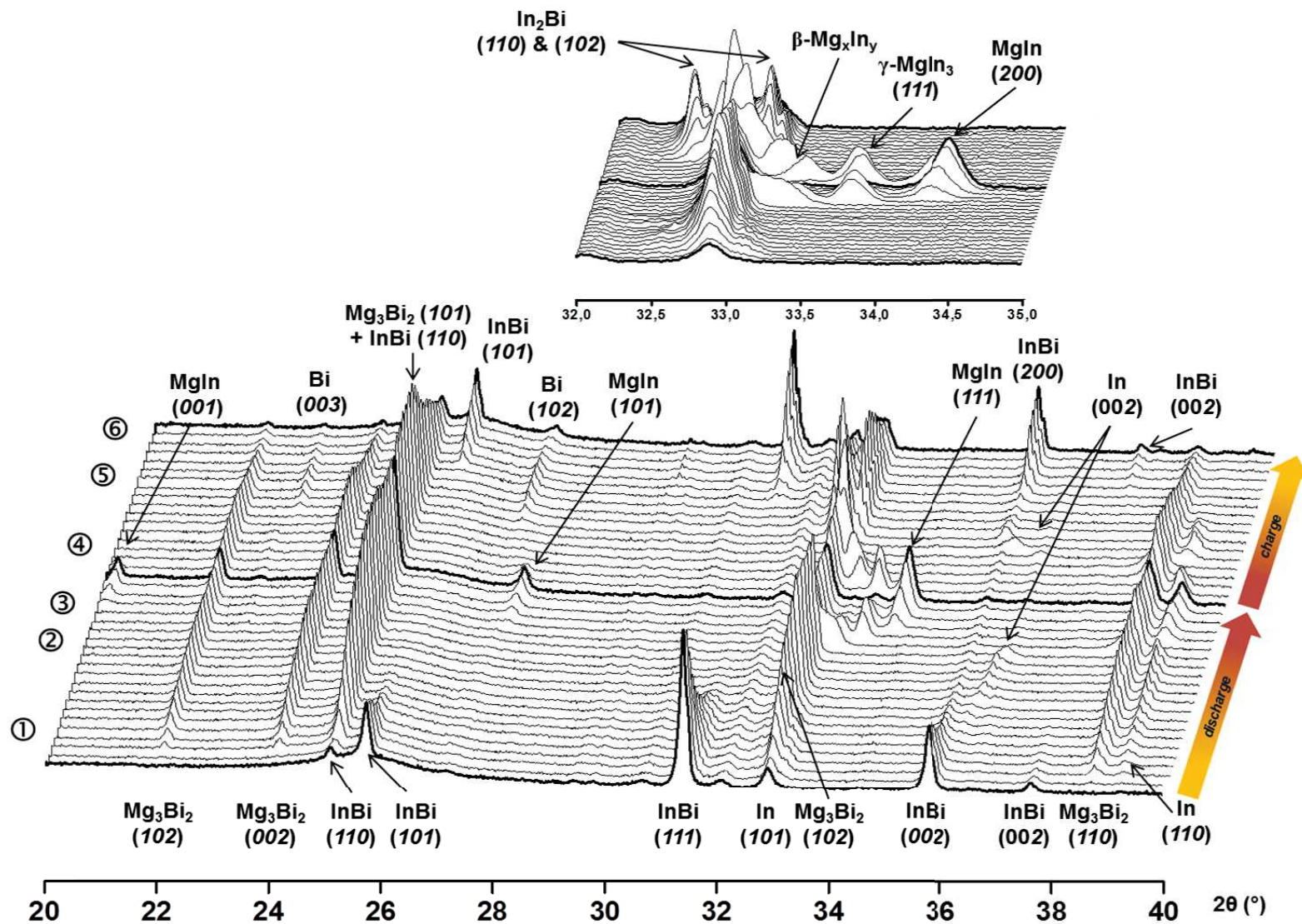
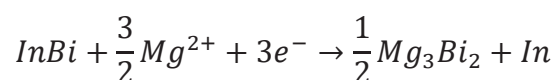


Figure 86 – Reversible magnesiation of a micrometric InBi-based electrode followed by *operando* XRD. Inset right: zoom on the In magnesiation zone; inset left: binary phase diagram of Mg-In (Adapted from [213]).

The analysis of the complicate phase evolution is discussed in the following points:

1. The early moments of the electrochemical reaction show a regular decrease of the InBi pattern, combined with a progressive increase of new diffraction peaks especially at 24.1° and 25.1°, which are characteristics of Mg₃Bi₂ and therefore confirms the magnesianation of Bi before that to In. Simultaneously, other diffraction peaks appear around 36.2° and 39.2°, corresponding to the formation of tetragonal In. The first step of the electrochemical reduction can be therefore summarized as follows:



It is worth noting that the main peaks of both Mg₃Bi₂ and In are located around 33°, which makes the analysis relatively complex (especially concerning pattern matching for In). In contrast, it is possible to get reliable values for the Mg₃Bi₂ cell parameters. The alloy grows with a defined composition and constant cell parameters in agreement with the Mg-Bi phase diagram and the recent literature.[189][190]

2. Around 1.5 moles of Mg reacted per mole InBi, after full consumption of the pristine InBi, there is a noteworthy change in the XRD patterns. First, the main diffraction peak around 33° significantly weakens. As the intensities of the Mg₃Bi₂ peaks at 24.1° and 25.1° remain stable, this significant decrease can be only explained by the gradual magnesianation of In metal. A slight shift of the In diffraction peak (002) around 36.2° is observed during the early moments of the In magnesianation. It should be linked to a weak decrease of the *c*-axis cell parameter. This feature might be explained by the possible weak insertion of magnesium in the lattice of indium metal. Literature data confirm that such solid solution is possible up to 5 at.% of Mg.[195]

3. The second step of In magnesianation is even more complex and deserved to be investigated in a specific enlarged view (Figure 86 - inset). The magnesianation is firstly characterized by the increase of a new broad peak around 33.2°. This peak rapidly shifts and vanishes while another peak grows at 33.7°. Its 2θ position is constant but its existence is also rather limited as it quickly disappears. Finally, at the late moments of the discharge, a third peak grows at 34.3°. At this stage of the electrochemical discharge, Mg₃Bi₂ is the main phase in the electrode and is characterized by several well-defined and distinguishable peaks. Therefore it can be used as reference for pattern matching refinements in order to estimate the *d*-spacing value corresponding to these unknown peaks and to interpret them on the basis of

the known literature on In-Mg system. Following the phase diagram nomenclature, the broad and shifting peak around 33.2° might be attributed to the main peak of the cubic β -phase Mg_xIn_y . Such broadness and shift can be explained by the large composition range of the β -phase with variations of the lattice parameters. Then, the diffraction peak at 33.7° may refer to major peak (111) of a second cubic phase, labelled γ' -phase, with a narrow chemical composition around MgIn_3 . [195][214] The final magnesiation stage corresponds to the formation of MgIn , which is clearly evidenced by XRD pattern collected at 0 V. Refined cell parameters are in line with the *ex situ* data presented above. For more clarity, the Mg-In binary phase diagram is again reported (Figure 87):

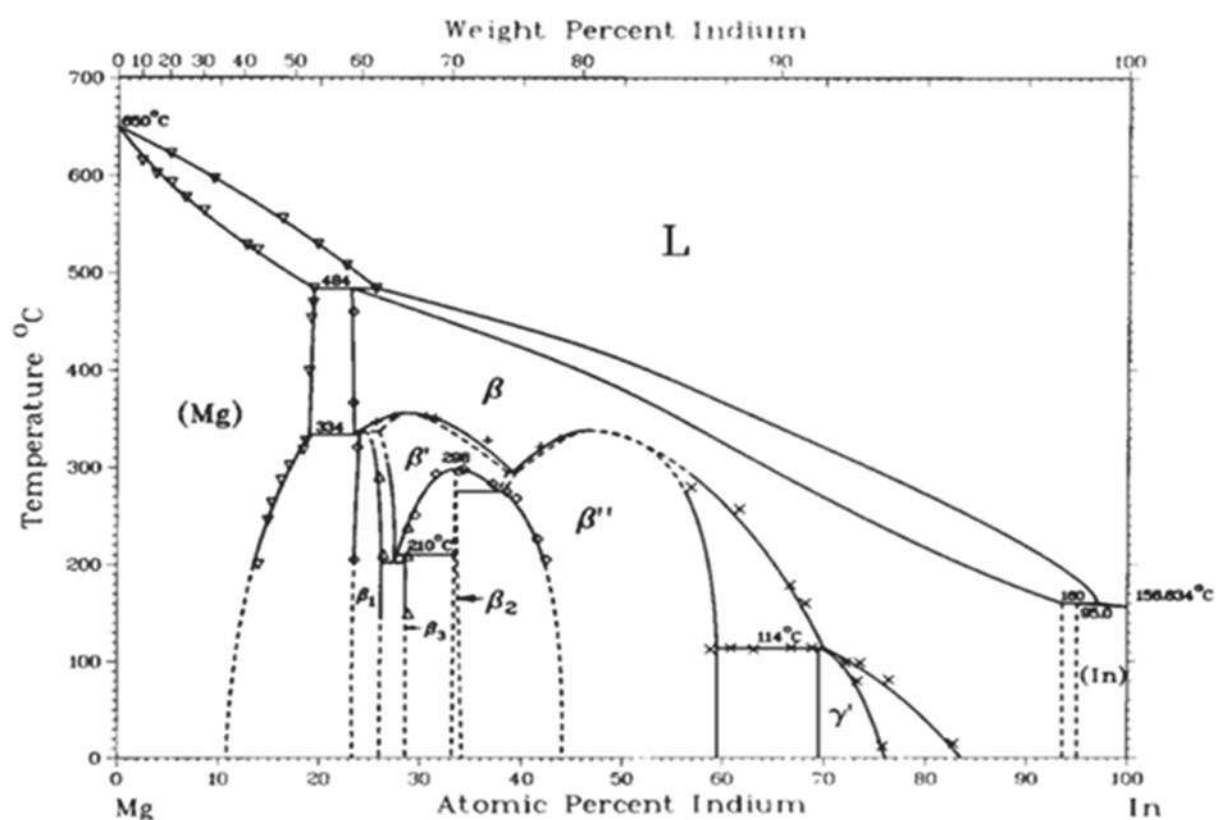


Figure 87 – Mg-In binary phase diagram is herein proposed again for the sake of clarity (Reproduction from [186]).

4. The XRD patterns collected during the first plateau in the beginning of the charge (0.16 V) show completely reversible phenomena in the $32 - 35^\circ$ 2θ range. MgIn is progressively de-magnesiated (decrease of its main peak at 34.4°) and gives place to γ' - MgIn_3 and then β - Mg_xIn_y . Similarly to the discharge, the diffraction peak of γ' - MgIn_3 does not evolve, while the broad peak β - Mg_xIn_y drastically shifts to lower angles. In parallel, there is an increase of the peak intensity around 33° , reflecting the

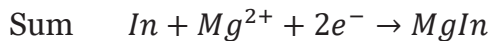
formation of de-magnesiated tetragonal indium. The very last moments of the de-magnesiumation (plateau at 0.16 V) is characterized by a significant shift of the diffraction peak at 36°. Analogous to what observed in discharge, this shift might be explained by a progressive removal of the interstitial Mg from the In metal lattice.

5. The highest voltage plateau (0.3 V) corresponds to the de-magnesiumation of Mg₃Bi₂. However, significant differences between XRD patterns collected during the discharge are observed. Obviously the diffraction peaks of Mg₃Bi₂ regularly decrease in intensity while the appearance of weak peaks at 23.0 and 27.1° is ascribed to the formation of metallic Bi traces. Surprisingly, the Bi amount remains low, and whereas two new intense diffraction peaks grow at 32.5° and 33.1°. They can be assigned to the main diffraction peaks (110) and (102) of In₂Bi, another alloy already reported in the In-Bi phase diagram.[211][215]

6. At the very end of the charge, the intermetallic compound InBi is reformed as the major product. Pattern matching refinement do not evidence any change in the cell parameters, which are those typical of the stable phase. Remaining In₂Bi, In and Mg₃Bi₂ residues might arise from uncompleted de-magnesiumation of the electrode.

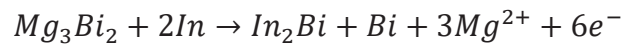
Summarising, In₂Bi and several Mg-In phases are identified as intermediate phases of the reversible magnesiumation of InBi material. The successive increase and rapid decrease of all diffraction peaks related to Mg-In intermediate phases seems to reflect a 3-step chain reaction governed by the magnesiumation rate:

1. $In + \frac{x}{y}Mg^{2+} + \frac{2x}{y}e^{-} \rightarrow \frac{1}{y}Mg_xIn_y \quad \left(\text{with } \frac{x}{y} < \frac{1}{3}\right)$
2. $\frac{1}{y}Mg_xIn_y + \left(\frac{1}{3} - \frac{x}{y}\right)Mg^{2+} + 2\left(\frac{1}{3} - \frac{x}{y}\right)e^{-} \rightarrow \frac{1}{3}MgIn_3$
3. $\frac{1}{3}MgIn_3 + \frac{2}{3}Mg^{2+} + \frac{4}{3}e^{-} \rightarrow MgIn$

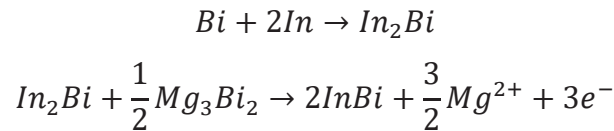


The formation of Mg-In intermediate phases is rather surprising, as they were not observed with pure In-based electrodes, which undergo simple and direct biphasic process (cf. o). The explanation might arise from the nature of the *in situ* formed In particles during InBi decomposition, which are expected to expose highly reactive surfaces. Taking a careful look onto the (002) In diffraction peak, a substantial shift to higher 2θ angles can be noticed, which corresponds to a sensible decrease of the c lattice parameter. The lower tetragonality (c/a) involves a quasi-cubic lattice that

might allow an easier formation of the first intermediate cubic β -phase Mg_xIn_y . This loss of tetragonality might be possible because of the nanosized nature of the In particles formed during magnesiation. The large composition range of the β -phase may also facilitate the formation of Mg-In intermediates. The presence of In_2Bi reflects a solid-state reaction between In and Bi resulting from Mg_3Bi_2 de-magnesiation:



However, there are only weak traces of pure Bi in all the *operando* XRD patterns. Then it might be assumed that the freshly-formed Bi is highly reactive and promptly alloys with the remaining In to form more In_2Bi , which finally reacts with Mg_3Bi_2 when no more In is available:



This last assumption is also supported by the observed decrease of In_2Bi diffraction peaks, which seems to correspond to the final growth of InBi.

It is also interesting to note that XRD patterns collected at the end of the charge present well-crystallized phases. Indeed, there is a clear difference in the shape of the diffraction peaks obtained at the beginning of the *operando* experiment: they appear sharper, so well-crystallized that contributions from copper $K_{\alpha 2}$ are distinguishable even at moderate angles. Thanks to this high crystallinity, the formation of intermediate In_2Bi can be clearly identified during the charge, whereas it was only hypothesized along the first discharge, with very weak and broad peaks around 32.5° and 33.1° .

As already observed before, the Mg_3Bi_2 de-magnesiation could have led to the simple formation of metallic Bi coexisting with metallic In previously formed. However, chemical reactions occur between In and Bi, leading to the reformation of InBi. This type of alloying process has been recently reported with nanocrystalline SnSb[216] and is directly induced by the starting crystallographic organization with chemically-bonded active elements. This effect can be demonstrated by cycling a reference electrode made up with a simple stoichiometric mixture of In and Bi powders as active materials instead of a ball-milled intermetallic InBi (Figure 88).

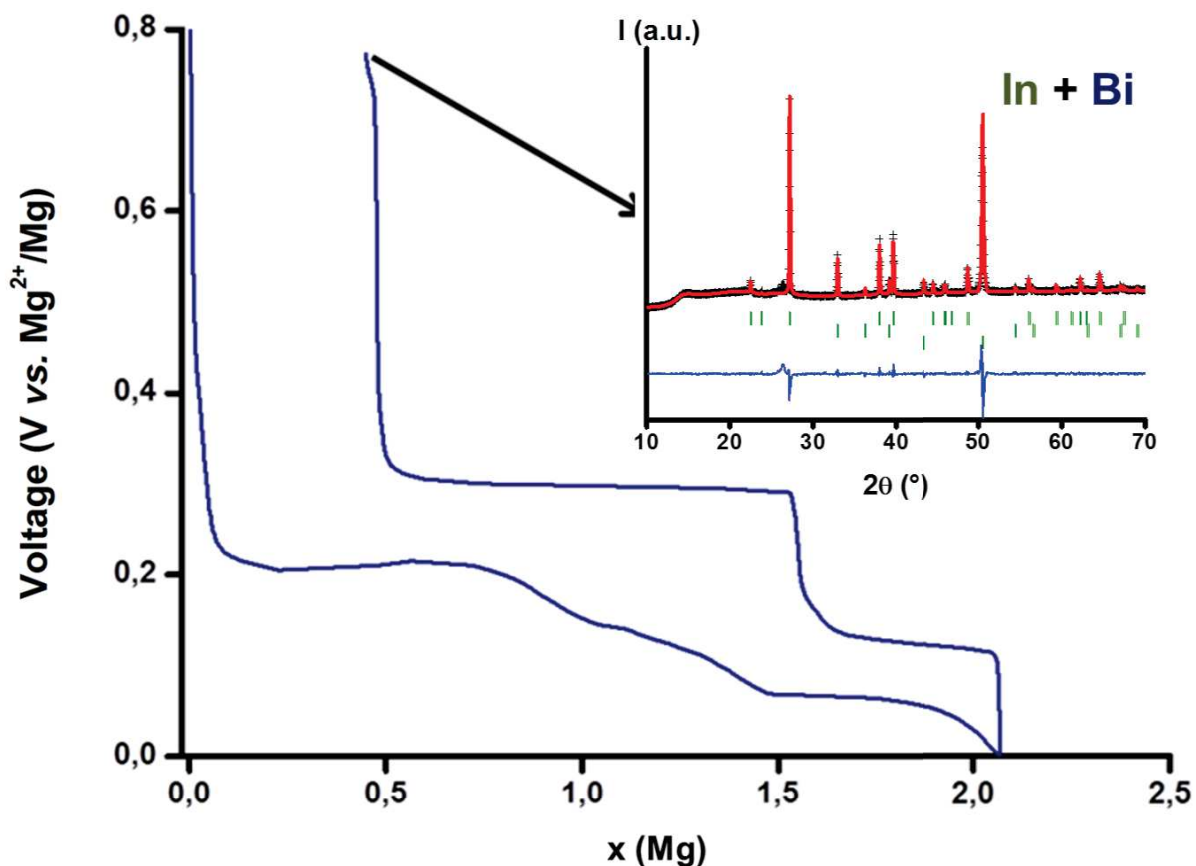


Figure 88 – First discharge and charge of an In-Bi based electrode (GCPL at C/100). As it possible to see from the ex situ XRD collected at the end of the charge, In and Bi were found as two distinct crystallographic phases and do not form any binary phases, unlike InBi-based electrodes. Non-indexed peak at 51° belongs to Cu current collector (Adapted from [213]).

As expected, Mg_3Bi_2 and $MgIn$ are obtained at the end of the discharge; however, distinguishable In and Bi metal are still observed after a complete de-magnesiumation, without any trace of intermetallic InBi.

4.3.2. Electrochemical performance

In the previous paragraphs, it was shown that the combined presence of In and Bi in the nominal chemical structure modifies the alloying mechanism. Bearing in mind that both indium and bismuth are rare elements with only hypothetical application in future commercialized Mg-ion devices, it is nevertheless interesting - from a fundamental point - to evaluate the electrochemical performance and to compare them with In- and Bi-based electrodes, presented in the Chapter III. The current rates definition (i.e. C/n) implied that $In_{0.5}Bi_{0.5}$ was chosen as the formula unit for a coherent comparison with pure In and Bi metals (Figure 89 - a).

The inset underlines the first discharge capacities obtained at $C/100$. The theoretical capacity is reached in the case of pure Bi ($C_{th.}=385 \text{ mAh g}^{-1}$), whereas only 90 % of the capacity is observed for In ($C_{th.}=467 \text{ mAh g}^{-1}$). The first discharge capacity for InBi is 410 mAh g^{-1} , which is very close to the theoretical value of 414 mAh g^{-1} . Thus, there is a clear synergy between In and Bi for the first discharge capacity. For current rates from $C/100$ to $C/5$, the capacity fading is more important for In than for Bi. Unfortunately, the capacity fading is also important for the $\text{In}_{0.5}\text{Bi}_{0.5}$ -based electrode. After $C/2$, the capacity totally vanishes for In and remains quite good for Bi. An intermediate behaviour is observed for $\text{In}_{0.5}\text{Bi}_{0.5}$. Indeed, even though the performance vanishing is delayed compared to pure In, the capacities are still significantly below those obtained for Bi.

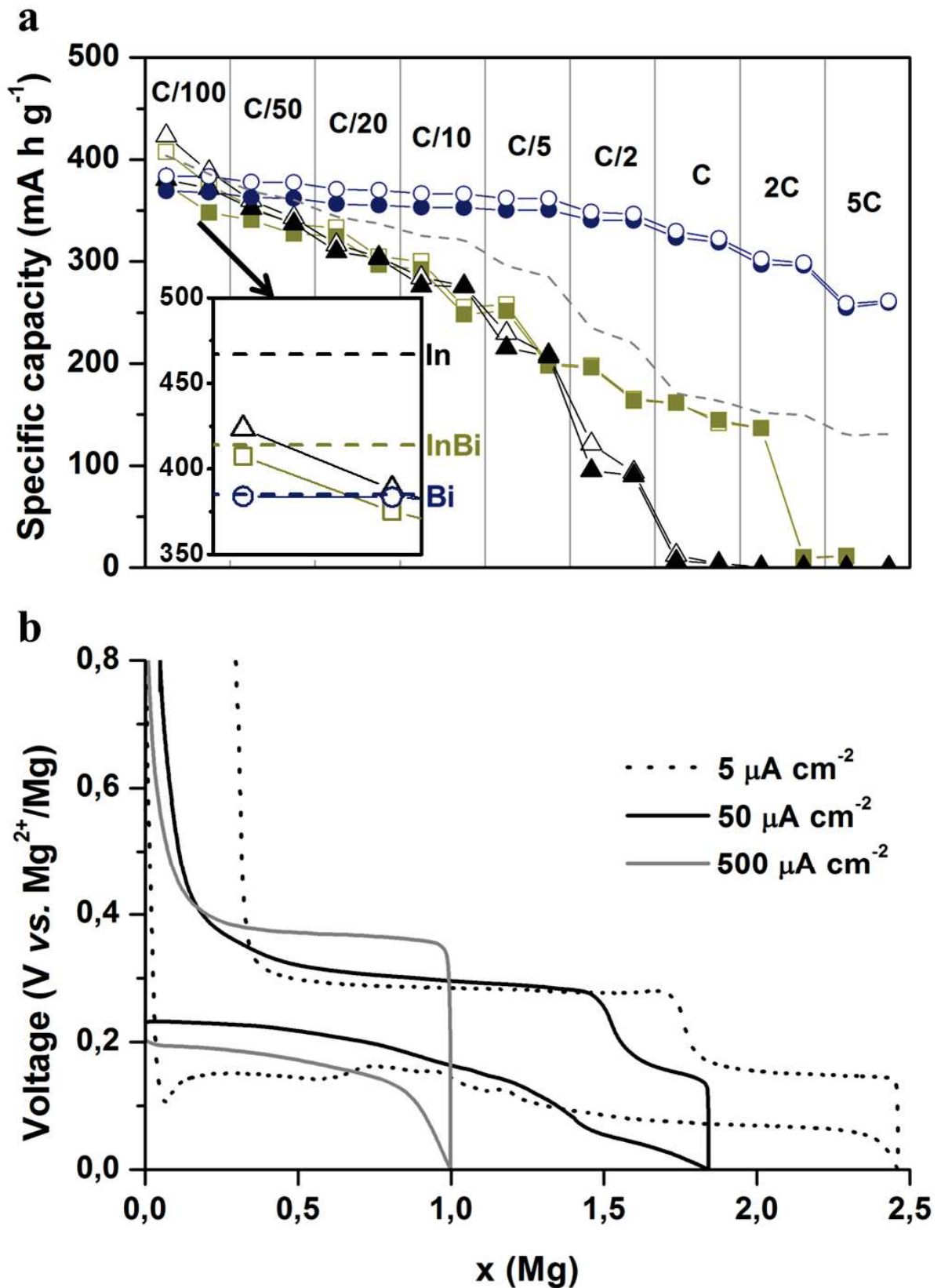


Figure 89 – a: Current rate comparison between In-, Bi- and InBi-based electrodes. An effective synergy can be noticed at very low current rate (C/100) but progressively decreases at higher C/n values. b: The capacity fading observed at high C-rate is mainly due to the poor cycling behaviour of In, whom plateaus becomes shorter and the overall polarization increases (Adapted from [213])

The capacity of $\text{In}_{0.5}\text{Bi}_{0.5}$ was also compared to an extrapolated value calculated by assuming that both In and Bi are active as if they were reacting alone, according to the following equation:

$$C_{calc.}(\text{In}_{0.5}\text{Bi}_{0.5}) = \frac{1}{2}C_{exp.}(\text{Bi}) + \frac{1}{2}C_{exp.}(\text{In})$$

For each current rate, the observed capacity is always below the calculated values (dashed grey line in Figure 89 - a). It is interesting to compare some galvanostatic profiles at various current densities: the lower voltage plateau is more affected by the increase of the rate, which demonstrates that the magnesianation of In is kinetically limited (Figure 89 - b). Moreover, it is evidenced that even Bi performance is affected in comparison with pure Bi electrodes, since the length of the alloying/de-alloying plateaus become shorter. Therefore, the synergy between In and Bi observed during the first discharge is unfortunately not preserved at higher current rates.

The electrochemical performance was evaluated in terms of cyclability at given C-rates. Figure 90 gathers the capacity evolution at C/20 and C/10.

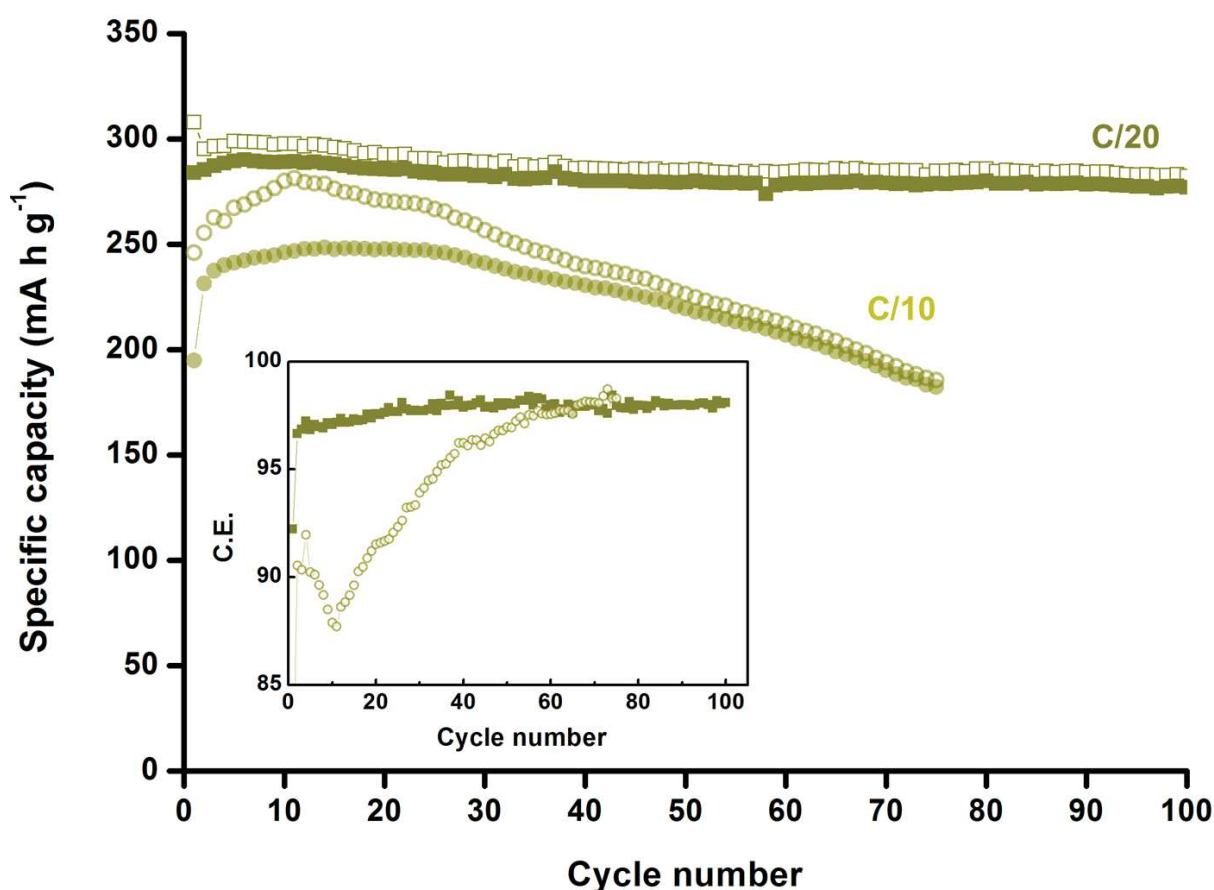


Figure 90 – Capacity evolution of two micrometric InBi-based electrodes cycled at C/20 and C/10, respectively. While the former shows a very stable capacity for 100 cycles, the latter exhibits rapid capacity fading after the 10th cycle. Inset: relative coulombic efficiencies (solid squares: C/20; hollow circles: C/10 – Adapted from [213]).

It is worth noting that a constant capacity of 280 mAh g⁻¹ is retained for 100 cycles at C/20. The coulombic efficiency is also stable but limited to 98%, which can be explained by regular parasitic reactions occurring at the electrode-electrolyte interface. At C/10, an activation period is necessary before reaching a capacity optimum around 275 mAh g⁻¹. However, the capacity rapidly fades upon further cycling. The role of metallic In should be here also pointed out to explain this poor electrochemical behaviour.

In conclusion, micrometric InBi was synthesized for the first time by high-energy ball-milling from In and Bi raw metal powders. The alloy is electrochemically active and reacts reversibly with Mg at low potential. As expected both Mg₃Bi₂ and MgIn are formed at the end of the discharge through an alloying process. Interestingly InBi is reformed during charge, making InBi a new example of mixed-metal alloy-type anode materials for Mg-battery. *Operando* XRD analysis reveals a more complex pathway than for the reaction of pure Bi and In, especially with the sequential reversible formation of In₂Bi and several Mg-In phases as intermediate steps along the overall electrochemical process. The formation of metallic In during the process might strongly influence the electrochemical cycling. Indeed InBi-based electrodes exhibits intermediate performance between those observed for pure Bi and In electrodes, without any synergetic effect. Nevertheless, it has been underlined the interesting electrochemical behaviour of *p*-block elements and confirmed that such compositions should be targeted to replace Mg when designing alternative negative electrode materials of Mg-ion battery.

4.4. Conclusions

In this Chapter several possible synergies were explored by combining the excellent electrochemical behaviour toward reversible magnesiation of Bi with the higher specific capacities of other *p*-block elements. The tested materials, characterised by different chemical natures ranging from a simple physical mixture (Sn-Bi) to intermetallic compounds (Bi_xSb_{1-x} and InBi), were all prepared by high-energy ball milling, using appropriate conditions. *Operando* XRD has represented a powerful tool for elucidating electrochemical reactions which could have been less complex at a first glance on the basis of the electrochemical tests. In some cases, it put on the light unexpected evolutions of the crystallographic phases when compared with the pure elements, which deeply influences the electrochemical cycling.

The results shown in this chapter open the gate to many promising perspectives in all the studied systems:

- In the case of the composite Sn-Bi, further tests are necessary in order to choose the most efficient ratio between the two elements. A particular attention should be devoted to better understand the role of Bi in the electrochemical activation of Sn. Moreover different new synthetic pathways can be envisaged to improve the efficiency of the Sn magnesiation, such as the realization of ternary composite Sn/Bi/C directly via mechanical milling.
- For the systems $\text{Bi}_x\text{Sb}_{1-x}$, the electrochemical alloying/de-alloying mechanism has been only partially elucidated, due to the complicate attribution of the peak position to the different magnesiated phases. Additional XAS analyses or solid state ^{25}Mg NMR could be helpful in order to better clarify the local Mg environment.
- Lastly, the analysis of InBi electrochemical behaviour shed light on the different alloying pathways that are influenced by the grain size of the active elements. Indeed, freshly-formed In particles seem more reactive as many Mg-In intermediates are visible, respect to the simple biphasic process in micrometric In magnesiation (cf. Chapter III). Therefore it would be interesting to re-open the study of pure In-based electrodes, moving from commercial micrometric powder to specially-designed nanosized particles.

V Perspectives – Toward a full Mg-ion battery

In the present work, the study of the electrochemical behaviour of several *p*-block elements toward Mg, alone and in binary combination has been undertaken. In order to propose simple, cost-effective and upscalable synthesis routes that can be seriously considered for large scale production, all materials were synthesized via high-energy ball milling, a method that fulfils all the above mentioned requirements. Thanks to the elevated crystallinity of the micrometric active materials and of the phases formed during cycling, we could elucidate the electrochemical mechanisms involved in all the studied reversible magnesiation reactions, in some cases confirming relatively simple biphasic reactions, but also discovering unexpected and more complex pathways.

Nevertheless, the evidences provided by this thesis, which can be interesting from a fundamental point of view, might appear incomplete in the wider optic of the realisation of a complete Mg-ion battery. Therefore, it has been thought necessary to match the improvement on this research of promising negative electrode materials with a more realistic setup, in a full Mg-ion cell. This should be considered as an important step toward the achievement of a promising Mg-based storage system, since the metallic Mg-free setup might allow using classic and therefore safer electrolyte formulations (compared to the Grignard-based ones actually available for Mg metal systems).

5.1. Synthesis of a “conventional” electrolyte: Mg(TFSI)₂ in DGM

One of the main interests of heading over to MIBs is that safer and hence more easily marketable electrolyte formulations can be employed instead of the highly air-sensitive electrolytes nowadays available for MBs (cf. 1.7.2). Thus, for testing in the complete-cell configuration (MIB), a different electrolyte was used. It consists of magnesium(II) bis(trifluoromethanesulfonyl)imide - Mg(TFSI)₂ - dissolved in diethylene glycol dimethyl ether (diglyme, DGM). As reported by Ha and co-workers, such electrolyte exhibits excellent anodic stability (exceeding 4 V with an Al current collector) and it allows reversible Mg insertion into Mo₆S₈.^[217] The reagents used to prepare such electrolyte are summarised in Table 19.

Product	Supplier	Purity stated	Quantity
Mg(TFSI) ₂	Solvionic	99.5%	2.923 g
DGM	Sigma-Aldrich	99.5%	10 ml

Table 19 - Components of the electrolyte for Mg-ion battery.

Prior to use, Mg(TFSI)₂ was dried under vacuum for 12 hours at 130 °C and DGM was further dried using molecular sieves. The final solution was stirred 12 hours prior to use. The final salt concentration in the electrolyte is 0.5 M.

5.2. Synthesis of the positive electrode for Mg-ion battery: Mo₆S₈

Despite many efforts for widening the range of possible positive Mg-battery electrodes, the binary CP Mo₆S₈ still represents the most employed of them (cf. 1.7.3.1)[93] and was chosen as the reference positive electrode in order to test the electrochemical properties of our negative electrodes in full cells. However, Mo₆S₈ is a metastable phase that can be only obtained from a ternary parent compound, such as Cu_xMo₆S₈ (where x lies between 2 and 2.5). The latter was firstly synthesized by Robert Chevrel in the 70's with a heating treatment of a stoichiometric mixture of the pure elements (Cu, Mo, S) in a sealed tube under vacuum.[97] This synthesis, however, is very dangerous since the high sulphur vapour pressure in the tube may result in its explosion. Hence, various improvements were subsequently proposed, such as replacing sulphur with MoS₂ to reduce the partial pressure of the former, and avoiding the use of sealed tubes by fluxing inert gases in the oven during the synthesis (cf. 1.7.3.1). In our work, Cu_{2.5}Mo₆S₈ was prepared taking inspiration from the protocol proposed by Choi *et al.*[218] In fact, it is possible to start from other Cu_xMo₆S₈ compositions containing a lower amount of Cu, considering that the latter must be subsequently removed to obtain the binary phase Mo₆S₈.

Cu, Mo and MoS₂ powders were thoroughly mixed together in a stoichiometric ratio and put in an open alumina crucible. The reaction was carried out in a tubular oven at 1100 °C for 24 hours under flowing Ar. The reagents with their respective purities and suppliers are listed on the following Table 20:

Reagent	Supplier	Purity stated	Particles size (μm)
Cu	Alfa-Aesar	99.9%	150 ± 45
Mo	Alfa-Aesar	99.95%	3 – 7
MoS ₂	Sigma-Aldrich	99%	< 2

Table 20 - Reagents for the high temperature solid-state synthesis of Cu_{2.5}Mo₆S₈

XRD pattern collected on the obtained powder are shown in Figure 91 – a . Full profile matching reveals the presence of a single phase in the R-3 space group. Cell parameters are in agreement with the formation of Cu₂Mo₆S₈. [219]

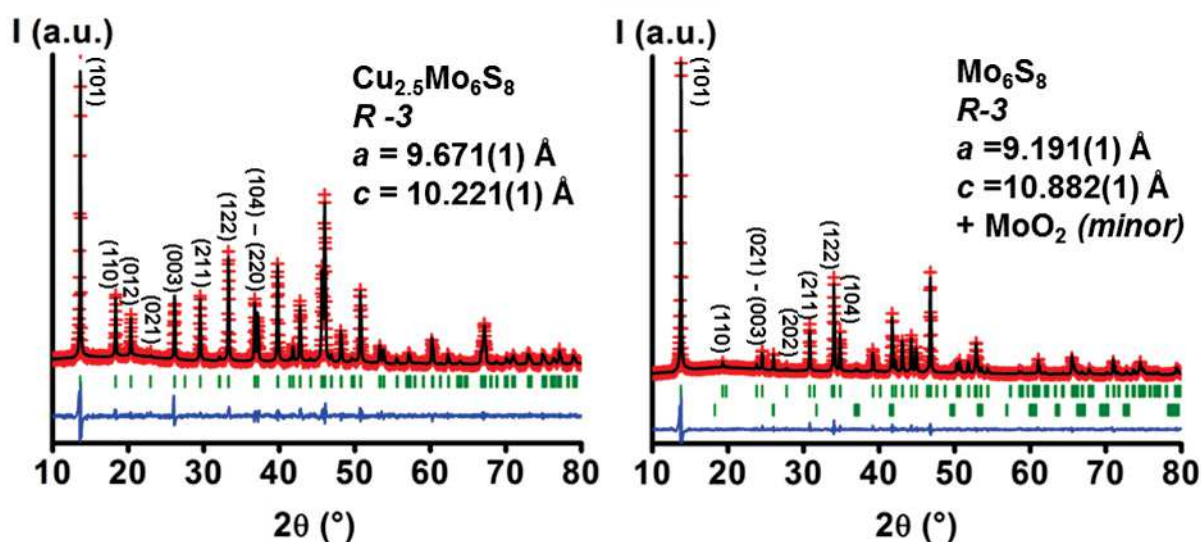


Figure 91 – XRD pattern of Chevrel phase Cu_{2.5}Mo₆S₈ (left) and after Cu removal (right). According to the literature the leaching treatment produces the Mo₆S₈ phase, which is employed as positive electrodes in MBs and MIBs. A very minor impurity of MoO₂ can be noticed in the Mo₆S₈ diffraction pattern, which is generated during the acidic treatment of the starting CP. Red crosses, black line and green strokes represent observed XRD points, interpolation and peak positions; blue line represents the difference between the observed values and the fit (Adapted from [190]).

In order to achieve the electrochemically active phase Mo₆S₈, copper has to been removed from the ternary CP by acidic leaching. This treatment consists in suspending the synthesised powder in concentrated HCl (6M) for 6 hours under continuous O₂ bubbling, as schematised in Figure 92.

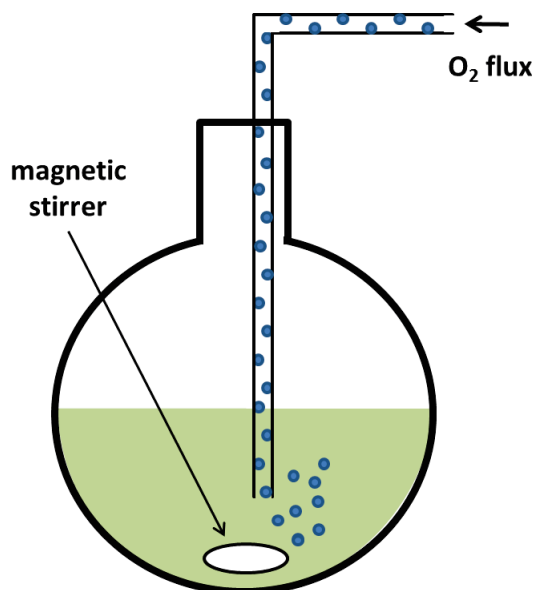


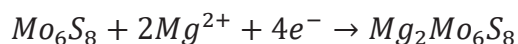
Figure 92 – Schematic representation of the leaching setup: in general 2 g of $\text{Cu}_{2.5}\text{Mo}_6\text{S}_8$ were mixed to 100 ml of HCl 6M and stirred overnight with a continuous O_2 flux.

The suspension was then centrifuged using a Centrifuge 5804 (Eppendorf) at a rotating speed of 11000 rpm, the solid washed twice with distilled water, and finally once with ethanol. Each washing step lasted 12 minutes. The obtained product was then dried in oven at 80 °C for 12 hours and subsequently stored in the glove box.

For comparison, XRD before and after the leaching treatment are presented in the Figure 91 - b. The variation of the cell parameters between the two patterns confirms the complete Cu removal from the ternary CP after the acidic treatment.[106] It is important to note the presence of minor amounts of MoO_2 as an impurity, most probably formed by the oxidation of some molybdenum during the acidic treatment.

5.3. Electrochemistry of Mo_6S_8 vs. Mg

In Figure 93 which shows the GCPL test of Mo_6S_8 vs. Mg, two well-distinct plateaus are found during magnesiation. The former is sloppy and ranges between 1.3 and 1.1 V, whereas the latter is steady at 1.1 V. According to the literature, they correspond to the sequential insertion of Mg into the two free insertion sites of the Mo_6S_8 structure (cf. 1.7.3.1). [72] The overall reaction allows inserting 2 moles of Mg^{2+} per mole of CP:



Theoretically, the specific capacity of Mo_6S_8 is 128.8 mAh g^{-1} .

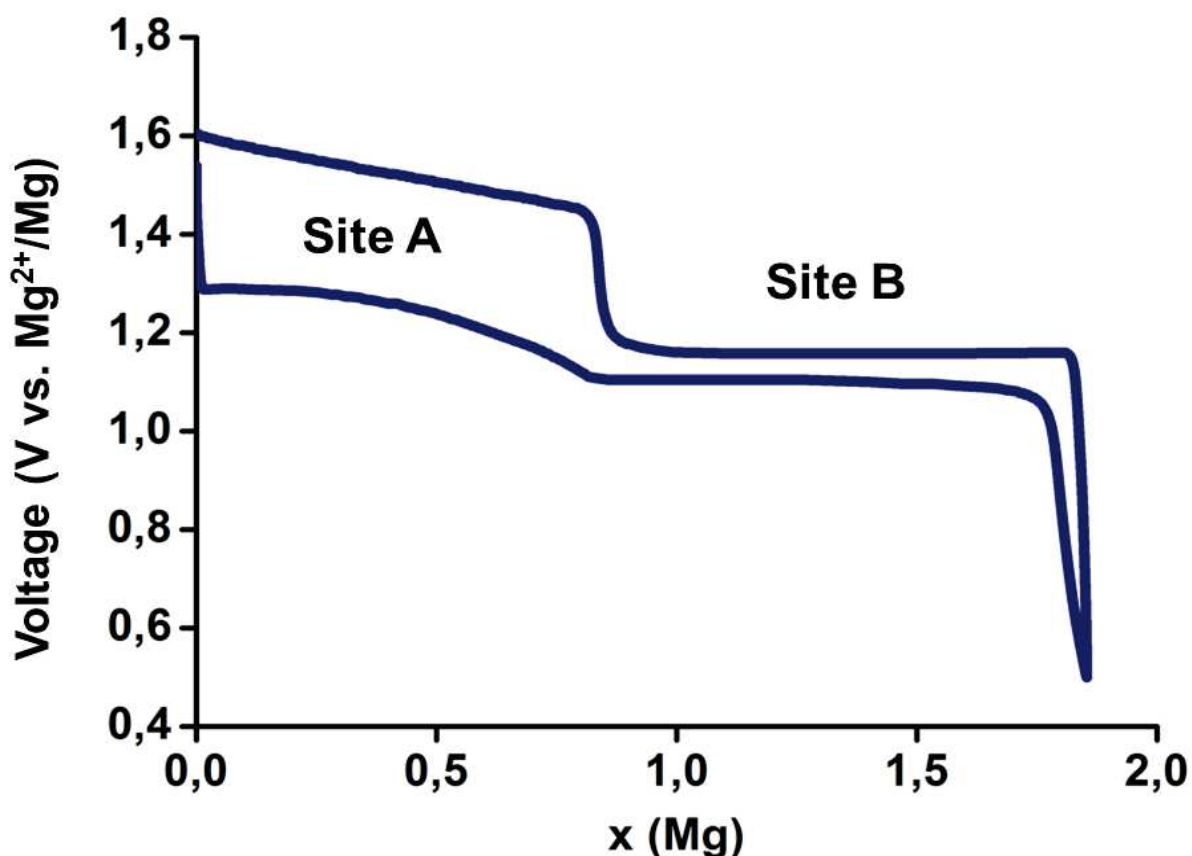


Figure 93 – First cycle in GCPL mode of a Mo_6S_8 -based electrode vs. Mg at the current rate of C/100 (Adapted from [190]).

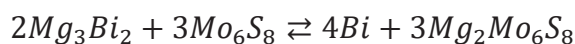
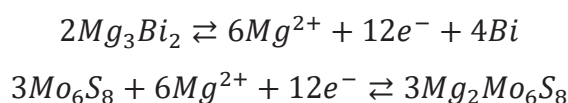
The number of inserted Mg exhibited by the half-cell is 1.85, which corresponds to 92% of the theoretical value. An excellent reversibility of the electrochemical phenomena is provided during the subsequent charge, with no apparent capacity loss after the first cycle. Analysing the kinetic aspects, the reaction involving the curve corresponding to the insertion of Mg in site B exhibits a small polarization with respect to that of the site A. This short electrochemical test was only carried out to confirm the electrochemical activity of the as-prepared Mo_6S_8 . Indeed, from one synthesis to another, some inactive synthesized batches were sometimes revealed.

5.4. Full Mg-ion cell: Mo_6S_8 vs. Mg_3Bi_2

Because of its quasi-thermodynamic Mg-alloying reaction and of its excellent cycling stability, micrometric Bi-based electrodes were targeted as promising candidates in a full Mg-ion setup test. In their previous work, Shao *et al.* associated a pre-magnesiated Bi-NTs with Chevrel phase Mo_6S_8 positive material for the first proof-of-concept of rechargeable Mg-ion battery with Bi-based electrode.[78] At C/10, a

reversible capacity of 60mAh g⁻¹ was measured. However without any further details on the equilibration between the electrodes, it is rather difficult to make up its own opinion on these results.

In Chapter 3, the interesting electrochemical behaviour of Mg₃Bi₂ prepared by mechanical alloying was underlined. Therefore, it was decided to implement this alloy in a new proof-of-concept of rechargeable Mg-ion battery. Supposing an ideal behaviour of the battery, the same amount of Mg²⁺ should reversibly move from the magnesiated electrode (Mg₃Bi₂) to the unmagnesiated one (Mo₆S₈). Therefore, the amount of active materials in both sides of the cell should be equilibrated in order to satisfy such condition. In the case presented here, the two reactions are:



It is also important to mention that in practice, industrial battery producers have to take into account the irreversible capacity loss that penalises each electrode material. Here, for sake of simplicity and because the target was only to prepare a laboratory-scale proof-of-concept, it was decided to intentionally set Mg₃Bi₂ as the limiting electrode. For this reason, a Mg₃Bi₂ negative electrode (loading of 1-2 mg/cm²) supported on Cu foil was associated to a thick self-supported Mo₆S₈ positive electrode (loading of 30 mg/cm²).

The first cycle is presented of such full cell is presented in Figure 94. Since Mo₆S₈ is present in large excess, the x scale used for the GCPL of the full cell corresponds to the amount of Mg that effectively is reversibly de-alloyed from the Mg₃Bi₂ negative electrode.

The first cycle is presented of such full cell is presented in Figure 94.

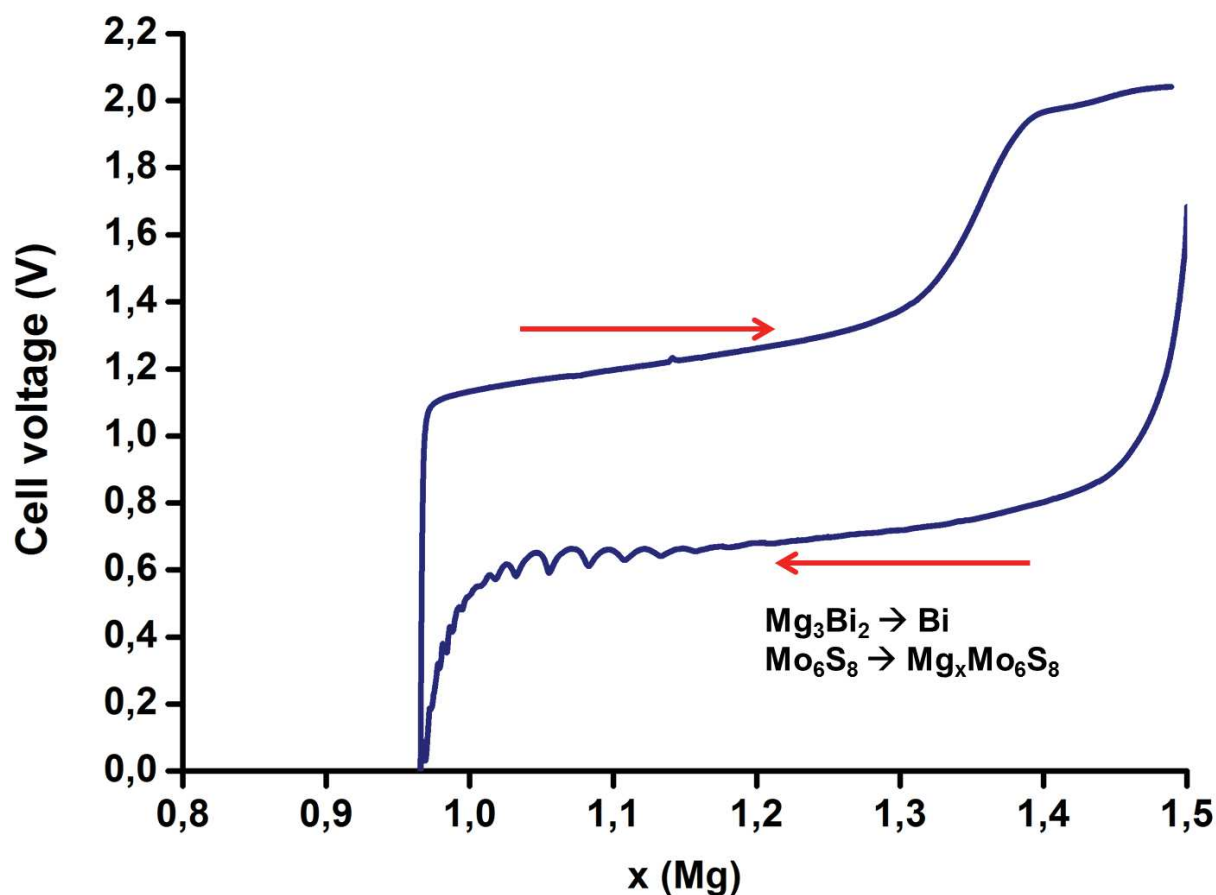


Figure 94 – GCPL gathering the first cycle of a full MIB. It is built with a Mg_3Bi_2 negative electrode supported on Cu foil and a self-supported Mo_6S_8 positive electrode. Mg_3Bi_2 is the limiting electrode and therefore the x on the curve corresponds to the moles of Mg reversibly de-alloyed from Mg_3Bi_2 . The current density of C/100 was set by considering the mass of Mg_3Bi_2 (Adapted from [190]).

In a 2-electrode configuration the recorded potential directly summarises the evolution of both electrodes. It is therefore not straightforward to analyse the electrochemical signature of such cell without an external reference electrode, or without performing half-cell preliminary tests. However, it is still possible to draw some interesting conclusions from this cycle.

Firstly, the average value in discharge (0.6 V) wholly matches with the magnesian potential of the Chevrel phase ($\sim 1.1\text{-}1.2$ V *vs.* Mg^{2+}/Mg ,) subtracted by the first de-magnesian Mg_3Bi_2 plateau (0.5 V *vs.* Mg^{2+}/Mg , cf. Figure 58). The slight potential oscillations at the end of discharge might express some intermittent contact losses.

Secondly, the global shape of the discharge and charge also matches with previous observations of $\text{Mo}_6\text{S}_8/\text{Mg}_3\text{Bi}_2$ and $\text{Mo}_6\text{S}_8/\text{Mg}_2\text{Sn}$ full cells.[78][77] Unfortunately, a complete de-magnesian of Mg_3Bi_2 could not be achieved. The rather high viscosity of diglyme might hinder the electrochemical process, and therefore limits the

demagnesian yield. This preliminary result is nevertheless encouraging, and validates the strategy of this thesis in investigating micrometric ball milled Mg_3Bi_2 as a viable Mg-containing negative electrode. However, challenges remain to optimize the full cell design and reach better overall performances.

5.5. A more efficient synthesis for ternary CP: solid-state microwave assisted reaction

The ubiquitous role of the Mo_6S_8 as a reference positive electrode in the research of MIBs makes the synthesis of their ternary parent compounds $\text{Cu}_x\text{Mo}_6\text{S}_8$ a crucial step in the realization of MIB prototypes. However, their synthetic protocols are relatively time-consuming, and greater improvement on the whole sector of MIBs might be achieved if a faster and simpler synthetic protocol were adopted. As discussed above (cf.1.7.3.1), several attempts have been made in order to decrease the synthesis time and the complexity of the setup, but they were often detrimental to the overall purity of the obtained CP.

Microwave heating is a promising technology allowing milder reaction conditions in aqueous or organic media, and was recently shown to be very efficient even in solid-state reactions for the preparation of oxides and intermetallic compounds. [181][220][221] As an open perspective of this thesis, a fast, inexpensive and high-yield microwave synthesis of the Chevrel phase $\text{Cu}_2\text{Mo}_6\text{S}_8$ is presented. This cost-effective technique enables the preparation of a highly pure product. Classical copper removal through acidic leaching leads to the binary Mo_6S_8 that is successfully tested as positive electrode in rechargeable Mg batteries.

Figure 95 reports a sketch of the setup adopted for the synthesis of the CP. In the same fashion of the conventional synthesis, MoS_2 , Cu and Mo in stoichiometric proportions were mixed in an agate mortar and then pressed together at 1.5 bar. The product of the microwave synthesis is an ingot that can be easily pulverized. The yield of the reaction is high, since 98% of the initial mass is retrieved after the thermal treatment. Such result can be explained by the very short time of the synthesis that significantly reduces the vaporization of sulphur.

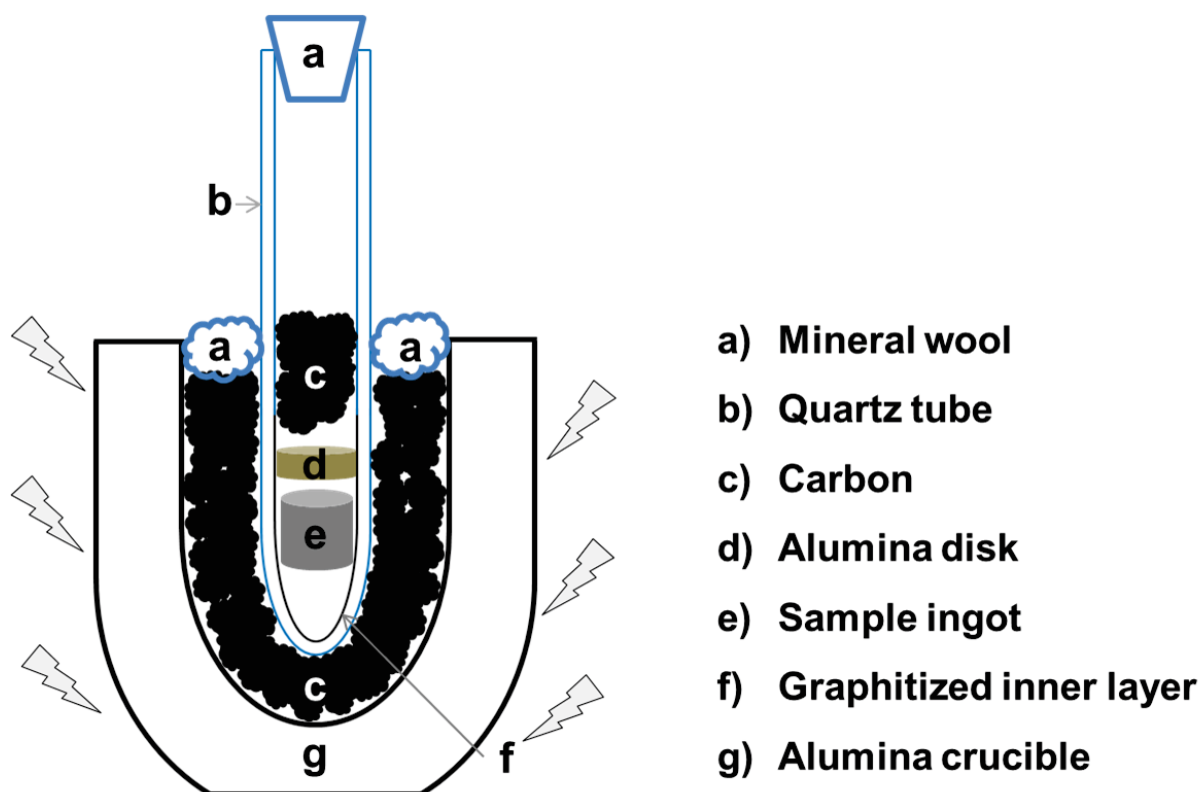


Figure 95 – Schematic representation of the setup adopted for the microwave synthesis of $\text{Cu}_2\text{Mo}_6\text{S}_8$. The thermal treatment was carried out in a Startsynth laboratory microwave (Milestone) for 400 s at 1200W (Adapted from [222]).

The powder XRD pattern (Figure 96 – a) can be indexed with a rhombohedral space group (R-3). Refined cell parameters through Le Bail method perfectly match with the literature and confirm the formation of $\text{Cu}_2\text{Mo}_6\text{S}_8$. [97][219] The so-obtained Chevrel phase is highly crystalline. Even though very small residuals of the precursor MoS_2 are sometimes found from one synthesis to another, the phase is usually obtained with a very high degree of purity, especially when compared to other fast reaction routes for which significant amounts of Mo, MoS_2 or Mo_2O_3 are often detected. [223] In microwave-assisted synthesis, carbon acts as a susceptor (*i.e.*, a material able to absorb the magnetic radiation and to convert it into heat). Here it also prevents from any oxidation of the starting metallic powders. SEM image evidences a large distribution of micrometric-sized particles with a regular, quasi-cubic shape. Well-faceted particles with defined morphologies are rather commonly obtained in solid-state microwave synthesis, and can be found for instance in intermetallic compounds prepared in similar conditions. [181][221]

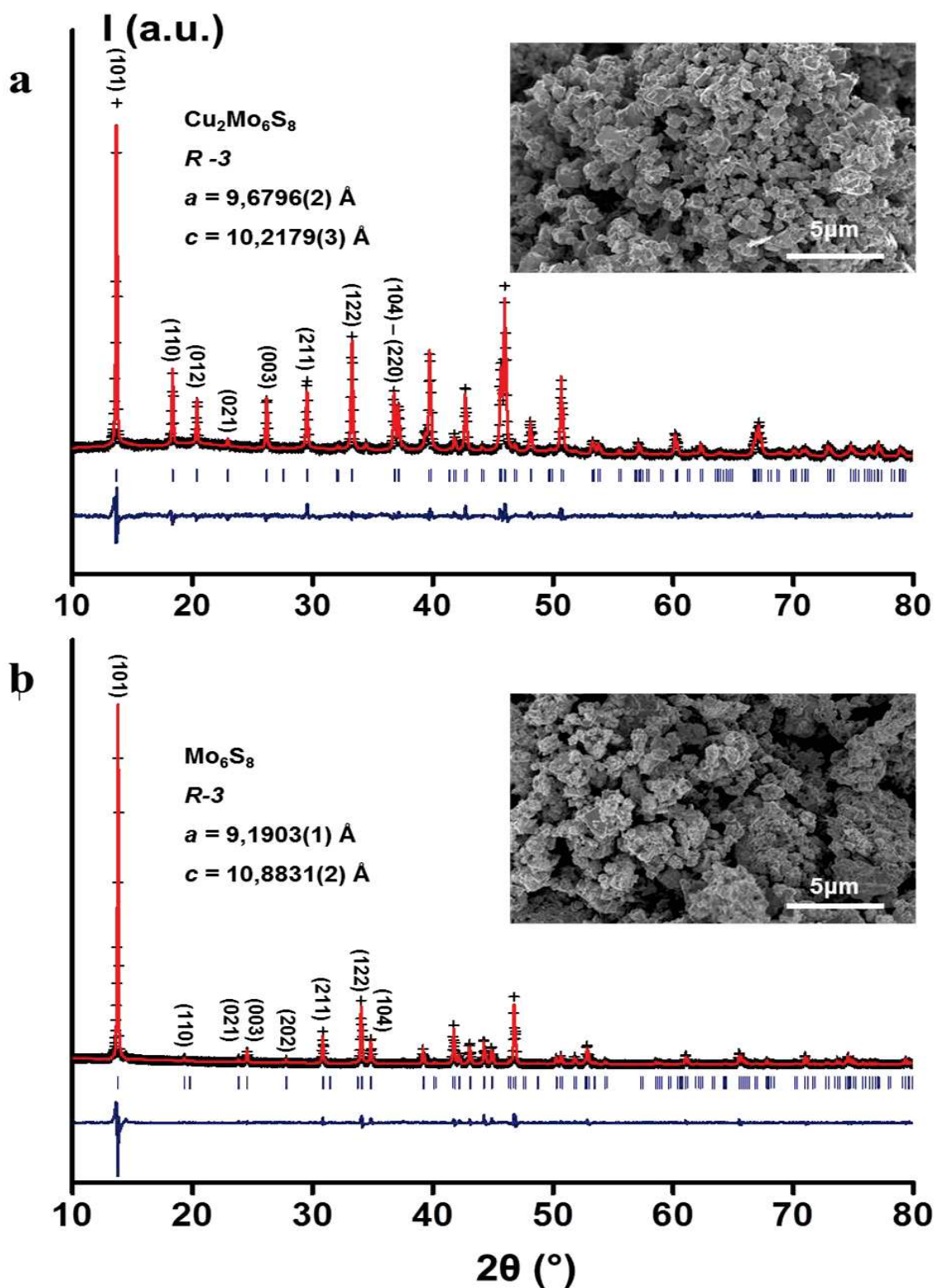


Figure 96 – a: XRD pattern of the powder obtained by solid-state microwave heating. Full profile matching confirms the formation of the $\text{Cu}_2\text{Mo}_6\text{S}_8$. Inset: SEM image of the so-obtained particles. b: XRD pattern collected after Cu removal, confirming the formation of the binary CP Mo_6S_8 . Inset: the acidic treatment barely changes the shape of the particles, which seem to have slightly modified their pristine cubic shape. For each pattern red crosses, black line and green strokes represent observed XRD points, interpolation and peak positions; blue line represents the difference between the observed values and the fit. (Adapted from [222]).

An acidic leaching treatment with concentrated HCl is necessary to remove the copper from the Chevrel phase to obtain the electrochemically active Mo_6S_8 . This topotactic chemical oxidation does not impact the overall Chevrel phase structure but only slightly modifies the cell parameters. The XRD pattern collected after the HCl leaching of the precursor powder evidences a weak shift of the peaks (Figure 96 - b). The refined values of the new cell parameters match with the literature and confirms the formation of the binary Chevrel phase Mo_6S_8 . [106] The acidic treatment does not change the powder grains size, but slightly alters the surfaces of the particles, which partially lose their regular and faceted shape.

The first galvanostatic cycles at C/20 of a $\text{Mo}_6\text{S}_8/\text{Mg}$ battery are shown in Figure 97. The first discharge evidences a sloppy plateau from 1 to 0.6 V before a final drop to 0 V. A very high capacity of 123 mAh g^{-1} is obtained and corresponds to the reaction of more than 1.9 magnesium cations.

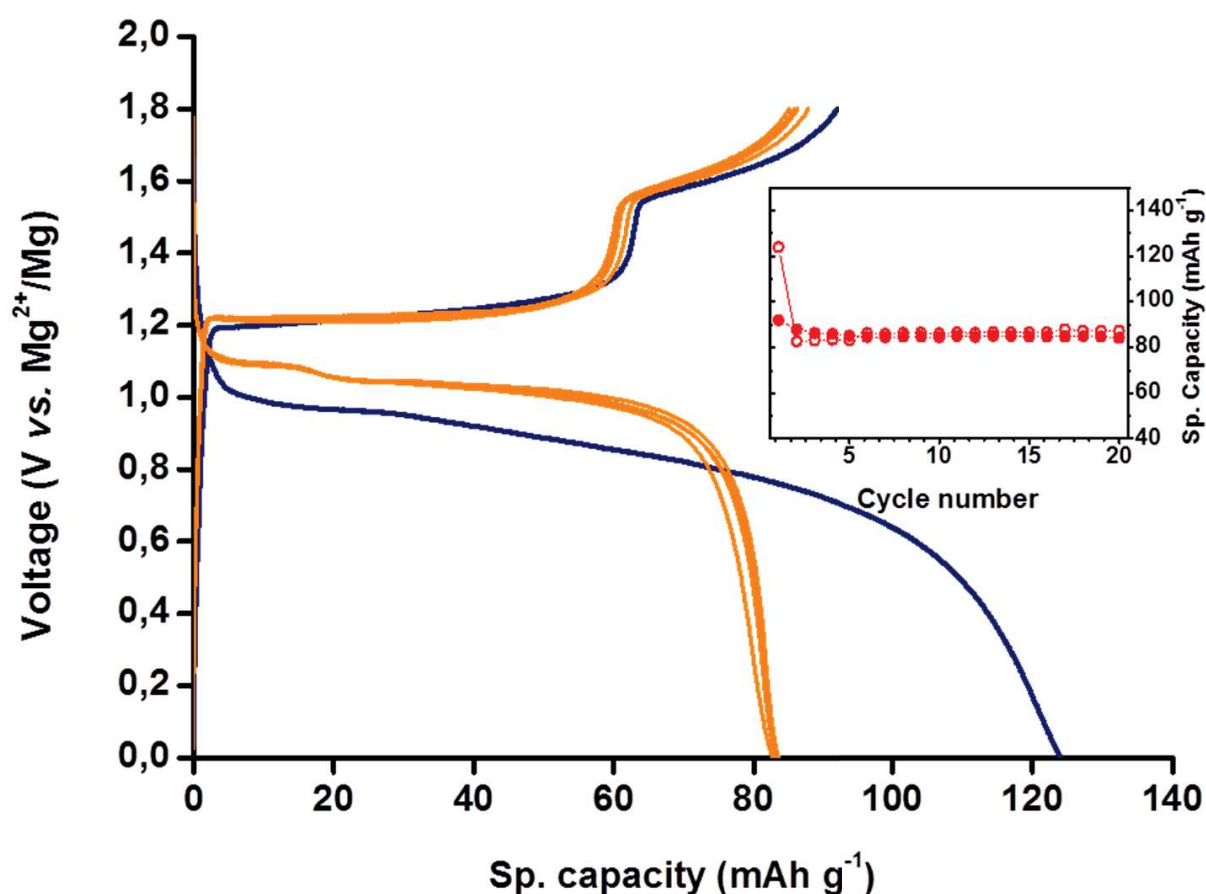


Figure 97 – GPC cycling of the Mo_6S_8 at the current rate of C/100. Although a sensible difference on the obtained specific capacity between first and subsequent discharges can be noticed, overall performance are analogous to the Mo_6S_8 obtained by classical protocol (Adapted from [222])

During the subsequent charge it is possible to distinguish two de-intercalation plateaus at 1.2 and 1.6 V. According to the literature, they correspond to the distinct de-magnesiumation of the two Mg sites, B and A, respectively.[72] The absence of plateau in the discharge profile was already observed in the literature and is mainly explained by intrinsic kinetic limitations.[224][225] It is not possible to remove all the magnesium cation during the charge (25 % of irreversible capacity loss). Nevertheless, subsequent cycles exhibit a high reversible process with very stable capacities above 80 mAh g⁻¹ is exhibited during the following cycles. It is worth mentioning that charge capacities slightly exceed discharge values, probably due to some electrolyte decomposition at relatively high voltage.[66] These first galvanostatic cycles completely match with both results of GCPL test on conventionally-synthesized CP (Figure 93) and previous studies devoted on the electrochemical performance of nanometric Chevrel-type Mo₆S₈ electrode, with similar discharge and charge capacities and voltage plateaus.[225]

Mo₆S₈ electrodes prepared by microwave-assisted synthesis were also tested at progressively increasing current densities, starting from C/20 up to 5C (Figure 98).

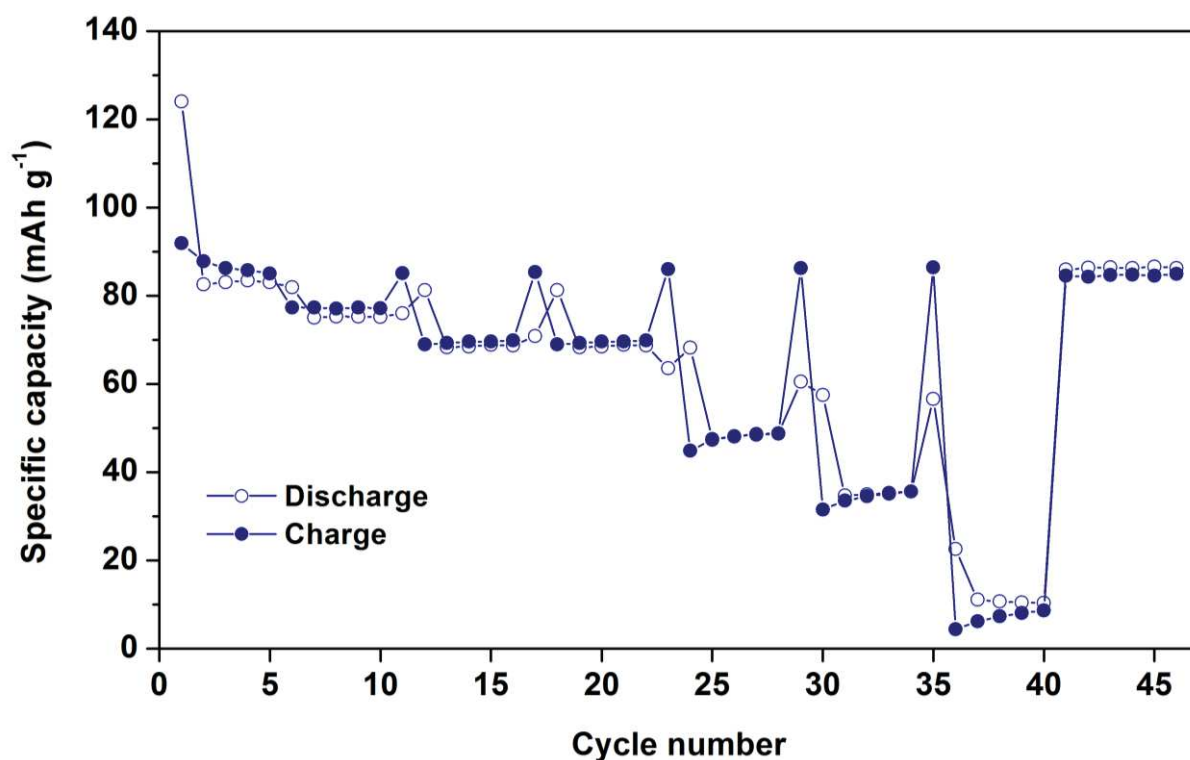


Figure 98 – Rate capability test performed on a CP Mo₆S₈-based electrode vs. Mg. The C-rate was progressively increased from C/20 to 5C. After each stint of 5 cycles at the same current ratio, a slower cycle at C/20 was performed, in order to check the resistance of the electrode at the current variations (Reproduction from [222])

As expected, the capacity progressively decreases when moving to higher current rates. A single cycle at C/20 between each stint allows evaluating the endurance of the electrode material to such high currents. During these single cycles the discharge capacity is lower than the following charge. Indeed, a slow charge enables the removal of all the accessible cations. Those that were originally trapped still do not participate to the electrochemical process, as the observed charge capacities are still limited near 85 mAh g⁻¹. Such value confirms the excellent capacity retention of the Mo₆S₈ – based electrode even after being submitted to strong current densities.

In summary, the Chevrel phase Cu₂Mo₆S₈ was successfully prepared by a very rapid microwave heating of a stoichiometric mixture of Cu, Mo and MoS₂. Compared to other conventional synthetic routes featured in literature, this approach presents several major advantages, such as an outstanding shortening of the time of synthesis (only 400 s instead of several days) and an extremely simplified reaction setup (neither sealed tubes nor inert gases are needed). This promising result opens the gate to easily upscalable protocols. A pure and well-crystallized phase was evidenced by XRD analysis, while SEM clearly shows the micrometric particle size of the obtained powder. From this precursor, the binary Chevrel phase Mo₆S₈ was obtained by a conventional acidic leaching. The electrochemical behaviour of Mo₆S₈-based electrode was evaluated in Mg-battery, and the observed performances are comparable with other micrometric Mo₆S₈ obtained by conventional synthesis already reported in literature, as well as with our results on Mo₆S₈ prepared following the classical synthetic routes. As the binary Chevrel phase Mo₆S₈ still represents the reference positive electrode for Mg batteries, proposing a faster, more efficient and upscalable synthesis of its principal precursor Cu₂Mo₆S₈ is an important achievement that can help improving research and development in this field.

VI General Conclusion

The main goal of this thesis was the investigation of the electrochemical properties of several *p*-block elements as possible negative electrode materials targeted to replace metallic Mg in Mg-based reversible storage systems. Characterised by attractive theoretical capacities and potential low production cost, Mg-based batteries are promising alternatives to the well-established Li-ion technology that, in a mid-term perspective, might not afford the still growing need in portable devices plugging, due to the relatively low abundance and uneven spreading of metallic lithium. Even if MB prototypes were presented at a laboratory scale, their further development is dramatically hampered by the low compatibility between metallic magnesium and classical electrolyte formulations, *i.e.* Mg-based inorganic salts dissolved in liquid carbonates. Indeed, electrochemical side reactions during cycling between these two components form a passivation layer on the surface of metallic Mg, hindering any further cycling. Therefore an alternative class of electrolytes was proposed, based on the combination of both a Lewis acid (in general an organohaloaluminate compound) and a Lewis base (a Grignard-reagent), dissolved in ethereal solvents. Such solutions are however extremely air- and moisture-sensitive and cannot be compatible with a further commercialization of batteries equipped with.⁹ Even if it obliges renouncing to its interesting theoretical capacities, replacing metallic magnesium with other negative electrodes, *i.e.*, materials able to reversibly react with Mg at low potential, can represent a solution of such electrode-electrolyte compatibility, since full MIB setup allows adopting conventional, thus safer, electrolyte formulations.

p-block elements are targeted as good candidates for negative electrodes in MIBs, because of their well-known ability to electrochemically alloy at low potential to other cations such Li⁺ and Na⁺. In last 3 years, some of them have been tested toward magnesiation, providing varied electrochemical performance. The electrode formulations proposed in the literature entail the use of nanosized active materials,

⁹ It is worth mentioning a very recent study showing a possible compatibility between Mg(PF₆)₂-based electrolytes and metallic magnesium that could circumvent this issue,[230] but this new result needs to be confirmed by further researches.

whose synthesis seems difficultly upscalable; moreover, the electrochemical mechanisms have been poorly elucidated, with a total lack of *operando* characterizations.

In this thesis, we have decided to fill this lack of knowledge by studying several elements belonging to the *p*-block, such as Sn, Sb, In and Bi. In contrast with the electrode formulations proposed in literature, we have decided to start from simple micrometric powders as active materials, also on the basis of previous experiences at ICGM – AIME with Li- and Na-based batteries, where it was shown that nanostructuring of alloy or conversion electrode materials is not always necessary to obtain electrodes with good cycling properties.[36] The initial part of this work was devoted to the optimization of the battery setup (electrolyte, current collectors, etc.) and of the electrode formulation. The latter was carried on mainly on the first studied element, Sn, and was then transferred to all the other studied active materials. If from both micrometric Sn and Sb poor results were obtained, In and especially Bi provided interesting electrochemical activities toward magnesium: In-Mg alloying reaction is, at present, the magnesiation that occurs at the lowest potential, while Bi magnesiation/de-magnesiation occurs in a quasi-thermodynamic fashion. *Operando* XRD was used as the main technique for the characterisation of the electrochemical mechanisms of the studied materials. In the case of In and Bi, it evidenced a biphasic process with neither amorphisation, nor intermediate phase formations. An important difference was however noticed in the comparison of their electrochemical performance: while μ -In suffers of poor cyclability at high current densities, μ -Bi has an excellent behaviour, which is in line with the results reported in the literature for Bi nanotubes.

Beyond these excellent features, it is important to remind that the alloying reaction of Bi with Mg provides a relatively low specific capacity (385 mAh g⁻¹) due to the elevated atomic weight of Bi. Therefore, possible synergetic effects combining the good electrochemical behaviour of Bi with the lightness of several other *p*-block elements, or with the lower alloying voltage, as in the case of In, were sought. According to the different properties of the studied elements and of their interaction with Bi, several types of materials have been proposed, starting from a simple, intimate physical mixture in Sn-Bi composites, to the solid solutions formed by Bi and Sb, to intermetallics in the case of In and Bi. All these active materials were prepared using the same simple, cost-effective and upscalable technique: mechanical

milling/alloying. Even though the obtained electrochemical performance have not necessarily led to a veritable improvement compared to that of pure Bi, some synergies were observed, such as the unexpected activation of the Sn in all the studied Sn-Bi composites, even with the addition of very small amounts of Bi. Furthermore, the detailed *operando* study of the alloying/de-alloying mechanisms sometimes evidenced more complex and unpredictable reaction pathways, as in the case of InBi, which were however necessary for a thorough understanding of the electrochemical performance.

A first perspective of this work is represented by the test of a micrometric-*p*-block element-based negative electrode in a full Mg-ion battery, using a conventional electrolyte formulation. Micrometric Bi, which showed the best performance in terms of cycling behaviour vs. magnesium, was tested toward Mo₆S₈, which is actually considered the reference positive electrode for MIBs. However, further improvements on the full-cell design are needed in order to achieve better electrochemical performance. In particular, it is necessary to study this system using a 3 electrode systems, which will allow a better evaluation of the whole cell performance.

A further progress towards the implementation of these materials in full cells has been achieved by proposing a more efficient synthesis of the Mo₆S₈'s precursor. In fact, our new synthetic protocol based on the microwave assistance for solid-state reaction, allows preparing the ternary CP Cu₂Mo₆S₈ with an excellent degree of purity in only 400 s and in an extremely simplified setup. Such synthetic method is an important improvement in the synthesis of the Chevrel phase compared to the many days of the classical high-temperature synthesis, but it may also represent a new efficient route for the exploration of other sulphide-based materials, which are expected to be the future class of positive electrodes for Mg-based storage systems. [79][138][226]

Other further perspectives, more linked to the negative electrodes, are related to the improvement in the preparation of the active materials, with a more deep study on the milling conditions but also on the optimization of electrode formulations. Moreover, other analytical techniques can be helpful to better clarify the alloying/de-alloying mechanism, such as X-ray absorption spectroscopy and the ²⁵Mg Nuclear magnetic resonance.

Further improvements of the cycling performance may come from a better understanding of the electrode/electrolyte interphase and of the electrolyte

degradation reactions taking place at the electrode surface. Such information can be obtained, for instance, by XPS or by vibrational spectroscopy. It must be noted that this is still an almost unexplored field in the exploration of Mg-based electrochemical systems.

Scientific production

Articles:

F. Murgia, L. Stievano, L. Monconduit, R. Berthelot:

Insight into the electrochemical behavior of micrometric Bi and Mg_3Bi_2 as high performance negative electrodes for Mg batteries

Journal of Material Chemistry A, 2015, 3, 16478.

F. Murgia, E. T. Weldekidan, L. Stievano, L. Monconduit, R. Berthelot

First investigation of indium-based electrode in Mg battery

Electrochemistry Communications, 2015, 60, 58.

F. Murgia, L. Monconduit, L. Stievano, R. Berthelot

Electrochemical magnesiumation of the intermetallic InBi through conversion-alloying mechanism

Electrochimica Acta – 2016, 209, 730.

F. Murgia, P. Antitomaso, L. Stievano, L. Monconduit, R. Berthelot

Express and low-cost microwave synthesis of the ternary Chevrel phase $\text{Cu}_2\text{Mo}_6\text{S}_8$ for application in rechargeable magnesium batteries

Journal of Solid State Chemistry, 2016, 242, 151.

Oral presentations:

F. Murgia, R. Berthelot, L. Stievano, L. Monconduit

Synthesis and characterization of Bi and Mg_3Bi_2 ball-milled materials as negative electrodes of Mg batteries

Groupe Français d'Étude des Composés d'Insertion, 2015

F. Murgia, R. Berthelot, L. Stievano, L. Monconduit

Electrochemical mechanism and performances of Bi and Mg₃Bi₂ as negative electrodes for Mg batteries

Lithium Battery Discussions, 2016

As co-author:

R. Berthelot, F. Murgia, L. Stievano, L. Monconduit

Intermetallics, alloys and composite materials for negative electrodes in supervalent-ion batteries

Oral presentation - EMN meeting, 2015

R. Berthelot, F. Murgia, L. Stievano, L. Monconduit

Mg-battery anodes based on p-block elements: performances and electrochemical mechanisms

Oral presentation - 227th ECS meeting, 2015

E. Weldekidan, F. Murgia, L. Stievano, L. Monconduit, R. Berthelot

Mechanochemistry for Bi-based negative electrode materials of Mg-battery

Poster - Mech'cheM, 2015

Romain Berthelot, Fabrizio Murgia, Lorenzo Stievano, Laure Mondonduit

Electrochemical magnesianation of the intermetallic InBi: A conversion-alloying mechanism

Poster - GFECI, 2015

Résumé étendu

1. Contexte de l'étude

L'histoire de l'Homme depuis son apparition sur Terre jusqu'aux sociétés contemporaines a été radicalement marquée par des révolutions énergétiques. D'abord le contrôle du feu, puis la domestication des animaux, l'esclavage, et finalement l'utilisation des combustibles fossiles comme le carbone et le pétrole : les sociétés ont atteint des niveaux de développement de plus en plus croissants. Pourtant, le maintien de ces conditions a souvent été subordonné à la recherche de nouveaux vecteur énergétiques ainsi que de ressources alternatives. Actuellement, ce scénario semble se préfigurer de nouveau, avec une demande croissante d'énergie représentée par une augmentation dans la consommation des combustibles fossiles (Figure 99).[1]



Figure 99 – Le Monde doit faire face à l'augmentation des besoins en énergie qui doit soutenir soit le progrès technologique dans les pays occidentaux, soit l'expansion des nouvelles économies (Reproduction depuis [1]).

Cette demande est provoquée à la fois par les pays développés mais surtout par les économies en voie de développement et, bien que la disponibilité de pétrole ait augmenté dans les dernières décennies,[2] les contraintes de nature géopolitique pour l'exploitation de cette source peuvent être rédhibitoires pour les pays non producteurs.

De plus, l'utilisation des combustibles fossiles doit être fortement limitée à cause de leur impact négatif sur le climat, due à la production de CO₂, responsable de l'augmentation de l'effet de serre naturel.[3]

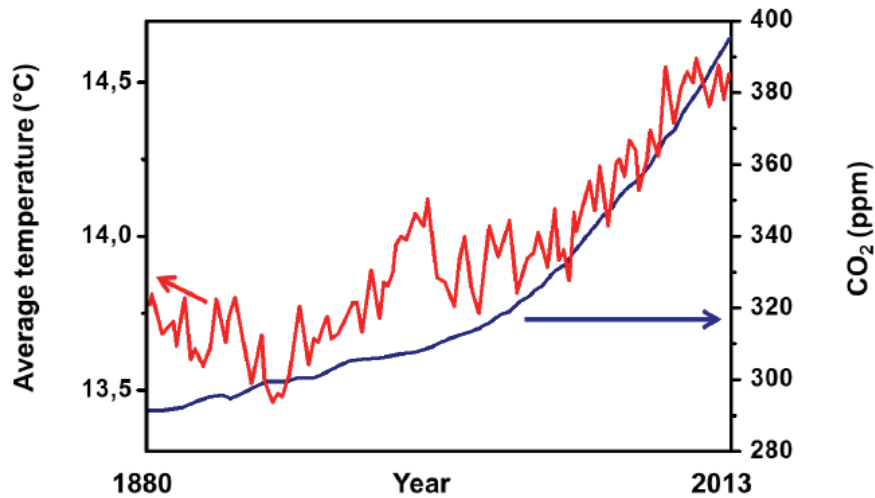


Figure 100 – Bien que la communauté scientifique ne soit pas complètement convaincue de la relation causale entre l'augmentation du CO₂ dans l'atmosphère et le réchauffement de la planète, ces deux phénomènes semblent reliés linéairement (Adapté de (3)).

Une alternative viable aux combustibles fossiles dans la production d'énergie est l'exploitation des sources renouvelables (soleil, vent, eau, etc.). Pourtant ces dernières présentent l'inconvénient de ne pas fonctionner de façon constante. Pour récupérer l'excès d'énergie qui est produit et la délivrer lorsque l'installation ne fonctionne pas, un système de stockage est nécessaire. Les batteries représentent une solution à cette limitation, en étant des dispositifs capables d'emmagasiner l'énergie électrique sous forme d'énergie chimique et de la reconvertir dès que c'est nécessaire. L'utilisation des combustibles fossiles pour la production d'énergie électrique n'est qu'une partie de la demande mondiale : 72% est employé pour alimenter les moyens de transport et ce pourcentage est censé augmenter dans les prochaines années.[1] Encore une fois les batteries représentent une alternative viable et les véhicules électriques et hybrides sont désormais une réalité qui peut rivaliser avec les véhicules conventionnels.[4][5][6]

Cette « révolution énergétique » moderne a été certainement favorisée par le développement des dispositifs de stockage à base de lithium et en particulier, la batterie aux ions lithium. Depuis sa commercialisation en 1991 par SONY, la batterie « Li-ion » est devenue la technologie de référence dans le stockage réversible d'énergie et son utilisation devient de plus en plus importante, même pour des

applications qui ont besoin d'importantes valeurs de densité d'énergie (comme les véhicules électriques).[16] Cependant, la possibilité que le lithium devienne le principal vecteur énergétique a été récemment mise en question,[17] pour diverses raisons :

- Le lithium est un élément relativement rare et peu répandu dans la croûte terrestre.[19][20] Son exploitation pourrait donc engendrer les mêmes problèmes géopolitiques des combustibles fossiles.[24]
- L'installation de dispositifs de stockage couplés avec des centrales de production d'énergie à partir de sources renouvelables serait économiquement désavantageuse pour le prix de certains composants (CO₂).
- Nonobstant les développements faits par la recherche fondamentale et les améliorations dans l'ingénierie de la pile pour augmenter les capacités massiques et volumiques (c.à.d. la quantité d'énergie stockée par unité de masse ou de volume), cette technologie semblerait avoir atteint son développement maximal.[17]

La recherche des systèmes de stockage réversible d'énergie autres que le lithium est donc une réalité et plusieurs efforts ont été fait dans les systèmes basés sur le sodium.[27] La recherche se dirige également vers les cations multivalents comme le magnésium, qui pourrait permettre d'atteindre des capacités plus élevées.[40]

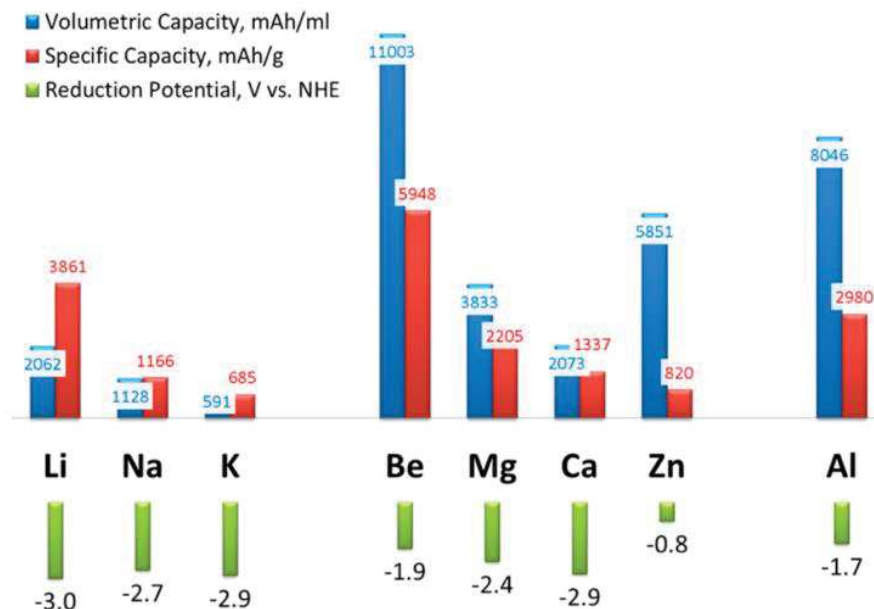


Figure 101 – Les éléments multivalents offrent des capacités spécifiques plus élevées que celles des éléments monovalents (Reproduction depuis [40]).

Le magnésium est le 7^{ème} élément le plus abondant dans la croûte terrestre et le 3^{ème} dans l'eau de mer.[59][61] Son exploitation est moins onéreuse que celle du lithium. De plus, c'est un élément non toxique, avec un point de fusion élevé (650 °C) et une plus faible réactivité vis-à-vis de l'air et de l'eau. Il est léger et plus dense que le Li (1.74 g cm⁻³ vs. 0.53 cm⁻³), son cation est divalent et il fournit une densité d'énergie volumique de 3837 mAh cm⁻³, qui est double par rapport à celle du Li.[62] Si son potentiel de réduction de 680 mV moins négatif par rapport à celui du couple Li⁺/Li questionne son utilisation pour des batteries à hautes densités d'énergie, sa capacité volumique élevée en fait un candidat crédible dans toutes les applications qui demandent l'espace le plus réduit possible pour l'installation de la batterie (voitures, robots, etc.).[61][62][63]

M ²⁺	Abondance dans la croûte terrestre (ppm)[59]	Coût (US\$/tonne)	T _f (°C)	E° (V vs. ESH)	g/mol e ⁻	Rayon ionique de Shannon (Å)[41]	Capacités théoriques[40]	
							(mAh g ⁻¹)	(mAh cm ⁻³)
Li ⁺	2	6400 ^a	180	-3.04	6.941	0.76	3800	2060
Na ⁺	23600	250 ^a	98	-2.71	22.99	1.02	1160	1140
Mg²⁺	23300	1990	650	-2.37	12.15	0.72	2200	3800
Ca ²⁺	41500	160 ^a	851	-2.87	20.04	1.00	1340	2060
Zn ²⁺	70	2280	420	-0.76	32.69	0.74	820	5851
Al ³⁺	80000	1635	660	-1.67	8.99	0.53	2980	8046

Tableaux 21 – Résumé de la disponibilité, du coût et des propriétés physiques et électrochimiques de différents éléments. ^a : coût d'une tonne de carbonate.

La limitation la plus contraignante dans les batteries au lithium est la formation de dendrites, qui peut causer des courts-circuits. Par contre, Matsui a prouvé que la déposition électrochimique de magnésium se fait sans la formation de dendrite, ce qui garantit une meilleure sécurité.[65] Pourtant, la réalisation d'une véritable batterie magnésium n'est pas évidente, à cause de l'incompatibilité entre les électrolytes conventionnels (solutions d'un sel contenant Mg dissout dans des solvants, organiques, habituellement des carbonates) et le magnésium métal : la réaction entre ces deux composants forme une couche de passivation sur la surface métallique qui empêche le fonctionnement de la cellule.[66]

Cette importante limitation n'a pas empêché la réalisation d'un prototype de batterie magnésium rechargeable, proposé par Aurbach *et al.* en 2000.[72] Les auteurs ont

utilisé un électrolyte basée sur la combinaison d'un acide de Lewis (AlCl_3) et une base de Lewis (MgR_2 , R = éthyl-, butyl-) dissous dans le THF, ce qui permet la déposition réversible de Mg. Ce dispositif, avec Mo_6S_8 comme électrode positive fournit une capacité spécifique de 60 mAh g^{-1} pendant 600 cycles.

En revanche, une éventuelle mise sur le marché de ce type de dispositifs est impossible, à cause de la réactivité élevée de cette gamme d'électrolytes. Une solution pourrait être le remplacement du magnésium métal avec d'autres électrodes négatives qui permettrait d'utiliser des électrolytes « conventionnels ». Les candidats comme électrodes négatives doivent être capables de réagir de façon réversible et à bas potentiel avec le Mg. Il a été démontré que certains éléments du bloc *p* sont capables de s'allier électrochimiquement avec le lithium et le sodium, parfois avec des mécanismes réactionnels assez différents.[36] La possibilité de former ces types d'alliages avec le magnésium a été explorée récemment : en 2011 Arthur *et al.* étudient la réaction d'alliage électrochimique du Mg avec Bi, Sb et $\text{Bi}_x\text{Sb}_{1-x}$. [147] Bien que la capacité en première décharge obtenue dans le cas du Sb soit le double par rapport à celle de Bi, ce dernier fournit une capacité assez stable pendant 100 cycles. Les propriétés intéressantes fournies par le Bi ont encouragé d'autres études. Par exemple, l'utilisation de nanotubes de Bi permet de garder des bonnes performances électrochimiques dans les tests à fortes densités de courant.[78]

L'étain, qui a été largement étudié dans les systèmes bases sur le lithium,[150][151][153] a été aussi testé par Singh *et al.* en 2013 sous forme des nanoparticules.[77] La magnésiation de l'étain est obtenue pendant la première décharge, mais une rapide chute des performances électrochimiques est observée. Celle-ci est probablement due à l'importante expansion volumique lors de la réaction d'alliage. Pour mitiger cette contrainte, Parent *et al.* en 2014 ont proposé une électrode composite graphène/ β -SnSb. Lors des premiers cycles, l'électrode subit un changement dans sa structure amenant la formation d'un réseau de nanoparticules d'étain, entouré par l'antimoine et carbone. Les capacités spécifiques observées entre 300 et 350 mAh g^{-1} représentent une amélioration par rapport au travail de Singh. Il est néanmoins nécessaire de souligner la perte de capacité constante après le 15^{ème} cycle et la difficulté dans le cyclage d'électrodes à base d'étain.[158]

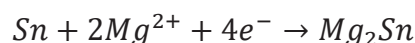
En 2015, Periyapperuma *et al.* ont démontré la magnésiation réversible du plomb, qui se produit à très pas potentiel (0.125 V). [164]

Toutes ces études démontrent la possibilité d'utiliser les éléments du bloc p comme alternative possible au magnésium métal dans des dispositifs de stockage basés sur le magnésium. Pourtant, la relative nouveauté dans l'investigation de ce type de dispositifs n'a pas encore permis l'élucidation des mécanismes réactionnels qui sont à la base de la formation électrochimique des alliages et qui est utile pour mieux comprendre les performances non optimales. En plus, une mise sur marché future de ce type de batteries nécessiterait des formulations d'électrode plus simples et économiquement avantageuses, tandis que celles proposées dans la littérature sont difficilement mises en œuvre à l'échelle industrielle. Les objectifs de cette thèse se résument en trois points :

- Étudier les propriétés électrochimiques vis-à-vis du Mg de certains éléments du bloc *p* sous forme de poudre micrométrique et en utilisant des formulations simples.
- Augmenter les performances des premières électrodes, en recherchant des possibles synergies qui pourraient être obtenue grâce à des composés binaires.
- Élucider les mécanismes de magnésiation/demagnésiation pour les matériaux actifs, avec l'utilisation des techniques *operando*.

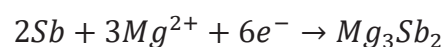
2. Résultats expérimentaux

Le premier élément qui a été étudié est l'étain. Depuis le diagramme de phase Mg-Sn il y a une seule phase intermétallique stable, Mg₂Sn.[186] En conséquence, la magnésiation complète de l'étain est donnée par l'équation suivante :



Cette réaction électrochimique fournit une capacité spécifique de 903 mAh g⁻¹. Les tests en mode galvanostatique sur les électrodes à base d'étain micrométrique n'ont pas été concluants. Les plateaux correspondants aux réactions de magnésiation et demagnésiation sont observés, mais la quantité Mg qui réagit est très faible et inférieure à la valeur théorique.

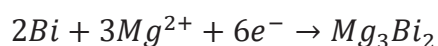
L'antimoine est le deuxième élément qui a été testé pendant cette thèse. La réaction d'alliage avec le Mg est la suivante :



En accord avec le diagramme de phase binaire Mg-Sb.[187] La capacité spécifique théorique est 660 mAh g⁻¹. Les tests électrochimiques n'ont montré aucune évidence

de réaction avec le Mg. Ce comportement est assez surprenant, si on le compare avec les bonnes propriétés électrochimiques de l'antimoine vis-à-vis du Li et du Na.[36][188]

Des meilleurs résultats ont été obtenus avec le Bi. Faisant partie du même groupe de l'antimoine, il forme aussi un seul composé intermétallique stable, Mg_3Bi_2 :



Avec une capacité spécifique de 380 mAh g^{-1} . À différence du Sb, Bi sous forme micrométrique est capable de s'allier électrochimiquement avec le Mg jusqu'à la valeur théorique de la capacité. La réaction d'alliage se traduit par un plateau à 0.23 V qui reste stable tout au long de la décharge. La formation de la phase Mg_3Bi_2 est confirmée par l'analyse du diffractogramme, collecté *ex situ* sur l'électrode après magnésiation. La charge suivante montre une réversibilité de la réaction élevée et une très faible polarisation (Figure 102).

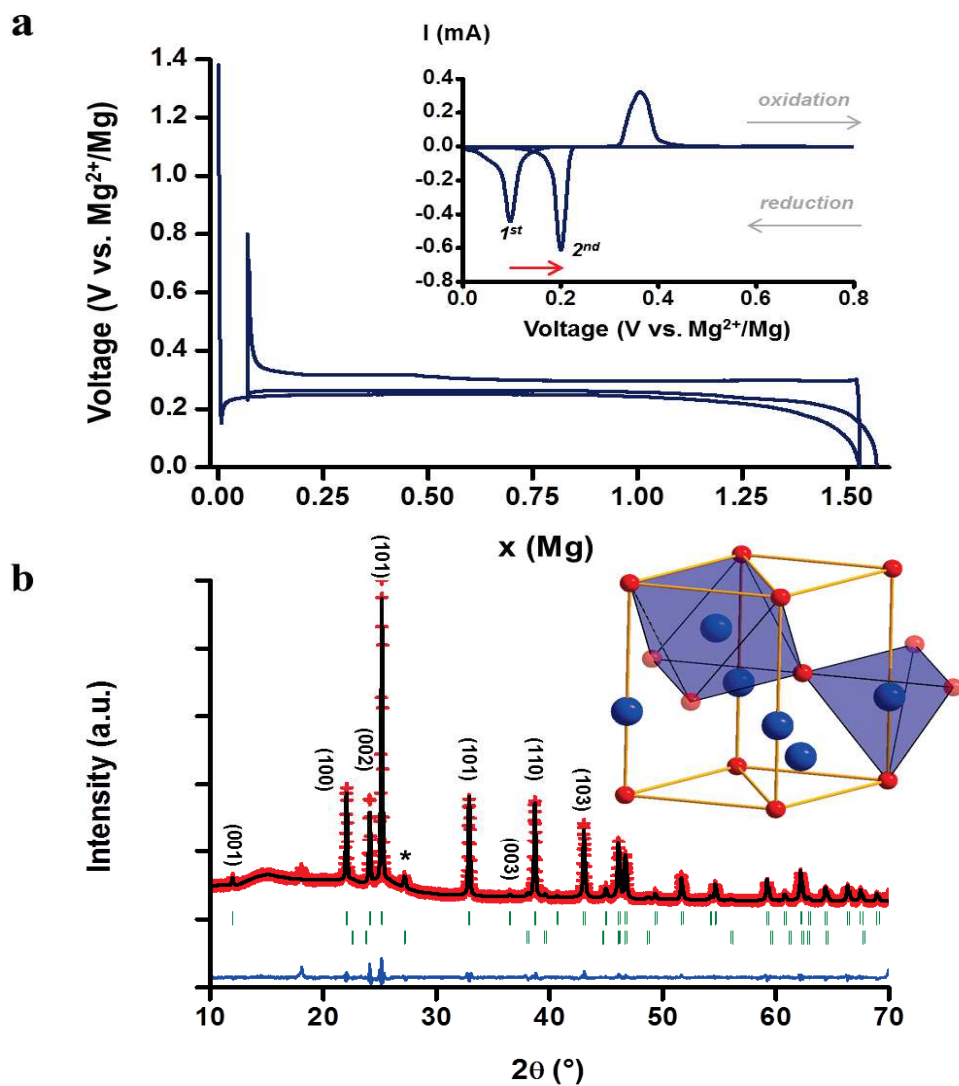


Figure 102 – a : courbe galvanostatique obtenue lors du cyclage d’une électrode à base de Bi micrométrique vis-à-vis du Mg. Électrolyte : $\text{EtMgCl} : 2\text{Et}_2\text{AlCl}$ dans THF. b : DRX *ex situ* confirmant la formation de Mg_3Bi_2 en fin de décharge (Adapté depuis [190]).

Une étude *operando* met en évidence la formation rapide de Mg_3Bi_2 avec un parfait biphasage, sans passer par une étape d'amorphisation (Figure 103). La démagnésiation montre une excellente réversibilité dans l'évolution des phases cristallographiques décrites auparavant. La charge suivante confirme le comportement déjà observé lors de la première magnésiation.

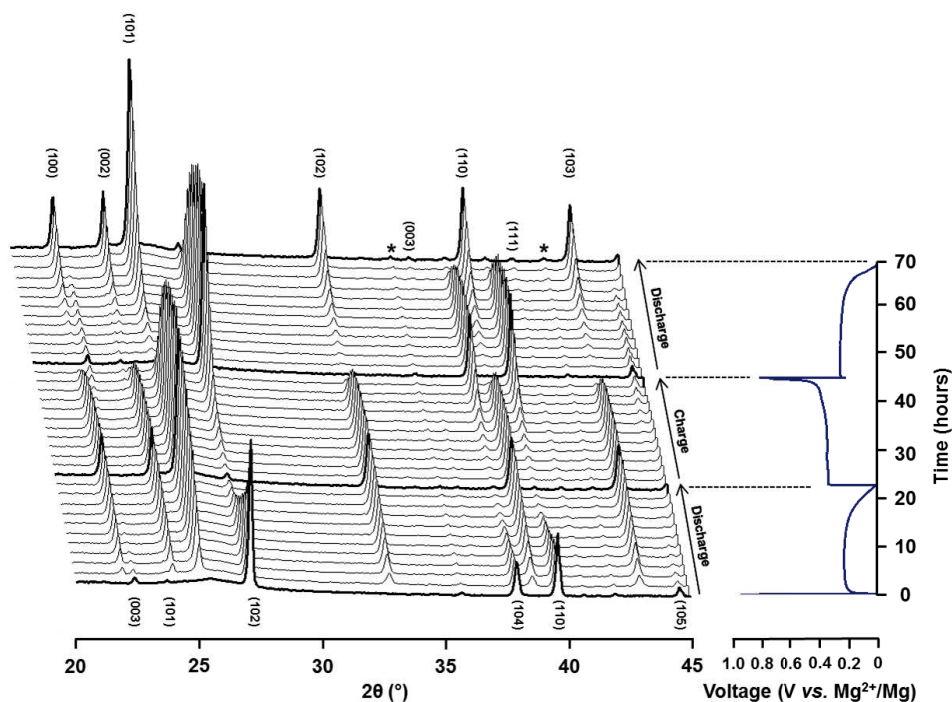


Figure 103 – DRX *operando* sur une électrode à base de Bi (Reproduction depuis [190]).

L'évaluation des performances a été menée grâce à des analyses à densités de courant croissantes, qui ont montré des capacités spécifiques comparables auxquelles offertes par les nanotubes de bismuth.

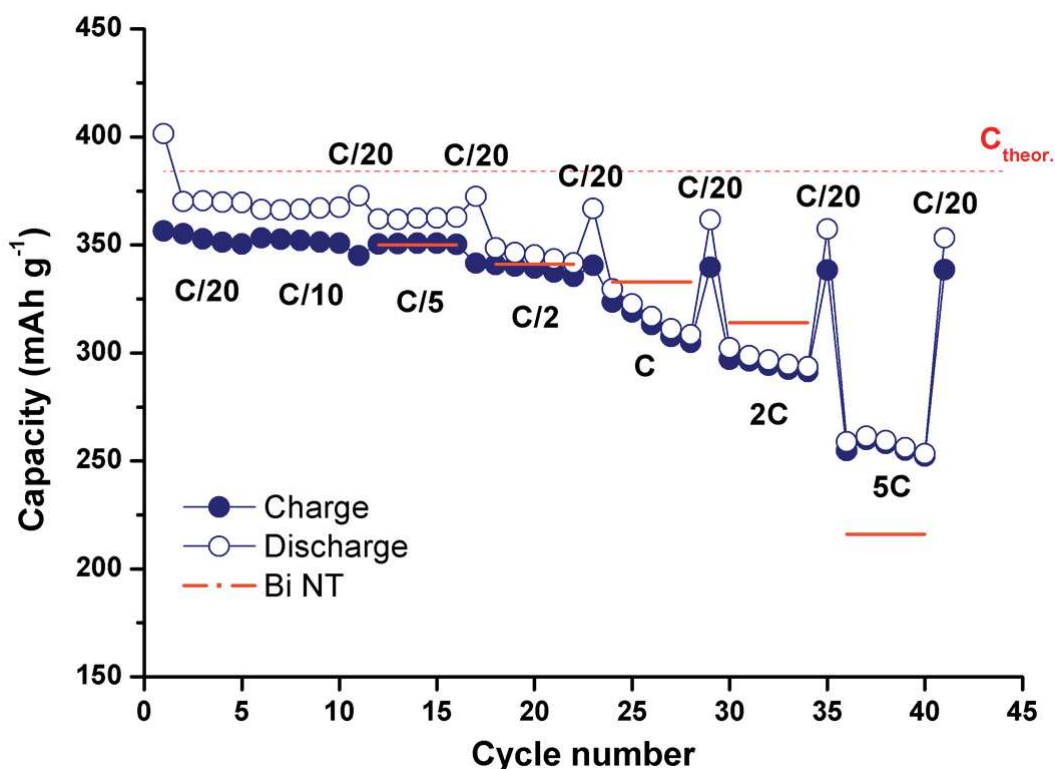
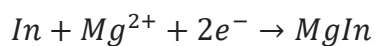


Figure 104 – Performances électrochimiques d’une électrode à base de Bi micrométrique à densités de courant croissantes et comparaison avec les résultats présents dans la littérature sur les nanotubes de Bi (Reproduction depuis [190]).

En prévision d’une application comme électrode négative dans une véritable batterie aux ions magnésium, c’est-à-dire sans Mg métal, la contrepartie magnésinée du Bi, Mg_3Bi_2 , a été synthétisée après 5 heures de broyage mécanique à haute énergie. L’analyse par diffraction des rayons X confirme l’obtention d’une phase pure qui correspond à Mg_3Bi_2 . Les images MEB confirment la taille micrométrique des particules qui composent le produit. Les propriétés électrochimiques des électrodes à bases de Mg_3Bi_2 ont été testées et ont été trouvées analogues à celles du Bi.

Dans l’idée de rechercher des éléments plus légers que le Bi, qui peuvent donc offrir des capacités théoriques plus élevées, le comportement électrochimique des électrodes à base d’In a été aussi testé.

Dans ce cas le diagramme de phase binaire Mg-In montre une plus grande variété de phases intermétalliques. Cependant, les tests électrochimiques en mode galvanostatique ont montré que seulement 0.92 moles de Mg ont réagi pour mole d’In. La formation de MgIn a été confirmée par DRX *ex situ* (Figure 105). Le processus électrochimique de magnésiation est donc :



La capacité spécifique théorique correspondante est de 467 mAh g⁻¹.

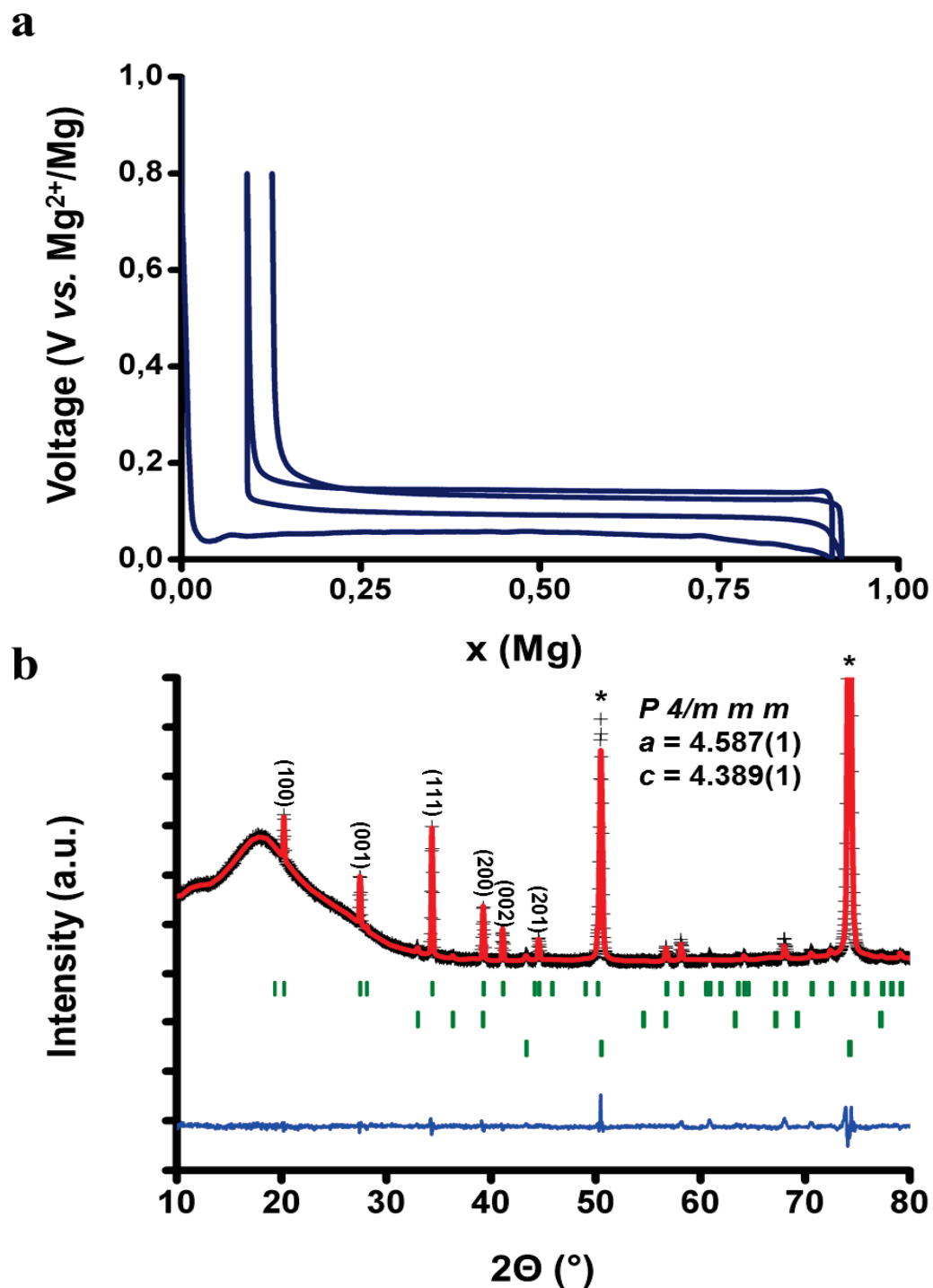


Figure 105 – Cyclage en mode galvanostatique d’une électrode à base d’In vis-à-vis de Mg. La formation de MgIn à la fin de la première décharge est confirmée par l’analyse DRX (Reproduction depuis [194]).

La première décharge a été étudiée par DRX operando. À différence de ce qu'on a observé dans le cas du Bi, la formation de la phase magnésinée n'est pas immédiate, soit à cause de la formation de particules nanométriques de MgIn qui ne sont pas visibles en DRX, soit à cause de la légère solubilité du Mg dans l'In (cf. diagramme de phase). Dans les diffractogrammes suivants il est possible d'observer la progressive formation de MgIn sans déplacement de raies.

L'évaluation des performances électrochimiques a amené à des résultats contradictoires : à faibles densités de courant les valeurs de capacités spécifiques sont supérieures par rapport à ceux du Bi et pourtant dans une plus haute gamme de courant on observe une chute des performances, qui démontrent des importantes limitations cinétiques dans ce système.

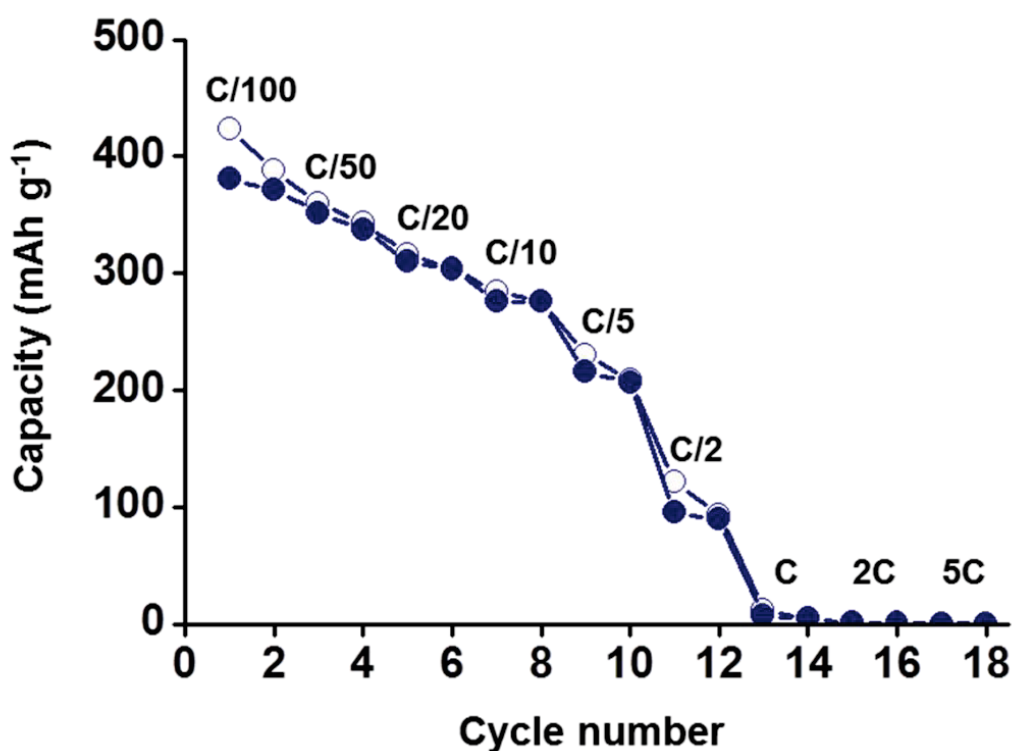


Figure 106 – Les performances des électrodes à base d'In sont limitées par des cinétiques lentes qui empêchent le cyclage à fortes densités de courant (Reproduction depuis [194]).

Comme dans le cas du Bi, les synthèses des phases binaires Mg-In ont été essayées par broyage à haute énergie. Parmi les compositions MgIn, Mg₂In et Mg₃In, il n'a été possible uniquement de synthétiser MgIn. Les tests électrochimiques menés sur des électrodes à base de MgIn ont donné des résultats en accord avec ceux obtenus en partant de l'In.

Inspirés par les excellentes performances électrochimiques du Bi vis-à-vis du Mg et dans l'idée d'augmenter les valeurs de capacité spécifique pour des électrodes à base de poudres micrométrique, il a été essayé de combiner le Bi avec les autres éléments plus légères précédemment étudiés.

Bi - Sn

Bi et Sn ne forment aucun composé intermétallique. Le mélange intime par mécanosynthèse permet la réalisation d'un composite Sn-Bi (50 :50 en moles). Dans ces conditions, il y a activation électrochimique de l'étain vis-à-vis du magnésium. Deux différents plateaux sont présents pendant la première décharge et correspondent à la magnésiation du bismuth et de l'étain, respectivement (Figure 107).

L'analyse DRX confirme la formation de Mg_2Sn après la première décharge. Malheureusement les processus ne sont pas complètement réversibles.

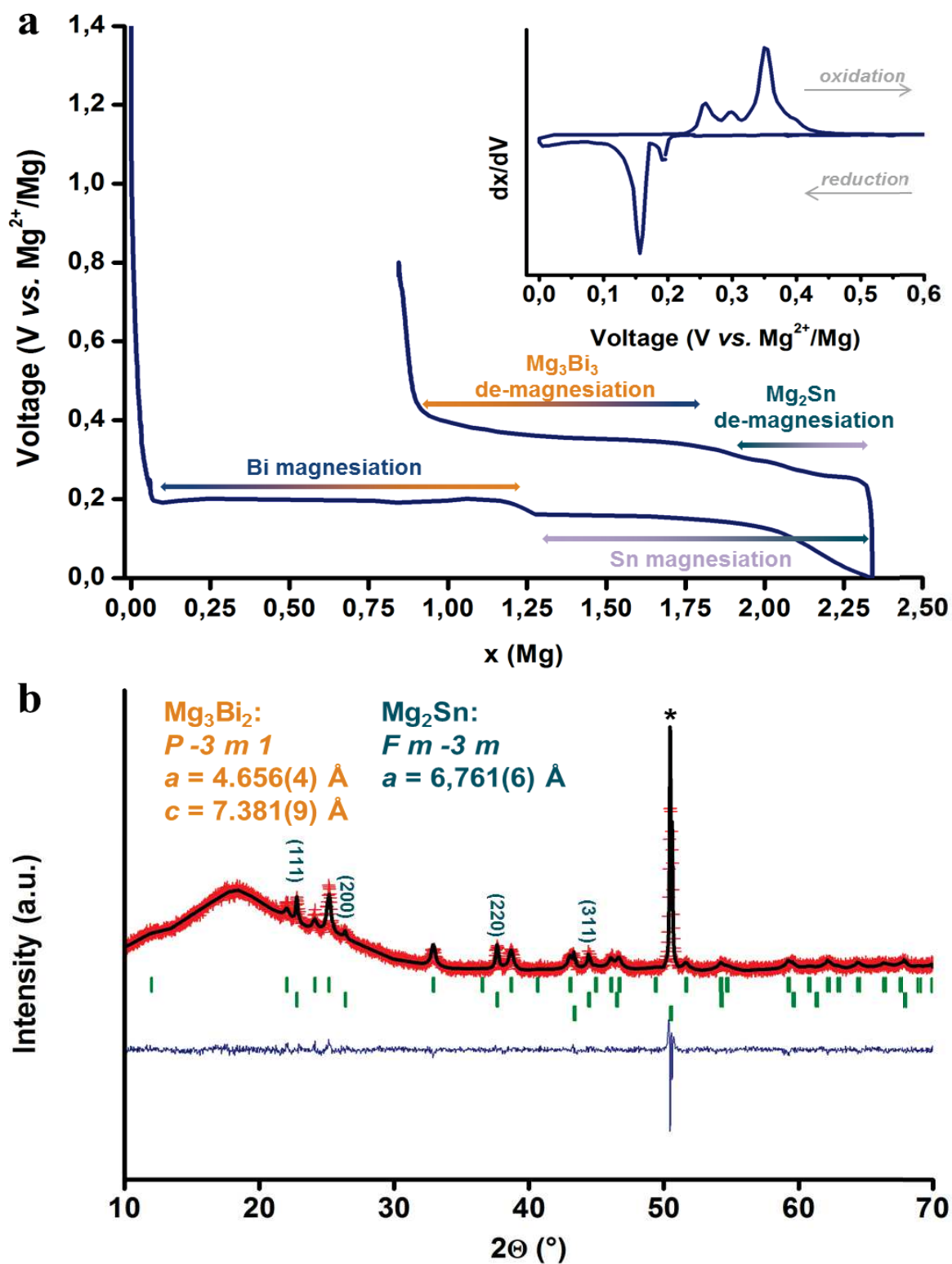


Figure 107 – Premier cycle en mode galvanostatique pour une électrode à base de $Sn_{50}Bi_{50}$. Au bout de la première décharge la formation de Mg_3Bi_2 ainsi que celle de Mg_2Sn est confirmée par la DRX *ex situ*.

L'étude *operando* a montré que les processus d'alliage sont les deux des biphasages et au premier abord, semblerait que la magnesiation ait lieu sur le bismuth et après sur

l'étain (Figure 108). Cependant, les pics de Mg_2Sn poussent légèrement du début, indiquant qu'une partie de l'étain réagit lors de la magnésiation du Bi, ce qui peut expliquer les fluctuations observées dans le premier plateau de décharge galvanostatique décrite précédemment.

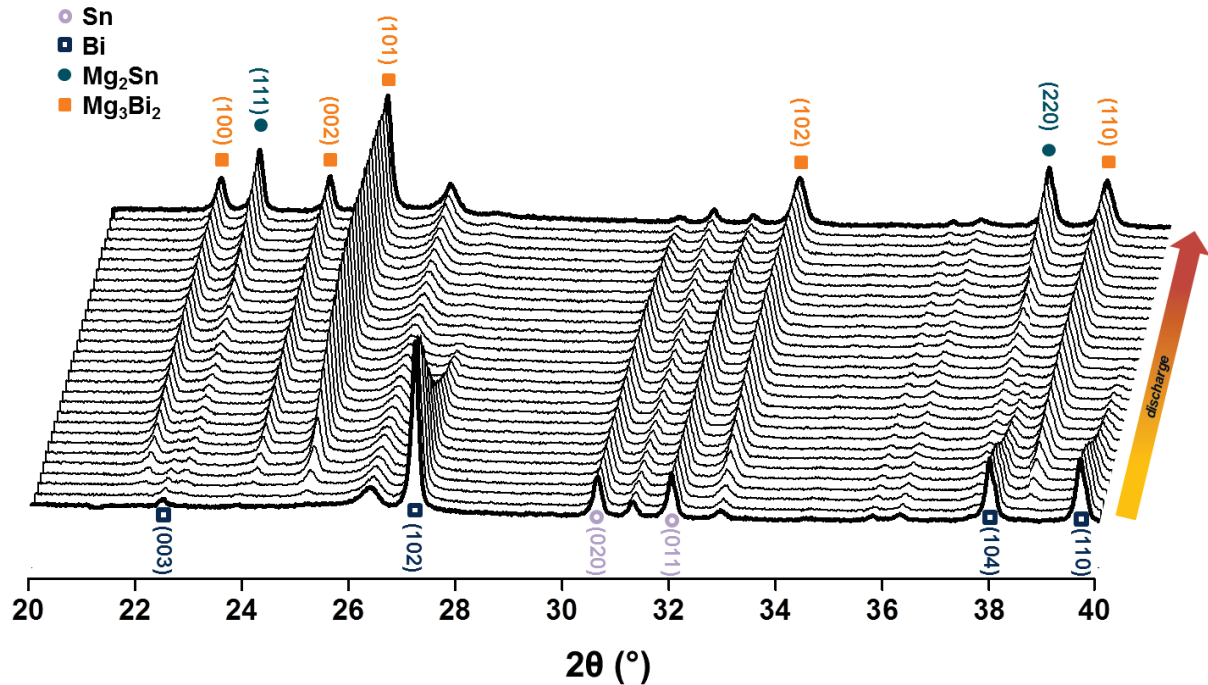


Figure 108 – Suivi de la première décharge d'une électrode à base de $Sn_{50}Bi_{50}$ par DRX *operando*.

L'évaluation des performances et l'influence du bismuth sur l'activité électrochimique de l'étain ont été évaluées, pour le composite 50 : 50 et pour d'autres rapports Sn : Bi. Dans tous les cas les deux phénomènes de magnésiation ont été observés. Les valeurs de capacité spécifiques obtenues à fortes densités de courant sont inférieures par rapport à celles du bismuth seul. L'effet « activateur » du bismuth a été prouvé même dans composites avec une très forte teneur en étain, comme dans le cas de $Sn_{0.95}Bi_{0.5}$ où il est toujours possible d'observer la magnésiation de l'étain. Ce résultat est étonnant, à la lumière de la quasi-totale absence d'activité électrochimique montrée par les électrodes complètement à base d'étain (Figure 109).

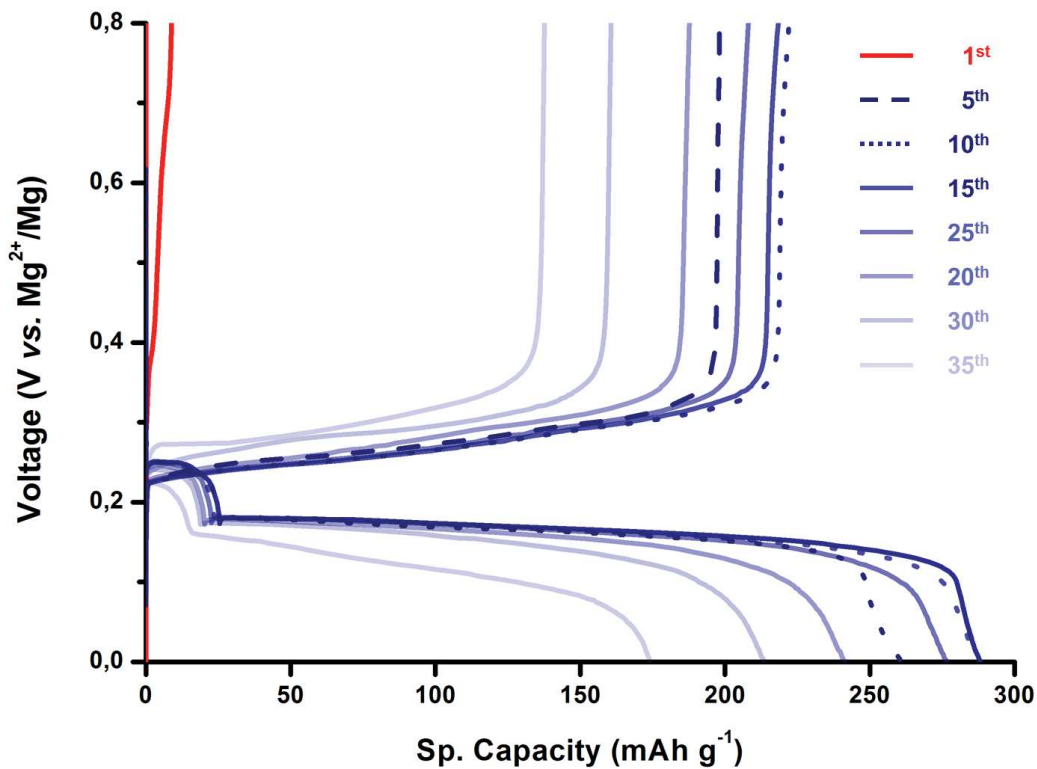


Figure 109 – La présence du bismuth a une influence positive dans l'activité électrochimique de l'Sn, même en faible quantité (5% en mole).

Bi - Sb

Le bismuth et l'antimoine font partie du même groupe dans le tableau périodique des éléments et leur diagramme de phase indique qu'ils sont complètement miscibles. Il a été donc possible de synthétiser par broyage à haute énergie plusieurs phases à différentes compositions le long de la solution solide. La magnésiation lors de la première décharge a été complète pour toutes les compositions. En revanche, la démagnésiation lors de la charge suivante est inversement proportionnelle à la quantité d'antimoine présent dans l'électrode.

Bi - In

Le diagramme de phase Bi – In présente une grande richesse de compositions, comme InBi, In₅Bi₂ et In₂Bi. Le broyage à haute énergie a seulement permis la seule synthèse du composé intermétallique InBi. Son comportement électrochimique vis-à-vis du Mg est montré dans la Figure 110.

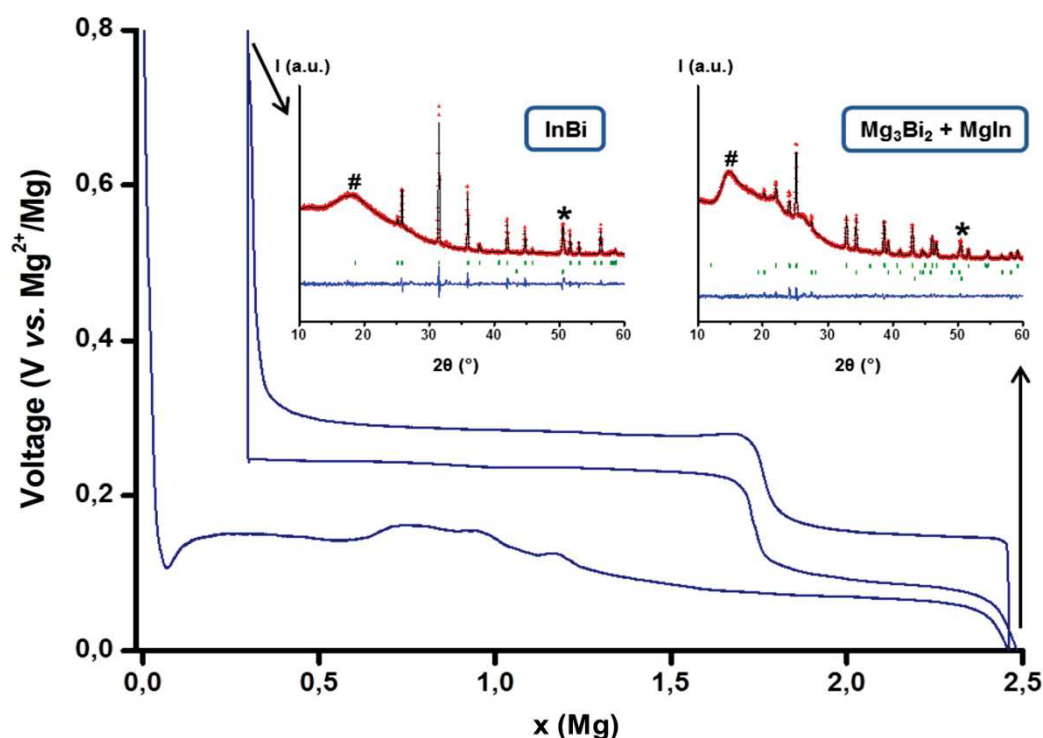
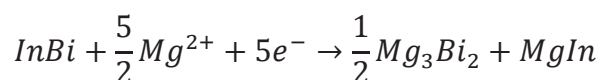


Figure 110 – Premier 1.5 cycle en mode galvanostatique d’une électrode à base de InBi. Les analyses DRX *ex situ* montrent la formation de Mg_3Bi_2 et $MgIn$ à la fin de la décharge mais aussi la reformation de InBi après la première charge (Reproduction depuis [227]).

On peut observer que 2.5 moles de magnésium ont réagi lors de la première décharge. Les analyses DRX *ex situ* en fin de décharge confirment la formation des deux alliages, bien que la signature électrochimique soit plus difficile à interpréter. Le processus électrochimique général est donc :



Dans la première charge on peut observer la demagnésiation de $MgIn$ et puis de Mg_3Bi_2 (plateaux à 0.16 et 0.29 V, respectivement). Étonnamment, à la fin de la première charge on reforme InBi.

L’étude *operando* sur cette électrode peut aider dans l’interprétation de l’allure de la première décharge et montre que la magnésiation de l’indium suit un parcours complètement différent par rapport à celle décrite dans le cas de l’indium seul, avec la formation et disparition des phases intermédiaires décrites dans le diagramme de phase Mg-In. Cette différence dans les chemins réactionnels peut être expliquée considérant la différence de taille des particules d’indium qui peut engendrer une différente réactivité.[227]

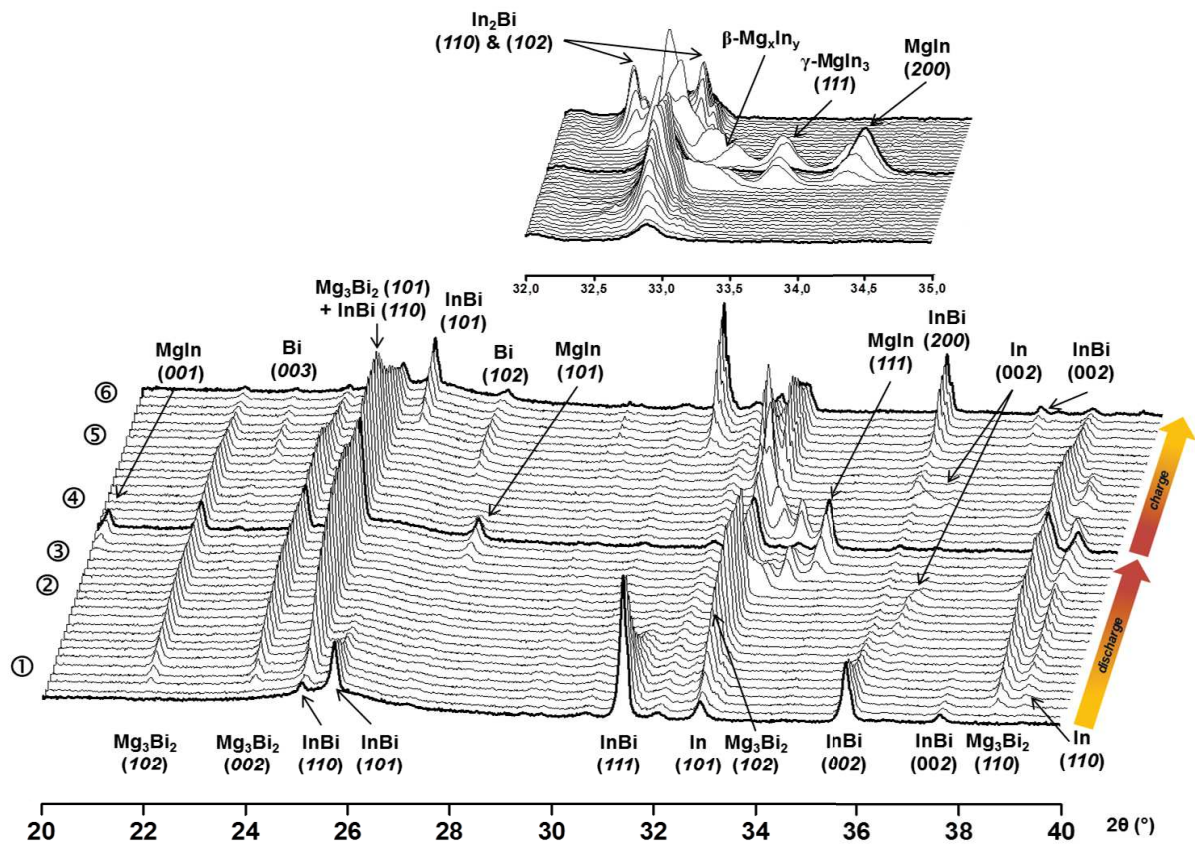


Figure 111 – Étude *operando* de la magnésiation et demagnésiation d’une électrode à base d’InBi (Reproduction depuis [227]).

Les propriétés électrochimiques de InBi sont intermédiaires entre celles des électrodes indium et bismuth seuls et les cinétiques lentes de l’indium semblent être rédhibitoires pour l’obtention de capacités élevées à fortes densités de courant.

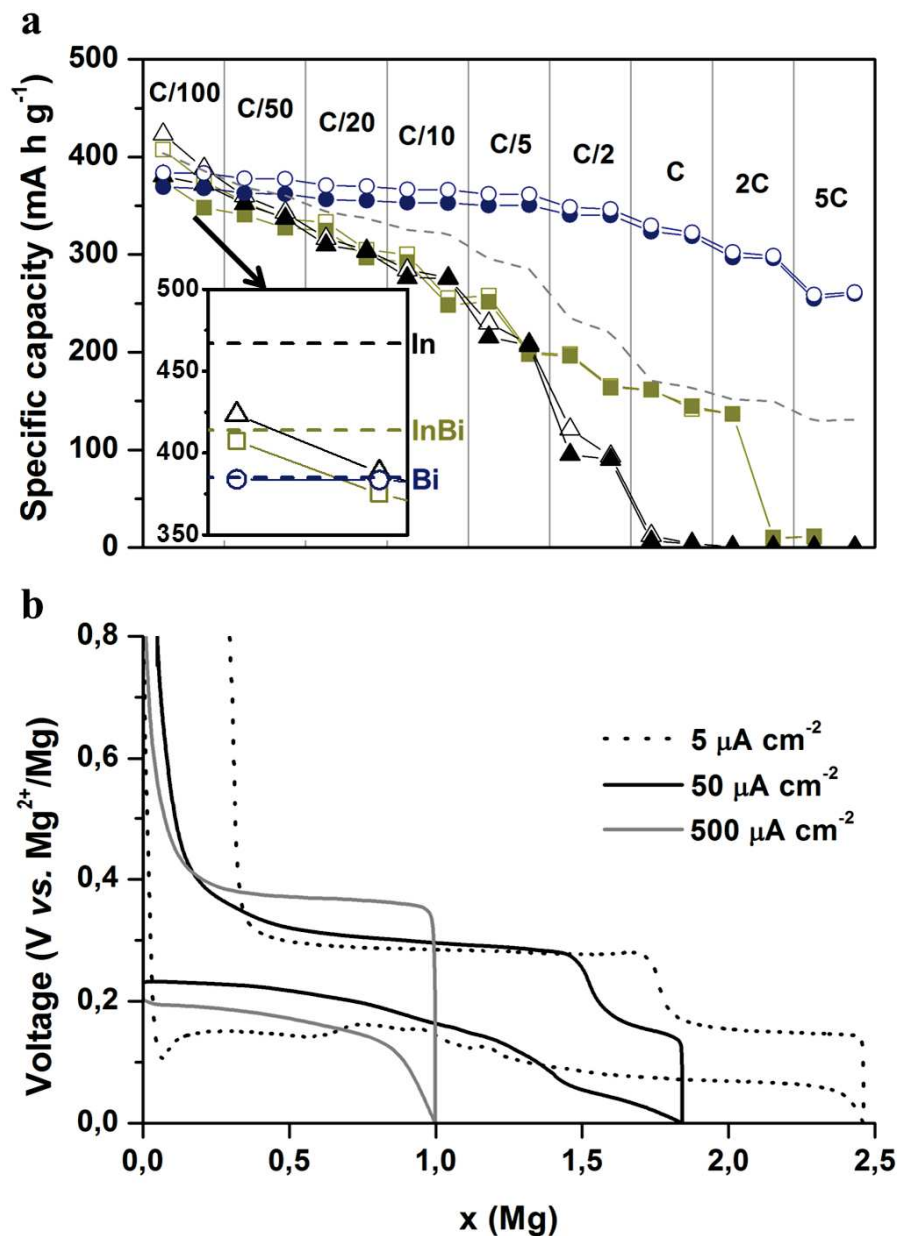


Figure 112 – Les performances électrochimiques de InBi sont intermédiaires entre celles du bismuth et de l'indium. Les cinétiques lentes de l'indium influencent négativement le cyclage à fortes densités de courant (Reproduction depuis [227]).

L'étude de ces matériaux d'alliage est aussi finalisée à la réalisation d'un prototype de batterie aux ions de magnésium avec des électrolytes conventionnels. Pour cela, le composé Mg_3Bi_2 , qui a fourni les meilleures propriétés électrochimiques en termes de stabilité de cyclage, a été testé vis-à-vis de Mo_6S_8 comme électrode positive, en utilisant $\text{Mg}(\text{TFSI})_2/\text{THF}$ comme électrolyte.

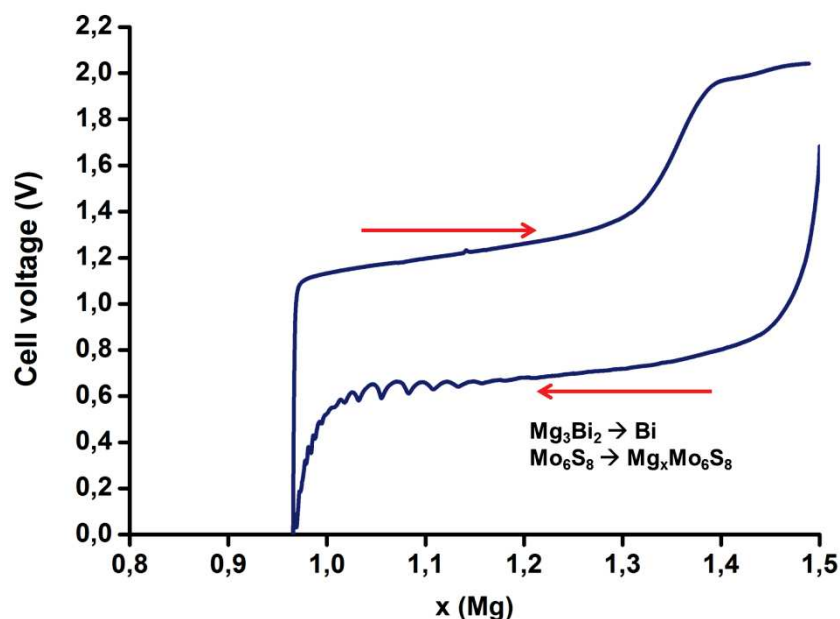


Figure 113 – Premier cycle d’une batterie Mg-ion, avec une électrode négative à base de Mg_3Bi_2 , une électrode positive à base de Mo_6S_8 et $\text{Mg}(\text{TFSI})_2/\text{THF}$ comme électrolyte (Adapté depuis [190]).

Il est important de souligner que la synthèse de la phase Mo_6S_8 ne peut pas être faite directement mais elle est obtenue après un traitement acide à partir du composé parent $\text{Cu}_2\text{Mo}_6\text{S}_8$. La préparation de celui-ci demande un long traitement thermique en tube scellé.[97] Pour réduire le temps de synthèse de la phase $\text{Cu}_2\text{Mo}_6\text{S}_8$, le traitement thermique classique a été remplacé par un chauffage micro-ondes qui permet de l’obtenir après seulement 400 s à une puissance de 1200 W.[222]

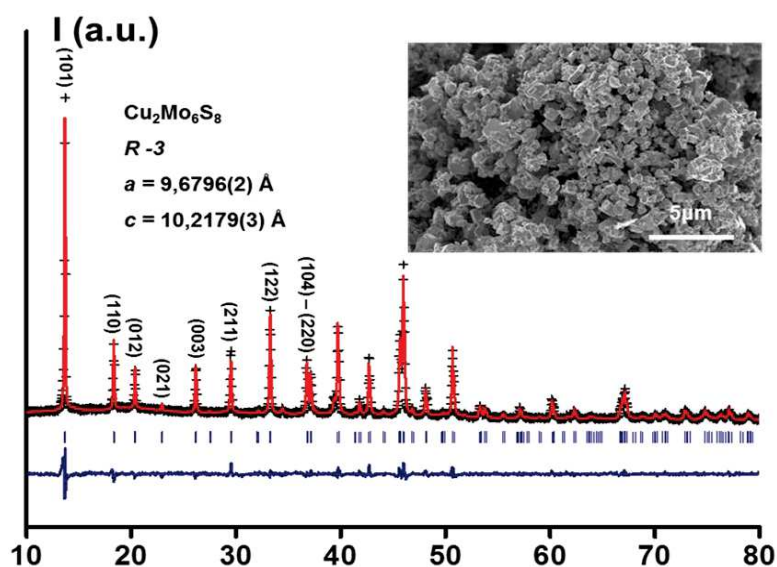


Figure 114 – DRX et MEB sur la poudre de $\text{Cu}_2\text{Mo}_6\text{S}_8$ obtenue par traitement micro-ondes (Reproduction depuis [222]).

Le cliché MEB confirme la taille micrométrique des particules. Les propriétés électrochimiques de Mo_6S_8 dérivé du $\text{Cu}_2\text{Mo}_6\text{S}_8$ obtenu par synthèse micro-ondes sont parfaitement superposables par rapport à celles fournies par la phase obtenue à l'issue de la synthèse classique.

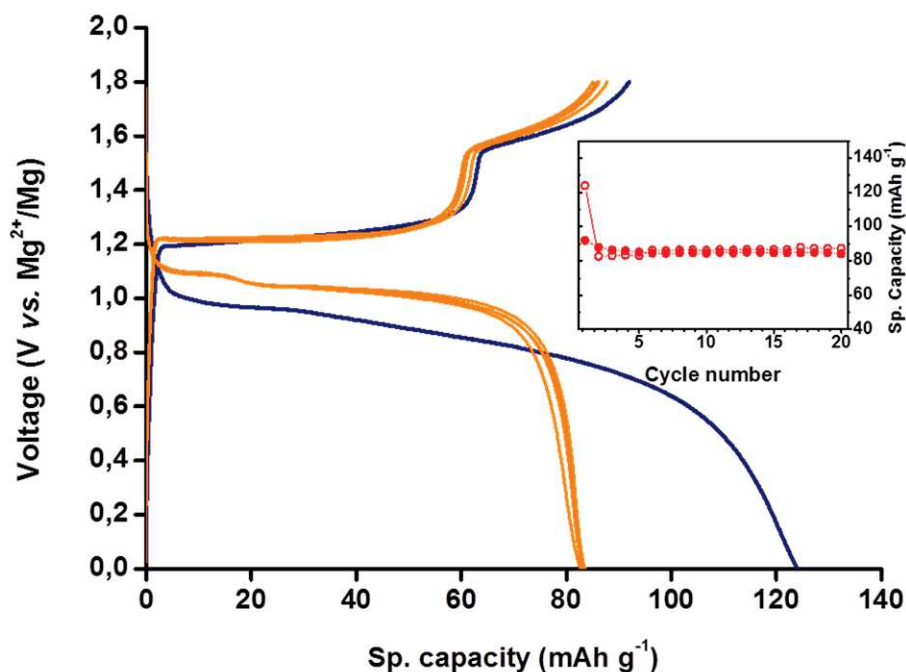


Figure 115 – Analyse en mode galvanostatique d'une électrode à base de Mo_6S_8 « micro-ondes » vis-à-vis du Mg (Reproduction depuis [222]).

3. Conclusion

Dans ces travaux de thèse, différents éléments du bloc p , seuls ou en combinaison, ont été testés comme électrodes négatives dans des batteries magnésium. La voie de synthèse choisie est le broyage à haute énergie puisque elle est simple, économique et adaptable à l'échelle industrielle. L'élucidation des mécanismes d'alliage a été effectuée par diffraction des rayons X en mode *operando*. Les propriétés électrochimiques des systèmes ont été étudiées et le meilleur candidat a été testé avec succès dans une véritable batterie Mg-ion équipée avec un électrolyte conventionnel.

Bibliography

- [1] World Energy Outlook 2015, 2015. doi:10.1787/weo-2015-en.
- [2] BP, BP Statistical Review of World Energy June 2016, 2013. <http://bp.com/statisticalreview>.
- [3] J.P. Holdren, K.D. Sullivan, Highlights of Climate Change Impacts in the United States: The Third National Climate Assessment, 2014. doi:10.7930/Jo1Z429C.On.
- [4] <https://www.tesla.com/model3>.
- [5] http://www.bmw.com/com/en/newvehicles/i/i3/2015/showroom/technical_data.html.
- [6] <https://www.daimler.com/products/trucks/mercedes-benz/urban-etruck.html>.
- [7] A.D. McNaught, A. Wilkinson, IUPAC Compendium of Chemical Terminology, 2nd ed., Blackwell, Oxford, 1997.
- [8] S. Martinet, Nouvelles générations de batteries des véhicules électriques et hybrides, Tech. Ingé. 203 (2012).
- [9] M.S. Whittingham, Electrical Energy Storage and Intercalation Chemistry, Science 192 (1976) 1126–1127.
- [10] E. Peled, The Electrochemical Behavior of Alkali and Alkaline Earth Metals in Nonaqueous Battery Systems—The Solid Electrolyte Interphase Model, J. Electrochem. Soc. 126 (1979) 2047–2051.
- [11] C.A. Vincent, B. Scrosati, Modern Batteries, Second Edi, Butterworth-Heinemann, 1997.
- [12] R. Yazami, P. Touzain, A reversible graphite-lithium negative electrode for electrochemical generators, J. Power Sources. 9 (1983) 365–371. doi:10.1016/0378-7753(83)87040-2.
- [13] K. Mizushima, P.C. Jones, P.J. Wiseman, J.B. Goodenough, Li_xCoO_2 ($0 < x < 1$): A new Cathode Material for Batteries of High Energy Density, Mater. Res. Bull. 4 (1981) 171–174.
- [14] B. Dunn, B. Dunn, H. Kamath, J. Tarascon, Electrical Energy Storage for the Grid : A Battery of Choices, Science. 928 (2012). doi:10.1126/science.1212741.
- [15] M. Armand, Issues and challenges facing rechargeable lithium batteries, Nature. 414 (2001) 359–367.
- [16] Global Lithium Market Outlook, 2016.
- [17] R. Van Noorden, The rechargeable revolution: A better battery, Nature. 507 (2014) 26–28. doi:10.1038/507026a.
- [18] J.B. Goodenough, K.S. Park, The Li-ion rechargeable battery: A perspective, J. Am. Chem. Soc. 135 (2013) 1167–1176. doi:10.1021/ja3091438.

- [19] N. Yabuuchi, K. Kubota, M. Dahbi, S. Komaba, Research Development on Sodium-Ion Batteries, *Chalcid Rev.* (2014). doi:/10.1021/cr500192f.
- [20] Mineral Commodity Summaries, 2016. doi:http://dx.doi.org/10.3133/70140094.
- [21] W. Tahil, *The Trouble With Lithium*, Meridian International Research. 2006. doi:10.1192/pb.33.10.396a.
- [22] S.W. Kim, D.H. Seo, X. Ma, G. Ceder, K. Kang, Electrode materials for rechargeable sodium-ion batteries: Potential alternatives to current lithium-ion batteries, *Adv. Energy Mater.* 2 (2012) 710–721. doi:10.1002/aenm.201200026.
- [23] <http://www.ffe.de/en/the-topics/resources-and-climate-protection/6-range-assessment-of-current-lithium-reserves>, (n.d.).
- [24] J.-M. Tarascon, Is lithium the new gold?, *Nat. Chem.* 2 (2010) 510. doi:10.1038/nchem.680.
- [25] <http://www.energie-rs2e.com/fr/news/batteries-sodium-ion-prototype-plein-promesses>.
- [26] <http://www.faradion.co.uk/technology/sodium-ion-technology/>.
- [27] K. Kubota, S. Komaba, Review—Practical Issues and Future Perspective for Na-Ion Batteries, *J. Electrochem. Soc.* 162 (2015) A2538–A2550. doi:10.1149/2.0151514jes.
- [28] M.M. Doeff, Y. Ma, S.J. Visco, L.C. De Jonghe, Electrochemical Insertion of Sodium into Carbon, *J. Electrochem. Soc.* 140 (1993) L169–L170.
- [29] M.H. Han, E. Gonzalo, G. Singh, T. Rojo, A comprehensive review of sodium layered oxides: powerful cathodes for Na-ion batteries, *Energy Environ. Sci.* 8 (2014) 81–102. doi:10.1039/C4EE03192J.
- [30] X. Xiang, K. Zhang, J. Chen, Recent advances and prospects of cathode materials for sodium-ion batteries, *Adv. Mater.* 27 (2015) 5343–5364. doi:10.1002/adma.201501527.
- [31] V.L. Chevrier, G. Ceder, Challenges for Na-ion Negative Electrodes, *J. Electrochem. Soc.* 158 (2011) A1011. doi:10.1149/1.3607983.
- [32] T.R. Jow, The role of conductive polymers in alkali-metal secondary electrodes, *J. Electrochem. Soc.* 134 (1987) 1730. doi:10.1149/1.2100746.
- [33] L. Baggetto, P. Ganesh, R.P. Meisner, R.R. Unocic, J.C. Jumas, C.A. Bridges, G.M. Veith, Characterization of sodium ion electrochemical reaction with tin anodes: Experiment and theory, *J. Power Sources.* 234 (2013) 48–59. doi:10.1016/j.jpowsour.2013.01.083.
- [34] S. Komaba, Y. Matsuura, T. Ishikawa, N. Yabuuchi, W. Murata, S. Kuze, Redox reaction of Sn-polyacrylate electrodes in aprotic Na cell, *Electrochem. Commun.* 21 (2012) 65–68. doi:10.1016/j.elecom.2012.05.017.
- [35] J. Qian, Y. Chen, L. Wu, Y. Cao, X. Ai, H. Yang, High capacity Na-storage and superior cyclability of nanocomposite Sb/C anode for Na-ion batteries, *Chem. Commun.* 48 (2012) 7070. doi:10.1039/c2cc32730a.
- [36] A. Darwiche, C. Marino, M.T. Sougrati, B. Fraisse, L. Stievano, L. Monconduit, Better cycling performances of bulk Sb in Na-ion batteries compared to Li-ion systems: an unexpected electrochemical mechanism., *J. Am. Chem. Soc.* 134 (2012) 20805–11.

doi:10.1021/ja310347x.

- [37] L. Xiao, Y. Cao, J. Xiao, W. Wang, L. Kovarik, Z. Nie, J. Liu, High capacity, reversible alloying reactions in SnSb/C nanocomposites for Na-ion battery applications, *Chem. Commun.* 48 (2012) 3321. doi:10.1039/c2cc17129e.
- [38] A. Darwiche, M.T. Sougrati, B. Fraisse, L. Stievano, L. Monconduit, Facile synthesis and long cycle life of SnSb as negative electrode material for Na-ion batteries, *Electrochem. Commun.* 32 (2013) 18–21. doi:10.1016/j.elecom.2013.03.029.
- [39] M.S. Islam, R. Dominko, C. Masquelier, C. Sirisopanaporn, A.R. Armstrong, P.G. Bruce, Silicate cathodes for lithium batteries: alternatives to phosphates?, *J. Mater. Chem.* 21 (2011) 9811–9818. doi:10.1039/C1JM10312A.
- [40] J. Muldoon, C.B. Bucur, T. Gregory, Quest for Nonaqueous Multivalent Secondary Batteries: Magnesium and Beyond, *Chem. Rev.* 114 (2014) 11683–11720.
- [41] R.D. Shannon, Revised effective ionic radii and systematic studies of interatomic distances in halides and chalcogenides, *Acta Crystallogr. Sect. A.* 32 (1976) 751–767. doi:10.1107/S0567739476001551.
- [42] M. Babai, M. Pallivathikal, Comparison of the behavior of the Li/SOCl₂ and Ca/SOCl₂ systems at elevated temperatures, *J. Power Sources.* 28 (1989) 325–334. doi:10.1016/0378-7753(89)80062-X.
- [43] A. Meitav, E. Peled, Calcium-Ca(AlCl₄)₂-Thionyl Chloride Cell: Performance and Safety, *J. Electrochem. Soc.* (1982).
- [44] R.J. Staniewicz, A Study of the Calcium-Thionyl Chloride Electrochemical System, *J. Electrochem. Soc.* 127 (1980) 782. doi:10.1149/1.2129758.
- [45] D. Aurbach, The Electrochemical Behavior of Calcium Electrodes in a Few Organic Electrolytes, *J. Electrochem. Soc.* 138 (1991) 3536. doi:10.1149/1.2085455.
- [46] A. Ponrouch, C. Frontera, F. Bardé, M.R. Palacín, Towards a calcium-based rechargeable battery, *Nat. Mater.* 15 (2015) 1–5. doi:10.1038/nmat4462.
- [47] A.L. Lipson, B. Pan, S.H. Lapidus, C. Liao, J.T. Vaughey, B.J. Ingram, Rechargeable Ca-Ion Batteries: A New Energy Storage System, *Chem. Mater.* 27 (2015) 8442–8447. doi:10.1021/acs.chemmater.5b04027.
- [48] G.. Amatucci, F. Badway, A. Singhal, B. Beaudoin, G. Skandan, T. Bowmer, I. Plitz, N. Pereira, T. Chapman, R. Jaworski, Investigation of Yttrium and Polyvalent Ion Intercalation into Nanocrystalline Vanadium Oxide, *J. Electrochem. Soc.* 148 (2001) A940–A950.
- [49] M. Cabello, F. Nacimiento, J.R. Gonzalez, G. Ortiz, R. Alcantara, P. Lavela, C. Pérez-Vicente, J.L. Tirado, Advancing towards a veritable calcium-ion battery: CaCo₂O₄ positive electrode material, *Electrochem. Commun.* 67 (2016) 59–64. doi:10.1016/j.elecom.2016.03.016.
- [50] C. Xu, Y. Chen, S. Shi, J. Li, F. Kang, D. Su, Secondary batteries with multivalent ions for energy storage, *Sci. Rep.* 5 (2015) 14120. doi:10.1038/srep14120.
- [51] G. Li, Z. Yang, Y. Jiang, C. Jin, W. Huang, X. Ding, Y. Huang, Towards polyvalent ion batteries: A zinc-ion battery based on NASICON structured Na₃V₂(PO₄)₃, *Nano Energy.* 25 (2016) 211–217. doi:10.1016/j.nanoen.2016.04.051.
- [52] Z. Rong, R. Malik, P. Canepa, G. Sai Gautam, M. Liu, A. Jain, K. Persson, G. Ceder,

- Materials Design Rules for Multivalent Ion Mobility in Intercalation Structures, *Chem. Mater.* 27 (2015) 6016–6021. doi:10.1021/acs.chemmater.5b02342.
- [53] S.D. Han, N.N. Rajput, X. Qu, B. Pan, M. He, M.S. Ferrandon, C. Liao, K.A. Persson, A.K. Burrell, Origin of Electrochemical, Structural, and Transport Properties in Nonaqueous Zinc Electrolytes, *ACS Appl. Mater. Interfaces.* 8 (2016) 3021–3031. doi:10.1021/acsami.5b10024.
- [54] Y. Li, M. Gong, Y. Liang, J. Feng, J.E. Kim, H. Wang, G. Hong, B. Zhang, H. Dai, Advanced zinc-air batteries based on high-performance hybrid electrocatalysts, *Nat Commun.* 4 (2013) 1805. doi:10.1038/ncomms2812.
- [55] N. Jayaprakash, S.K. Das, L. a. Archer, The rechargeable aluminum-ion battery, *Chem. Commun.* 47 (2011) 12610. doi:10.1039/c1cc15779e.
- [56] H. Sun, W. Wang, Z. Yu, Y. Yuan, S. Wang, S. Jiao, A new aluminium-ion battery with high voltage, high safety and low cost., *Chem. Commun.* 51 (2015) 11892–5. doi:10.1039/c5cc00542f.
- [57] L. Geng, G. Lv, X. Xing, J. Guo, Reversible Electrochemical Intercalation of Aluminum in Mo6S8, *Chem. Mater.* 27 (2015) 4926–4929. doi:10.1021/acs.chemmater.5b01918.
- [58] M.-C. Lin, M. Gong, B. Lu, Y. Wu, D.-Y. Wang, M. Guan, M. Angell, C. Chen, J. Yang, B.-J. Hwang, H. Dai, An ultrafast rechargeable aluminium-ion battery, *Nature.* 520 (2015) Pages: 324–328. doi:10.1038/nature14340.
- [59] D.R. Lide, W.M.M. Haynes, G. Baysinger, L.I. Berger, H. V Kehiaian, D.L. Roth, D. Zwillinger, M. Frenkel, R.N. Goldberg, *CRC Handbook of Chemistry and Physics*, 90th Edit, 2009.
- [60] M. Halka, B. Nordstrom, *Alkali & Alkaline Earth Metals*, First Edit, New York, 2010. doi:10.1017/CBO9781107415324.004.
- [61] H. Kim, G. Jeong, Y.-U. Kim, J.-H. Kim, C.-M. Park, H.-J. Sohn, Metallic anodes for next generation secondary batteries., *Chem. Soc. Rev.* 42 (2013) 9011–34. doi:10.1039/c3cs60177c.
- [62] H.D. Yoo, I. Shterenberg, Y. Gofer, G. Gershinsky, N. Pour, D. Aurbach, Mg rechargeable batteries: an on-going challenge, *Energy Environ. Sci.* 6 (2013) 2265. doi:10.1039/c3ee40871j.
- [63] C.B. Bucur, T. Gregory, A.G. Oliver, J. Muldoon, Confession of a Magnesium Battery, *J. Phys. Chem. Lett.* (2015) 3578–3591. doi:10.1021/acs.jpcclett.5b01219.
- [64] I. Yoshimatsu, T. Hirai, J. Yamaki, Lithium Electrode Morphology during Cycling in Lithium Cells, *J. Electrochem. Soc.* 135 (1988) 2422–2427.
- [65] M. Matsui, Study on electrochemically deposited Mg metal, *J. Power Sources.* 196 (2011) 7048–7055. doi:10.1016/j.jpowsour.2010.11.141.
- [66] D. Aurbach, I. Weissman, Y. Gofer, E. Levi, Nonaqueous magnesium electrochemistry and its application in secondary batteries., *Chem. Rec.* 3 (2003) 61–73. doi:10.1002/tcr.10051.
- [67] P.B. Balbuena, Y. Wang, eds., *Lithium-Ion Batteries - Solid-electrolyte Interphase*, Imperial College Press, London, 2004.
- [68] E. Peled, H. Stranze, M. Brand, 26th ISE Meet. Vienna, 1975.

- [69] D. Aurbach, Y. Gofer, Z. Lu, A. Schechter, O. Chusid, H. Gizbar, Y. Cohen, V. Ashkenazi, M. Moshkovich, R. Turgeman, E. Levi, A short review on the comparison between Li battery systems and rechargeable magnesium battery technology, *J. Power Sources*. 97–98 (2001) 28–32. doi:10.1016/S0378-7753(01)00585-7.
- [70] T.D. Gregory, R.J. Hoffman, R.C. Winterton, *Nonaqueous Electrochemistry of Magnesium*, *J. Electrochem. Soc.* 137 (1990) 775–780.
- [71] Y. Muramatsu, T. Harada, Catalytic asymmetric alkylation of aldehydes with Grignard reagents, *Angew. Chemie - Int. Ed.* 47 (2008) 1088–1090. doi:10.1002/anie.200704963.
- [72] D. Aurbach, Z. Lu, A. Schechter, Y. Gofer, H. Gizbar, R. Turgeman, Y. Cohen, M. Moshkovich, E. Levi, Prototype systems for rechargeable magnesium batteries, 407 (2000) 13–16.
- [73] L.F. Wan, D. Prendergast, The solvation structure of Mg ions in dichloro-complex solutions from first-principles molecular dynamics and simulated X-ray absorption spectra, *J. Am. Chem. Soc.* 1 (2014) 1–7.
- [74] H. Gizbar, Y. Vestfrid, O. Chusid, Y. Gofer, H.E. Gottlieb, V. Marks, D. Aurbach, Alkyl group transmetalation reactions in electrolytic solutions studied by multinuclear NMR, *Organometallics*. 23 (2004) 3826–3831. doi:10.1021/om049949a.
- [75] D. Aurbach, G.S. Suresh, E. Levi, A. Mitelman, O. Mizrahi, O. Chusid, M. Brunelli, Progress in rechargeable magnesium battery technology, *Adv. Mater.* 19 (2007) 4260–4267. doi:10.1002/adma.200701495.
- [76] O. Mizrahi, N. Amir, E. Pollak, O. Chusid, V. Marks, H. Gottlieb, L. Larush, E. Zinigrad, D. Aurbach, Electrolyte Solutions with a Wide Electrochemical Window for Rechargeable Magnesium Batteries, *J. Electrochem. Soc.* 155 (2008) A103. doi:10.1149/1.2806175.
- [77] N. Singh, T.S. Arthur, C. Ling, M. Matsui, F. Mizuno, A high energy-density tin anode for rechargeable magnesium-ion batteries., *Chem. Commun.* 49 (2013) 149–51. doi:10.1039/c2cc34673g.
- [78] Y. Shao, M. Gu, X. Li, Z. Nie, P. Zuo, G. Li, T. Liu, J. Xiao, Highly Reversible Mg Insertion in Nanostructured Bi for Mg Ion Batteries, *Nano Lett.* 20 (2014) 255–260.
- [79] H.S. Kim, T.S. Arthur, G.D. Allred, J. Zajicek, J.G. Newman, A.E. Rodnyansky, A.G. Oliver, W.C. Boggess, J. Muldoon, Structure and compatibility of a magnesium electrolyte with a sulphur cathode., *Nat. Commun.* 2 (2011) 427. doi:10.1038/ncomms1435.
- [80] F. Wang, Y. Guo, J. Yang, Y. Nuli, S. Hirano, A novel electrolyte system without a Grignard reagent for rechargeable magnesium batteries, *Chem. Commun.* 48 (2012) 10763. doi:10.1039/c2cc35857c.
- [81] E.G. Nelson, J.W. Kampf, B.M. Bartlett, Enhanced oxidative stability of non-Grignard magnesium electrolytes through ligand modification., *Chem. Commun.* 50 (2014) 5193–5. doi:10.1039/c3cc47277a.
- [82] P. Bian, Y. Nuli, Z. Abudoureyimu, J. Yang, J. Wang, A novel thiolate-based electrolyte system for rechargeable magnesium batteries, *Electrochim. Acta.* 121 (2014) 258–263. doi:10.1016/j.electacta.2013.12.184.
- [83] J. Muldoon, C.B. Bucur, A.G. Oliver, T. Sugimoto, M. Matsui, H.S. Kim, G.D. Allred, J.

- Zajicek, Y. Kotani, Electrolyte roadblocks to a magnesium rechargeable battery, *Energy Environ. Sci.* 5 (2012) 5941. doi:10.1039/c2ee03029b.
- [84] J. Muldoon, C.B. Bucur, A.G. Oliver, J. Zajicek, G.D. Allred, W.C. Boggess, Corrosion of magnesium electrolytes: chlorides – the culprit, *Energy Environ. Sci.* 6 (2013) 482. doi:10.1039/c2ee23686a.
- [85] R. Mohtadi, F. Mizuno, Magnesium batteries: Current state of the art, issues and future perspectives, *Beilstein J. Nanotechnol.* 5 (2014) 1291–1311. doi:10.3762/bjnano.5.143.
- [86] R. Mohtadi, M. Matsui, T.S. Arthur, S.-J. Hwang, Magnesium borohydride: from hydrogen storage to magnesium battery., *Angew. Chem. Int. Ed. Engl.* 51 (2012) 9780–3. doi:10.1002/anie.201204913.
- [87] Y. Shao, T. Liu, G. Li, M. Gu, Z. Nie, M. Engelhard, J. Xiao, D. Lv, C. Wang, J.-G. Zhang, J. Liu, Coordination chemistry in magnesium battery electrolytes: how ligands affect their performance., *Sci. Rep.* 3 (2013) 3130. doi:10.1038/srep03130.
- [88] R.E. Doe, R. Han, J. Hwang, A.J. Gmitter, I. Shterenberg, H.D. Yoo, N. Pour, D. Aurbach, Novel, electrolyte solutions comprising fully inorganic salts with high anodic stability for rechargeable magnesium batteries., *Chem. Commun.* 50 (2013) 243–245. doi:10.1039/c3cc47896c.
- [89] O. Chusid, Y. Gofer, H. Gizbar, Y. Vestfrid, E. Levi, D. Aurbach, I. Riech, Solid-State Rechargeable Magnesium Batteries, *Adv. Mater.* 15 (2003) 627–630. doi:10.1002/adma.200304415.
- [90] M.L. Aubrey, R. Ameloot, B.M. Wiers, J.R. Long, Metal–organic frameworks as solid magnesium electrolytes, *Energy Environ. Sci.* 7 (2014) 667. doi:10.1039/c3ee43143f.
- [91] S. Higashi, K. Miwa, M. Aoki, K. Takechi, A novel inorganic solid state ion conductor for rechargeable Mg batteries., *Chem. Commun.* 50 (2014) 1320–2. doi:10.1039/c3cc47097k.
- [92] P. Novak, W. Scheifele, O. Haas, Magnesium insertion batteries - an alternative to lithium?, *J. Power Sources.* 54 (1995) 479–482. doi:10.1016/0378-7753(94)02129-Q.
- [93] E. Levi, Y. Gofer, D. Aurbach, On the Way to Rechargeable Mg Batteries: The Challenge of New Cathode Materials, *Chem. Mater.* 22 (2010) 860–868. doi:10.1021/cm9016497.
- [94] P. Novak, R. Imhof, O. Haas, Magnesium insertion electrodes for rechargeable nonaqueous batteries – a competitive alternative to lithium?, *Electrochim. Acta.* 45 (1999) 351–367.
- [95] P. Saha, M.K. Datta, O.I. Velikokhatnyi, A. Manivannan, D. Alman, P.N. Kumta, Rechargeable magnesium battery: Current status and key challenges for the future, *Prog. Mater. Sci.* 66 (2014) 1–86. doi:10.1016/j.pmatsci.2014.04.001.
- [96] M.M. Huie, D.C. Bock, E.S. Takeuchi, A.C. Marschilok, K.J. Takeuchi, Cathode materials for magnesium and magnesium-ion based batteries, *Coord. Chem. Rev.* 287 (2015) 15–27. doi:10.1016/j.ccr.2014.11.005.
- [97] R. Chevrel, M. Sergent, J. Prigent, Sur de nouvelles phases sulfurées ternaires du Molybdène, *J. Solid State Chem.* 3 (1971) 515–519. doi:10.1016/0022-4596(71)90095-8.
- [98] T. Hughbanks, R. Hoffmann, Molybdenum chalcogenides: clusters, chains, and

- extended solids. The approach to bonding in three dimensions, *J. Am. Chem. Soc.* 105 (1983) 1150–1162. doi:10.1021/ja00343a014.
- [99] E. Levi, G. Gershinsky, D. Aurbach, O. Isnard, G. Ceder, E. Levi, G. Gershinsky, D. Aurbach, O. Isnard, G. Ceder, New Insight on the Unusually High Ionic Mobility in Chevrel Phases, *Chem. Mater.* 21 (2009) 1390–1399. doi:10.1021/cm900033v.
- [100] Ø. Fischer, Chevrel phases: Superconducting and normal state properties, *Appl. Phys.* 16 (1978) 1–28. doi:10.1007/BF00931416.
- [101] B. Seeber, M. Decroux, Ø. Fischer, Status and prospect of superconducting Chevrel phase wires for high magnetic field applications, *Phys. B.* 155 (1989) 129–135.
- [102] D.I. Kochubey, V.A. Rogov, V.P. Babenko, Low-temperature synthesis of supported hydrodesulfurization catalysts based on chevrel phases, *Kinet. Catal.* 50 (2009) 270–274.
- [103] M. Ohta, A. Yamamoto, H. Obara, Thermoelectric Properties of Chevrel-Phase Sulfides $M_xMo_6S_8$ (M: Cr, Mn, Fe, Ni), *J. Electron. Mater.* 39 (2009) 2117–2121. doi:10.1007/s11664-009-0975-0.
- [104] B.T. Matthias, M. Marezio, E. Corenzwit, A.S. Cooper, H.E. Barz, High-Temperature Superconductors, the First Ternary System, *Science.* 175 (1972) 1465–1466.
- [105] O. Peña, Chevrel phases: Past, present and future, *Phys. C Supercond. Its Appl.* 514 (2015) 95–112. doi:10.1016/j.physc.2015.02.019.
- [106] R. Chevrel, M. Sergent, J. Prigent, Un nouveau sulfure de molybdene : Mo_3S_4 preparation, proprietes et structure cristalline, *Mater. Res. Bull.* 9 (1974) 1487–1498. doi:10.1016/0025-5408(74)90095-6.
- [107] J.M. Tarascon, F.J. Disalvo, D.W. Murphy, G.W. Hull, E.A. Rietman, J. V. Waszczak, Stoichiometry and physical properties of ternary molybdenum chalcogenides $M_xMo_6X_8$ (X = S, Se; M = Li, Sn, Pb), *J. Solid State Chem.* 54 (1984) 204–212. doi:10.1016/0022-4596(84)90147-6.
- [108] W.R. McKinnon, J.R. Dahn, Structure and electrochemistry of $Li_xMo_6S_8$, *Phys. Rev. B.* 31 (1985) 3084–3087. doi:10.1016/0167-2738(87)90074-9.
- [109] E. Gocke, R. Schollhorn, G. Aselmann, W. Muller-Warmuth, Molybdenum Cluster Chalcogenides Mo_6X_8 : Intercalation of Lithium via Electron/Ion Transfer, *Inorg. Chem.* 26 (1987) 1805–1812.
- [110] J.M. Tarascon, G.W. Hull, P. Marsh, T. Haar, Electrochemical, Structural and Physical Properties of the Sodium Chevrel Phases $Na_xMo_6X_{8-y}I_y$ (X = S, Se and y = 0 to 2), *J. Solid State Chem.* 66 (1987) 204–224. doi:10.1016/0022-4596(87)90190-3.
- [111] E. Lancry, E. Levi, Y. Gofer, M. Levi, G. Salitra, D. Aurbach, Leaching chemistry and the performance of the Mo_6S_8 cathodes in rechargeable Mg batteries, *Chem. Mater.* 16 (2004) 2832–2838. doi:10.1021/cm034944.
- [112] E. Levi, E. Lancry, A. Mitelman, D. Aurbach, O. Isnard, D. Djurado, Phase Diagram of Mg Insertion into Chevrel Phases, $Mg_xMo_6T_8$ (T = S, Se). The Crystal Structure of Triclinic $MgMo_6Se_8$, *Chem. Mater.* 18 (2006) 3705–3714. doi:10.1021/cm060715m.
- [113] M.D. Levi, E. Lancry, H. Gizbar, Y. Gofer, E. Levi, D. Aurbach, Phase transitions and diffusion kinetics during Mg^{2+} - and Li^+ -ion insertions into the Mo_6S_8 chevrel phase compound studied by PITT, *Electrochim. Acta.* 49 (2004) 3201–3209.

doi:10.1016/j.electacta.2004.02.034.

- [114] M.D. Levi, H. Gizbar, E. Lancry, Y. Gofer, E. Levi, D. Aurbach, A comparative study of Mg^{2+} and Li^+ ion insertions into the Mo_6S_8 Chevrel phase using electrochemical impedance spectroscopy, *J. Electroanal. Chem.* 569 (2004) 211–223. doi:10.1016/j.jelechem.2004.03.004.
- [115] M.D. Levi, D. Aurbach, A comparison between intercalation of Li and Mg ions into the model Chevrel phase compound ($M_xMo_6S_8$): Impedance spectroscopic studies, *J. Power Sources.* 146 (2005) 349–354. doi:10.1016/j.jpowsour.2005.03.014.
- [116] M.D. Levi, E. Lancry, E. Levi, H. Gizbar, Y. Gofer, D. Aurbach, The effect of the anionic framework of Mo_6X_8 Chevrel Phase ($X = S, Se$) on the thermodynamics and the kinetics of the electrochemical insertion of Mg^{2+} ions, *Solid State Ionics.* 176 (2005) 1695–1699. doi:10.1016/j.ssi.2005.04.019.
- [117] M. Smeu, M.S. Hossain, Z. Wang, V. Timoshevskii, K.H. Bevan, K. Zaghbi, Theoretical investigation of Chevrel phase materials for cathodes accommodating Ca^{2+} ions, *J. Power Sources.* 306 (2016) 431–436. doi:10.1016/j.jpowsour.2015.12.009.
- [118] a Mitelman, M.D. Levi, E. Lancry, E. Levi, D. Aurbach, New cathode materials for rechargeable Mg batteries: fast Mg ion transport and reversible copper extrusion in $Cu_yMo_6S_8$ compounds, *Chem. Commun.* (2007) 4212–4214. doi:10.1039/b710743a.
- [119] J.P. Pereira-Ramos, R. Messina, J. Perichon, Electrochemical formation of a magnesium vanadium bronze $Mg_xV_2O_5$ in sulfone-based electrolytes at $150^\circ C$, *J. Electroanal. Chem.* 218 (1987) 241–249. doi:10.1016/0022-0728(87)87019-5.
- [120] P. Novák, J. Desilvestro, Electrochemical Insertion of Magnesium in Metal Oxides and Sulfides from Aprotic Electrolytes, *J. Electrochem. Soc.* 140 (1993) 140. doi:10.1149/1.2056075.
- [121] P. Novák, W. Scheifele, F. Joho, O. Haas, Electrochemical Insertion of Magnesium into Hydrated Vanadium Bronzes, *J. Electrochem. Soc.* 142 (1995) 2544. doi:10.1149/1.2050051.
- [122] G. Gershinsky, H.D. Yoo, Y. Gofer, D. Aurbach, Electrochemical and spectroscopic analysis of Mg^{2+} intercalation into thin film electrodes of layered oxides: V_2O_5 and MoO_3 , *Langmuir.* 29 (2013) 10964–10972. doi:10.1021/la402391f.
- [123] T.S. Arthur, K. Kato, J. Germain, J. Guo, P.-A. Glans, Y.-S. Liu, D. Holmes, X. Fan, F. Mizuno, Amorphous $V_2O_5 - P_2O_5$ as high-voltage cathodes for magnesium batteries, *Chem. Commun.* 51 (2015) 15657–15660. doi:10.1039/C5CC07161E.
- [124] Y. Cheng, Y. Shao, V. Raju, X. Ji, B.L. Mehdi, K.S. Han, M.H. Engelhard, G. Li, N.D. Browning, K.T. Mueller, J. Liu, Molecular Storage of Mg Ions with Vanadium Oxide Nanoclusters, *Adv. Funct. Mater.* 26 (2016) 3446–3453. doi:10.1002/adfm.201505501.
- [125] R. Zhang, X. Yu, K.W. Nam, C. Ling, T.S. Arthur, W. Song, A.M. Knapp, S.N. Ehrlich, X.Q. Yang, M. Matsui, α - MnO_2 as a cathode material for rechargeable Mg batteries, *Electrochem. Commun.* 23 (2012) 110–113. doi:10.1016/j.elecom.2012.07.021.
- [126] J.S. Kim, W.S. Chang, R.H. Kim, D.Y. Kim, D.W. Han, K.H. Lee, S.S. Lee, S.G. Doo, High-capacity nanostructured manganese dioxide cathode for rechargeable magnesium ion batteries, *J. Power Sources.* 273 (2015) 210–215. doi:10.1016/j.jpowsour.2014.07.162.

- [127] S. Rasul, S. Suzuki, S. Yamaguchi, M. Miyayama, High capacity positive electrodes for secondary Mg-ion batteries, *Electrochim. Acta.* 82 (2012) 243–249. doi:10.1016/j.electacta.2012.03.095.
- [128] T.S. Arthur, R. Zhang, C. Ling, P.A. Glans, X. Fan, J. Guo, F. Mizuno, Understanding the electrochemical mechanism of K- α MnO₂ for magnesium battery cathodes, *ACS Appl. Mater. Interfaces.* 6 (2014) 7004–7008. doi:10.1021/am5015327.
- [129] C. Ling, R. Zhang, T.S. Arthur, F. Mizuno, How General is the Conversion Reaction in Mg Battery Cathode: A Case Study of the Magnesium of α -MnO₂, *Chem. Mater.* 27 (2015) 5799–5807. doi:10.1021/acs.chemmater.5b02488.
- [130] T. Ichitsubo, T. Adachi, S. Yagi, T. Doi, Potential positive electrodes for high-voltage magnesium-ion batteries, *J. Mater. Chem.* 21 (2011) 11764. doi:10.1039/c1jm11793a.
- [131] Y. Nuli, J. Yang, J. Wang, Y. Li, Electrochemical Intercalation of Mg²⁺ in Magnesium Manganese Silicate and Its Application as High-Energy Rechargeable Magnesium Battery Cathode, *J. Phys. Chem. C.* 113 (2009) 12594–12597.
- [132] Y. NuLi, Y. Zheng, Y. Wang, J. Yang, J. Wang, Electrochemical intercalation of Mg²⁺ in 3D hierarchically porous magnesium cobalt silicate and its application as an advanced cathode material in rechargeable magnesium batteries, *J. Mater. Chem.* 21 (2011) 12437. doi:10.1039/c1jm10485c.
- [133] Y. NuLi, J. Yang, Y. Li, J. Wang, Mesoporous magnesium manganese silicate as cathode materials for rechargeable magnesium batteries., *Chem. Commun.* 46 (2010) 3794–3796. doi:10.3724/SP.J.1077.2011.00129.
- [134] Y. Orikasa, T. Masese, Y. Koyama, T. Mori, M. Hattori, K. Yamamoto, T. Okado, Z.-D. Huang, T. Minato, C. Tassel, J. Kim, Y. Kobayashi, T. Abe, H. Kageyama, Y. Uchimoto, High energy density rechargeable magnesium battery using earth-abundant and non-toxic elements., *Sci. Rep.* 4 (2014) 5622. doi:10.1038/srep05622.
- [135] J. Wu, G. Gao, G. Wu, B. Liu, H. Yang, X. Zhou, J. Wang, MgVPO₄F as a one-dimensional Mg-ion conductor for Mg ion battery positive electrode: a first principles calculation, *RSC Adv.* 4 (2014) 15014–15017. doi:10.1039/C4RA00199K.
- [136] Z. Huang, T. Masese, Y. Orikasa, T. Mori, T. Minato, C. Tassel, Y. Kobayashi, H. Kageyama, Y. Uchimoto, MgFePO₄F as a feasible cathode material for magnesium batteries, *J. Mater. Chem. A.* 2 (2014) 11578–11582. doi:10.1039/c4ta01779j.
- [137] V. Mathew, S. Kim, J. Kang, J. Gim, J. Song, J.P. Baboo, W. Park, D. Ahn, J. Han, L. Gu, Y. Wang, Y.-S. Hu, Y.-K. Sun, J. Kim, Amorphous iron phosphate: potential host for various charge carrier ions, *NPG Asia Mater.* 6 (2014) e138. doi:10.1038/am.2014.98.
- [138] X. Sun, P. Bonnicksen, V. Duffort, M. Liu, G. Ceder, L.F. Nazar, A High Capacity Thiospinel Cathode for Mg Batteries, *Energy Environ. Sci.* 9 (2016) 2273–2277. doi:10.1039/C6EE00724D.
- [139] Z.-L. Tao, L.-N. Xu, X.-L. Gou, J. Chen, H.-T. Yuan, TiS₂ nanotubes as the cathode materials of Mg-ion batteries., *Chem. Commun.* (2004) 2080–2081. doi:10.1039/b403855j.
- [140] K. Taniguchi, Y. Gu, Y. Katsura, T. Yoshino, H. Takagi, Rechargeable Mg battery cathode TiS₃ with d-p orbital hybridized electronic structures, *Appl. Phys. Express.* 9 (2016) 1–5. doi:10.7567/APEX.9.011801.

- [141] B. Liu, T. Luo, G. Mu, X. Wang, D. Chen, G. Shen, Rechargeable Mg-Ion Batteries Based on WSe₂ Nanowire Cathodes, *ACS Nano*. 7 (2013) 8051–8058. doi:10.1021/nn4032454.
- [142] Z. Zhao-Karger, X.-M. Lin, C. Bonatto Minella, D. Wang, T. Diemant, R.J. Behm, M. Fichtner, Selenium and selenium-sulfur cathode materials for high-energy rechargeable magnesium batteries, *J. Power Sources*. 323 (2016) 213–219. doi:10.1016/j.jpowsour.2016.05.034.
- [143] Y. Liang, Z. Tao, J. Chen, Organic electrode materials for rechargeable lithium batteries, *Adv. Energy Mater.* 2 (2012) 742–769. doi:10.1002/aenm.201100795.
- [144] J. Bitenc, K. Pirnat, T. Bancic, M. Gaberscek, B. Genorio, A. Randon-Vitanova, R. Dominko, Anthraquinone-Based Polymer as Cathode in Rechargeable Magnesium Batteries, *ChemSusChem*. 8 (2015) 4128–4132. doi:10.1002/cssc.201500910.
- [145] J. Bitenc, K. Pirnat, G. Mali, B. Novosel, A.R. Vitanova, R. Dominko, Poly(hydroquinoyl-benzoquinonyl sulfide) as an active material in Mg and Li organic batteries, *Electrochem. Commun.* 69 (2016) 1–5. doi:10.1016/j.elecom.2016.05.009.
- [146] N. Wu, Y.-C. Lyu, R.-J. Xiao, X. Yu, Y.-X. Yin, X.-Q. Yang, H. Li, L. Gu, Y.-G. Guo, A highly reversible, low-strain Mg-ion insertion anode material for rechargeable Mg-ion batteries, *NPG Asia Mater.* 6 (2014) e120. doi:10.1038/am.2014.61.
- [147] T.S. Arthur, N. Singh, M. Matsui, Electrodeposited Bi, Sb and Bi_{1-x}Sb_x alloys as anodes for Mg-ion batteries, *Electrochem. Commun.* 16 (2012) 103–106. doi:10.1016/j.elecom.2011.12.010.
- [148] R. A. DiLeo, Q. Zhang, A. C. Marschilok, K.J. Takeuchi, E.S. Takeuchi, Composite Anodes for Secondary Magnesium Ion Batteries Prepared via Electrodeposition of Nanostructured Bismuth on Carbon Nanotube Substrates, *ECS Electrochem. Lett.* 4 (2014) A10–A14. doi:10.1149/2.0081501eel.
- [149] R. Zhang, F. Mizuno, Preparation of high energy-density electrode materials for rechargeable magnesium batteries, *US 2014/0322595 A1*, 2014.
- [150] P.G. Bruce, B. Scrosati, J.-M. Tarascon, Nanomaterials for rechargeable lithium batteries, *Angew. Chemie*. 47 (2008) 2930–46. doi:10.1002/anie.200702505.
- [151] H. Tian, F. Xin, X. Wang, W. He, W. Han, High capacity group-IV elements (Si, Ge, Sn) based anodes for lithium-ion batteries, *J. Mater.* 1 (2015) 153–169. doi:10.1016/j.jmat.2015.06.002.
- [152] B. Wang, B. Luo, X. Li, L. Zhi, The dimensionality of Sn anodes in Li-ion batteries, *Mater. Today*. 15 (2012) 544–552. doi:10.1016/S1369-7021(13)70012-9.
- [153] R. Raccichini, A. Varzi, S. Passerini, B. Scrosati, The role of graphene for electrochemical energy storage., *Nat. Mater.* 14 (2015) 271–9. doi:10.1038/nmat4170.
- [154] J. Hassoun, B. Scrosati, Review—Advances in Anode and Electrolyte Materials for the Progress of Lithium-Ion and beyond Lithium-Ion Batteries, *J. Electrochem. Soc.* 162 (2015) A2582–A2588. doi:10.1149/2.0191514jes.
- [155] <http://www.sony.net/SonyInfo/News/Press/200502/05-006E/>.
- [156] N. Loeffler, D. Bresser, S. Passerini, Secondary Lithium-Ion Battery Anodes: From First Commercial Batteries to Recent Research Activities, *Johnson Matthey Technol. Rev.* 59 (2015) 34–44. doi:10.1595/205651314X685824.

- [157] O.I. Malyi, T.L. Tan, S. Manzhos, In search of high performance anode materials for Mg batteries: Computational studies of Mg in Ge, Si, and Sn, *J. Power Sources*. 233 (2013) 341–345. doi:10.1016/j.jpowsour.2013.01.114.
- [158] L.R. Parent, Y. Cheng, P. V. Sushko, Y. Shao, J. Liu, C.M. Wang, N.D. Browning, Realizing the full potential of insertion anodes for Mg-ion batteries through the nanostructuring of Sn, *Nano Lett.* 15 (2015) 1177–1182. doi:10.1021/nl5042534.
- [159] A. Darwiche, C. Marino, M.T. Sougrati, B. Fraisse, L. Stievano, L. Monconduit, Better cycling performances of bulk Sb in Na-ion batteries compared to Li-ion systems: an unexpected electrochemical mechanism, *J. Am. Chem. Soc.* 134 (2012) 20805–20811. doi:10.1021/ja310347x.
- [160] Y. Cheng, Y. Shao, L.R. Parent, M.L. Sushko, G. Li, P. V. Sushko, N.D. Browning, C. Wang, J. Liu, Interface Promoted Reversible Mg Insertion in Nanostructured Tin-Antimony Alloys, *Adv. Mater.* 27 (2015) 6598–6605. doi:10.1002/adma.201502378.
- [161] A. Balinska, V. Kordan, R. Misztal, V. Pavlyuk, Electrochemical and thermal insertion of lithium and magnesium into Zr_5Sn_3 , *J. Solid State Electrochem.* 19 (2015) 2481–2490. doi:10.1007/s10008-015-2895-7.
- [162] M.N. Obrovac, V.L. Chevrier, Alloy Negative Electrodes for Li-Ion Batteries M.N. Obrovac, *Chem. Rev.* 114 (2014) 11444–11502. doi:10.1021/cr500207g.
- [163] R. Alcantara, M. Tillard-Charbonnel, L. Spina, C. Belin, J.L. Tirado, Electrochemical reactions of lithium with Li_2ZnGe and Li_2ZnSi , *Electrochim. Acta.* 47 (2002) 1115–1120.
- [164] K. Periyapperuma, T.T. Tran, M.I. Purcell, M.N. Obrovac, The Reversible Magnesiumation of Pb, *Electrochim. Acta.* 165 (2015) 162–165. doi:10.1016/j.electacta.2015.03.006.
- [165] F. Delogu, G. Mulas, L. Schiffini, G. Cocco, Mechanical work and conversion degree in mechanically induced processes, *Mater. Sci. Eng. A.* 382 (2004) 280–287. doi:10.1016/j.msea.2004.05.047.
- [166] A. Calka, Formation of titanium and zirconium nitrides by mechanical alloying, *Appl. Phys. Lett.* 59 (1991) 1568–1569. doi:10.1063/1.106285.
- [167] C. Suryanarayana, Mechanical alloying and milling, *Prog. Mater. Sci.* 46 (2001) 1–184. doi:10.1016/S0079-6425(99)00010-9.
- [168] C. Suryanarayana, *Mechanical Alloying and Milling*, 10th ed., New York, 2004.
- [169] J.S. Benjamin, Dispersion strengthened superalloys by mechanical alloying, *Metall. Trans.* 1 (1970) 2943–2951. doi:10.1007/BF03037835.
- [170] H.F. Merrick, L.R. Curwick, Y.G. Kim, Development of oxide dispersion strengthened turbine blade alloy by mechanical alloying, 1977.
- [171] C.C. Koch, O.B. Cavin, C.G. McKamey, J.O. Scarbrough, Preparation of “amorphous” $Ni_{60}Nb_{40}$ by mechanical alloying, *Applied Phys. Lett.* 43 (1983) 1017.
- [172] H. Gleiter, Nanocrystalline Materials, *Prog. Mater. Sci.* 33 (1989) 223–315. doi:10.1016/0079-6425(89)90001-7.
- [173] V. V. Tcherdyntsev, S.D. Kaloshkin, E. V. Shelekhov, A.I. Salimon, S. Sartori, G. Principi, Quasicrystalline phase formation in the mechanically alloyed Al-Cu-Fe system, *Intermetallics*. 13 (2005) 841–847. doi:10.1016/j.intermet.2005.01.009.

- [174] E. Ivanov, T. Grigorieva, G. Golubkova, V. Boldyrev, A.B. Fasman, O.T. Kalinina, Synthesis of Nickel Alumides by mechanical alloying, *Mater. Lett.* 7 (1988) 51–54.
- [175] S.L. James, C.J. Adams, C. Bolm, D. Braga, P. Collier, T. Friscic, F. Grepioni, K.D.M. Harris, G. Hyett, W. Jones, A. Krebs, J. Mack, L. Maini, A.G. Orpen, I.P. Parkin, W.C. Shearouse, J.W. Steed, D.C. Waddell, T. Friščić, F. Grepioni, K.D.M. Harris, G. Hyett, W. Jones, A. Krebs, J. Mack, L. Maini, A.G. Orpen, I.P. Parkin, W.C. Shearouse, J.W. Steed, D.C. Waddell, Mechanochemistry: Opportunities for New and Cleaner Synthesis, *Chem. Soc. Rev.* 41 (2012) 413–447. doi:10.1039/c1cs15171a.
- [176] G.-W. Wang, Mechanochemical organic synthesis., *Chem. Soc. Rev.* 42 (2013) 7668–700. doi:10.1039/c3cs35526h.
- [177] V. V. Boldyrev, Mechanochemical modification and synthesis of drugs, *J. Mater. Sci.* 39 (2004) 5117–5120. doi:10.1023/B:JMISC.0000039193.69784.1d.
- [178] M.K. Beyer, H. Clausen-Schaumann, Mechanochemistry: The mechanical activation of covalent bonds, *Chem. Rev.* 105 (2005) 2921–2948. doi:10.1021/cro30697h.
- [179] A. Le Bail, H. Duroy, J.L. Fourquet, Ab-initio structure determination of LiSbWO₆ by X-ray powder diffraction, *Mater. Res. Bull.* 23 (1988) 447–452. doi:10.1016/0025-5408(88)90019-20.
- [180] H.M. Rietveld, A profile refinement method for nuclear and magnetic structures, *J. Appl. Crystallogr.* 2 (1969) 65–71. doi:10.1107/S0021889869006558.
- [181] P. Antitomaso, B. Fraisse, M.T. Sougrati, F. Morato-Lallemand, S. Biscaglia, D. Aymé-Perrot, P. Girard, L. Monconduit, Ultra-fast dry microwave preparation of SnSb used as negative electrode material for Li-ion batteries, *J. Power Sources.* 325 (2016) 346–350. doi:10.1016/j.jpowsour.2016.06.010.
- [182] N. Pour, Y. Gofer, D.T. Major, D. Aurbach, Structural analysis of electrolyte solutions for rechargeable Mg batteries by stereoscopic means and DFT calculations, *J. Am. Chem. Soc.* 133 (2011) 6270–6278. doi:10.1021/ja1098512.
- [183] EC-Lab Software : Techniques and Applications, 2014.
- [184] J.B. Leriche, S. Hamelet, J. Shu, M. Morcrette, C. Masquelier, G. Ouvrard, M. Zerrouki, P. Soudan, S. Belin, E. Elkaïm, F. Baudalet, An Electrochemical Cell for Operando Study of Lithium Batteries Using Synchrotron Radiation, *J. Electrochem. Soc.* 157 (2010) A606. doi:10.1149/1.3355977.
- [185] R.W.G. Wyckoff, *Crystal Structures*, 1963.
- [186] A.A. Nayeb-Hashemi, J.B. Clark, The Mg-Sn (Magnesium-Tin) System, *Bull. Alloy Phase Diagrams.* 5 (1984) 466–476.
- [187] H. Okamoto, Mg-Sb (Magnesium-Antimony), *J. Phase Equilibria Diffus.* 31 (2010) 1. doi:10.1007/s11669-010-9784-7.
- [188] L. Baggetto, P. Ganesh, C.-N. Sun, R. a. Meisner, T. a. Zawodzinski, G.M. Veith, Intrinsic thermodynamic and kinetic properties of Sb electrodes for Li-ion and Na-ion batteries: experiment and theory, *J. Mater. Chem. A.* 1 (2013) 7985–7994. doi:10.1039/c3ta11568b.
- [189] H. Okamoto, Phase Diagram Updates, *J. Phase Equilibria.* 12 (1991) 390. doi:10.1007/BF02649933.
- [190] F. Murgia, L. Stievano, L. Monconduit, R. Berthelot, Insight into the electrochemical

- behavior of micrometric Bi and Mg₃Bi₂ as high performance negative electrodes for Mg batteries, *J. Mater. Chem. A*. 3 (2015) 16478–16485. doi:10.1039/C5TA04077A.
- [191] E. Zintl, E. Husemann, *Z. Phys. Chem.*, *Z. Phys. Chem.* 21 (1933) 138.
- [192] S. Yagi, A. Tanaka, Y. Ichikawa, T. Ichitsubo, E. Matsubara, Effects of water content on magnesium deposition from a Grignard reagent-based tetrahydrofuran electrolyte, *Res. Chem. Intermed.* 40 (2014) 3–9. doi:10.1007/s11164-013-1449-9.
- [193] N. Singh, M. Matsui, Indium-Tin binary anodes for rechargeable Magnesium-ion batteries, US 2013/0323582 A1, 2008.
- [194] F. Murgia, E.T. Weldekidan, L. Stievano, L. Monconduit, R. Berthelot, First investigation of indium-based electrode in Mg battery, *Electrochem. Commun.* 60 (2015) 56–59. doi:10.1016/j.elecom.2015.08.007.
- [195] A.A. Nayeb-Hashemi, J.B. Clark, The In-Mg (Indium-Magnesium) System, *Bull. Alloy Phase Diagrams.* 6 (1985) 149–160.
- [196] N. Ino, M. Hirabayashi, S. Ogawa, X-ray and Thermal Analyses of the Order-Disorder Transition in Magnesium-Indium Alloys, *Trans. Jap. Inst. Met.* 6 (1965) 172–178.
- [197] H. Iwasaki, X-Ray Study of the Compression of the Alloy MgIn, *Acta Metall.* 26 (1978) 647–650.
- [198] ASM Alloy Phase Diagram Database, n.d.
- [199] R.W.G. Wyckoff, *Crystal Structures*, *Cryst. Struct.* 1 (1963) 7.
- [200] M. Hansen, K. Anderko, *Constitution of Binary Alloys*, McGraw Hill Book Co., New York, 1958.
- [201] G.E. Smith, R. Wolfe, Thermoelectric properties of bismuth-antimony alloys, *J. Appl. Phys.* 33 (1962) 841–846. doi:10.1063/1.1777178.
- [202] W.M. Yim, A. Amith, BiSb alloys for magneto-thermoelectric and thermomagnetic cooling, *Solid State Electron.* 15 (1972). doi:10.1016/0038-1101(72)90173-6.
- [203] B. Lenoir, M. Cassart, J.P. Michenaud, H. Scherrer, S. Scherrer, Transport properties of Bi-rich Bi-Sb alloys, *J. Phys. Chem. Solids.* 57 (1996) 89–99. doi:10.1016/0022-3697(95)00148-4.
- [204] M.A. Short, J.J. Schott, Preparation of Homogeneous Single-Crystal Bismuth-Antimony Alloys, *J. Appl. Phys.* 36 (1965) 659. doi:10.1063/1.1714055.
- [205] B. Lenoir, A. Demouge, D. Perrin, H. Scherrer, S. Scherrer, M. Cassart, J.P. Michenaud, Growth of Bi_{1-x}Sb_x alloys by the traveling heater method, *J. Phys. Chem. Solids.* 56 (1995) 99–105. doi:10.1016/0022-3697(94)00142-1.
- [206] R. Martin-Lopez, M. Zandon, H. Scherrer, Mechanical alloying of Bi₉₀Sb₁₀, *J. Mater. Sci. Lett.* 15 (1996) 16–18.
- [207] D. Cadavid, J.E. Rodriguez, Thermoelectric properties of Bi-Sb samples grown by mechanical alloy, *Phys. Status Solidi C Conf.* 2 (2005) 3677–3680. doi:10.1002/pssc.200461721.
- [208] P. Cucka, C.S. Barrett, The crystal structure of Bi and of solid solutions of Pb, Sn, Sb and Te in Bi, *Acta Crystallogr.* 15 (1962) 865–872. doi:10.1107/S0365110X62002297.

- [209] W.P. Binnie, The structural crystallography of indium bismuthide, *Acta Crystallogr.* 9 (1956) 686–687.
- [210] K. Takano, T. Sato, Thermal Expansion Of InBi, *Phys. Lett.* 44 (1973) 309–310.
- [211] R. Kubiak, Röntgenographische Untersuchungen der intermetallischen Phasen In_5Bi_3 , In_2Bi und InBi zwischen +60 und -135°C, *Z. Anorg. Allg. Chem.* 267 (1977) 261–267.
- [212] R. Kubiak, J. Janczak, Rietveld X-ray powder analysis of InBi crystalline structure at low temperatures Ryszard, *J. Alloy. Compd.* 196 (1993) 117–119.
- [213] F. Murgia, L. Monconduit, L. Stievano, R. Berthelot, Electrochemical magnesiumation of the intermetallic InBi through conversion-alloying mechanism, *Electrochim. Acta.* 209 (2016) 730–736. doi:10.1016/j.electacta.2016.04.020.
- [214] K. Hiraga, M. Koiwa, M. Hirabayashi, Constitution of the Indium-rich portion of the Indium-Magnesium system, *J. Less-Common Met.* 5 (1968).
- [215] P.D. Currie, T.R. Finlayson, T.F. Smith, The Phase Diagram For In-rich In-Bi Alloys, *J. Less-Common Met.* 62 (1978) 13–24.
- [216] Y. Cheng, Y. Shao, L.R. Parent, M.L. Sushko, G. Li, P. V. Sushko, N.D. Browning, C. Wang, J. Liu, Interface Promoted Reversible Mg Insertion in Nanostructured Tin-Antimony Alloys, *Adv. Mater.* (2015) n/a-n/a. doi:10.1002/adma.201502378.
- [217] S. Ha, Y. Lee, S.W. Woo, B. Koo, J. Kim, J. Cho, K.T. Lee, N. Choi, Magnesium (II) Bis (trifluoromethane sulfonyl) Imide-Based Electrolytes with Wide Electrochemical Windows for Rechargeable Magnesium Batteries, *ACS Appl. Mater. Interfaces.* 6 (2014) 4063–4073.
- [218] S.-H. Choi, J.-S. Kim, S.-G. Woo, W. Cho, S.Y. Choi, J. Choi, K.-T. Lee, M.-S. Park, Y.-J. Kim, Role of Cu in Mo_6S_8 and Cu Mixture Cathodes for Magnesium Ion Batteries, *ACS Appl. Mater. Interfaces.* 7 (2015) 7016–7024. doi:10.1021/am508702j.
- [219] S. Kondo, K. Takada, Y. Yamamura, H. Gyoten, S. Yoshida, A new synthetic method for Chevrel-phase compounds, *Solid State Ionics.* 57 (1992) 147–151.
- [220] J.W. Lekse, T.J. Stagger, J.A. Aitken, Microwave Metallurgy: Synthesis of Intermetallic Compounds via Microwave Irradiation, *Chem. Mater.* 19 (2007) 3601–3603. doi:10.1021/cm0707410.
- [221] A. Kadhim, A. Hmood, H. Abu Hassan, Characterizations of solid-state microwave-synthesized Sb_2Te_3 -based alloys with various compositions of bismuth in $\text{Bi}_{2x}\text{Sb}_{2(1-x)}\text{Te}_3$, *Mater. Sci. Semicon. Proc.* 15 (2012) 549–554. doi:10.1016/j.mssp.2012.04.006.
- [222] F. Murgia, P. Antitomaso, L. Stievano, L. Monconduit, R. Berthelot, Express and low-cost microwave synthesis of the ternary Chevrel phase $\text{Cu}_2\text{Mo}_6\text{S}_8$ for application in rechargeable magnesium batteries, *J. Solid State Chem.* 242 (2016) 151–154. doi:10.1016/j.jssc.2016.07.022.
- [223] G. Gershinsky, O. Haik, G. Salitra, J. Grinblat, E. Levi, G. Daniel Nessim, E. Zinigrad, D. Aurbach, Ultra fast elemental synthesis of high yield copper Chevrel phase with high electrochemical performance, *J. Solid State Chem.* 188 (2012) 50–58. doi:10.1016/j.jssc.2012.01.016.
- [224] Y. Gofer, D. Aurbach, M.D. Levi, E. Lancry, H. Gizbar, Z. Lu, E. Levi, Kinetic and Thermodynamic Studies of Mg^{2+} and Li^+ Ion Insertion into the Mo_6S_8 Chevrel Phase, *J. Electrochem. Soc.* 151 (2004) 1044–1051. doi:10.1149/1.1758811.

- [225] Y. Cheng, L.R. Parent, Y. Shao, C. Wang, V.L. Sprenkle, G. Li, J. Liu, Facile synthesis of chevrel phase nanocubes and their applications for multivalent energy storage, *Chem. Mater.* 26 (2014) 4904–4907. doi:10.1021/cm502306c.
- [226] X. Sun, P. Bonnicksen, L.F. Nazar, Layered TiS_2 Positive Electrode for Mg Batteries, *ACS Energy Lett.* 1 (2016) 297–301. doi:10.1021/acsenergylett.6b00145.
- [227] F. Murgia, L. Monconduit, L. Stievano, R. Berthelot, Electrochemical magnesianation of the intermetallic InBi through conversion-alloying mechanism, *Electrochim. Acta.* 209 (2016) 730–736. doi:10.1016/j.electacta.2016.04.020.
- [228] F. Cheng, J. Chen, Metal–air batteries: from oxygen reduction electrochemistry to cathode catalysts, *Chem. Soc. Rev.* 41 (2012) 2172. doi:10.1039/c1cs15228a.
- [229] C.R. Hauser, H.G.J. Walker, Condensation of Certain Esters by Means of Diethylaminomagnesium Bromide, *J. Am. Chem. Soc.* 69 (1947) 295–297. doi:10.1021/ja01194a040.
- [230] E.N. Keyzer, H.F.J. Glass, Z. Liu, P.M. Bayley, S.E. Dutton, C.P. Grey, D.S. Wright, $\text{Mg}(\text{PF}_6)_2$ -Based Electrolyte Systems: Understanding Electrolyte-Electrode Interactions for the Development of Mg-Ion Batteries, *J. Am. Chem. Soc.* 138 (2016) 8682–8685. doi:10.1021/jacs.6b04319.